UNIVERSITY OF SOUTHAMPTON

FACULTY OF ENGINEERING AND THE ENVIRONMENT

Institute of Sound and Vibration Research

Active Vibration Control of Doubly-Curved Panels

by

Delphine Suzanne Nourzad

Thesis for the degree of Doctor of Philosophy

January 2014

UNIVERSITY OF SOUTHAMPTON

ABSTRACT

FACULTY OF ENGINEERING AND THE ENVIRONMENT

Doctor of Philosophy

ACTIVE VIBRATION CONTROL OF DOUBLY-CURVED PANELS

by Delphine Suzanne Nourzad

This thesis considers active control of the vibration of doubly-curved panels. Such panels are widely used in vehicles such as cars and aircraft, whose vibration is becoming more problematic as the weight of these vehicles is reduced to control their CO_2 emissions. The dynamic properties of doubly-curved panels are first considered and an analytic model which includes in-plane inertia is introduced. The results of this analytical model are compared with those from numerical modelling. Of particular note is the clustering of lower-order modes as the curvature becomes more significant. The influence of these changes in dynamics is then studied by simulating the performance of a velocity feedback controller using an inertial actuator. The feasibility of implementing such an active control system on a car roof panel is then assessed.

Experiments and simulations are also conducted on a panel, mounted on one side of a rigid enclosure, which is curved by pressurising the enclosure. The active control of vibration on this panel is then implemented using compensated velocity feedback control and novel inertial actuators. It is found that the performance of the feedback control initially improves as the curvature increases, since the fundamental natural frequency of the panel becomes larger compared with the actuator resonance frequency, but then the performance is significantly degraded for higher levels of curvature, since the natural frequencies of many of the panel modes cluster together. Finally, the integration of a compensator filter in the control system ensures the robustness of the system, despite changes in curvature, which makes it a good candidate for future multi-channel implementations.

Contents

List of tables

List of figures

Declaration of Authorship

I, Delphine Suzanne Nourzad, declare that the thesis entitled

Active Control of Vibration in Doubly-Curved Panels

and the work presented in the thesis are both my own, and have been generated by me as the result of my own original research. I confirm that:

- This work was done wholly or mainly while in candidature for a research degree at this University;
- Where any part of this thesis has previously been submitted for a degree or any other qualification at this University or any other institution, this has been clearly stated;
- Where I have consulted the published work of others, this is always clearly attributed;
- Where I have quoted from the work of others, the source is always given. With the exception of such quotations, this thesis is entirely my own work;
- I have acknowledged all main sources of help;
- Where the thesis is based on work done by myself jointly with others, I have made clear exactly what was done by others and what I have contributed myself;

- Parts of this work have been published as:

1. D.S. Nourzad, S.J. Elliott, E. Rustighi and J. Rohlfing, "Active Vibration Control of Curved Panels", in *Proceedings of the 8th International Conference on Structural Dynamics EURODYN2011*, Leuven, Belgium, 2011.

2. D.S. Nourzad, S.J. Elliott, M. Ghanchi-Tehrani and E. Rustighi, "Active Vibration Control of a Doubly-Curved Panel Under Pressurisation", in

Proceedings of the 19th International Congress on Sound and Vibration ICSV2012, Vilnius, Lithuania, 2012.

3. Y. Zhang, X. Zhang, S.J. Elliot and D.S. Nourzad, "Active Vibration Control of a Double-Curved Shell with a Laminated Polyvinylidene Fluoride Actuator", *International Journal of Aerospace and Lightweight Structures*, **2**(2), 199-219, 2012.

Signed: ……..

Date: …….

Acknowledgements

First and foremost, I would like to thank my supervisor Professor Steve Elliott for giving me the opportunity to work in the field of active control in the Signal Processing and Control Group at the ISVR and benefit from his deep knowledge and expertise in this field. Not only has he provided me with technical guidance throughout the course of my PhD research, but he has also encouraged and motivated me during the difficult times.

Special thanks go to all the people who have helped me in different ways towards the completion of thesis research and my years at the ISVR:

- The funding for this PhD research which was provided by the "Green City Car Project" project, as part of the European commission FP7 programme.
- Professor Paolo Gardonio for his help and support during the first months of my PhD.
- Dr. Emiliano Rustighi, my second supervisor for the first and second years, for his help and support and for teaching me about finite element analysis and ANSYS.
- Dr. Maryam Ghandchi-Tehrani, my second supervisor for the last year, for her help in using LMS for experimental modal analysis.
- Dr. Jens Rohlfing for teaching me how to conduct experiments in my first year and reminding me to check that everything is plugged in before measurements!
- The technicians at the ISVR, Antony Wood, Alan Waddilove and Andy Westerman, for providing me with equipment and parts and advice with electrical components, Phil Oxborrow, Chris Oliver and Steve White, who have helped me with experimental rigs.
- Dr. Anna Barney for allowing me to use her air compression tank for my pressurisation experiments.
- The ISVR for providing me with a welcoming environment and facilities to conduct my research.
- The ISVR secretaries, Maureen Mew, Sue Brindle, Sue Greenwood, Jon Lawn and Natasha Webb for their support with administrative, university, and sometimes even personal matters.

Finally, a very big thank you to my family and to my close friends Hugh Hopper, Mark Abbott, Natasha Fairbairn and Ken Mimasu for making the PhD years very enjoyable and to Jordan Cheer for all your help and patience throughout the thesis and most importantly for putting up with my difficult moods!

Nomenclature

A	Area
A_e	Area of a single element
a	Cylindrical shell radius
a_n	Complex amplitude of the nth acoustic mode
b	Beam width
C	Damping coefficient
C'	Modified damping coefficient
C_a	Damping coefficient of the actuator
c	Phase speed
c_0	Speed of sound (in air)
c_F	Flexural phase speed
c_L	Longitudinal phase speed
D	Bending stiffness
E	Young modulus of elasticity
$E(s)$	Error signal
E_k	Structural kinetic energy
E_p	Acoustic potential energy
e_1, e_2, e_3	Acoustic modal normalisation factors
$F_p(s)$	Laplace transform of primary disturbance

$F_s(s)$	Laplace transform of secondary excitation
f	Frequency
$\mathbf{f_a}$	Vector of actuator force
$\mathbf{f_b}$	Vector of forces exerted on the elements of the cavity
$\mathbf{f_c}$	Vector of control forces $[N_c \times 1]$
$f_{critical}$	Critical frequency
$\mathbf{f_e}$	Vector of point forces applied at the centre of each element $[N_e \times 1]$
$\mathbf{f_{M_a}}$	vector of the force exerted by the moving mass to the actuator spring
f_r	Ring frequency
$G(s)$	Laplace transform of the plant transfer function or open-loop response
$\mathbf{G_{ca}}$	Vector of the open-loop response of a feedback control system with actuator
$\mathbf{G_{ee}}$	Matrix containing the point and transfer mobility functions for all the elements of the panel
g	Feedback loop gain
g_a	Acceleration gain
g_{margin}	Gain margin
g_d	Displacement gain
g_v	Velocity gain
$\mathbf{H}$	Diagonal matrix of control system gains

$H(s)$	Feedback or feedforward controller transfer function
h	Shell or panel thickness
$\mathbf{I}$	Identity matrix
I	Second moment of inertia
i	Index
i_a	Current of the actuator coil
j	$\sqrt{-1}$
K	Stiffness coefficient
K'	Modified stiffness coefficient
K_a	Stiffness coefficient of the actuator
k_0	Acoustic wavenumber
k_F	Flexural wavenumber
k_L	Longitudinal wavenumber
k_{f_n}	Bending wavenumber of the nth natural frequency
k_x	Wavenumber in the x-direction
k_y	Wavenumber in the y-direction
L_e	Actuator coil inductance
$L_{i,j}$	Elements of Eigen matrix
l_x	Shell, panel or enclosure length
l_y	Shell, panel or enclosure width

l_z	Enclosure height
M	Mass
M'	Modified mass
M_a	Inertial actuator moving mass
M_x	Bending moment
M_y	Bending moment
M_{base}	Base mass
M_e	Mass of each element
M_{proof}	Proof mass
m	Modal index
N	Tensile force
N_e	Number of elements over the area
N_v	Number of elements over the volume
N_x	Tensile force in the x-direction
N_y	Tensile force in the y-direction
n	Modal index
n_1, n_2, n_3	Acoustic modal integers
$P(s)$	Laplace transform of the primary path for the disturbance
$\mathbf{P}_{\mathbf{rad}}$	Vector of radiated sound power

P_{rad}	Radiated sound power
p_a	External force or distributed load expressed in terms of pressure
$p(x,t)$	External distributed load on a beam
$p_0(x,y,\omega)$	Near field acoustic pressure
$p(x,\omega)$	Complex acoustic pressure
$p(x,y,t)$	Sound pressure field
$p_i(\omega)$	Complex pressure phasor
$\mathbf{q_e}$	Vector of elemental source strength
q_p	Acoustic source strength
q_v	Source strength of individual monopoles
q_{vol}	Source strength distribution inside the enclosure
$\mathbf{R_{rad}}$	Radiation resistance matrix
R	Radius of curvature
R_e	Actuator coil electrical resistance
R_x	Radius of curvature in the x-direction
R_y	Radius of curvature in the y-direction
R_{xy}	Twist in the surface
$\mathbf{S_{EE}}$	Total kinetic energy spectral density matrix
$\mathbf{S_{PP}}$	Total radiated power spectral density matrix

$\mathbf{S_{ff}}$	Matrix of power and cross-spectral density of the forces exciting each element
T_a	Active impedance
$T_{blocked}$	Blocked force transfer function
T_{em}	Transduction coefficient
T_x	Normal stress resultant in the x-direction
T_y	Normal stress resultant in the y-direction
T_{xy}	Shear stress resultant
t	Time
U_{strain}	Strain energy
U_b	Strain energy due to bending
U_s	Strain energy due to stretching
u	Component of motion in the x-direction or tangential component
$\ddot{u}$	Second derivative of the component of motion in the x-direction
V	Volume
V_a	Voltage across the electrical inputs to the actuator
V_{cavity}	Volume of the enclosure
υ	Component of motion in the y-direction
$\ddot{\upsilon}$	Second derivative of the component of motion in the y-direction
$W(s)$	Laplace transform of the response measured by the error sensor

$\dot{\mathbf{w}}_{\mathbf{b}}$	vector of the complex velocities at the centre of the cavity elements
$\dot{\mathbf{w}}_{\mathbf{c}}$	Vector of complex control velocities $[N_c \times 1]$
$\dot{\mathbf{w}}_{\mathbf{e}}$	Vector of complex velocities at the centre of each element $[N_e \times 1]$
$\dot{\mathbf{w}}_{\mathbf{M_a}}$	Complex velocity vector of the moving masses for a multi-channel control system
w	Component of motion in the z-direction or radial component
$\ddot{w}$	Second derivative of the component of motion in the z-direction
$\dot{w}_{M_a}$	Complex velocity vector of the actuator moving mass for a single-channel control system
$X(s)$	Laplace transform of the reference signal
x_c	x-coordinate of the control point
x_e	x-coordinate of the centre of an element
x_p	x-coordinate of the primary force or disturbance
$\mathbf{Y}_{\mathbf{cc}}$	Matrix of point and transfer mobilities at the control points $[N_c \times N_c]$
Y_{cc}	Point mobility at the point of control for a single-channel system
$\mathbf{Y}_{\mathbf{ce}}$	Matrix of transfer mobilities between the control points and the centre of the elements $[N_c \times N_e]$
$\mathbf{Y}_{\mathbf{ec}}$	Matrix of transfer mobilities between the centre of the elements and the control points $[N_e \times N_c]$
$\mathbf{Y}_{\mathbf{ee}}$	Matrix of point and transfer mobilities at the centre of each element $[N_e \times N_e]$

$\mathbf{Y}_{\mathbf{M}_a}$ Diagonal matrix of the mobility of the moving mass for multi-channel system

Y_{M_a} mobility of the actuator moving mass for a single-channel system

$\mathbf{y}_{\mathbf{ce}}$ Vector of transfer mobilities between the point of control and the centre of elements for a single-channel system $[1 \times N_e]$

$\mathbf{y}_{\mathbf{ec}}$ Vector of transfer mobilities between the centre of elements and the point of control for a single-channel system $[N_e \times 1]$

y_c y-coordinate of the control point

y_e y-coordinate of the centre of an element

y_p y-coordinate of the primary force or disturbance

Z_0 Specific impedance of air

$\mathbf{Z}_{\mathbf{a}}$ Diagonal matrix of the impedances of actuators spring-damper systems for the multi-channel system

Z_a Impedance of the actuator spring-damper system for a single-channel system

Z_c Base impedance of the actuator

$\mathbf{Z}_{\mathbf{bb}}$ Matrix of acoustic impedance between the elements on the top layer of the cavity $[N_e \times N_e]$

$\mathbf{Z}_{\mathbf{bp}}$ Acoustic transfer impedance vector between the primary excitation for the top layer of the cavity and the monopole source $[N_e \times 1]$

Z_{eb} Blocked electrical impedance of the actuator

Z_{mech} Mechanical impedance

z_c	Rise at the centre of the shell or panel
β	Stiffness factor for cylindrical shell
ε_0	Strain at mid-surface
ε_x	Normal strain in the x-direction
ε_y	Normal strain in the y-direction
ε_{xy}	Shear strain
ζ_a	Actuator modal damping ratio
ζ_c	Compensator modal damping ratio
ζ_n	Modal damping ratio
ϕ	Azimuthal angle in the *xy*-plane
ϕ_c	Phase margin
ϕ_n	Natural structural modes
ψ_a	Voice coil coefficient
ψ_n	Natural acoustic modes
κ	Curvature at mid-surface
κ_x	Curvature in the x-direction
κ_y	Curvature in the y-direction
κ_{xy}	Twisting
λ	Wavelength

λ_0	Acoustic wavelength
λ_F	Flexural wavelength
λ_L	Longitudinal wavelength
λ_x	Wavenumber in the *x*-direction
λ_y	Wavenumber in the *y*-direction
$\mathbf{\Omega}$	Diagonal modal normalisation matrix
Ω	Non-dimensional frequency
θ	Angle of incidence from the normal to the surface in the z-direction
ν	Poisson ratio
ρ	density
ρ_0	Density of air
τ	Time delay
τ_{xy}	Shear stress
σ	Axial stress
σ_x	Normal stress in the x-direction
σ_y	Normal stress in the y-direction
ω	Angular frequency
ω_n	Natural frequency
ω_r	Angular ring frequency
ANC	Active Noise Control

ASAC	Active Structural Acoustic Control
ATVA	Active Tuned Vibration Attenuator
AVC	Active Vibration Control
MIMO	Multi-Input Multi-Output
MR	Magneto-rheological actuator
SDOF	Single Degree of Freedom
SISO	Single-Input Single-Output
PID	Proportional Integral Derivative
PVDF	Polyvinylidene Fluoride
PZT	Lead Zirconate Titanate patch
∂	Partial differentiation
∇	Gradient
$\mathcal{L}$	Lagrangian

1. Introduction

1.1 Motivation

The fast rate of technological developments over the past century has significantly contributed to the increase in mobility in our society. The rapid increase in air and road traffic also means that larger populations are becoming more and more exposed to transport noise and CO2 emissions. European legislation has been put into place since the 1970s in an attempt to reduce the noise of aircraft and road vehicles [1]. New upcoming European directives will also address the problem of CO2 emission and air pollution.

In order to comply with these European directives, aircraft and car manufacturers have continued to concentrate on improving the fuel efficiency of their vehicles. In the aircraft industry, the design of more aerodynamic fuselages and the use of lightweight carbon fibre composite panels in the structure allow efficient fuel combustion without diminishing the structural strength [2]. In the automotive industry, the most cost effective and direct solutions for improving fuel efficiency consist of reducing both the engine size and the vehicle mass.

Both the reduction in engine size and the reduction in vehicle mass contribute to a significant increase in the noise transmitted to the interior of the vehicle, particularly at low frequencies. Stiff and lightweight shell structures employed in new aircraft and automotive designs provide poor acoustic insulation and are radiators of engine, wind and road noise. Structural vibrations are responsible for more than 70% of vehicle interior noise [3]. Interior noise influences the level of comfort of the passengers as well as the occurrence of fatigue or motion sickness [4]. Consequently, the reduction of structural vibrations and interior noise in passenger vehicles has become of increasing importance in order to achieve both customer satisfaction and reduction in emissions. For this purpose, NVH (noise, vibration and harshness) has become an important aspect of the behaviour that has been integrated into the design process [5].

The vibrations of the structure can be attenuated via passive and/or active control methods. Passive control techniques usually involve the application of mass, damping and stiffness treatments to the vibrating surface [6]. Active control of sound and vibration relies on the cancellation of disturbances through the generation of excitations that are out of phase with respect to those created by the source. The out-of-phase excitations are generated by transducers such as loudspeakers and actuators installed on the surface of the structure [5] [7] [8].

While, in general, the use of passive treatments efficiently attenuates high frequency vibrations, they are less successful on the low frequency range without adding significant weight to the vehicle. Consequently, with the rising demand for quieter, lighter and more fuel efficient vehicles, active structural control may be able to achieve more effective and lighter weight solutions than passive vibration control techniques [8]. Active control techniques have already been shown to be more efficient than passive control at low frequencies in applications such as the control of engine boom in cars and propeller noise inside aircraft [9] [10] [11] [12] [13] [14].

Although as described below, adaptive feedforward control has previously been used to control periodic disturbances, there is a need for feedback control if the disturbance is less predictable, such as road noise in cars or jet noise in aircraft. There is also an increasing trend for actuators and sensors to be collocated and controlled locally, since such a decentralised arrangement can be readily scaled up for very large numbers of actuators and sensors and can be robust to the failure of individual units [15].

This thesis concentrates on the study and implementation of decentralised velocity feedback control systems on doubly-curved panels. The outcomes of this research will be important to the application of active control systems in the automotive and aircraft industries, where curved lightweight shells are the major components of the body structure.

The first part of this thesis provides a study of the free vibrations of shells through the analytical and numerical modelling of doubly-curved thin panels with different curvatures. Then, simulations of velocity feedback control using electrodynamic proof-mass actuators are performed on an aluminium homogeneous rectangular panel with simply-supported boundary conditions. The curvature of the modelled panel is gradually increased in order to investigate the influence of surface deformation on the

performance and stability of the control system. This section of the thesis is concluded by a case study of active vibration control on a car roof panel subjected to various boundary conditions.

In the second part of the thesis, the effects of increasing curvature on the radiated sound power and kinetic energy are investigated experimentally when an aluminium panel is part of an enclosure with rigid walled boundary conditions. The practical implementation is carried out on a homogeneous aluminium panel clamped on top of a rigid-walled Perspex enclosure, first with offline simulations based on measured data, and then with real-time experiments of feedback control conducted on the experimental set-up. Proof-mass actuators with low natural frequencies have been selected for this purpose and paired with a compensation filter and a second-order high-pass filter that preserve the stability of the system. The curvature of the panel is altered through the pressurisation of the enclosure. The aim of this study is to imitate the deformation of sections of an aircraft fuselage caused by pressure loading.

1.2 Research Background and Literature Review

This section provides a summary of the sources of noise in road vehicles and aircraft, along with an overview of past and current applications of active noise and vibration control methods in the automotive and aeronautical industries.

1.2.1 Sources of Noise in a Road Vehicle

The sources of noise in a road vehicle can be divided into three main categories: (1) engine and transmission excitations, (2) road surface noise and (3) aerodynamic or wind noise. Engine noise is of a periodic nature and results from inlet and exhaust noise, piston crank and combustion-induced noise. The resulting cylinder firing frequency depends on the number of cylinders and the engine speed. For example, in [16], this frequency can vary from around 7 Hz when the engine is at idle, to around 50 Hz when engine speed is around 6000 rpm. Road noise is random and comes from the vibrations of the tyres on the road surface. The noise levels are directly influenced by vehicle

speed, tyre design and road characteristics. Finally, aerodynamic or wind noise is generated by the airflow around and over the vehicle and depends on the speed of travel [1] [17].

Noise can be transmitted into the passenger compartment through structure-borne or airborne paths. In the car body, structural vibrations are generated by the engine, the wheels, the chassis and the airflow, and propagate through the entire vehicle. The low damping of lightweight car bodies, often made of materials such as carbon steel, aluminium and carbon fibre, causes the sound generated by these vibrations to be efficiently transmitted to the interior of the car [18]. The vibration of panels and shell structures such as the roof of the vehicle results in high levels of structure-borne noise. The level of noise transmission via airborne paths depends on the isolation of the cabin from the engine compartment and the exterior. The dominant contributors to interior noise at low and mid-frequencies are categorised into 3 mechanisms: (1) direct transmission, (2) 'mass law' transmission and (3) acoustic radiation. Direct transmission is caused by the vibration of air through the cabin holes or gaps in door seals leading to direct noise radiation into the cabin. This type of transmission mainly contributes to the noise level at high frequencies. Mass law transmission is due to the transmission of noise from the power unit into the cabin through the walls. Finally, acoustic radiation results from the vibration of cabin walls, which can be caused by air turbulence, engine operation and/or road-tyre interactions. The first two mechanisms described above are airborne, while the third one can be structure-borne or airborne, depending on the transmission path [19].

The contribution of structure-borne and airborne sources to the interior noise spectrum of a medium-size saloon car, calculated by Lalor and Bharj for a travelling speed of 100 km/h, is shown in Figure 1.1 [19]. Since the contribution of wind noise to the interior level only becomes important for speeds above 110 km/h, its effect cannot be seen in the graphs. The effects of structure-borne noise are highest below 500 Hz and start to roll off above this frequency.

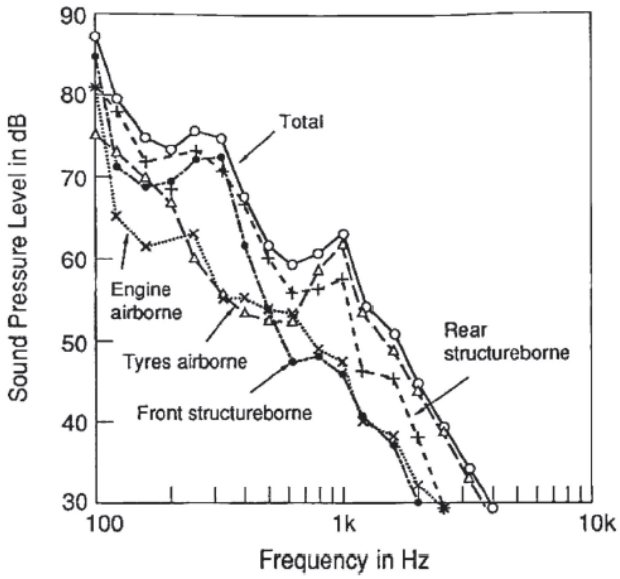

Figure 1.1 – Spectrum of interior noise levels in a saloon car calculated by Lalor and Bharj [19]. The vibrations of the engine and front tyres contribute to the 'Front' structure-borne spectrum, whereas the vibrations of the rear tyres contribute to the 'Rear' structure-borne spectrum.

The mechanism of noise transmission through the vehicle cabin walls and the characteristics of the frequency response have been analysed by Jha and Priede [19] and Jha [4]. The dynamic response of a car body expressed in terms of mobility (velocity per unit force) shows that structure-borne noise from the engine, the transmission system and the road occupies the frequency range up to 400 Hz where a large number of resonances appear, while airborne noise dominates above 400 Hz.

A schematic diagram of the major sources of resonance has been illustrated by Jha and can be seen in Figure 1.2 [4]. Up to 10 Hz, the modes correspond to rigid body vibrations caused by the suspension and the wheels. The 15-40 Hz content is due to the vibrations at the engine mounts being transmitted to the car body and producing torsional vibration of the structure. The region of interest for noise and vibration control is situated in the 70-200 Hz frequency band, where the car body is being excited by the road and the engine's first harmonics. The first acoustic cavity modes occur in the 80-90 Hz, 130-140 Hz and 150-160 Hz regions, depending on the specific dimensions of the car cabin.

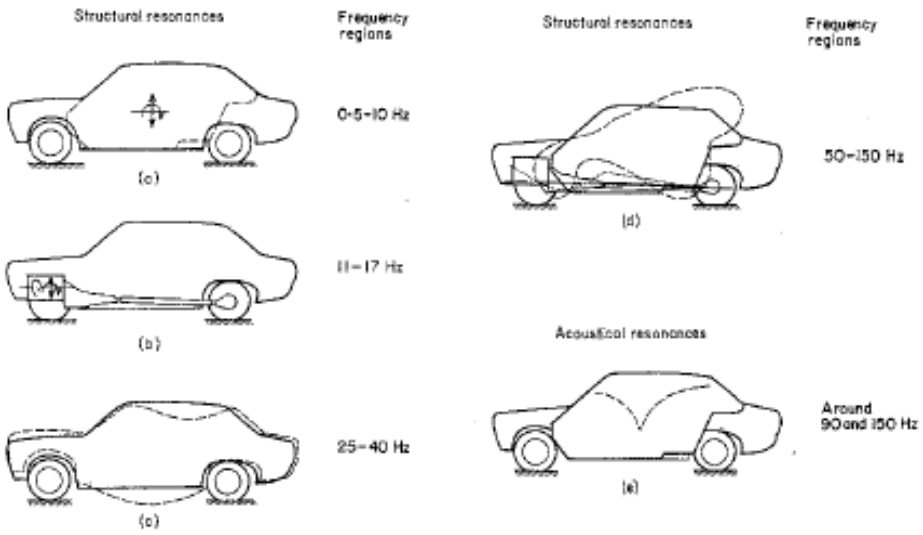

Figure 1.2 – Diagram of major sources of resonance in a passenger vehicle [4]

In the 70-200 Hz frequency range, the car body shell exhibits bending modes, referred to by Jha as ‘ring modes’ or ‘circumferential modes’ due to their resemblance to modes of vibrations observed in cylindrical shells. One of the main contributors to the bending modes in the passenger compartment are the large vibration levels of the roof panel. As these low-frequency modes are responsible for the propagation of high levels of noise into the passenger cabin, their attenuation is of great importance in NVH-related problems in the industry [4].

1.2.2 Sources of Noise in an Aircraft

This section is based on the information in references [20] [21] [22] [23] [24]. In an aeroplane, the interior cabin noise originates from: (1) the power plant such as the propeller or jet propulsion, (2) the turbulent boundary layer over the outer surface or airframe of the plane and (3) engine-induced vibrations due to reciprocating, turbofan and jet engines and finally (4) running equipment such as air conditioners.

Aircraft propulsion systems such as propellers and jets are one of the major contributors of noise inside the cabin. The near-field noise produced by the propeller is the result of the air-volume displacement due to the rotating blades. The propeller noise is mainly of deterministic nature and its sound power spectrum is composed of periodic discrete frequency peaks corresponding to the blades’ passing frequency and its harmonics, as shown in Figure 1.3. Random broadband noise is produced by the turbulent airflow over

the surface of the blades, although its contribution is not as important in propeller aircraft.

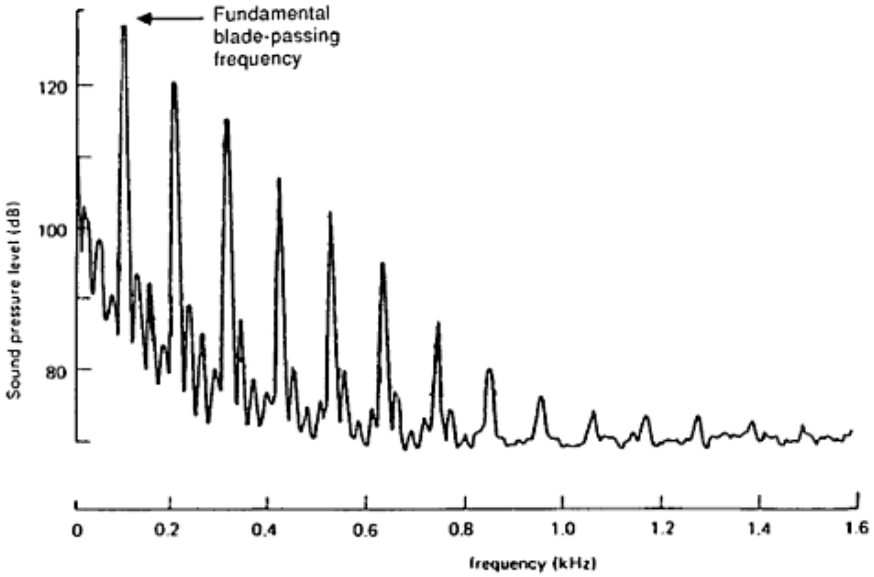

Figure 1.3 – Propeller noise spectrum, displaying the harmonics of the blade passing frequency decaying at a constant rate [21].

The amount of noise generated by the propellers depends on various factors such as the size, shape and number of blades, the speed and direction of rotation and consequently the direction and uniformity of air inflow into the propeller. The response of the fuselage and sound transmission into the interior are directly influenced by the rotational speed and passing frequency of the blades.

The interior noise and vibration levels in two lightweight propeller aircraft were studied by Jha et al. during various tests and the major contributors of noise were assessed [22] [23]. As shown in Figure 1.4 taken from [22], the main content of the interior noise spectrum during a flight at cruising speed (111 knot, engine speed 2400 rpm), occupies the frequency range up to 1 kHz. The noise spectrum mainly consists of harmonics and sub-harmonic due to the blade passing frequency and the engine firing frequency. The sub-harmonic at ½ the engine firing frequency in the bottom graph of Figure 1.4 is due to the uneven firing of the engine cylinders.

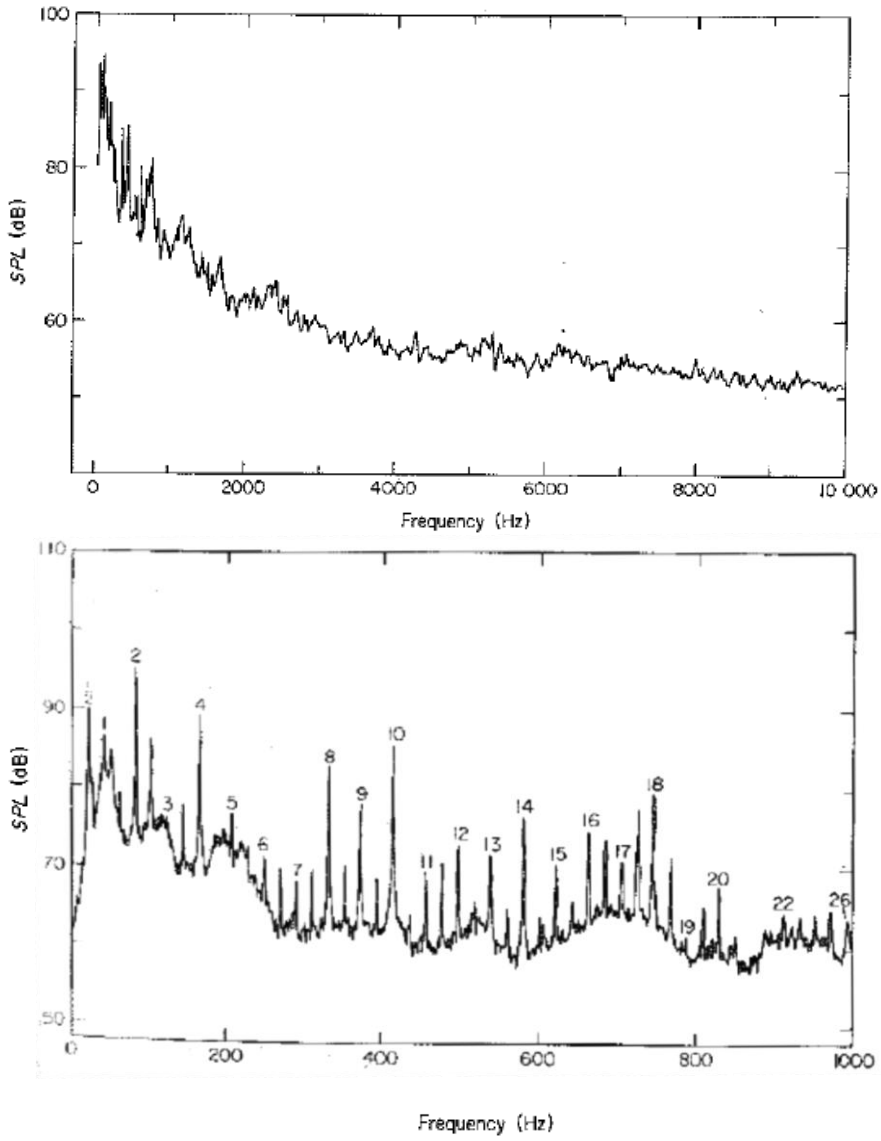

Figure 1.4 – Interior Noise spectrum of a small propeller aeroplane measured up to 10 kHz (top) and 1 kHz (bottom) at the pilot's head position during flight at cruising speed. The numbers refer to the harmonics of the blade passing frequency [22].

The vibration spectrum is similarly composed of discrete harmonic frequencies originating from the engine and propeller rotation. The vibration spectra measurements performed at the aircraft floor over the 0-1 kHz frequency range during cruising speed also reveal several broadband peaks with the largest situated in the frequency region up to 500 Hz and an additional large peak around 700 Hz [22] [23]. The graphs presented by Jha et al. are shown in Figure 1.5. The vibration spectra were measured for different engine rpms and aircraft speeds in order to understand the occurrence of the resonance peak around 700 – 800 Hz. Results indicated that the response at this resonance was not influenced by these changes, leading to the conclusion that it was due to the structural

properties of the cabin floor. Further measurements performed on the aircraft during ground tests displayed similar interior noise and vibration characteristics.

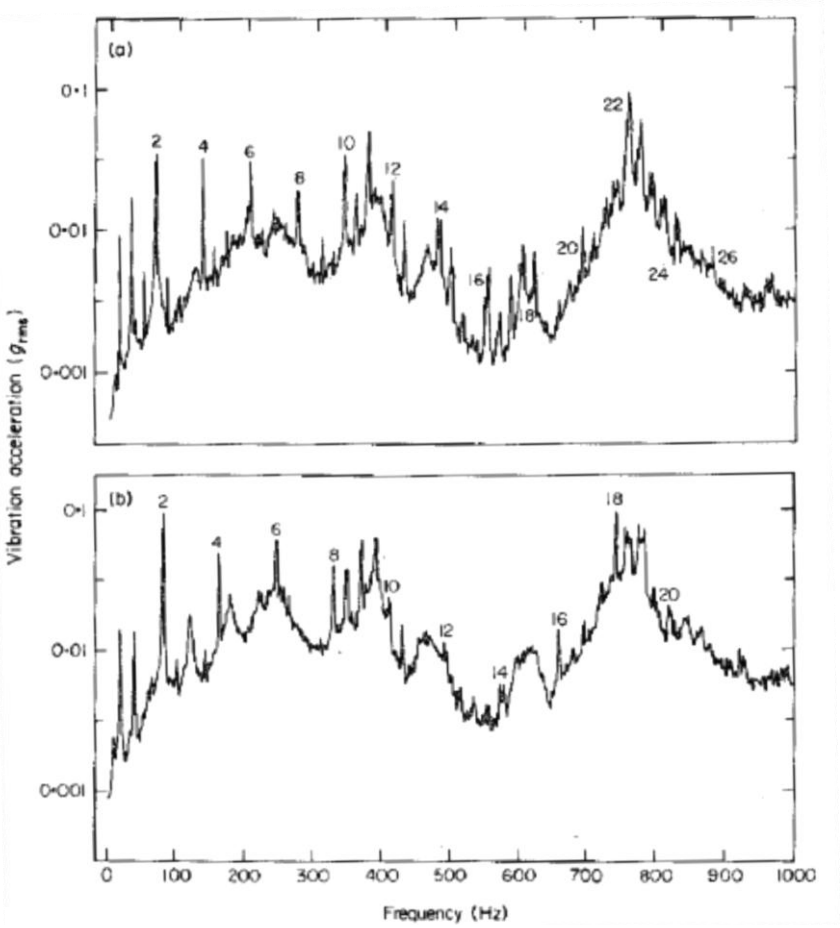

Figure 1.5 – Vibration spectra obtained at the aircraft floor for frequencies up to 1 kHz: (top) 86 knot and 2000 rpm, (bottom) 113 knot and 2400 rpm. The numbers refer to the harmonics of the blade passing frequency [22].

Jet noise mainly occurs in aircraft with wing-mounted engines. Jet noise results from the mixing of compressed jet exhaust gases and the airflow near the nozzle exit. This random broadband excitation mainly contributes to the interior noise during take-off and climb.

Due to the high travelling speed, aerodynamic noise or turbulent boundary layer-induced noise significantly contributes to the mid- and high-frequency noise levels inside the cabin during flights. The airflow over the outer layer of the fuselage exerts a random fluctuating pressure field on the surface which results in the excitation of the cabin walls and the radiation of sound into the passenger compartment. The airframe is

the main path of sound transmission to the interior of the aircraft. Sources of airframe noise taken from [21] are shown in Figure 1.6.

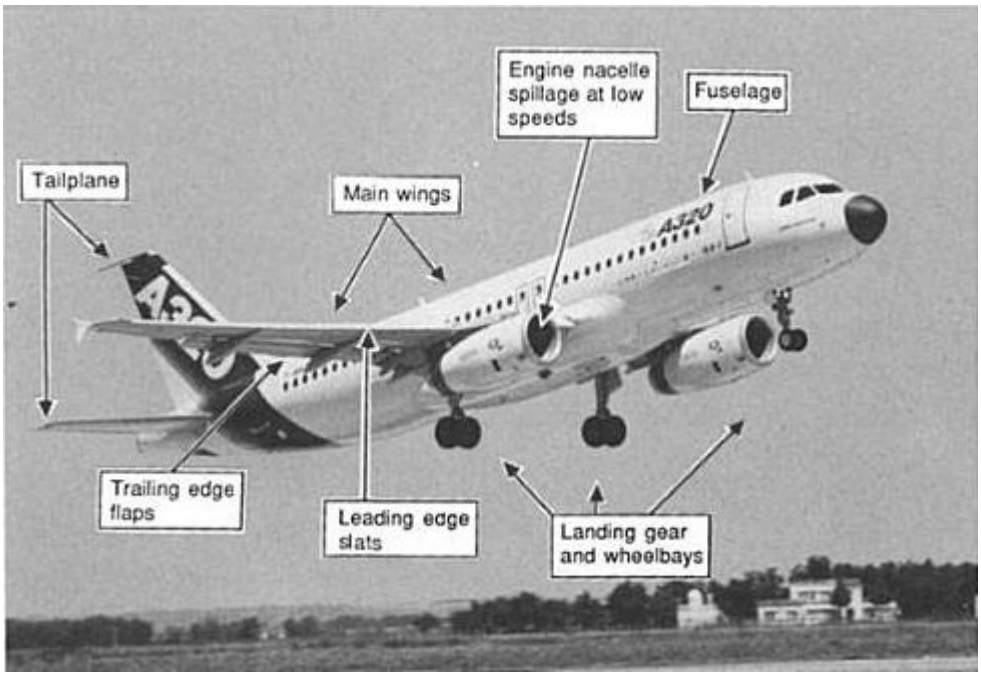

Figure 1.6 – Sources of airframe noise in an aircraft [21]

During take-off and climb, the turbulent boundary layer causes vibrations in the aircraft fuselage which contribute to the interior noise. During landing, the deployment of the trailing edge flaps, the leading edge slats and the landing gears significantly increases interior cabin noise, due to their interaction with the turbulent flow. Under cruising flight conditions, the main wings and tailplane are the main sources of noise due to turbulent flow on the airframe. The contribution of aerodynamic noise is dominant for frequencies above 400 Hz.

In addition to the turbulent airflow over and around the aircraft, the engine noise also contributes to the structure-borne and airborne excitations. In jet-powered aeroplanes where the engine is mounted close to the fuselage and under the wings, the engine noise is transmitted via the fuselage to the regions of the cabin that are near the exhaust. In turbofan aeroplanes where the engine is directly mounted on the rear of the fuselage, the lack of isolation and the coupling with the structure creates a direct transmission path leading to the passenger compartment. Due to the different nature of the sources of excitation, the sound power spectrum of structure-borne noise can contain both deterministic and random broadband components.

1.2.3 Active Control of Sound and Vibration

Passive control techniques, such as added absorption or damping treatments, are efficient for attenuating mid and high frequency vibration, in general, but are not as successful at low frequencies without a significant increase in weight. The use of active structural control solutions, instead or in addition to passive control, may provide a more effective and lighter weight solution. Active control of sound and vibration consists of the destructive interference between a primary acoustic or structural disturbance, and a controllable secondary source, producing excitations that are out of phase with respect to the ones created by the primary source [25]. Active control strategies can be divided into five groups. In active noise control (ANC), effective noise attenuation is achieved by ensuring that in the region of control, the sound field produced by the secondary source is close in magnitude but out-of-phase with the primary sound field [17]. In active vibration control (AVC), the vibrations of the system are attenuated through the modification of the dynamics of the system and its structural response, rather than directly cancelling the sound, so that the vibrations that contribute to efficient sound radiation from the structure are reduced [26]. The active noise-vibration (ANVC) technique works similarly to both ANC and AVC in the sense that the secondary structural and acoustic sources excite the structure with the aim of attenuating the interior sound field. Active structural acoustic control (ASAC) seems to offer a better solution than ANC and AVC because both structural vibrations and sound transmissions are attenuated [17] [27]. Finally, Active boundary control (ABC) which is used in the aircraft industry, consists of the integration of smart trim panels with stiff segments in order to reduce the near-field radiations from the trim panels [24].

For all cases, there exist two main control approaches, feedforward and feedback control. The application of feedforward strategies is successful in the attenuation of tonal periodic disturbances such as the noise from rotating machinery, aeroplane propellers or road vehicles' engines, where a tachometer signal can be used as reference, but is impractical and uneconomical when the primary excitation is composed of several uncorrelated sources. For the latter case, feedback control should be used, since limited information can be obtained in advance of the random broadband excitations, for example, in the case of structure-borne excitation of lightweight and

lightly damped panels used in the automotive and aircraft industries. A feedforward control system must generally be made adaptive to cope with changes in the disturbance. On the other hand, feedback control does not require an independent reference signal and adaptive filtering of the error signal, as it uses error sensors to obtain real-time information of the system's behaviour, thus saving large amounts of computation time. Feedback control systems are also easily built with analogue circuits and integrated into the structure that needs to be controlled [28].

The concept of active control has been around since the 1930s. The patent for active sound control filed by Lueg in 1936 described a single channel feedforward system controlling tonal disturbances such as plane waves moving in a pipe or an acoustic source propagating in a 3-dimensional free-field [17] [29]. The diagrams proposed by Lueg for each case can be seen in Figure 1.7 [29]. The first single channel analogue systems were developed two decades later. Olsen and May proposed a Helmholtz resonator sound absorber composed of a microphone, loudspeaker and amplifier that acted like a single channel feedback system and reduced the sound pressure near the microphone [30]. Three years later, a feedforward control system was designed by William Conover for reducing the noise from large mains transformers [31]. However, the practical application of active control systems only started in the late 1970s with the use of digital signal processing (DSP) techniques and the fast development of adaptive digital controllers and micro-circuits [32].

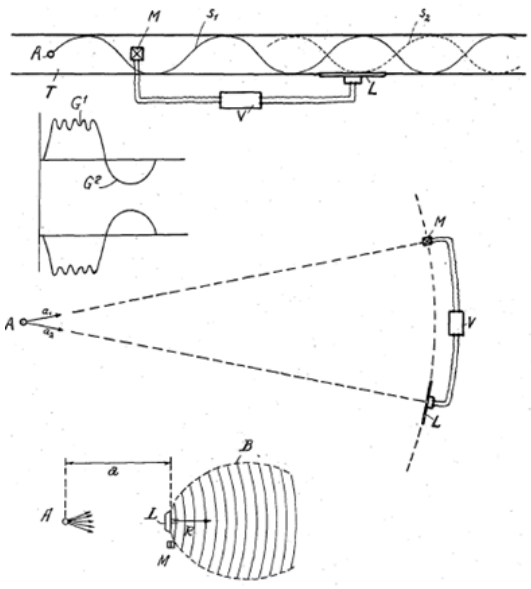

Figure 1.7 – Diagram proposed by Lueg for the first active control system [29].

Practical implementations of Lueg's patent have been widely used in the field of active control of noise in ducts, such as the design of a broadband active sound control system for sound absorption in air-conditioning ducts and ventilation shafts [7]. One of the applications of Olson's and May's design is in aircraft and automotive industries where the sound absorber can be installed in the backrest of the passenger seat in order to reduce the low-frequency noise near the passenger's ears [30] [32]. Balas et al. have investigated the application of feedback active control techniques for reducing the vibrations of large space structures [33] [34]. Recent advances in active control applications to automotive and aircraft industries will be described in Section 1.2.6.

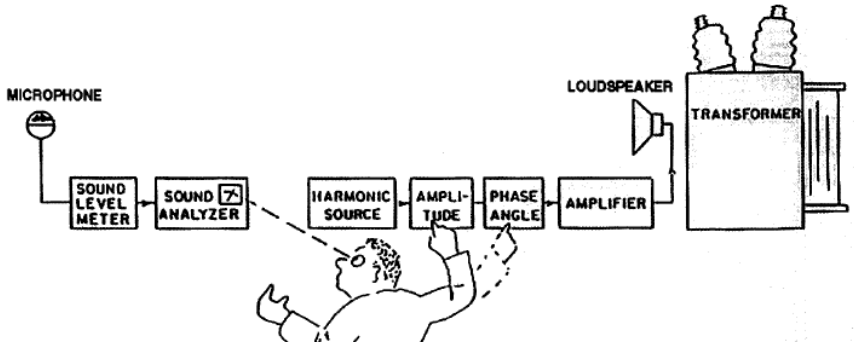

Figure 1.8 – Feedforward control system designed by William Conover for reducing mains transformer noise [31].

1.2.4 Feedback Control Strategies

For a linear time-invariant system (LTI), two main active vibration control strategies have been established: feedback control and feedforward control. Both active control systems are composed of the same main components, namely, a sensor coupled with an actuator via an electronic controller. The vibrations of the structure are detected by the sensor while the controller and actuator respectively alter the detected signal and affect the structural response.

One of the main criteria in choosing between the two active control strategies depends on the availability of a reference signal correlated with the primary disturbance, i.e. a direct measurement of the primary excitation. If such a measurement is not available, feedback control can be used for attenuating the structural excitations. A block diagram of a single-channel feedback control system is shown in Figure 1.9. The response of the

system is fed back to the controller and the net difference between the primary disturbance and this secondary excitation, which is called the error signal $E(s)$, is applied to the plant. The 'plant' refers to the physical system between the input to the secondary source and the output of the error sensor.

As explained in [17] [26], the output of the mechanical system, as measured by the error sensor, can be expressed in terms of Laplace transforms and transfer functions as

$$E(s) = F_p(s) + G(s)F_s(s), \tag{1.1}$$

where $F_p(s)$, $G(s)$ and $F_s(s)$ are the Laplace transforms of the primary disturbance, the plant and the secondary excitation respectively, when the secondary excitation is given by

$$F_s(s) = -H(s)E(s), \tag{1.2}$$

where $H(s)$ is the transfer function of the feedback controller. Consequently, the closed loop response of the feedback control system can be calculated as

$$\frac{E(s)}{F_p(s)} = \frac{1}{1 + H(s)G(s)}. \tag{1.3}$$

The closed-loop response function in Equation (1.3) is also referred to as the 'sensitivity function' and is used for assessing the effectiveness and stability of the controller [17].

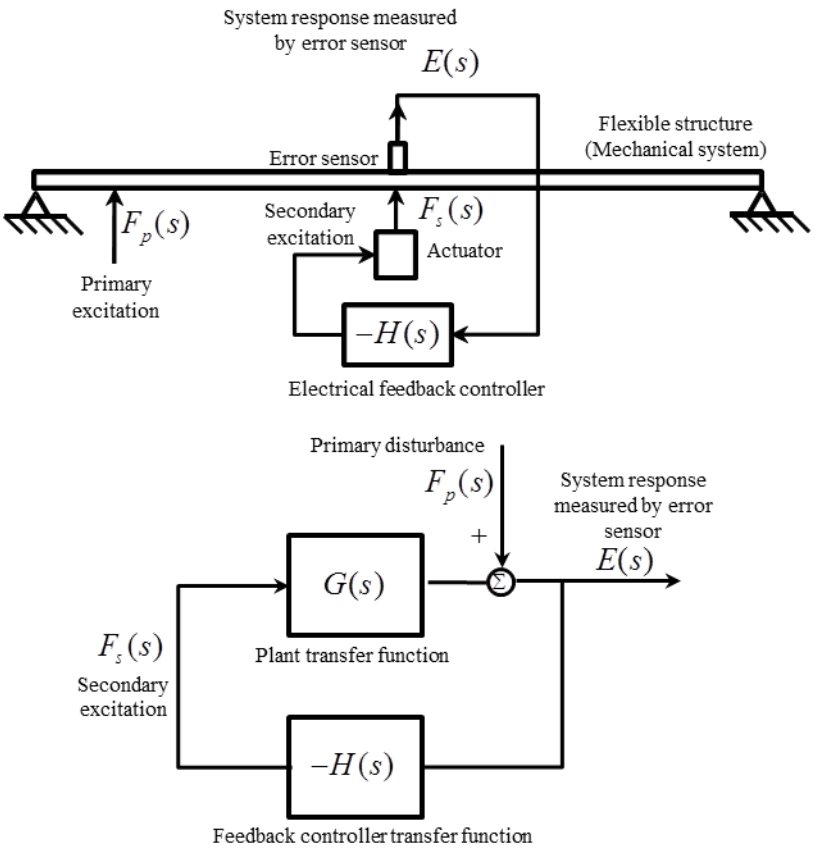

Figure 1.9 – Components of a single-channel feedback control system (top) and block diagram (bottom) [17] [26]

For single degree of freedom (SDOF) system consisting of a mass, linear spring and viscous damper, as shown in Figure 1.10, based on the system's equation of motion, the plant transfer function $G(s)$ in the absence of control can be written as

$$G(s) = \frac{W(s)}{F_p(s)} = \frac{1}{Ms^2 + Cs + K}, \tag{1.4}$$

where $W(s)$ is the Laplace transform of the displacement response, measured by the error sensor, and M, K and C are the mass, stiffness and damping coefficients of the system respectively.

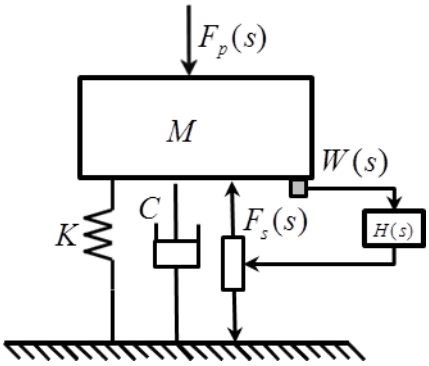

Figure 1.10 – Feedback controller implemented to an SDOF

The controller $H(s)$ is assumed to generate a secondary force with components proportional to acceleration, velocity and displacement of the mass. Based on this assumption, the secondary force can be expressed in the time and Laplace domains respectively as

$$f_s(t) = g_a \ddot{w}(t) + g_v \dot{w}(t) + g_d w(t) \tag{1.5}$$

$$F_s(s) = g_a s^2 W(s) + g_v s W(s) + g_d W(s), \tag{1.6}$$

where g_a, g_v and g_d are the gain parameters for acceleration, velocity and displacement respectively. The transfer function of the controller $H(s)$ can then be written as

$$H(s) = \frac{F_s(s)}{W(s)} = g_a s^2 + g_v s + g_d. \tag{1.7}$$

Such a controller is referred to as a PID (Proportional Integral Derivative) controller and the gain parameters can be adjusted in order to ensure the stability and improve the performance of the system.

In this case, the closed-loop response for the SDOF system can be written as

$$W(s) = G(s)\big(F_p(s) - F_s(s)\big), \tag{1.8}$$

where $F_s(s) = H(s)W(s)$, so that using Equations (1.4) and (1.7)

$$\frac{W(s)}{F_p(s)} = \frac{G(s)}{1+H(s)G(s)} = \frac{1}{M's^2 + C's + K'}, \tag{1.9}$$

where $M' = M + g_a$, $C' = C + g_v$ and $K' = K + g_d$ are respectively the effective mass, damping and stiffness of the system. The effective mass, damping and stiffness can thus, in principle, be independently controlled with the feedback gains g_a, g_v and g_d, although for stability, M', C' and K' are all required to be positive [26]. Velocity feedback control remains the most robust out of the three techniques as it increases the damping without bringing any significant change to the mass and stiffness of the system.

The main disadvantage of feedback control lies within the trade-off between stability and performance. The stability of the feedback loop is assessed from the poles of the sensitivity function defined in Equation (1.3) which are the roots of the characteristic equation

$$1 + H(s)G(s) = 0. \tag{1.10}$$

The real parts of all these poles need to be negative for the system to be stable. The stability of the control system can also be assessed using graphical means such as the root-locus method and the Nyquist criterion. The root-locus method is the graphical representation of the poles of the sensitivity function in the complex plane. For the system to be unconditionally stable, the loci curves of the roots should be located in the left-hand side or the real-negative part of the graph for all values of feedback gain. The Nyquist criterion depends, by contrast, on the polar plot of the open-loop frequency response $H(j\omega)G(j\omega)$ which is called the Nyquist plot. The stability assessment of practical control systems is often performed using the Nyquist plot, rather than the root-locus method, because the factorisation of the sensitivity function in terms of its poles and zeros is often difficult, or the pole-zero representation is not available, either due to the system model being of very high order or due to existing variability in the system [35]. Assuming that the plant and controller are each individually stable, the closed-loop response of the system is also stable under the Nyquist criterion, if the Nyquist plot does not enclose the point (-1,0) as the frequency is varied from $-\infty$ to $+\infty$. An example of a

Nyquist plot of a stable system, taken from [17], can be found in Figure 1.11. The 'control spillover' circle centred at (-1,0) shown in Figure 1.11 is a region in which the response is enhanced rather than reduced by the feedback loop, although the system remains stable, as long as the Nyquist plot does not cross the axis at (-1,0).

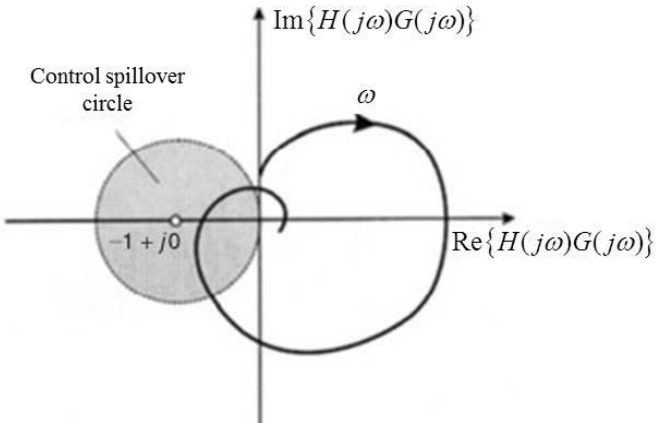

Figure 1.11 – Nyquist plot of a stable feedback control system with the circle enclosing the limit of instability at the point (-1,0) shown in grey [17].

Within this 'control spillover' circle, $|1+G(j\omega)H(j\omega)|<1$, so that the modulus of the sensitivity function is greater than unity

$$\left|\frac{1}{1+G(j\omega)H(j\omega)}\right|>1, \tag{1.11}$$

indicating enhancement of the disturbance.

In addition to the definition of the limit of stability for a control system, the relative stability of the system can be determined through the definition of stability margins. The use of such margins can guarantee that changes in the control system will not compromise the system stability, i.e. the Nyquist plot of the system showed that it was already very close to the point (-1,0) and therefore, very sensitive to changes in feedback loop. Two parameters called the gain margin and phase margin are used for ensuring the relative stability of the control system. The gain margin g_{margin} corresponds to the maximum allowed amplification in the feedback loop before the open-loop response crosses the axis at -1, and the phase margin ϕ_c refers to the maximum additional phase shift allowed for maintaining the system's stability, before the overall

phase shift reaches the critical 180° phase which leads to instability. The gain margin can be formulated in dB as

$$g_{margin} = -20\log_{10}(g_c), \tag{1.12}$$

where g_c is the distance between the origin and the point at which the open-loop response crosses the real axis. The g_c and ϕ_c parameters have been indicated in the Nyquist plot of Figure 1.12. If the gain and phase margins are set such that the system remains stable despite changes in the feedback loop, then the system can be defined as robust. The task of setting the appropriate gain and phase margin values can be difficult in practical control systems due to the uncertainties arising in the plant caused by changes in physical conditions or nonlinearities in the controller [17]. A 6-dB gain margin and 30° phase margin are commonly used for ensuring robust stability. A 6-dB gain margin corresponds to setting a geometric constraint in the Nyquist plot such that it does not intersect a circle of radius ½ centred at (-1,0) at any point on the circle, and means that the enhancement in the open-loop response will be no larger than 6 dB at any frequency ω [35].

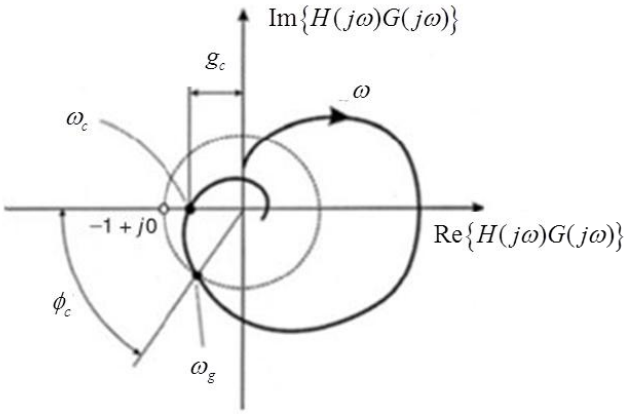

Figure 1.12 – Nyquist plot of the open-loop response of a relatively stable system with the parameters g_c and φ_c for gain and phase margin have been indicated [17].

The stability of a control system may be compromised by different factors. Instability may arise at higher levels of control gain due to the contribution of residual modes to the overall response of the system. A 180° phase shift is introduced into the response causing a change of sign in the response from negative to positive and leading to the

enhancement of the error signal [8] [26]. Another reason for instabilities in the system can be the presence of time delays in the feedback controller, which appear in the system as additional unmodelled phase shifts. Such phase shifts can be limited by collocation and duality between the force actuator and velocity sensor so that the plant response is proportional to the input mobility of the structure, which is positive real, i.e. its real part is positive. A sensor-actuator pair is said to be collocated when they are placed in the same position for point actuators, or over the same area of the structure for distributed actuators. Duality between an actuator and a sensor occurs when they excite a structure and detect the resulting vibrations in the same manner, such that the product of the excitation and the detected response is proportional to the input power to the system [17] [26] [36] [37].

Time delays tend to be common in digital implementations of active control due to the use of anti-aliasing and reconstruction filters required in the digitisation of the controller. They cause the effective mass and damping to be modified and the system to become unstable if the damping is reduced to a negative value [26]. The effects of time delays on the performance of the feedback loop and the closed-loop frequency response have been discussed in further details by Elliott in [35], who noted that the bandwidth over which control can be obtained is inversely proportional to the delay, such that

$$Bandwidth(Hz) < \frac{1}{6\tau}. \tag{1.13}$$

In general, feedback control strategies for vibration control (ASAC and AVC) can be categorised into: (1) single-input single-output (SISO), (2) fully-coupled multiple-input multiple-output (MIMO) and (3) decentralised MIMO systems. A SISO feedback control systems consist of a sensor-actuator pair that is designed to reduce the local vibration. MIMO systems are composed of arrays of sensor-actuator pairs which can be either fully-coupled or independent pairs. These systems are respectively referred to as centralised and decentralised feedback control systems [38].

1.2.5 Actuators and Sensors for Active Control

The performance of the control system depends on the number of actuators and sensors employed, their position on the structure and their dynamic responses.

Actuators can be categorised as semi-active or fully-active. Semi-active transducers, such as shape memory alloy actuators, are essentially passive devices, but their mechanical properties (mass, stiffness and damping) can be varied in real-time by a control signal. The small power required to drive these actuators and the reduced cost of such control systems make them an attractive solution for semi-active suspension systems in road vehicles [39]. Furthermore, a semi-active transducer can still work in passive conditions, should the active system fail to operate. One example of semi-active actuators which may be applied to vehicle suspension systems, are dampers filled with electrorheological (ER) or magnetorehological (MR) fluids. The viscosity of these smart fluids is varied by changes in electric field and magnetic field strengths [40].

Fully-active actuators require much larger amounts of power than semi-active actuators. They operate by producing control forces that destructively interfere with the vibrations of the structure and thus attenuate the structure's response. Fully-active actuators are generally divided into two categories: grounded or reactive actuators and space realisable actuators. The naming of the first category comes from the fact that these actuators need to react against a fixed base or support. An example of such an actuator is an electrodynamic shaker. Space realisable actuators generate both passive structural (reacting against a support) and active forces (voltage-generated). Some examples of this category include point force transducers such as inertial actuators and distributed transducers such as electrostrictive and piezoelectric actuators [26] [41].

Proof-mass actuators are a type of inertial actuator in which a magnet is suspended and supported by a spring and damper. The moving mass and the stiffness of the actuator are largely provided by the magnet and the voice coil. When the actuator is driven by a voltage or current source, the inertial mass reacts off the surface of the structure (or an additional base mass) and the control force is generated at the position of the actuator on the structure. This type of actuator will be described in further detail in Chapter 4.

Piezoelectric actuators can come in the form of PZT (Lead-Zirconate-Titanate) patches or PVDF (Polyvinylidene Fluoride) films. They can be used as single strips or as stacks depending on the properties of the response of the structure. Due to their shape and lightweight, they couple well with the structure and can be easily implemented or embedded as distributed actuators on the surface and are widely used in smart

structures. Consequently, piezoelectric actuators represent an attractive option for satisfying the cost and weight limitations in the automotive and aircraft industries. In addition to the transverse control force, these actuators generate line moments along their edges allowing a more efficient control of both in-plane and bending vibrations. As demonstrated by Elliott et al in [27], the use of these actuators can achieve high levels of control similar to those of a decentralised MIMO control system composed of point force actuator collocated with error sensors.

In comparison to point force inertial actuators, however, the use of piezoelectric actuators in practical systems can present several significant disadvantages. It is not easy to achieve collocation and duality when piezoelectric actuators are used as distributed actuators and the stability of these control systems is harder to ensure at higher frequencies in comparison to multi-channel point force actuators. Another disadvantage of piezoelectric actuators, in comparison to inertial actuators, is their requirement for high-voltage amplifiers to generate reactive forces against the surface. Additionally, if these voltage levels are too high, the actuators are known to generate harmonic distortions that are detrimental to the performance of the control system. The length and size of the actuator also has a strong impact on the frequency range over which the actuation force is effective, and the fragility and brittleness of these actuators puts a significant limit on their size and on the tolerable levels of strain caused by the deformations of the structure on which they are implemented (i.e. during aircraft cabin pressurisation or when mounted on helicopters struts). Finally, the maintenance of control systems equipped with piezoelectric actuators is far more expensive than those with inertial actuators [24].

In order to satisfy the requirements for a cost-effective, robust and easy to implement control system, the research work done for this thesis has been based on the use of inertial actuators.

1.2.6 Review of Active Control Applications in Industry

The use of active control techniques for noise and vibration reduction in the aircraft and automotive industry is strongly governed by the cost-effectiveness of the system. Over the recent years, the increasing availability of inexpensive sensors and microprocessors with suitable specifications for active control system has started to make the practical

implementation of such systems in mass-produced vehicles affordable. However, factors such as number of channels in the controller and number of actuators and sensors distributed on the structure still have a significant impact on the feasibility of the implementation of the control system, both in terms of cost and weight addition.

This section provides a review of some of the active control technologies for noise and vibration in road vehicles and aircraft.

Application of active control in road vehicles:

The rising demand from customers for a quieter and more comfortable ride along with the weight reduction and fuel efficiency objectives from car manufacturers have increased the popularity and appeal of active control techniques. Structure-borne noise caused by the vibrations of the cabin walls, which is known to occur in the low-frequency region (20-200 Hz), may be more successfully attenuated by active noise and vibration control strategies than passive control solutions. Over the past 20 years, different experimental studies have demonstrated the practical implementation of active noise and vibration control in road vehicles. However, the high cost and complexity of such systems has made it difficult up to now for the automotive industry to commercialise an affordable vehicle with such integrated control systems [39].

In addition to the characteristics of the sources of excitation, under 200 Hz, the vehicle interior noise is governed by acoustic resonances, structural modes of vibration and the structural-acoustic coupling between the two. Depending on the nature of the disturbance, different control strategies may be considered to reduce low frequency noise and vibration in a road vehicle [42].

For controlling tonal engine noise, feedforward noise control works most efficiently. The reference signal is taken from the engine so that the control system can be adapted to changes in the engine speed [8] [10]. Various numerical and experimental studies have been conducted to demonstrate the performance of feedforward engine noise control in cars. In addition, several OEMs such as Audi and Honda have implemented this technology in order to attenuate the noise due to the deactivation of some the engine

cylinders for fuel efficiency. This technology has been implemented as part of the standard package, in some of these OEMs vehicles which are currently available on the market [43] [44] [45]. Recent studies carried out on a cabin mock-up with concrete walls by De Oliveira et al. [46] consist of both FEM simulations and experimental assessment of engine noise reduction inside the cabin. A picture of the experimental rig and a diagram of the cabin mock-up with the locations of the microphones and sources indicated is shown in Figure 1.13. The vehicle mock-up was composed of two parts: the passenger compartment and the engine compartment which were connected to each other via a flexible firewall. The engine noise was transmitted to the cabin through the firewall. The primary disturbance was created using a real-time engine simulator and both velocity feedback control and adaptive feedforward control were investigated for the reduction of engine noise inside the passenger cabin. The results showed that noise from engine orders could only be controlled by adaptive feedforward control. However, feedback control provided an efficient broadband noise reduction and could be potentially used for the attenuation of random road and wind noise [47] [48].

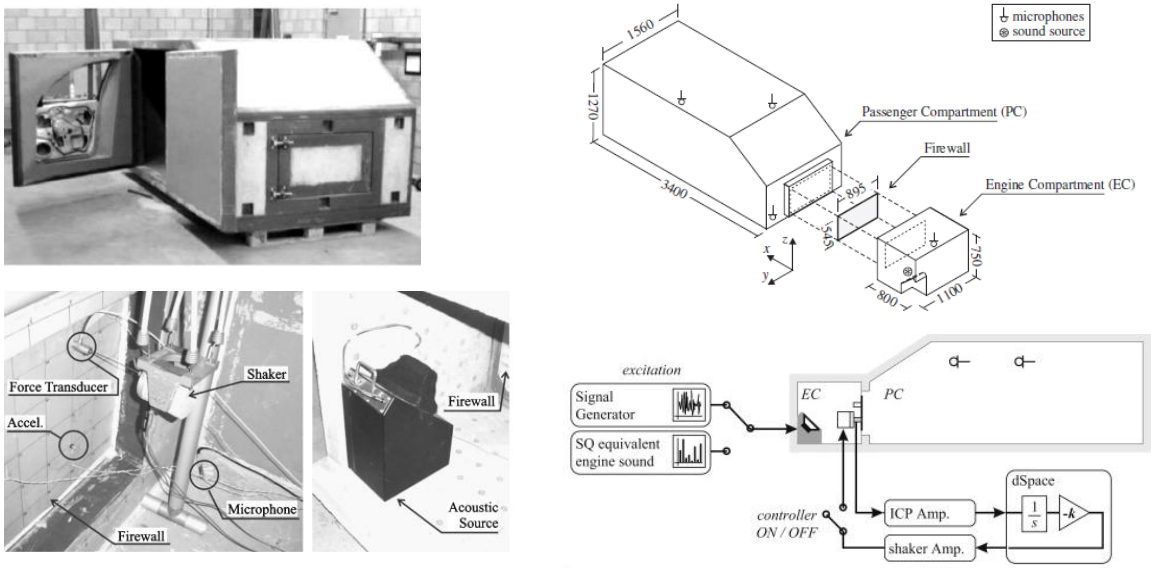

Figure 1.13 – Vibro-acoustic cabin mock-up presented by De Oliveira et al. [46] [47] [48]: (left) Picture of experimental rig, source and sensors positions, (right) diagram of the cabin mock-up and active control system.

Feedforward control can also be used to attenuate random broadband road noise. However, the large number of sensors required to capture reference signals from the different input noise sources and the importance of their positioning makes the implementation of such adaptive feedforward control systems too complex and

expensive for a commercial application. In this case, feedback control strategies can be an attractive replacement for feedforward control, as they require no reference signals. The two control strategies may also be combined together in order to optimise the reduction of noise in the cabin. The implementation of a combined feedback-feedforward system in a Honda station wagon has been discussed by Sano et al. in [49]. A feedback control was implemented to reduce the booming noise at the front seats. A feedforward control system was implemented to prevent enhancements in the noise level at the rear seats. A diagram of the system and the positioning of the error sensors, reference sensors and the controller are shown in Figure 1.14.

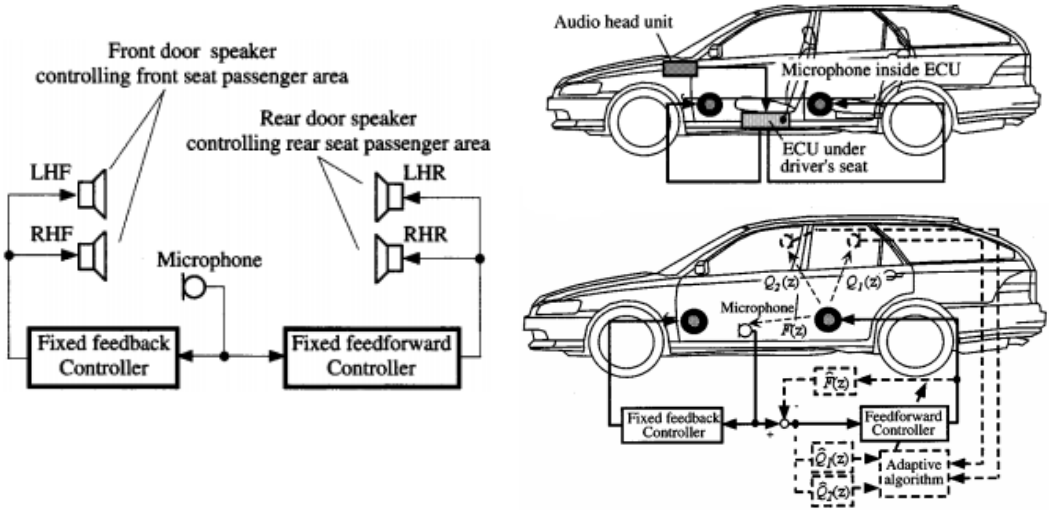

Figure 1.14 – Active noise control system implemented in the Honda station wagon vehicle by Sano et al. [49], from top to bottom and left to right: Diagram of the combined feedback-feedforward system and positioning of each control system in the vehicle.

For isolating structural vibrations, either feedback or feedforward control techniques can be implemented, depending on whether the source of vibration is periodic or random. Adaptive feedforward control can be used for isolating the vibrations of rotating machinery such as the engine, and reduce idling and booming noise.

One of the earliest active vibration control solutions for cars, proposed by Freudenberg, consisted of the design of an active engine mount. The transmission of the vibrations from the engine to the chassis of the vehicle was attenuated via active damping with an electromagnetic actuator [50]. A feedforward control system based on this design was implemented by McDonald et al. in a Volkswagen Golf GTI for experimental studies

[26]. Nakaji et al. have developed a feedforward active engine mounting system which employs electromagnetic actuators, hydraulic mounts and an adaptive filter. The filter algorithm allows the adjustment of the control system with respect to different driving conditions. The front and rear of the engine of a Nissan sport-utility car was equipped with the active engine mounts while passive mounts were left on the sides of the engine. The performance of both active and passive mounts was assessed and compared, with measurements of engine booming noise and floor structural vibrations taken at the driver's seat location. The implementation of active mounts resulted in a significant reduction of transmitted noise (over 10 dB) [51].

Other designs of active engine mounts using electromagnetic actuators have been proposed in [52] [53] [54] [55]. Figure 1.15 taken from [55] shows a low-cost prototype for an active engine mount system with an electromagnetic actuator. The outcomes of experimental studies revealed about up to 13 dB attenuation in engine-induced vibrations. Recent designs of active engine mounts incorporate piezoceramic instead of electromagnetic actuators, because of their high-speed response [56] [57]. Among OEMs that have implemented active engine mounts in their current vehicle, Audi can be cited [58] [59].

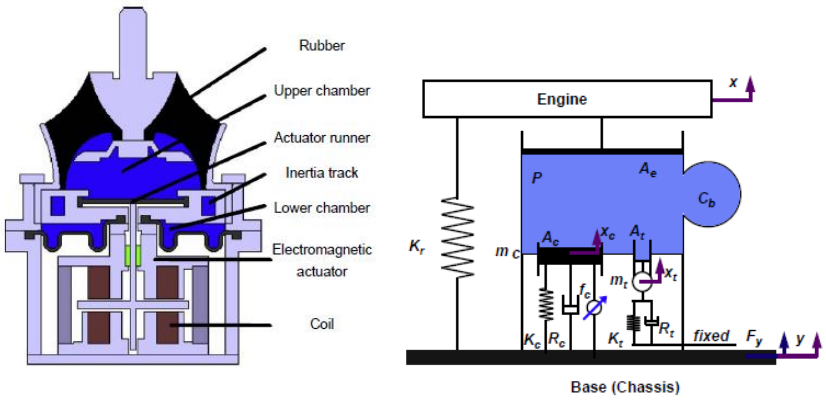

Figure 1.15 – Active engine mount system with an electromagnetic actuator. The vibrations transmitted from the engine to the chassis are attenuated through the active control of pressure in the upper chamber by the actuator [55].

Feedback vibration control works best for cases such as the vehicle suspension system or the reduction of structural vibrations of the cabin, which are caused by broadband random road or wind noise. Passive suspension strategies need to be a trade-off between isolating the cabin from external disturbances and ensuring good handling performance,

which is hard to achieve with existing conventional spring-damper systems. With the use of force-generating actuators, on-board microprocessors and real-time optimisation, active suspension systems have experienced growing interest over the years. One of the early designs of active suspension comprising a hydraulic actuator was implemented in the Lotus 91 F1 racing car and in the Lotus Esprit experimental vehicle in the 1980s [60] [61]. The first commercial vehicles fitted with active suspension systems were manufactured by Nissan and Toyota [62]. A review of the research conducted on different active suspension systems and the corresponding control methods can be found in [61]. Recent studies have focused on adaptive feedback suspension systems that take into account the non-linear dynamic parameters [63] [64].

Controlling the structural vibrations of the car body and panels such as the roof can be achieved with feedback control and the use of structural sensors and actuators. These techniques could replace the currently employed passive methods which consist of treating the cabin walls with vibration damping and porous materials.

Numerical and experimental work on the application of active vibration control to a car body can be found in [18] [65]. The actuators and sensors used for these experiments were PVDF sheets which were attached on the floor and centre panels of the car body. The use of PVDF actuators allowed the generation of distributed control forces on the structure. The control algorithm was implemented on a DSP board. The modal control approach and state-space formulation of the modal displacements and modal velocities were performed for the centre panel of the car. The floor panel of the car was controlled with the implementation of proportional feedback control. The frequency range of interest was 150 – 600 Hz. The amplitude of the 4 dominant resonance peaks of the centre panel was significantly reduced. However, some limitations still exist in the definition of the appropriate control bandwidth and the stability of the system may be compromised by the spillover of uncontrolled modes. A low-pass analogue filter was used in the above studies to overcome the problems caused by modal spillover.

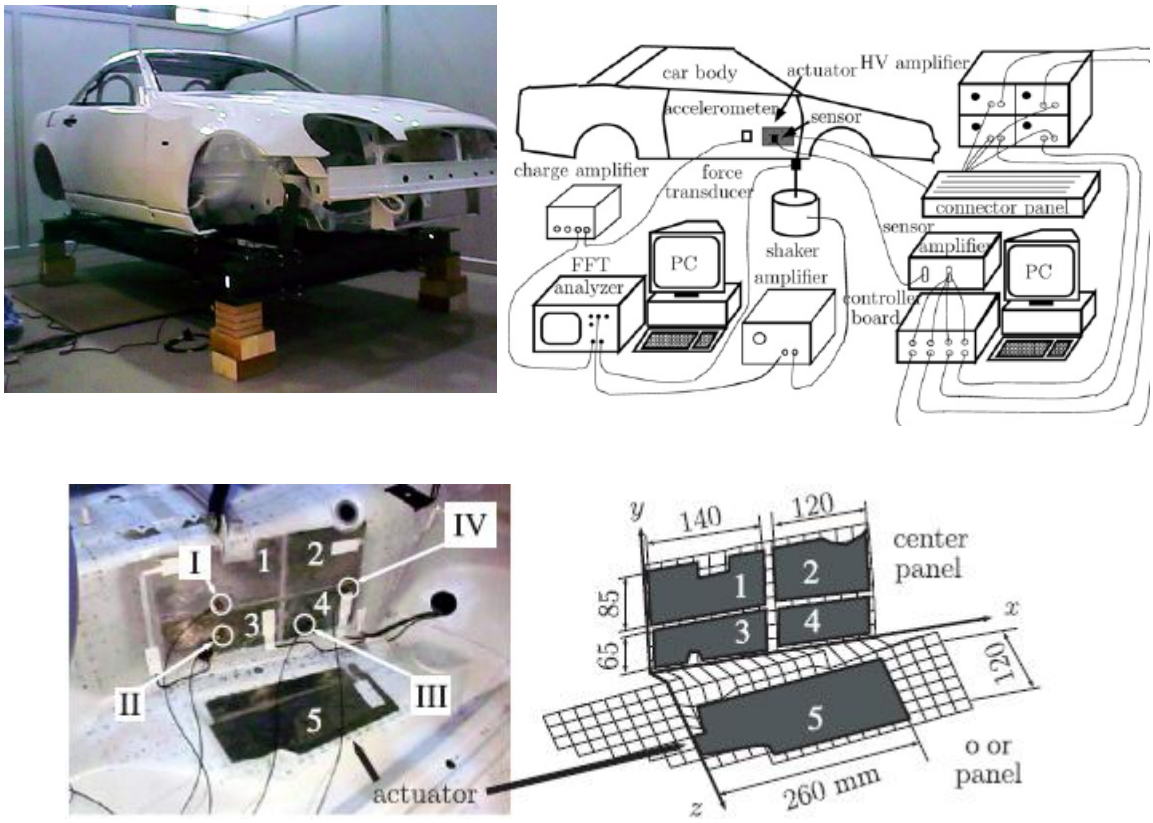

Figure 1.16 – Experimental set-up of the car for modal analysis (left), Diagram of the experimental set-up for active vibration control, (bottom) positioning of the actuator and sensor on the centre panel of the car body [18] [65].

Another study conducted by Song et al. has focused on the design and implementation of an active vibration control system for reducing the interior noise of the vehicle cabin [66]. The effects of structural-acoustic coupling were taken into account by the combination of results from experimental modal analysis on a half-scaled model of a vehicle and acoustic finite element modelling of the 3-dimensional cavity, in order to allow for the identification of the region of the cabin and the dominant modes contributing to the interior noise. As a result, the panels corresponding to the front window and the cabin floor were identified as the regions with the strongest structural-acoustic coupling, and the floor panel was selected for the implementation of control. Piezoelectric actuators and sensors were positioned on the cabin floor and the interior noise levels were measured at the driver and rear seat positions. The controller model was defined using the state-space formulation. Although the frequency range for real-time experiments was initially set between 100 – 300 Hz, the frequency range had to be extended in order to include the contribution of a mode located at 505 Hz which caused

the system to go unstable. The experimental results showed efficient attenuations in the region up to 300 Hz [66].

In the long run, active vibration control could be more effective than active noise control as it allows the reduction of noise at the source or very close to it. However, in automotive applications, in comparison to active noise cancellation technologies, it is at much earlier stages, due to issues related to the stability of the control system and issues related to the cost of implementation due to the number of actuators required.

Application of active control in aircraft:

In an aircraft, the control and reduction of interior noise and vibrations caused by the different sources described in Section 1.2.2 represent an important challenge. Not only can the vibrations of the fuselage or the airframe due to these disturbances affect passengers comfort, but also high levels of vibration cause fatigue which can eventually lead to structural damage [24]. The combination of passive treatments which are only effective at mid and high frequencies, with active noise and vibration control technologies that are capable of reducing low frequency noise and vibration, can help in achieving efficient reduction in the interior noise levels. The different sources of noise and vibration in aerospace vehicles and the active and passive techniques used for their attenuation have been extensively reviewed by Gardonio in [24].

The practical implementation of active noise and vibration control for aerospace applications has been a subject of growing interest of recent decades, and these technologies are available on several passenger and military aircraft.

One of the early studies on active noise control of aircraft interior noise has been performed by Elliott et al. on a BAE 748 aircraft for the application active noise control solutions on open rotor aircraft [13]. The aim of the study was to reduce the interior noise due to the propellers. For engines' speed of 14,200 rpm, the fundamental blade passing frequency of the propellers was 88 Hz. Different arrangements of 16 loudspeakers for the secondary sources and 32 microphones for measuring the error signal were tested in the passenger compartment in order to determine the optimal

configuration for which the maximum reduction in the interior noise field could be achieved. The levels of the loudspeakers signals were adjusted by the adaptive feedforward control algorithm in order to minimise the sum of the squares of the error signals measured by the microphones. Experiments of active control were performed both on the ground when the engines were running at full speed and during flights. The fundamental frequency was attenuated by 13 dB for uniform and circumferential distributions of the loudspeakers [13]. A similar control system has been made available by Saab on Saab 340 aircraft [67]. The control system developed by Saab consists of 24 secondary sources fitted in the trim panels by the overhead luggage compartment and on the floor near the seats, and 48 error microphones distributed throughout the cabin and positioned at head heights for both seated and standing aisle configurations. This arrangement allowed attenuations in the interior noise at the head level of up to 10 dB [67].

The reduction of interior noise can also be achieved by active structural acoustic control (ASAC) and active vibration control. Examples of investigations of ASAC can be found in [68] [69], where piezoceramic actuators have been mounted on the trim panels and fuselage in order to attenuate both structural vibration and interior noise levels.

Among ASAC systems available in passenger aircraft, the Bombardier Q400 can be cited in which active structural acoustic control (ASAC) is achieved to reduce the tonal propeller-induced noise in the passenger compartment. The control system is a multi-channel feedforward control system consisting of inertial shakers fitted on the aircraft fuselage acting as secondary sources, accelerometers which are positioned on the seat rails to measure the reference signals, and microphones fitted behind the aircraft trim panels and overhead bins to measure the error signal [70]. The block diagram of the control system can be viewed in Figure 1.17.

The inertial shakers used in this system are Active Tuned Vibration Attenuators (ATVAs) manufactured by Ultra-Electronics [70], which consists of a mass-spring system with a natural frequency tuned to the dominant frequency of the noise spectrum which needs to be controlled. The mass-spring system is composed of a proof mass mounted between two springs in a coil and attached to the casing by thin flexible supports. The mass is driven by a force generated from an electrical current flowing through the coil. A diagram of the ATVA actuator and its mounting position are

displayed in Figure 1.17. A minimum of 48 ATVAs were identified for achieving good control performance during the measurements [70].

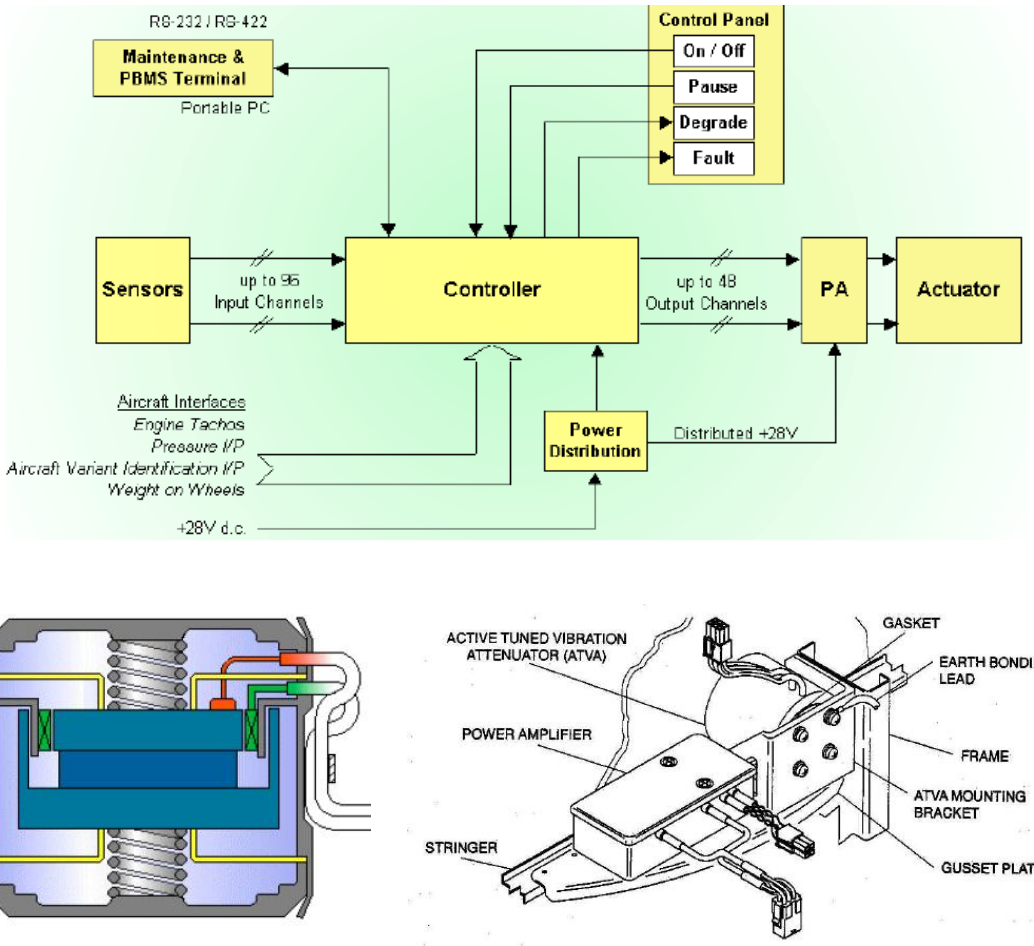

Figure 1.17 – Block diagram of the control system for reducing the interior noise due to tonal propeller noise (top), internal diagram of the ATVA actuator manufactured by Ultra-Electronics and the mounting position of the actuator (bottom) [70].

The implementation of active structural acoustic control and active vibration control techniques have also been widely investigated for helicopters. One of the contributing sources of noise to the interior of the cabin is the vibrations of the airframe. Experiments of active control have been performed by Petitjean et al. on helicopter honeycomb sandwich panel in [71], using both feedback and feedforward control techniques. Different arrangements were tested for the actuators and sensors on a square honeycomb panel using 8 polyvinylidene fluoride (PVDF) collocated with 8 PZT (lead titanate/zirconate) patches, 2 sets of accelerometers where 3 out of 4 were collocated

with secondary dynamic shakers, and 3 error microphones located 0.1 m away from the panel to measure the noise level. The structure was excited by a shaker with either tonal or random noise for a frequency range of 0 – 800 Hz. Tonal noise was reduced via adaptive feedforward control and random noise was reduced with feedback control. Although both approaches showed good attenuations levels, the use of feedback control and distributed actuator/sensor pairs allowed a better attenuation in the sound pressure over the whole surface of the structure, without the need for reference pressure measurements [71]. Decentralised feedback control was performed by Lepage et al. in [72], when piezoceramic actuators were fitted in a square portion of a helicopter trim panel to reduce the structural vibrations of the structure and reduce the radiate sound power inside the cabin.

One of the main causes of fuselage vibration in a helicopter is the vibration of the gearbox at its mounting points on the body. The application of active vibration control to this problem has been investigated by a number of researchers. Vibration due to the main rotor of the AgustaWestland EH101 helicopter is already actively controlled using hydraulic actuators in the engine struts [73].

1.3 Scope and Objectives

The purpose of this thesis is to investigate the effects of curvature on the behaviour of a panel, as well as on the efficiency and robustness of a direct velocity feedback control system. The panel used in the theoretical, numerical and experimental work is a thin homogeneous aluminium panel of rectangular shape. The feedback control unit consists of an electrodynamic proof-mass actuator collocated with a velocity sensor positioned at its base. The aluminium panel is either excited by a point force (shaker, impact hammer) or an acoustic field (loudspeaker).

The main objectives of this thesis are:

- To derive a relevant analytical model for vibrations in doubly-curved thin panels.

- To model and study the performance and stability of a velocity feedback control system, composed of one or more inertial actuators, when it is installed on a thin panel of different curvatures.
- To assess the performance of a velocity feedback control system installed on a car roof panel.
- To investigate the effects of structural-acoustic coupling in a doubly-curved panel as part of a rigid-walled enclosure.
- To present a practical implementation of a velocity feedback control system on a pressurised enclosure with one flexible aluminium panel of different curvatures.

1.4 Structure and Organisation

This thesis consists of 7 chapters divided into two parts: the first part of this thesis – chapters 2 through 5 – covers the topic of feedback control on doubly-curved shells. The second part of the thesis – Chapter 6 – presents the application of feedback control to doubly-curved shells that form part of an enclosure.

Chapter 2 provides a comprehensive study of doubly-curved panels' theory. The objective of this section is to understand the mechanisms of wave propagation and free vibrations in shallows shells. General equations for the estimation of the natural frequencies of the system in the absence and presence of in-plane inertia are proposed for simply-supported and clamped-clamped boundary conditions.

Chapter 3 presents analytical and numerical (FEM) models of a simply-supported homogeneous aluminium panel with increasing curvature. Modal analysis is performed on both models. The results are re-arranged and validated using Modal Assurance Criterion (MAC). A comparison of the mode shapes and natural frequencies is performed for several levels of curvature in order to observe the trends with respect to curvature increase.

Chapter 4 presents the results of simulations of a smart panel for active vibration control (AVC) with increasing curvature in both x and y directions. The simply-supported panel

modelled in Chapter 3 is used for simulations of velocity feedback control and electrodynamic proof-mass actuators are modelled on the surface. The passive effects of the actuator have not been taken into account in this Chapter but are considered in Chapter 6. The influence of curvature change on the performance of the system, number and position of required actuators and stability of the control system has been investigated.

Chapter 5 presents a case study investigating the implementation of active vibration control systems a road vehicle roof panel made of carbon steel. The first past of the chapter concentrates on experimental modal analysis work performed on the roof. The second part of the chapter includes the FEM model of the car roof panel and the modal analysis performed under clamped-free boundary conditions. The third part of the chapter provides a comparison of the two methods. Finally, simulations of feedback control based on numerical and experimental results are presented.

Chapter 6 concentrates on the practical implementation of velocity feedback control on a curved panel which is part of an otherwise rigid enclosure. The first part of the chapter explains the steps involved in the design of the control unit and a compensation filter responding to the stability requirements of the system has been proposed. The proposed control system has been installed on an experimental rig in which an aluminium panel has been fixed on a rigid-walled Perspex enclosure. The enclosure has been pressurised in order to alter the curvature of the panel. A study of the effect of pressure changes on the performance of the active control system has been conducted.

Finally Chapter 7 provides a summary of the results and outcomes of the research, followed by concluding remarks and recommendations for future work.

1.5 Contributions of this Thesis

The original contributions of this thesis can be organised into the following groups:

- Derivation of analytical models for doubly-curved panels, which include the contribution of in-plane inertia, for two boundary conditions, supported by shear diaphragms along all edges, and clamped along all edges.

- Theoretical and numerical analysis of velocity feedback control on doubly-curved panels.
- Practical implementation of velocity feedback control with an inertial actuator on a panel curved by pressurisation.

2. Dynamic Behaviour of Curved Panels

2.1 Overview of Shallow Shell Theory

A shell can be defined as a three-dimensional structure, confined by two parallel surfaces, where the distance between these two parallel surfaces is small compared to the other dimensions of the structure [74]. Based on Vlasov's definition, a shallow shell is a thin-walled structure where the thickness is small compared with the other dimensions, and the radii of curvature are larger than the other dimensions of the shells [75].

From a structural point of view, shells tend to have some advantageous properties compared to flat plates. Their bending stiffness makes them considerably stiffer than plates and more resistant to deformation, thus allowing manufacturers to produce stiffer and stronger structures for a given weight. Furthermore, their high resistance to compression provides a more stable structure. For these reasons, shells and curved panels are widely used in the aerospace and aeronautic industries and their application has become increasingly popular in the automotive and civil engineering fields [74] [76].

Based on their curvature, shells can be categorised into singly-curved (cylindrical and conical shells) or doubly-curved (spherical, paraboloidal and other shells of revolution). A large amount of literature can be found on the vibration of curved shells. The free vibration of shells was thoroughly reviewed by Leissa in a NASA monograph published in 1973, where over 1000 references have been cited to cover the research and the various modelling techniques conducted on the topic up to the 1970s [77]. An extensive review of the recent research and advances in modelling techniques for the vibration of homogeneous shells has been presented by Qatu in [76], which covers the work done between 1989 and 2000. Finally, the case of stiffened shallows shells have been extensively investigated by Langley, for the application to aircraft panels [78] [79] [80] [81].

The analysis of the dynamic behaviour and vibration of a structure can be studied through either analytical or numerical modelling. The analytical approaches are based

on mathematical models describing the motion of the structure under specific constraints and boundary conditions. This involves the derivation of the differential equations of motion or energy equations. As it is not always possible to obtain an exact solution, approximate solutions can be estimated from available theories such as Rayleigh-Ritz, Galerkin and Timoshenko for example. In numerical approaches, finite element methods are used to approximate the dynamic behaviour at discrete points on the structure. A discretised representation of the structure of interest is thus obtained and the equations of motion are derived for each point.

The deformation of a shell is investigated in a similar manner to that of a plate: the shell geometry and displacements are described at its mid-surface. However, unlike plates, the in-plane components of motion for shells are coupled with the transverse components of motion, which means that the shear forces and bending and twisting moments must be combined with membrane forces. These coupling interactions between the transverse and in-plane motions introduce difficulties in the accurate mathematical modelling of the structure, as the resulting differential equations of motion have an order of 8 – instead of having an order of 4 in the case of plates – and are expressed in terms of three dependant variables in the *x*, *y* and *z* directions. Another problem arises from the accuracy of the modelled boundary conditions and the selection of trial functions that can satisfy the equations of motion [77] [82].

Approximate thin shell theories that can be applied to simplified cases have been developed in order to reduce the order of the equations from 8 to 4. In general, shell theories have been categorised into: (1) membrane theory, (2) bending theory, (3) shear deformation and rotary inertia theory. The latter category also includes the contribution of bending and membrane stresses and displacements. While using any of these theories, it is important to consider the limit of validity of each, in order to choose the appropriate one for the structure of interest, without inducing errors in the displacement and stress estimations [83].

Among the three categories listed above, Rayleigh's membrane theory, Love's extension and bending theory, Flügge's theory, Arnold and Warburton's theory and Kennard's theory can be cited [83]. In his approximations, Rayleigh uses the expressions for kinetic and potential energy. However, only the contribution of extension is taken into account in the calculation of potential energy and bending has

been neglected. In Love and Flügge's theories, calculations are directly performed on the equations of motion rather than the kinetic and potential energy equations. Both bending and extension are considered in the approximation. Normal stress is also initially taken into account but neglected in the approximations. Kennard's work is also based on deriving the equations of motion but ignoring the higher order terms of stresses. Arnold and Warburton follow the Rayleigh-Ritz method and the energy equations in their work. The Lagrange equation is then used for the estimation of the natural frequencies of the system. Despite eliminating the contribution of in-plane components of inertia and only calculating the kinetic energy for transverse displacement, there is a general agreement between their analytical and experimental work [75] [83].

Because of their advantageous dynamic properties, and their use in the maritime, aircraft and automotive industries, an understanding of their structural behaviour is necessary in the implementation of active vibration control systems, which are of current interest in these industries.

2.2 Wave Propagation and Transmission in Curved Structures

In order to gain a better understanding of the dynamic behaviour of curved shells, it is important to study the mechanisms of structural excitation and wave propagation. Wave propagation through a structure can be transverse or longitudinal. Transverse, bending or flexural waves cause the particles in the structure to move normal to the wave direction, while longitudinal or extensional or in-plane waves excite the particles along the direction of motion. This section provides an overview of wave propagation and motion in curved structures, first for thin beams, then for thin shells with curvature in one or two dimensions.

2.2.1 Wave Propagation in Thin Straight Beams

One of the earliest studies on the dynamic behaviour and mechanism of wave propagation in curved structures was performed by Lamb in 1888 and considered the

analysis of vibrations of lightly-curved beams through the derivation of the equation of motion for a ring segment with free-free boundary conditions [84]. In 1928, Den Hartog used the Rayleigh-Ritz approach to calculate the natural frequencies of the first two modes of circular arcs with fixed and hinged boundary conditions. Other theoretical studies of curved beams such as those of Archer, Lang, Morley, Den Hartog and Volterra followed extending the results to more general cases with higher curvatures and non-circular arcs [85]. An extensive review of the work conducted on curved beams and arches has been performed by Leissa and Chidamparam [86].

The independent propagation of longitudinal and flexural waves in flat, uncurved beams is briefly reviewed before the complex case for curved beams is outlined, mostly based on the materials found in [17] [26].

The longitudinal wave equation of free motion for an element of a thin, straight, uncurved beam can be expressed as

$$E\frac{\partial^2 u}{\partial x^2} - \rho\frac{\partial^2 u}{\partial t^2} = 0, \tag{2.1}$$

where u is the component of motion in the axial x-direction, E is the Young's modulus of elasticity and ρ is the density of the material. The longitudinal wavenumber k_L is then obtained as

$$k_L = \frac{\omega}{c_L}, \tag{2.2}$$

where the phase speed c_L is $c_L = \sqrt{E/\rho}$. It can be seen from the equation for c_L that it is not frequency dependant, which means that longitudinal waves are non-dispersive. The general solution to the differential Equation (2.1) can be written in terms of positive and negative travelling waves with complex amplitudes, A and B as

$$u(x,t) = Ae^{j(\omega t - k_L x)} + Be^{j(\omega t + k_L x)}, \tag{2.3}$$

where ω is the angular frequency in rad/s and $\omega = 2\pi f$, where f is the frequency in hertz.

The equation of motion for bending waves in a thin straight beam is uncoupled from the longitudinal motion and can be expressed as

$$EI\frac{\partial^4 w}{\partial x^4}+\rho A\frac{\partial^2 w}{\partial t^2}=p(x,t)\,, \tag{2.4}$$

where $p(x,t)$ is the external load acting on the beam and distributed over its length, w is its out-of-plane displacement, $I=bh^3/12$ is the second moment of inertia of the cross-section of a rectangular beam of width b and height h, and A is the cross-sectional area of the beam. Equation (2.4) is also referred to as the Euler-Bernoulli thin beam equation. The flexural wavenumber and phase speed for a thin beam can be obtained from the following equations

$$k_F=\sqrt[4]{\frac{\rho A\omega^2}{EI}} \tag{2.5}$$

$$c_F=\frac{\omega}{k_F}\,. \tag{2.6}$$

In the absence of damping, the flexural wavenumber calculated in Equation (2.5) is real positive. Because of the frequency-dependence of the phase speed c_F, bending waves are dispersive. The general solution for the fourth order equation of motion of Equation (2.4) is:

$$w(x,t)=Ae^{j(\omega t-k_F x)}+Be^{j(\omega t+k_F x)}+A_n e^{(j\omega t-k_F x)}+B_n e^{(j\omega t+k_F x)} \tag{2.7}$$

The two last terms in the above equation are the evanescent or near-field solutions that decay in the direction of motion – increasing x for positive travelling waves and decreasing x for negative travelling waves. The relationship between wavenumber and angular frequency, and between phase speed and frequency for longitudinal and bending waves are shown in the graphs of Figure 2.1.

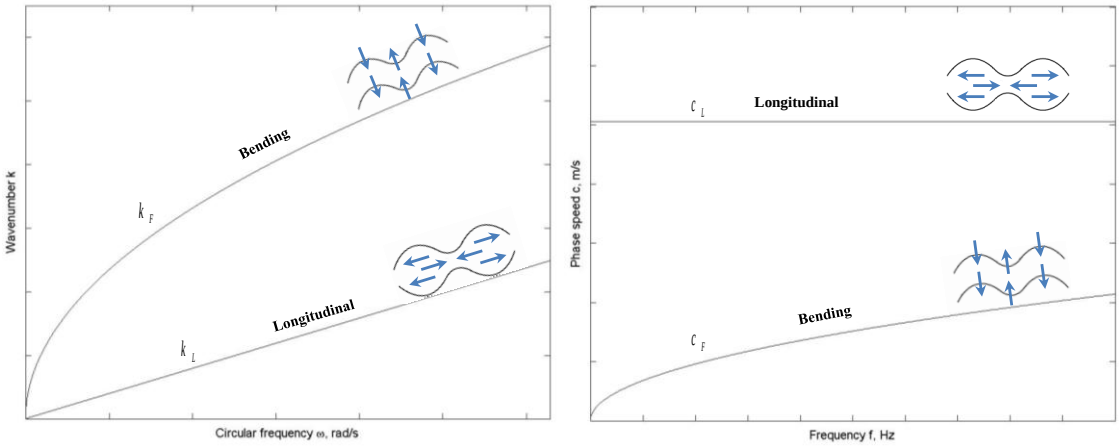

Figure 2.1 - Wavenumber *k* plotted against circular frequency for longitudinal and bending waves (left), Phase speed *c* plotted over frequency for longitudinal and bending waves (right).

While using the Euler-Bernoulli beam theory, it is assumed that the cross-sectional plane section perpendicular to the longitudinal axis of the beam is rigid, i.e. it remains plane and perpendicular to the axis of the beam. The deformation is considered to be purely due to bending and as a result, the transverse normal stress is neglected. While this assumption can be used for the case of thin beams, it cannot accurately represent the structural excitation for thick beams, composite beams or shells where the interactions between bending and shear deformations need to be taken into account. For an Euler-Bernoulli beam in pure bending, the natural frequencies can be estimated from Equation (2.4), when it is subjected to free vibration, $p(x,t)=0$, leading to the general equation

$$\omega_n = \sqrt{\frac{EI}{\rho A}} k_{F,n}^2, \tag{2.8}$$

where $k_{F,n}$ corresponds to the bending wavenumber of the nth natural frequency and varies depending on the boundary conditions. The natural frequencies obtained from Equation (2.8) tend to become inaccurate for higher order modes. Consequently, the Euler-Bernoulli beam theory should be more specifically applied to thin beams in which the thickness is much smaller than wavelength. For more general cases, Timoshenko' beam theory or Rayleigh-Ritz approach can be used instead of Euler-Bernoulli, because the contribution of shear distortion and rotary inertia of the cross-section are included in the derivations and the distribution of shear stress on the cross section of the beam is no

longer considered even. Kinetic and strain energy equations are used for calculating the natural frequencies with the Rayleigh-Ritz approach [87].

2.2.2 Wave Propagation in Thin Curved Beams

When a curved beam is considered, because of the coupling between the transverse and in-plane components of motion, Equations (2.1) and (2.3) are no longer sufficient for an accurate representation of the deflection of the structure. Based on the choice of theory and assumptions made for approximating the characteristics of the surface, there are different ways of expressing the equations of motion for a curved beam. However, the common starting point in all methods is the characterisation of a curved beam at its mid-surface, in terms of polar coordinates R and θ, where R is the radius of curvature of the beam for a given angle θ. A general diagram of a curved beam and the defined parameters are shown in Figure 2.2.

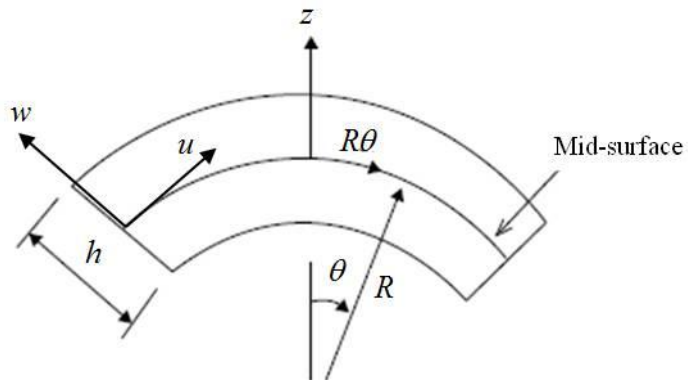

Figure 2.2 – Diagram of the cross section of a curved beam [88].

The strain and curvature at the mid-surface can be formulated respectively as [88]

$$\varepsilon_0 = \frac{1}{R}\frac{\partial u}{\partial \theta} + \frac{w}{R} \tag{2.9}$$

$$\kappa = \frac{1}{R^2}\left(-\frac{\partial^2 w}{\partial \theta^2} + \frac{\partial u}{\partial \theta}\right), \tag{2.10}$$

where u and w are the tangential and radial components of displacement. Their direction has been indicated in Figure 2.2.

The equations of motion for a curved beam of uniform curvature are generally obtained by calculating the sum of forces in the radial and tangential directions and the bending moments for an element of the beam of thickness *h* and mid-surface length $Rd\theta$. The bending moment *M* and tensile force *N* are calculated from the integration of axial stress σ over the beam thickness

$$M = b\int_{-h/2}^{h/2} z\sigma dz = \frac{Ebh^3}{12}\kappa \tag{2.11}$$

$$N = b\int_{-h/2}^{h/2} \sigma dz = EA\varepsilon_0, \tag{2.12}$$

where *b* is the width of the beam.

The equations of motion have been derived by Lee et al in [89] [90] at the mid-surface of a thin uniform curved beam, based on Flügge's strain-displacement theory, as

$$-EI\left(\frac{\partial^4 w}{\partial s^4} + \frac{2}{R^2}\frac{\partial^2 w}{\partial s^2} + \frac{w}{R^4}\right) - \frac{EA}{R}\left(\frac{w}{R} + \frac{\partial u}{\partial s}\right) = \rho A\frac{\partial^2 w}{\partial t^2}, \tag{2.13a}$$

$$EA\left(\frac{\partial^2 u}{\partial s^2} + \frac{1}{R}\frac{\partial w}{\partial s}\right) = \rho A\frac{\partial^2 u}{\partial t^2}, \tag{2.13b}$$

where *s* is the circumferential coordinate at the mid-surface and $ds = Rd\theta$. The contributions of rotary inertia, shear deformation and damping are neglected in the above equations. The diagram in Figure 2.3 shows the cross section of the beam and the direction of the components of motion. The bending moment M, shear force Q and the tensile force N have been indicated in Figure 2.3. φ refers to the rotation of the beam cross-section and is given by $\varphi = -\frac{u}{R} + \frac{\partial w}{\partial s}$.

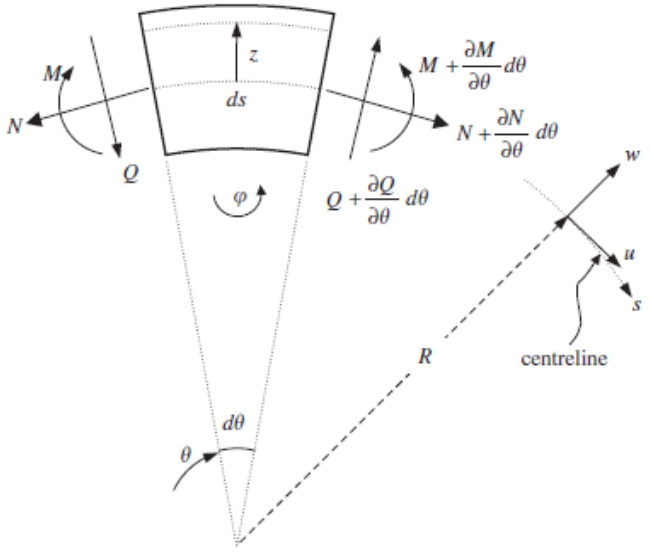

Figure 2.3 - Diagram of a curved beam with the components of motion and their direction indicated [89] [90].

The harmonic wave solutions *u* and *w* which must satisfy the equations of motion defined in (2.13a) and (2.13b) are

$$w(s,t) = C_w e^{j(\omega t - ks)}, \tag{2.14a}$$

$$u(s,t) = C_u e^{j(\omega t - ks)}, \tag{2.14b}$$

where C_w and C_u are arbitrary constants for the radial and tangential wave amplitudes respectively, k is the wavenumber and ω is the frequency [90]. The substitution of Equations (2.14a-b) into the equations of motion defined in Equations (2.13a-b) and further simplifications lead to

$$k^6 - \left(\frac{\rho\omega^2}{E} + \frac{2}{R^2}\right)k^4 + \left(\frac{1}{R^4} - \frac{\rho A\omega^2}{EI} + \frac{2\rho\omega^2}{ER^2}\right)k^2 - \frac{\rho\omega^2}{E}\left(\frac{1}{R^4} + \frac{A}{IR^2} - \frac{\rho A\omega^2}{EI}\right) = 0 \tag{2.15}$$

Using the longitudinal and flexural wavenumbers defined for a straight beam in Equations (2.2) and (2.5), the above equation can be further modified to formulate the dispersion equation in terms of k_L, k_F and curvature κ, such that [90]

$$k^6 - \left(k_L^2 + 2\kappa^2\right)k^4 + \left(\kappa^4 - k_F^4 + 2\kappa^2 k_L^2\right)k^2 - \left(\kappa^4 k_L^2 + \kappa^2 k_F^4 - k_L^2 k_F^4\right) = 0, \tag{2.16}$$

where $\kappa = \frac{1}{R}$. The 6th order polynomial of Equation (2.15) has 6 roots for k which corresponds to 3 waves travelling in the positive direction and 3 travelling in the negative direction. Depending on frequency and curvature, these roots can be organised into four categories: (1) all six roots real, (2) two real and four complex roots, (3) two real and four imaginary roots, and (4) four real and two imaginary roots [85]. For very small values of κ, the above equation reduces to the dispersion equation for a straight beam, expressed in terms of longitudinal and flexural wavenumber, as

$$\left(k^4 - k_F^4\right)\left(k^2 - k_L^2\right) = 0 \tag{2.17}$$

The six wavenumber solutions to the above equation have been defined as the "straight beam limit" in [90]. Out of these six solutions, 4 are the asymptotic limits to bending wavenumbers and 2 are the asymptotic limits to the longitudinal wavenumbers.

When the wavenumber is set to 0, the dispersion equation in Equation (2.16) becomes a function of the curvature κ

$$\kappa^4 k_L^2 + \kappa^2 k_F^4 - k_L^2 k_F^4 = 0. \tag{2.18}$$

Substituting for $\kappa = \frac{1}{R}$, and k_L and k_F from Equations (2.2) and (2.5) in the above equation, the equation for the cut-off frequency in curved beams is obtained as

$$\omega_{cut-off} = \frac{c_L}{R}\sqrt{1 + \frac{I}{AR^2}}, \tag{2.19}$$

where the term $\frac{I}{AR^2}$ is due to the use of Flügge's theory. The above equation reduces to $\omega_{cut-off} = \frac{c_L}{R}$, if the derivation of the equations of motion is done following Love's theory [85] [26] [90]. When displacement is purely radial, the wavelength is equal to the circumference and the beam is known to resonate at the ring frequency which is $\omega_r = \omega_{cut-off}$.

2.3 Vibration of Thin Cylinders

The use of singly-curved structures such as cylindrical shells is common in aircraft and naval industries, for example, in aircraft fuselages, submarine hulls, rockets or other load bearing structures. Figure 2.4 displays the diagram of a closed circular cylindrical shell where the parameters and direction of components of motion are indicated.

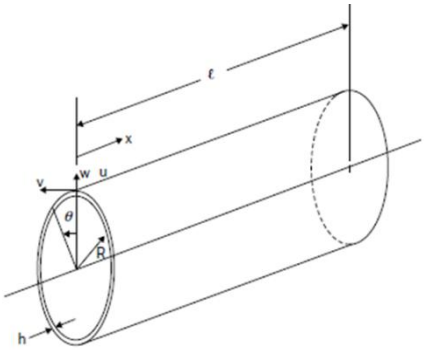

Figure 2.4 – Cylindrical shell with parameters and directions of motion indicated [82].

A large number of theories can be found for describing the equations of motion for thin cylindrical shells and estimating the natural frequencies through different approximation methods, among which Warburton, Donnell-Mushtari and Vlasov's approaches can be cited. Warburton's work is based on deriving the equations of motion based on Flügge's theory, in which rotary inertia and shear deformation are neglected, and estimating the natural frequencies using the Rayleigh-Ritz approximation for clamped and free end boundary conditions [91]. The Donnell-Mushtari and Vlasov's equations of motion, calculated *in-vacuo* for a thin cylindrical shell, are one of the simplest and most widely used [26] [92]. These are given by

$$\frac{\partial^2 u}{\partial x^2}+\frac{(1-\nu)}{2R^2}\frac{\partial^2 u}{\partial \theta^2}+\frac{(1+\nu)}{2R}\frac{\partial^2 \upsilon}{\partial x \partial \theta}+\frac{\nu}{R}\frac{\partial w}{\partial x}-\frac{\ddot{u}}{c_L^2}=0 \tag{2.20a}$$

$$\frac{(1+\nu)}{2R}\frac{\partial^2 u}{\partial x \partial \theta}+\frac{(1-\nu)}{2}\frac{\partial^2 u}{\partial x^2}+\frac{1}{R^2}\frac{\partial^2 \upsilon}{\partial \theta^2}+\frac{1}{R^2}\frac{\partial w}{\partial \theta}-\frac{\ddot{\upsilon}}{c_L^2}=0 \tag{2.20b}$$

$$\frac{\nu}{R}\frac{\partial u}{\partial x}+\frac{1}{R^2}\frac{\partial \upsilon}{\partial \theta}+\frac{w}{R^2}+\beta^2\left(R^2\frac{\partial^4 w}{\partial x^4}+2\frac{\partial^4 w}{\partial x^2 \partial \theta^2}+\frac{1}{R^2}\frac{\partial^4 w}{\partial \theta^4}\right)+\frac{\ddot{w}}{c_L^2}=\frac{p_a(1-\nu^2)}{Eh}, \tag{2.20c}$$

where the effects of transverse shearing-stress in the circumferential direction are assumed to be negligible. The term β in the above equations is the stiffness factor which is defined as $\beta^2 = \frac{h^2}{12R^2}$. The term p_a in Equation (2.20c) is the external force or distributed load expressed in terms of pressure.

The solution to this set of equations is typically expressed, for example in [92], in terms of the non-dimensional frequency term $\Omega = \frac{\omega R}{c_L}$, where the normalising frequency $\frac{c_L}{R}$ is known as the ring frequency. This is the frequency at which the wavelength of the longitudinal waves travelling around the shell is equal to its circumference ($\lambda = 2\pi R$), so that the motion is radial and the shell resonates as a ring.

The presence of curvature in the structure increases the speed of bending waves. However, the level of increase in wave speed with curvature depends on whether the modal frequency of the shell is above or below the ring frequency. For modes of vibration below the ring frequency, the rate of increase in wave speed is much steeper. Above the ring frequency, the shell is predominantly in bending and thus, behaves in a similar way to a flat plate, and the increase in wave speed with curvature is much lower [26] [93].

2.4 Vibration of Doubly-Curved Shells

In a similar manner to curved beams and cylindrical shells, the displacement equation for a doubly-curved shallow shell is generally formulated at the mid-surface. However, due to the presence of two radii of curvature this equation must be expressed as a quadratic surface given by [82]

$$z = \frac{1}{2}\left(\frac{x^2}{R_x} + \frac{y^2}{R_y}\right) = \frac{x^2}{2R_x} + \frac{xy}{R_{xy}} + \frac{y^2}{2R_y}. \tag{2.21}$$

For a cylindrical shell, where curvature is only in one direction, the above equation further simplifies to a more specific case where $R_x = R$ and $R_y = R_{xy} = \infty$, such that, $z = \frac{x^2}{2R}$.

As illustrated in Figure 2.5, R_x and R_y are the radii of curvature along the *x* and *y* directions and R_{xy} refers to the twist in the surface. As stated in [82], there are different ways of measuring the shallowness of a curved shell. The parameter used in this thesis will be the rise-to-thickness ratio $\frac{z_c}{h}$, where z_c is the rise at the centre of the shell.

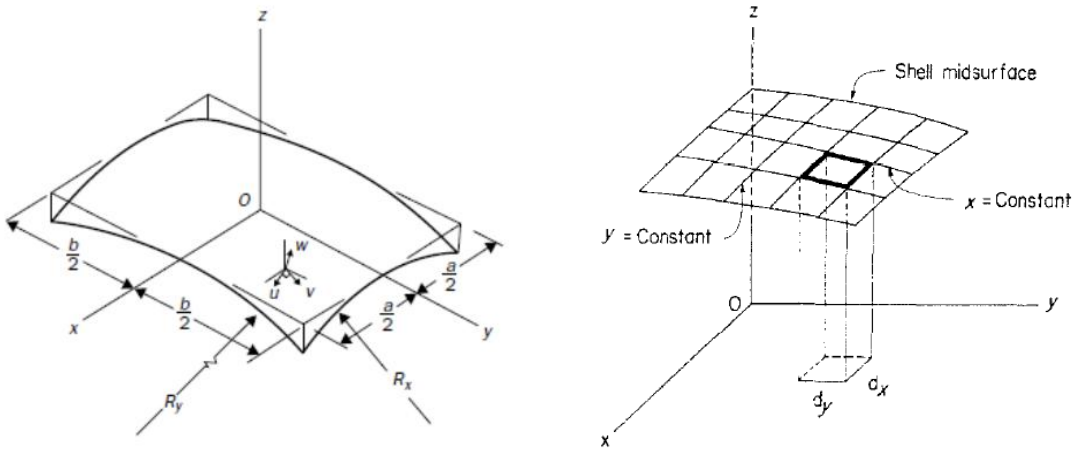

Figure 2.5 – Diagram of a curved shallow shell with a rectangular base plane projection (left) [82] and shell element defined at the mid-surface for the calculations of the equations of motion (right) [94]. The direction of the components of displacement *u*, *v* and *w* has been indicated in the diagram.

A general equation of motion for shallow shells has been derived in [82], in which a small element is considered on the surface of the shell as shown in Figure 2.5. In the first stage, the sum of the forces in the *z*-direction and the sum of the moments about the *x* and *y* axes were calculated. It was assumed that the Kirchhoff hypothesis for thin plates was applicable, such that the component of strain due to bending which is normal to the mid-surface remained normal and unstretched, and the thickness of the shell remained unchanged during deformation. The bending stresses were integrated over the shell thickness and the combination of the above steps led to

$$D\nabla^4 w+\rho h\frac{\partial^2 w}{\partial t^2}=q+T_x\left(\frac{\partial^2 w}{\partial x^2}-\frac{1}{R_x}\right)+T_y\left(\frac{\partial^2 w}{\partial y^2}-\frac{1}{R_y}\right)+2T_{xy}\left(\frac{\partial^2 w}{\partial x\partial y}-\frac{1}{R_{xy}}\right), \tag{2.22}$$

where *D,* is the bending stiffness of the shell calculated from $D=\frac{Eh^3}{12(1-\nu^2)}$ where ν is the Poisson ratio, $T_x=\sigma_x h$ and $T_y=\sigma_y h$ are the normal stress resultants, and $T_{xy}=\tau_{xy}h$ is the shear stress resultant at the mid-surface and these are caused by the deformations of the structure. σ_x, σ_y and τ_{xy} are defined in terms of the mid-surface normal strains ε_x, ε_y and shear strain ε_{xy} as

$$\sigma_x=\frac{E}{(1-\nu^2)}(\varepsilon_x+\nu\varepsilon_y), \tag{2.23}$$

$$\sigma_y=\frac{E}{(1-\nu^2)}(\varepsilon_y+\nu\varepsilon_x), \tag{2.24}$$

$$\tau_{xy}=\frac{E}{2(1+\nu)}\varepsilon_{xy}, \tag{2.25}$$

where the strains in *x* and *y* directions in the above equations are

$$\varepsilon_x=\frac{\partial u}{\partial x}+\frac{w}{R_x}, \tag{2.26}$$

$$\varepsilon_y=\frac{\partial \upsilon}{\partial y}+\frac{w}{R_y}, \tag{2.27}$$

$$\varepsilon_{xy}=\frac{\partial \upsilon}{\partial x}+\frac{\partial u}{\partial y}+2\frac{w}{R_{xy}}. \tag{2.28}$$

In the above equations, u,υ and *w* are the components of displacement in the *x*, *y* and *z* directions. *u* and υ are the in-plane, and *w* is the transverse component of displacement.

The initial models for doubly-curved shallow shells were proposed by Love (1944), Reissner (1955) and Vlasov (1964), who excluded the contribution of in-plane inertia in their derivations [75] [94] [95]. In Vlasov's analysis, it was assumed that if the

thickness of the shell was less than 5% of the edge dimensions, the effect of shear deformation and in-plane motion could be neglected [75] [94]. The different theories for thin elastic shells and their related equations of motion have been reviewed by Leissa in his NASA monograph [77] and have been derived in [94] [82]. A comprehensive study of shallow shells has been conducted by Liew et al. in which the influence of transverse shear and inertia have been investigated for thin, moderately thin and thick shallow shells [96].

In order for a doubly-curved shell similar to the one illustrated in Figure 2.5 to fall under the shallow shell category, the maximum rise $z_c = h_{\max}$ and the shortest length l of the structure must satisfy $h_{\max} \le \frac{l}{5}$. Due to the small rise, the curved length and width of the shell can be approximated by their corresponding lengths on the base plane projection [75]. However, for cases where the above condition is not met ($h_{\max} > \frac{l}{5}$), this approximation no longer holds and the difference between the curved length and the projected base length must be taken into consideration. The components of displacement in the *x*, *y* and *z* direction, *u*, υ and *w*, have been indicated in the diagram of Figure 2.5. The component of displacement *w* is normal to the shell surface.

The general equation of motion formulated in Equation (2.23) can be further reduced and adapted to doubly-curved shallow shells. In the analytical model derived by Leissa in [94] for a doubly-curved shallow shell, supported by shear diaphragms along all 4 edges which are assumed to be perpendicular to the surface, these equations are simplified by neglecting in-plane components of displacement *u* and *v* for twisting and changes in curvature

$$\frac{\partial^2 u}{\partial x^2} + \frac{(1-\nu)}{2}\frac{\partial^2 u}{\partial y^2} + \frac{(1+\nu)}{2}\frac{\partial^2 \upsilon}{\partial x \partial y} + \left(\frac{1}{R_x} + \frac{\nu}{R_y}\right)\frac{\partial w}{\partial x} = \rho\frac{(1-\nu^2)}{E}\frac{\partial^2 u}{\partial t^2}, \tag{2.29a}$$

$$\frac{(1+\nu)}{2}\frac{\partial^2 u}{\partial x \partial y} + \frac{(1-\nu)}{2}\frac{\partial^2 \upsilon}{\partial x^2} + \frac{\partial^2 \upsilon}{\partial y^2} + \left(\frac{\nu}{R_x} + \frac{1}{R_y}\right)\frac{\partial w}{\partial y} = \rho\frac{(1-\nu^2)}{2}\frac{\partial^2 \upsilon}{\partial t^2}, \tag{2.29b}$$

$$\left(\frac{1}{R_x}+\frac{\nu}{R_y}\right)\frac{\partial u}{\partial x}+\left(\frac{\nu}{R_x}+\frac{1}{R_y}\right)\frac{\partial \upsilon}{\partial y}+\frac{1}{R_x^2}+\frac{2\nu}{R_xR_y}+\frac{1}{R_y^2}+\frac{h^2}{12}\nabla^4 w=\rho\frac{(1-\nu^2)}{E}\frac{\partial^2 w}{\partial t^2}. \quad (2.29c)$$

The use of shear diaphragm boundary conditions, which are equivalent to simple supports, allows the assumption of in-plane rigidity along the edges and the neglecting of the bending resistance. Figure 2.6 shows the diagram of the shell with shear diaphragm supports along 2 edges. For a shallow shell with a rectangular base plane projection of dimensions $l_x \times l_y$, these boundary conditions are defined as

$$w=\upsilon=N_x=M_x=0, \qquad x=0, x=l_x. \quad (2.30a)$$

$$w=u=N_y=M_y=0, \qquad y=0, y=l_y. \quad (2.30b)$$

These boundary conditions can be satisfied by using the following trial functions for *u*, υ and *w* (for $m=1,2,...$ and $n=1,2,...$):

$$u=U\cos\left(\frac{m\pi}{l_x}x\right)\sin\left(\frac{n\pi}{l_y}y\right)e^{j\omega t}, \quad (2.31a)$$

$$\upsilon=V\sin\left(\frac{m\pi}{l_x}x\right)\cos\left(\frac{n\pi}{l_y}y\right)e^{j\omega t}, \quad (2.31b)$$

$$w=W\sin\left(\frac{m\pi}{l_x}x\right)\sin\left(\frac{n\pi}{l_y}y\right)e^{j\omega t}. \quad (2.31c)$$

By substituting the above *u*, υ and *w* into the equations of motion, and solving the resulting eigenvalue problem, the natural frequencies of the shallow shell were estimated in [94] over various levels of curvature. The aim of the study was not only to study the effect of curvature on the natural frequencies but also demonstrate the resulting increase in stiffness.

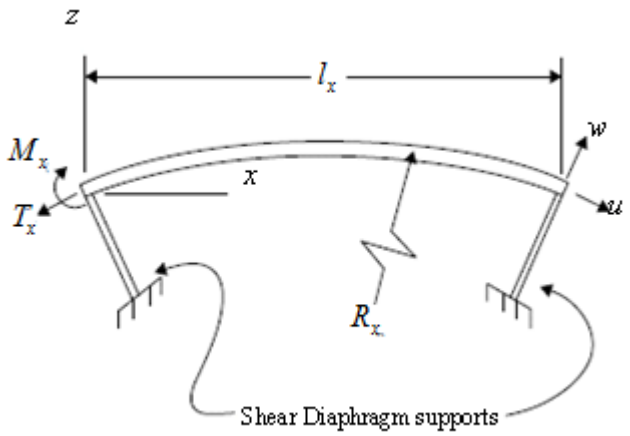

Figure 2.6 – Side-view diagram of a doubly-curved shallow shell showing curvature in the *x*-direction and shear diaphragm boundary conditions [82].

The remaining part of this chapter will concentrate on the estimation of the natural frequencies of doubly-curved shallow shells through the derivation of analytical models, in a similar manner to the theory discussed in [75] [82] [94]. These analytical models will be used to investigate the effect of curvature change on the mode shapes and natural frequencies whilst taking into account the effect of in-plane inertia, for different boundary conditions. The results of this analytical study will provide a basis for the simulations and experiments discussed in the later chapters of this thesis.

2.5 Estimation of the Natural Frequencies of Doubly-Curved Shells

The analytical models and general formulations for the natural frequencies of a doubly-curved shell derived for this thesis were initially obtained based on Warburton's theory, which was then modified using methods based on those of Leissa. While it can be argued that more complex theories and more recent models are available for determining the natural frequencies of doubly-curved shallow shells, Leissa's approach remains amongst one of the most cited and widely used to date and, as it will be demonstrated in the later chapters of this thesis, provides accurate results.

2.5.1 Analytical Model Based on Warburton's Approach

The natural frequencies of a shallow shell similar to the one displayed in Figure 2.7 with dimensions of $l_x \times l_y \times h$, were derived based on the Rayleigh-Ritz method by Warburton in [75], who ignored the effect of in-plane inertia. The shallow shell was assumed to be subjected to shear diaphragm boundary conditions along all four edges and the contribution of the in-plane inertia was neglected.

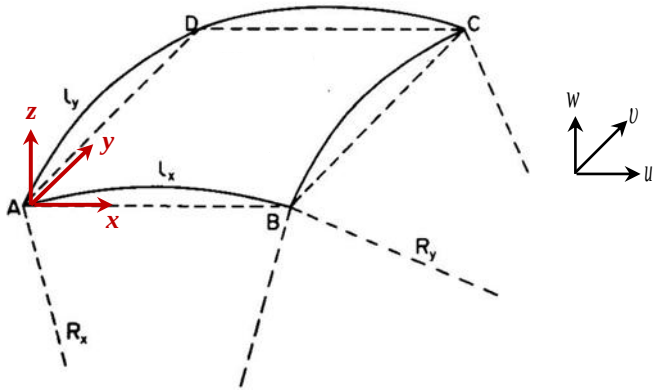

Figure 2.7 – Diagram of a doubly-curved shallow shell with the direction of components of motion indicated [75].

The assumed mode shapes for these boundary conditions, as defined in [75], are

$$u = U(t)\cos(\lambda_x x)\sin(\lambda_y y) \tag{2.32a}$$

$$\upsilon = V(t)\sin(\lambda_x x)\cos(\lambda_y y) \tag{2.32b}$$

$$w = W(t)\sin(\lambda_x x)\sin(\lambda_y y), \tag{2.32c}$$

where the wavenumbers λ_x and λ_y are $\lambda_x = \frac{m\pi}{l_x}$ and $\lambda_y = \frac{n\pi}{l_y}$ respectively. The equation for the transverse component of displacement *w* is based on beam modal functions while the in-plane components of displacement *u* and υ are based on harmonic functions. According to Warburton's theory, the natural frequency of mode *(m,n)* can be generally expressed as

$$\frac{\rho}{E}\omega_{mn_{curved}}^2\left(\lambda_x^2+\lambda_y^2\right)^2=\left(\frac{\lambda_x^2}{R_y}+\frac{\lambda_y^2}{R_x}\right)^2+\frac{h^2}{12\left(1-\nu^2\right)}\left(\lambda_x^2+\lambda_y^2\right)^4. \tag{2.33}$$

For the more specific case of a shallow shell with a square base plane projection where $l_x=l_y=l$ and $R_x=R_y=R$, the above equation can be further simplified to:

$$\omega_{mn_{curved,square}}^2=\frac{E}{\rho R^2}+\frac{Eh^2}{12\rho\left(1-\nu^2\right)}\left(\lambda_x^2+\lambda_y^2\right)^2. \tag{2.34}$$

The above equation can be further manipulated in order to reflect the relation between the natural frequencies of a curved square shell and its equivalent flat shape. That is, since the natural frequencies of an equivalent flat plate are given by

$$\omega_{mn_{flat}}=\sqrt{\frac{Eh^2}{12\rho\left(1-\nu^2\right)}}\left(\lambda_x^2+\lambda_y^2\right), \tag{2.35}$$

Equation (2.36) can be written in terms of $\omega_{mn_{flat}}$ as

$$\omega_{mn_{curved,square}}^2=\omega_{mn_{flat}}^2\left(1+\frac{1}{R^2}\cdot\frac{12l^4\left(1-\nu^2\right)}{h^2\pi^4\left(m^2+n^2\right)^2}\right). \tag{2.36}$$

The relationship between the radius of curvature and the length of the panel, as shown in the diagram in Figure 2.8, can be expressed as

$$R^2=\left(\frac{l}{2}\right)^2+(R-z_c)^2$$

$$R^2=\left(\frac{l}{2}\right)^2+R^2-2Rz_c+z_c^2$$

$$2Rz_c=\left(\frac{l}{2}\right)^2+z_c^2. \tag{2.37}$$

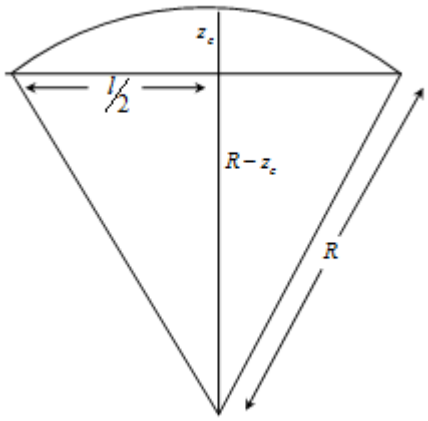

Figure 2.8 – Geometric representation of a side of a doubly-curved shell

For cases where the maximum rise in height at the centre point of the panel z_c is less than 5% of the length ($z_c \leq 0.05l$), Equation (2.39) can be reduced to:

$$2Rz_c = \left(\frac{l}{2}\right)^2 \Rightarrow R = \frac{l^2}{8z_c} \tag{2.38}$$

The term z_c^2 can be neglected from Equation (2.37) as it is much smaller than $\left(\frac{l}{2}\right)^2$.

Using the above approximation for larger values of z_c will reduce the accuracy of the calculations.

Finally, the substitution of Equation (2.38) into Equation (2.36) and further simplification leads to the following relationship between the natural frequencies of a doubly-curved panel with a square base-plane projection and the natural frequencies of a square flat panel of the same dimensions

$$\omega^2_{mn_{curved,square}} = \omega^2_{mn_{flat}} \left(1 + \frac{768\left(1-\nu^2\right)}{\pi^4\left(m^2+n^2\right)^2} \cdot \left(\frac{z_c}{h}\right)^2\right). \tag{2.39}$$

A similar approach can be used for the formulation of the natural frequencies of a doubly-curved rectangular shell. In this case, as the radii of curvature are different along the length and width of the panel, the natural frequencies depend on both l_x and l_y and are given by

$$\omega^2_{mn_{curved,\text{rectangular}}} = \omega^2_{mn_{flat}} \left(1 + \frac{768\left(1-\nu^2\right)\left(l_x l_y\right)^4 \left(m^2+n^2\right)^2}{\pi^4 \left(\left(ml_y\right)^2 + \left(nl_x\right)^2\right)^2} \left(\frac{z_c}{h}\right)^2 \right), \tag{2.40}$$

As the Warburton theory on shallow shells vibration derived in this section only estimates the natural frequencies due to the transverse component of motion, it is necessary to verify the contribution of in-plane modes on the vibrational behaviour of the structure. This can be achieved through the inclusion of the in-plane inertia in the derivations. The next section will provide more general analytical models for doubly-curved shells subjected to two different boundary conditions and include the contribution of in-plane inertia. The basis for both is a modified version of Warburton's theory adapted to more general cases of rectangular shallow shells.

2.5.2 Analytical Model of Doubly-Curved Shallow Shell Including the Effect of In-Plane Inertia

In order to derive an analytical model for a doubly-curved shell supported along all 4 edges with shear diaphragms, the mid-surface strains can be defined using Equations (2.26)-(2.28). The changes in curvature are written as:

$$\kappa_x = -\frac{\partial^2 w}{\partial x^2}, \qquad \kappa_y = -\frac{\partial^2 w}{\partial y^2}, \qquad \kappa_{xy} = -\frac{\partial^2 w}{\partial x \partial y} \tag{2.41}$$

As the Rayleigh-Ritz approximation is used here for the estimation of the natural frequencies, the equations for the kinetic energy and the strain energy for a doubly-curved shallow shell need to be defined. The kinetic energy is calculated by integrating over the length and the width of the shell, the sum of the squared velocities in the *x*, *y* and *z* directions multiplied by the mass per unit area, which gives [75]

$$E_k = \frac{1}{2}\rho h \int_0^{l_x}\int_0^{l_y} \left[\left(\frac{\partial u}{\partial t}\right)^2 + \left(\frac{\partial \upsilon}{\partial t}\right)^2 + \left(\frac{\partial w}{\partial t}\right)^2 \right] dydx. \tag{2.42}$$

The overall strain energy defined at the mid-surface of the shell in terms of the stretching and bending strain components, U_s and U_b, is given by [75] [82]

$$U_{strain} = U_s + U_b, \tag{2.43}$$

Where

$$U_s = \frac{E}{2(1-\nu^2)} \int_0^{l_x} \int_0^{l_y} \int_{-h/2}^{h/2} \left\{ \varepsilon_x^2 + \varepsilon_y^2 + 2\nu\varepsilon_x\varepsilon_y + \frac{1}{2}(1-\nu)\varepsilon_{xy}^2 \right\} dzdydx, \tag{2.44}$$

And

$$U_b = \frac{1}{2} \int_0^{l_x} \int_0^{l_y} D\left\{ \kappa_x^2 + \kappa_y^2 + 2\nu\kappa_x\kappa_y + 2(1-\nu)\kappa_{xy}^2 \right\} dydx, \tag{2.45}$$

where D is the bending stiffness as defined in Section 2.4. The total strain energy can be written by combining Equations (2.44) and (2.45)

$$\begin{aligned} U_{strain} = \frac{E}{2(1-\nu^2)} \Bigg[& \int_0^{l_x} \int_0^{l_y} \int_{-h/2}^{h/2} \left\{ \varepsilon_x^2 + \varepsilon_y^2 + 2\nu\varepsilon_x\varepsilon_y + \frac{1}{2}(1-\nu)\varepsilon_{xy}^2 \right\} dzdydx \\ & + \frac{h^2}{12} \int_0^{l_x} \int_0^{l_y} \left\{ \kappa_x^2 + \kappa_y^2 + 2\nu\kappa_x\kappa_y + 2(1-\nu)\kappa_{xy}^2 \right\} dydx \end{aligned} \tag{2.46}$$

Substituting Equations (2.26)-(2.28) for strain and Equation (2.41) for curvature change into Equation (2.46) leads to

$$\begin{aligned} U_{strain} = \frac{Eh}{2(1-\nu^2)} \int_0^{l_x} \int_0^{l_y} \Bigg[& \left(\frac{\partial u}{\partial x} + \frac{w}{R_x} \right)^2 + \left(\frac{\partial \upsilon}{\partial y} + \frac{w}{R_y} \right)^2 + 2\nu \left(\frac{\partial u}{\partial x} + \frac{w}{R_x} \right) \left(\frac{\partial \upsilon}{\partial y} + \frac{w}{R_y} \right) \\ & + \left(\frac{1-\nu}{2} \right) \left(\frac{\partial \upsilon}{\partial x} + \frac{\partial u}{\partial y} \right)^2 \\ & + \frac{h^2}{12} \left\{ \left(\frac{\partial^2 w}{\partial x^2} \right)^2 + \left(\frac{\partial^2 w}{\partial y^2} \right)^2 + 2\nu \left(\frac{\partial^2 w}{\partial x^2} \right) \left(\frac{\partial^2 w}{\partial y^2} \right) + 2(1-\nu) \left(\frac{\partial^2 w}{\partial x \partial y} \right)^2 \right\} \Bigg] dydx \end{aligned} \tag{2.47}$$

The analytical model for a doubly-curved shallow shell will be derived in the next two subsections in order to estimate the natural frequencies of the shell for two different boundary conditions: (1) shear diaphragm supports along 4 edges and (2) clamped along 4 edges.

Shear Diaphragm boundary conditions:

The mode shapes defined in Equations (2.32) used for the components of motion *u*, *υ* and *w* were substituted into the kinetic and strain energy equations:

$$E_k = \frac{1}{2}\rho h\left(\frac{l_x l_y}{4}\right)\left(\dot{U}^2 + \dot{V}^2 + \dot{W}^2\right) \tag{2.48}$$

$$\begin{aligned} U_{strain} = \frac{Ehl_x l_y}{8(1-\nu^2)}\Bigg\{ & (\lambda_x)^2 U^2 + \left(\frac{1}{R_x}\right)^2 W^2 - \frac{2}{R_x}(\lambda_x)UW + (\lambda_y)^2 V^2 + \left(\frac{1}{R_y}\right)^2 W^2 \\ & - \frac{2}{R_y}(\lambda_y)VW + 2\nu\left[(\lambda_x\lambda_y)UV - \frac{1}{R_y}(\lambda_x)UW - \frac{1}{R_x}(\lambda_y)VW + \frac{1}{R_x R_y}W^2\right] \\ & + \left(\frac{1-\nu}{2}\right)\left[(\lambda_x)^2 V^2 + (\lambda_y)^2 U^2 + 2(\lambda_x\lambda_y)UV\right] \\ & + \frac{h^2}{12}\left[(\lambda_x)^4 W^2 + (\lambda_y)^4 W^2 + 2\nu(\lambda_x\lambda_y)^2 W^2 + 2(1-\nu)(\lambda_x\lambda_y)^2 W^2\right]\Bigg\}. \end{aligned} \tag{2.49}$$

Assuming harmonic motion in all three directions ($\ddot{U} = -\omega^2 U$, $\ddot{V} = -\omega^2 V$ and $\ddot{W} = -\omega^2 W$), and applying the Lagrange equation, the general equations of motion for *u*, *υ* and *w* are found as follow:

$$\mathcal{L} = E_k - U_{strain} \tag{2.50}$$

$$\frac{d}{dt}\left(\frac{\partial L}{\partial \dot{U}}\right) - \frac{\partial L}{\partial U} = 0, \qquad \frac{d}{dt}\left(\frac{\partial L}{\partial \dot{V}}\right) - \frac{\partial L}{\partial V} = 0, \qquad \frac{d}{dt}\left(\frac{\partial L}{\partial \dot{W}}\right) - \frac{\partial L}{\partial W} = 0 \tag{2.51}$$

The substitution of Equations (2.48) and (2.49) into (2.51) leads to

$$\begin{aligned} & -\frac{\rho}{E}\omega^2 U \\ & + \frac{1}{2(1-\nu^2)}\left\{2U\left(\lambda_x^2 + \left(\frac{1-\nu}{2}\right)\lambda_y^2\right) - 2W\lambda_x\left(\frac{1}{R_x} + \frac{\nu}{R_y}\right) + V(\lambda_x\lambda_y)(1+\nu)\right\} = 0 \end{aligned} \tag{2.52a}$$

$$-\frac{\rho}{E}\omega^2 V$$
$$+\frac{1}{2(1-\nu^2)}\left\{2V\left(\left(\frac{1-\nu}{2}\right)\lambda_x^2+\lambda_y^2\right)-2W\lambda_y\left(\frac{\nu}{R_x}+\frac{1}{R_y}\right)+U\left(\lambda_x\lambda_y\right)(1+\nu)\right\}=0 \tag{2.52b}$$

$$-\frac{\rho}{E}\omega^2 W$$
$$+\frac{1}{2(1-\nu^2)}\left\{2W\left[\left(\frac{1}{R_x}\right)^2+\left(\frac{1}{R_y}\right)^2+2\nu\left(\frac{1}{R_xR_y}\right)+\frac{h^2}{12}\left(\lambda_x^2+\lambda_y^2\right)^2\right]\right.$$
$$\left.-2U\lambda_x\left(\frac{1}{R_x}+\frac{\nu}{R_y}\right)-2V\lambda_y\left(\frac{\nu}{R_x}+\frac{1}{R_y}\right)\right\}=0 \tag{2.52c}$$

Finally, the natural frequencies of a doubly-curved shallow shell can be expressed as an Eigenvalue problem which can be solved for different levels of curvature,

$$\begin{bmatrix}L_{11} & L_{12} & L_{13}\\ L_{21} & L_{22} & L_{23}\\ L_{31} & L_{32} & L_{33}\end{bmatrix}\begin{bmatrix}U\\V\\W\end{bmatrix}=-\begin{bmatrix}\ddot{U}\\\ddot{V}\\\ddot{W}\end{bmatrix}=\omega^2\begin{bmatrix}U\\V\\W\end{bmatrix}, \tag{2.53}$$

where the elements of the Eigenvalue matrix are

$$L_{11}=\frac{E\left(\lambda_x^2+\left(\frac{1-\nu}{2}\right)\lambda_y^2\right)}{\rho(1-\nu^2)} \tag{2.54a}$$

$$L_{12}=\frac{E\left(\lambda_x\lambda_y\right)(1+\nu)}{2\rho(1-\nu^2)} \tag{2.54b}$$

$$L_{13}=\frac{-\lambda_x E\left(\frac{1}{R_x}+\frac{\nu}{R_y}\right)}{\rho(1-\nu^2)} \tag{2.54c}$$

$$L_{21} = \frac{E\left(\lambda_x \lambda_y\right)(1+\nu)}{2\rho(1-\nu^2)} \tag{2.54d}$$

$$L_{22} = \frac{E\left(\left(\frac{1-\nu}{2}\right)\lambda_x^2 + \lambda_y^2\right)}{\rho(1-\nu^2)} \tag{2.54e}$$

$$L_{23} = \frac{\lambda_y E\left(\frac{\nu}{R_x} + \frac{1}{R_y}\right)}{\rho(1-\nu^2)} \tag{2.54f}$$

$$L_{31} = \frac{\lambda_x E\left(\frac{1}{R_x} + \frac{\nu}{R_y}\right)}{\rho(1-\nu^2)} \tag{2.54g}$$

$$L_{32} = \frac{\lambda_y E\left(\frac{\nu}{R_x} + \frac{1}{R_y}\right)}{\rho(1-\nu^2)} \tag{2.54h}$$

$$L_{33} = -\frac{E\left[\left(\frac{1}{R_x}\right)^2 + \left(\frac{1}{R_y}\right)^2 + 2\nu\left(\frac{1}{R_x R_y}\right) + \frac{h^2}{12}\left(\lambda_x^2 + \lambda_y^2\right)^2\right]}{\rho(1-\nu^2)} \tag{2.54i}$$

Clamped Edges Boundary Conditions (CCCC):

In order to derive an analytical model for a shallow shell clamped along all four edges, the equations for the kinetic energy and the strain energy were derived at the shell's mid-surface using the same steps as for the shell subjected to shear diaphragm boundary conditions. The characteristic beam functions for a clamped edge were used for the boundary conditions in the transverse direction and can be found in Appendix A. Based on the difference between the odd and even modal indices, four different equations were used for describing the transverse boundary conditions as follows:

1) *m* and *n* both odd:

$$w = w(t)\left(\cos\gamma_{m,i}\left(\frac{x}{l_x}-\frac{1}{2}\right)+\kappa_m\cosh\gamma_{m,i}\left(\frac{x}{l_x}-\frac{1}{2}\right)\right)$$

$$\left(\cos\gamma_{n,i}\left(\frac{y}{l_y}-\frac{1}{2}\right)+\kappa_n\cosh\gamma_{n,i}\left(\frac{y}{l_y}-\frac{1}{2}\right)\right), \tag{2.55a}$$

2) *m* odd *n* even:

$$w = w(t)\left(\cos\gamma_{m,i}\left(\frac{x}{l_x}-\frac{1}{2}\right)+\kappa_m\cosh\gamma_{m,i}\left(\frac{x}{l_x}-\frac{1}{2}\right)\right)$$

$$\left(\sin\gamma_{n,j}\left(\frac{y}{l_y}-\frac{1}{2}\right)+\kappa_n\sinh\gamma_{n,j}\left(\frac{y}{l_y}-\frac{1}{2}\right)\right), \tag{2.55b}$$

3) *m* even *n* odd:

$$w = w(t)\left(\sin\gamma_{m,j}\left(\frac{x}{l_x}-\frac{1}{2}\right)+\kappa_m\sinh\gamma_{m,j}\left(\frac{x}{l_x}-\frac{1}{2}\right)\right)$$

$$\left(\cos\gamma_{n,i}\left(\frac{y}{l_y}-\frac{1}{2}\right)+\kappa_n\cosh\gamma_{n,i}\left(\frac{y}{l_y}-\frac{1}{2}\right)\right), \tag{2.55c}$$

4) *m* and *n* both even:

$$w = w(t)\left(\sin\gamma_{m,j}\left(\frac{x}{l_x}-\frac{1}{2}\right)+\kappa_m\sinh\gamma_{m,j}\left(\frac{x}{l_x}-\frac{1}{2}\right)\right)$$

$$\left(\sin\gamma_{n,j}\left(\frac{y}{l_y}-\frac{1}{2}\right)+\kappa_n\sinh\gamma_{n,j}\left(\frac{y}{l_y}-\frac{1}{2}\right)\right). \tag{2.55d}$$

For the in-plane vibration, cross sliding-cross sliding boundary conditions taken from [97] were used in the model:

$$u = U(t)\cos(\lambda_x x)\sin(\lambda_y y) \tag{2.56a}$$

$$\upsilon = V(t)\sin(\lambda_x x)\cos(\lambda_y y), \tag{2.56b}$$

where $\lambda_x = \frac{m\pi}{l_x}$ and $\lambda_y = \frac{n\pi}{l_y}$.

The Rayleigh-Ritz method was used with the general expressions for kinetic and strain energy stated in Equations (2.48) and (2.49). Assuming harmonic motion in all three directions, the Lagrange equation was then applied using Equations (2.50) and (2.51) in order to obtain the equations of motion for *u*, υ and *w*. Finally, the general formula for the rectangular panel's natural frequencies can be expressed as the Eigenvalue problem stated in Equation (2.53).

The expressions for the matrix elements and their derivations can be found in Appendix B. This eigenvalue problem can be solved for different levels of curvature.

2.5.3 Effects of Curvature on the Modal Frequencies

This section discusses the effect of increasing curvature on the modes of a panel. For this purpose, an aluminium panel, with assumed properties listed in Table 2.1, was used in the estimation of the natural frequencies. These dimensions are based on an existing flat panel which has been used for simulations and experimental work on active vibration control in [2] [98] and will therefore allow later comparison with measured data.

Table 2.1 – Geometry and physical properties of the aluminium panel.

Parameter	Value	Units
Dimensions	$l_x = 278$	mm
	$l_y = 247$	mm
Thickness	$h = 1$	mm
Density	$\rho = 2700$	kgm^{-3}
Young's Modulus	$E = 7 \times 10^{10}$	Nm^{-2}
Poisson Ratio	$\nu = 0.33$	
Modal Damping Ratio	$\xi_n = 0.01$	

Figure 2.9 calculated natural frequencies of the panel modes, plotted as a function of rise-to-thickness ratio $\frac{z_c}{h}$, which is used here as a measure of curvature. The panel was assumed to be supported by shear diaphragms along its four edges. Figure 2.10 shows the same results when the panel is clamped along all four edges.

The overall trend of the top graph in Figure 2.9 indicates that with the increase in the curvature of the structure, the natural frequencies of the modes increase. However, this increase is not the same for all the modes. The natural frequencies of the lower order modes show a more pronounced increase, while the higher order modes are less affected by the curvature of the panel. For example, the natural frequency of the first mode increases from 71 Hz when the panel is flat to 940 Hz when the deflection at the centre of the panel is $z_c = 10\,mm$, whereas the natural frequency of the last mode shown in this figure only increases from 3.9 kHz to 4.1 kHz. This is caused by the more significant effect of stiffening due to the curvature on the lower order modes. This difference in the effect of curvature on different modes leads to the creation of a cluster of modes near the highest level of curvature shown in the graph. The comparison of the left-hand side of the graph where the panel is flat with the right-hand side where $z_c = 10\,mm$, shows that the spacing between the modes is significantly reduced at all frequencies (the frequency range they occupy is reduced by 700 Hz). The ratio of the highest to lowest

natural frequency for the 6 lower order modes in the lower graph of Figure 2.9 is reduced from about 4, with no curvature, to about 1.1 when $\frac{z_c}{h} = 10$. Similar results can be seen in the top graph of Figure 2.10 for the clamped panel model.

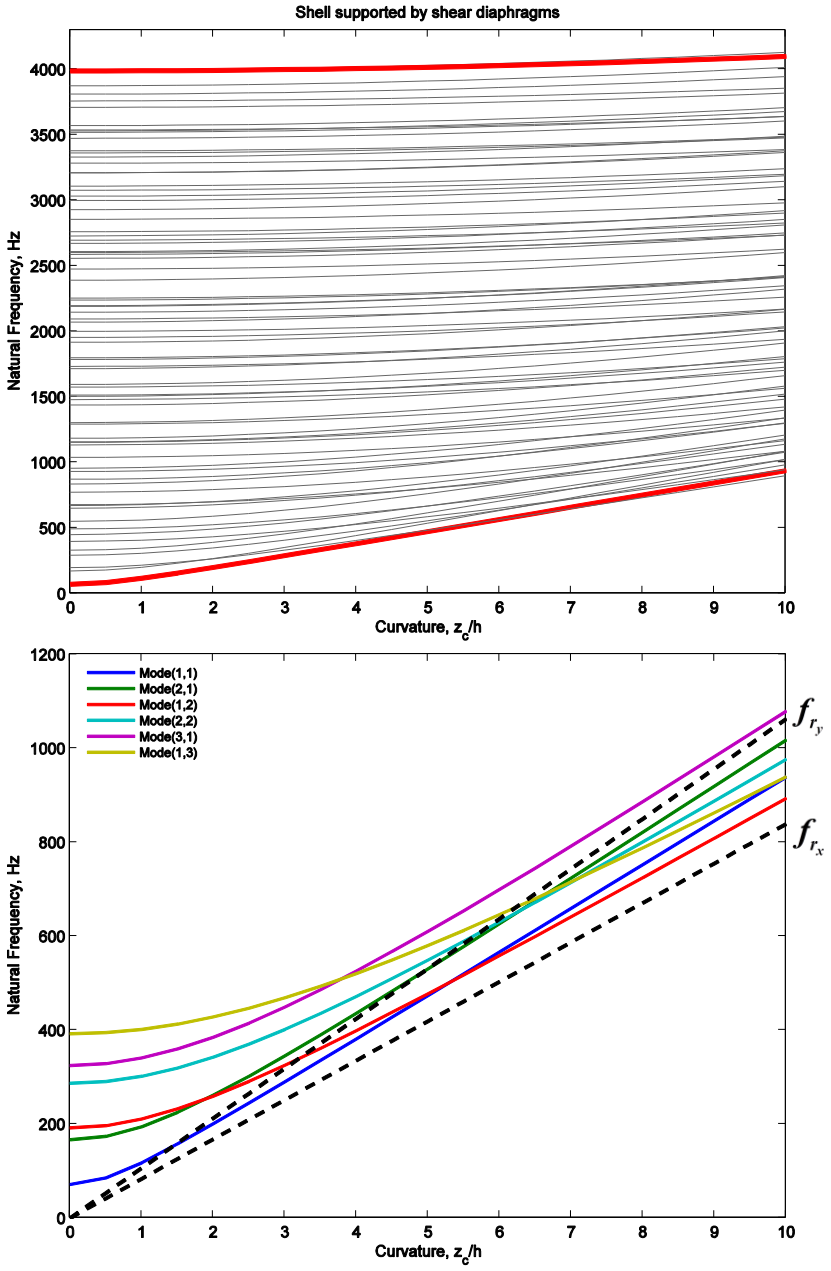

Figure 2.9 – Behaviour of the natural frequencies of the modes of a panel supported by shear diaphragms boundary conditions for increasing curvature, which is expressed here in terms of rise-to-thickness ratio: overall behaviour for 77 modes (top), behaviour of the first 6 modes. Also plotted in black dotted lines are the ring frequencies in the two planes, f_{rx} and f_{ry} from Equation (2.58).

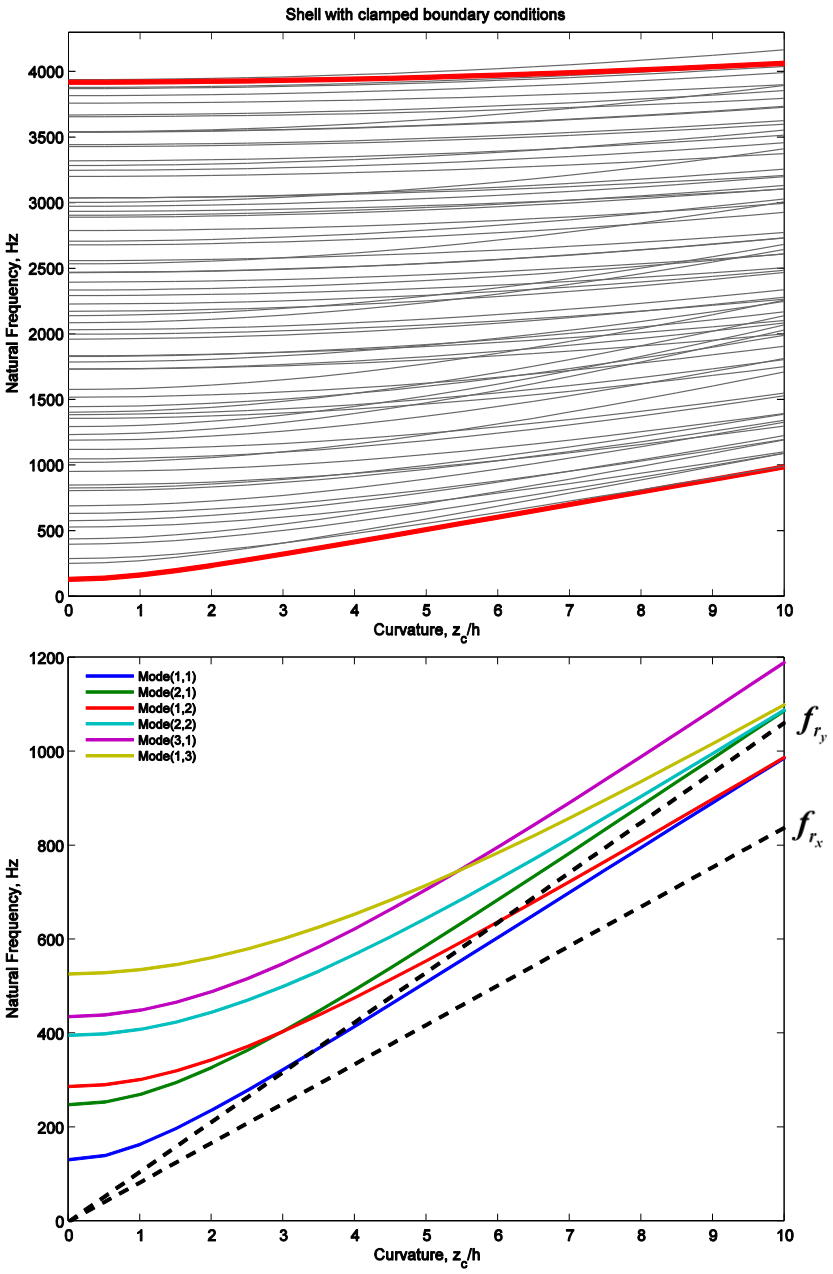

Figure 2.10 – Behaviour of the natural frequencies of the modes of a clamped panel for increasing curvature, which is expressed here in terms of rise-to-thickness ratio: overall behaviour for 77 modes (top), behaviour of the first 6 modes. Also plotted in black dotted lines are the ring frequencies in the two planes, f_{rx} and f_{ry} from Equation (2.58)

The effect of curvature increase and the increase in the modal density for shells have been investigated by [93] [99] [100] [101]. The equations for the natural frequencies and modal density of a simply-supported cylindrical shell have been provided by Heckl in [99]. The presence of curvature in the structure increases the speed of bending waves and the rate of increase varies depending on whether the structural modes are below or

above the ring frequency [93]. For a doubly-curved shell, the ring frequency can be defined in terms of the radii of curvature in the *x* and *y* directions as

$$f_{r,x} = \frac{1}{2\pi}\frac{c_L}{R_x} \quad , \quad f_{r,y} = \frac{1}{2\pi}\frac{c_L}{R_y}. \tag{2.57}$$

Since *R* is inversely proportional to the out-of-plane deflection z_c, the two ring frequencies are thus directly proportional to the curvature and can be written in terms of the rise-to-thickness ratio $\frac{z_c}{h}$ as

$$f_{r,x} = \left(\frac{4c_L h}{\pi l_x^2}\right)\frac{z_c}{h} \quad , \quad f_{r,y} = \left(\frac{4c_L h}{\pi l_y^2}\right)\frac{z_c}{h}. \tag{2.58}$$

The ring frequency occurs at the point where there is a transition in the modes from predominantly bending into longitudinal motion [93]. For low-order modes whose natural frequency is situated well below f_r, the rate of increase in bending wave speed is steep, while for higher order modes, this rate gradually diminishes. For frequencies well above the ring frequency, the vibration behaviour of a curved shell is like the one of an equivalent flat plate and curvature does not affect the modes of vibration [17].

For an aluminium panel with dimensions and properties listed in Table 2.1, when $\frac{z_c}{h} = 10$, the ring frequencies occur at about 800 Hz and 1 kHz. Therefore, in Figure 2.9 and Figure 2.10, this would explain the clustering of modes starting from $\frac{z_c}{h} \approx 2$ onwards, and the rapid increase in the natural frequencies of the modes initially below 1 kHz in comparison to those above this frequency.

A closer look at the lower order modes – the first six modes have been plotted in the lower graphs of Figure 2.9 and Figure 2.10 – also reveals several regions of intersection between the curves, for example at $z_c = 2\,mm$, $z_c = 5\,mm$ and $z_c = 7\,mm$, which is caused by the difference in the curvature of the panel in the *x* and *y* direction due to its rectangular shape $\left(R_x \neq R_y\right)$. These intersection regions also mean that the natural frequency of 2 or 3 modes could be the same as the panel deflects. For example, in

Figure 2.10, the second and fourth modes which are Modes (2,1) and (2,2) respectively, occur at 1096 Hz and 1098 Hz, when the panel is deflected by 10 mm.

2.6 Summary

In this chapter, analytical models of doubly-curved shells with rectangular base projections were formulated. The geometry and displacement were described at the mid-surface of the shell to show the coupled interactions between the transverse and in-plane components of motion. Warburton's theory was initially used as a basis for the derivation of the analytical models and estimation of the natural frequencies. Subsequently, the contribution of in-plane inertia which was omitted in Warburton's work, was included in the derivations. The natural frequencies were estimated for a doubly-curved shell supported by shear diaphragms on all sides and for a doubly-curved shell clamped along all four sides. The analysis of the mode shapes of the shell with increasing curvature showed an increase in the natural frequency of each mode. However, this increase was not uniform for all modes; the lower order modes showed a more pronounced increase, while the natural frequency of the higher order modes did not significantly change with curvature. As a result, at some of the curvature levels, regions of intersection between the modes could be observed, indicating that at those curvature levels, more than one mode could occur at a single frequency or very nearby. Furthermore, towards the highest level of curvature in the defined range, with the difference in the rate of increase for lower-order and higher order modes, modal clustering occurred. This is believed to be near the ring frequency of the shell.

The differences between the predictions from Warburton's analytical model and the analytical model with in-plane inertia will be further discussed in the next chapter.

3. Finite Element Modelling

The use of finite element modelling methods has become increasingly popular over the past decades due to the availability of different commercial software packages, such as Ansys, Comsol and Nastran. The finite element method allows engineers and researchers to simulate complex real-life engineering problems and systems. Finite element modelling (FEM) or finite element analysis (FEA) uses computational methods to approximate the solution to a mathematical problem with defined boundary conditions [102]. FEA is particularly attractive because it allows changes in the structure to be accurately modelled and solutions to partial differential equations to be more rapidly estimated than with analytical techniques. However, solutions obtained from FEA must be validated against experimental or analytical results before being used as a reference and should not be used as a black box, without independent support for the results.

This chapter presents the numerical (FEM) models created for an isotropic aluminium panel of increasing curvature and the finite element analysis (FEA) performed to obtain the natural frequencies and mode shapes of the system. The results are then compared with those obtained from the elemental versions of the two analytical models derived in Chapter 2, in order to assess the importance of the contribution of in-plane components of motion and validate the finite element models.

3.1 Panel Model and Elemental Resolution

For the purpose of the study, the finite element model of a rectangular aluminium panel with the properties listed in Table 3.1 was created. These dimensions are based on an existing flat panel which has been used for simulations and experimental work on active vibration control in [2] and [98], and will therefore allow for comparison with measured data. It was assumed that the panel was arranged in the *xy* plane and that the elevation in the panel due to curvature increase was along the *z*-axis. The elevation in the centre of the panel and the resulting curvatures in the *x* and *y* directions were limited such that the structure could fall under Vlasov's definition for a shallow shell, as noted in the

previous chapter. In other words, based on the length, width and thickness dimensions of the panel in Table 3.1, the elevation from the centre of the panel was varied from 0 to 10 mm. The consideration of higher rises would lead to violation of the assumptions made for shallow shells in Chapter 2.

It was assumed that the panel was subjected to harmonic excitation and the incident pressure field on the surface of the panel was modelled as excitation forces exerted at the centre of each element of the model. The panel was assumed to be excited in air, which is a medium which will only lightly load a 1-mm aluminium panel. Consequently, the effects of fluid loading on the structure were neglected [17].

The maximum frequency of interest was defined to 4 kHz, in order to take into account the contribution of higher frequency residual modes of vibration. The rise z_c from the centre of the panel, ranging from 0 to 10 mm, was included in the model generation steps for the investigation of the effect of curvature increase on the behaviour of the system.

Table 3.1 – Geometry and physical properties of the aluminium panel

Parameter	Value	Units
Dimensions	$l_x = 278$	mm
	$l_y = 247$	mm
Thickness	$h = 1$	mm
Density	$\rho = 2700$	kgm^{-3}
Young's Modulus	$E = 7 \times 10^{10}$	Nm^{-2}
Poisson Ratio	$\nu = 0.33$	
Modal Damping Ratio	$\xi_n = 0.01$	

The minimum number of elements required in an elemental model must provide a resolution of 4 elements per wavelength in order to avoid spatial aliasing. In a structural model, the bending wavelength is of importance, whereas in an acoustical model, the

elemental resolution must be set based on the acoustic wavelength. If both acoustical and structural responses are to be obtained from the same model, then the shortest of the acoustical and bending wavelengths must be used for calculating the elemental resolution. Although this chapter only focuses on the structural behaviour of the panel, in order to remain consistent with the results presented in the following chapter, which considers both acoustical and structural responses, the minimum of either acoustic or bending wavelengths will be used to define the elemental resolution of the model.

The estimation of the minimum number of elements in the finite element model and analytical elemental models starts with the calculation of the acoustic and bending wavelengths λ_0 and λ_F respectively, their corresponding wavenumbers, k_0 and k_F, and the bending phase speed c_F. The acoustic wavenumber and wavelength are given by [17]

$$k_0 = \frac{2\pi f}{c_0} \quad , \quad \lambda_0 = \frac{c_0}{f} \quad , \quad c_0 = 343 ms^{-1}, \tag{3.1}$$

where c_0 is the speed of sound in air. The bending wavenumber and wavelength are given by

$$k_F = \sqrt[4]{\frac{m\omega^2}{EI}} \quad , \quad \lambda_F = \frac{2\pi}{k_F} \quad , \quad c_F = \frac{\omega}{k_F} \tag{3.2}$$

The dispersion curves for the acoustic and bending waves for a thin aluminium panel, obtained from plotting the acoustic and bending wavenumbers calculated using the above formulae over frequency are shown in Figure 3.1 up to 20 kHz. The acoustic and bending phase speed can be obtained from the ratio of ω to k in each case $\left(c = \frac{\omega}{k} \right)$. The point of intersection between the two curves is the critical frequency or the lowest coincidence frequency $f_{critical}$, which was found to be 12 kHz for this case.

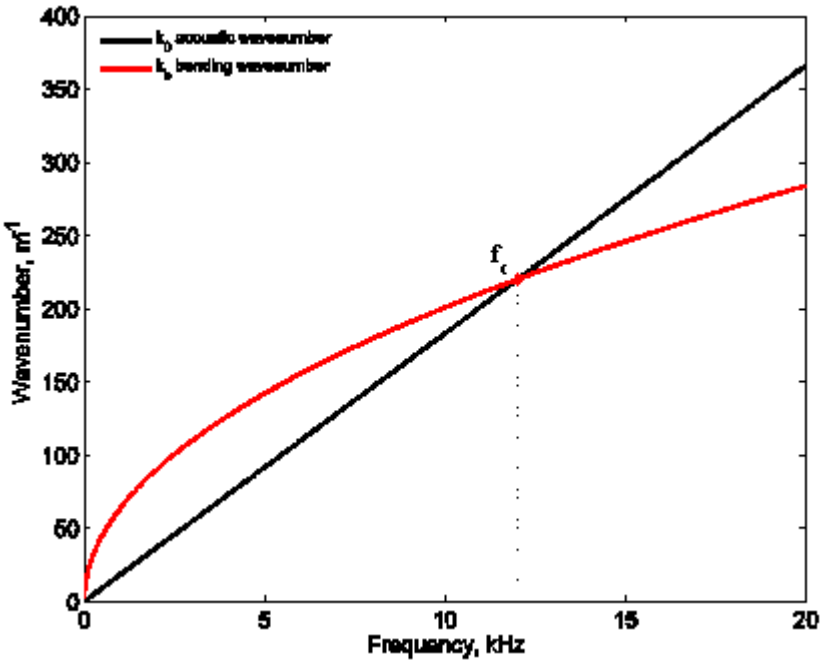

Figure 3.1 – Dispersive curves for acoustic and bending waves on a 1-mm aluminium panel. The critical frequency f_c which is the point of intersection between the two curves has been indicated in the graph.

Below the critical frequency, where the acoustic wavenumber is smaller than the bending wavenumber, the bending wave is slower than the acoustic wave (subsonic). For frequencies above the critical frequency, this relationship is reversed and the bending wave travels faster than the acoustic wave (supersonic). The acoustic curve increases at a uniform rate over frequency which is due to the fact that acoustic waves are longitudinal and non-dispersive, as explained in Chapter 2.

In order to determine the number of elements N_x and N_y per lengths l_x and l_y of the panel, the shortest wavelength out of λ_0 and λ_F , calculated at 4 kHz, was divided by the minimum elemental resolution per wavelength, 4, which is acceptable for the calculation frequency range of up to 4 kHz defined for the model. In the frequency range below the critical frequency, the bending wavelength is shorter, therefore, N_x and N_y are obtained from Equation (3.3a). For frequencies above the critical frequency, the acoustic wavelength is shorter, and N_x and N_y are calculated from Equation (3.3b).

$$N_x = \frac{l_x}{\lambda_F / resolution} \quad , \quad N_y = \frac{l_y}{\lambda_F / resolution} \qquad (f \le f_c) \tag{3.3a}$$

$$N_x = \frac{l_x}{\lambda_0 / resolution} \quad , \quad N_y = \frac{l_y}{\lambda_0 / resolution} \qquad (f > f_c) \tag{3.3b}$$

Based on the above formulae, the number of elements for each length was found to be $N_x = 16$ and $N_y = 15$, leading to $N_e = 240$ elements in total. The generated elemental grid for the aluminium panel can be seen in Figure 3.2. The centre of each element has been indicated.

Since the natural frequencies of a curved panel are known to be greater than that for the corresponding flat panel, the minimum number of elements calculated above for a curved panel should exceed that ever required for a curved panel.

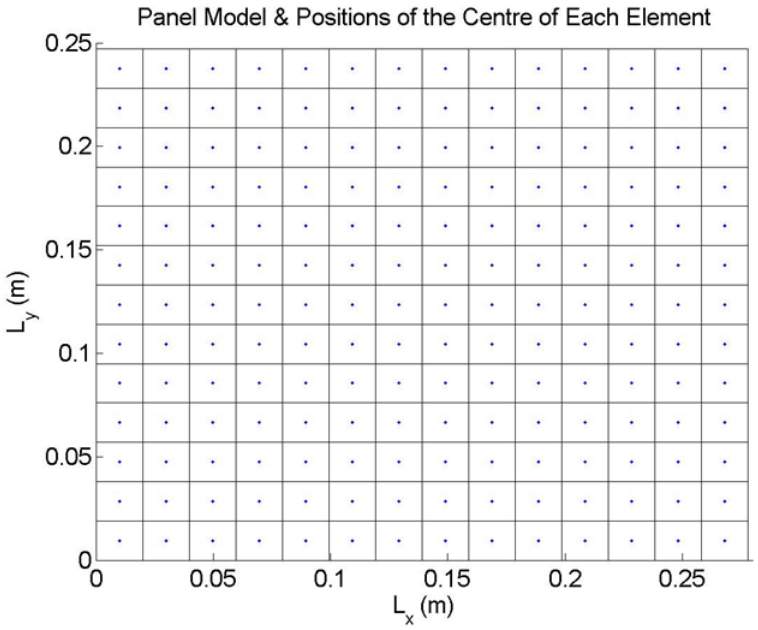

Figure 3.2 – Representation of the modelled panel divided into a grid of equal-sized elements.

3.2 Finite element Modelling

Finite element models (FEM) of the rectangular panel with properties and dimensions described in Section 3.1 were implemented in ANSYS with z_c ranging from 0 to 10 mm. All panel models were assumed to be subjected to shear diaphragm boundary conditions in order to follow the same boundary conditions as used in the analytical models of Chapter 2.

The surface of the panel was modelled using 3-dimensional shell elements. The SHELL63 elastic shell element with 6 DOFs at each node (translation and rotation along *x, y* and *z*) was used for creating the mesh over the surface of the panels. The reason for choosing this shell element was the fact that it takes into account both membrane and bending stresses and allows both transverse and in-plane components of motion to be studied. The equations of motion used in SHELL63 are based on the Kirchhoff-Love theory. It is important to note that the transverse component of shear stress is not taken into account in Love's theory. As the modelled panel can be considered a thin shell, this simplification does not significantly affect the accuracy of the approximation. However, this could be a potential problem when dealing with thick shells or laminated shells because it can result in the underestimation of the deflection of the surface [103] [104]. For the latter case, a shell element such as SHELL281 could be chosen, in which the derivations are based on the 1-order shear-deformation theory, referred to as Reissner-Mindlin. The triangular element shape of SHELL63 was chosen over the rectangular one for meshing the surface, in an attempt to follow more accurately the gradient of the curved surface.

In order to obtain an accurate geometry for a rectangular structure curved in two dimensions, the panel was modelled as a rectangular section on the surface of a torus where the radius of the tube cross-section is $r = R_y$ and the distance from the centre of the tube cross-section to the centre of the torus is $R = R_x - R_y$. A diagram of a torus with the dimensions required for the shell models is shown in Figure 3.3.

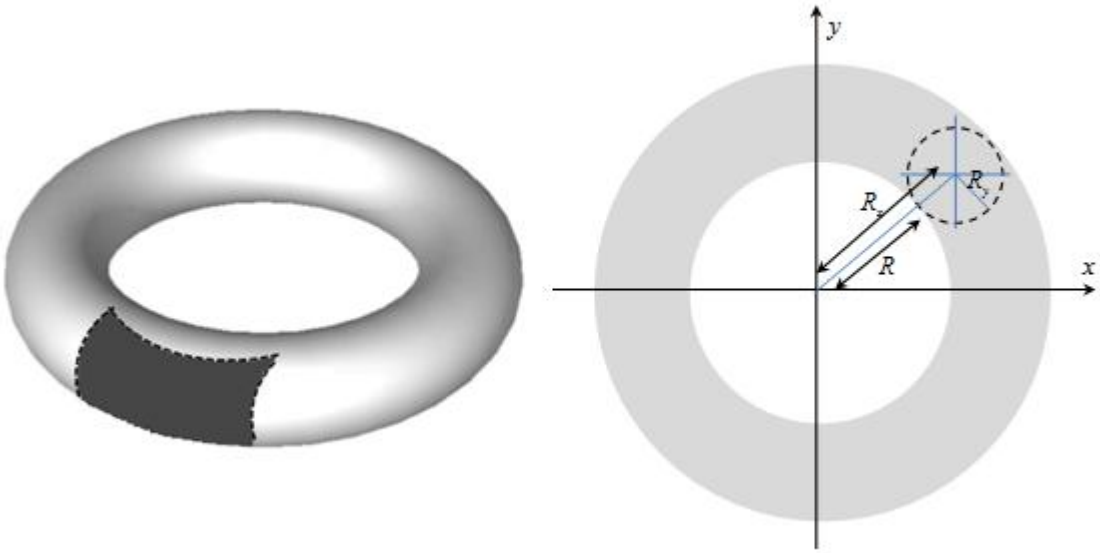

Figure 3.3 – Diagram of a torus with the high-lighted section on which the FEM of the doubly-curved panel is based (left), Representation of the dimensions of the torus used in the FEM.

The mesh geometry was created in ANSYS in using a cylindrical coordinate system. Figure 3.4 shows the finite element model of the rectangular panel, supported by shear diaphragms, when the rise from the centre z_c is 4 mm. The relation between the radii of curvature R_x and R_y , and z_c has been given in Equation (2.37) of Chapter 2.

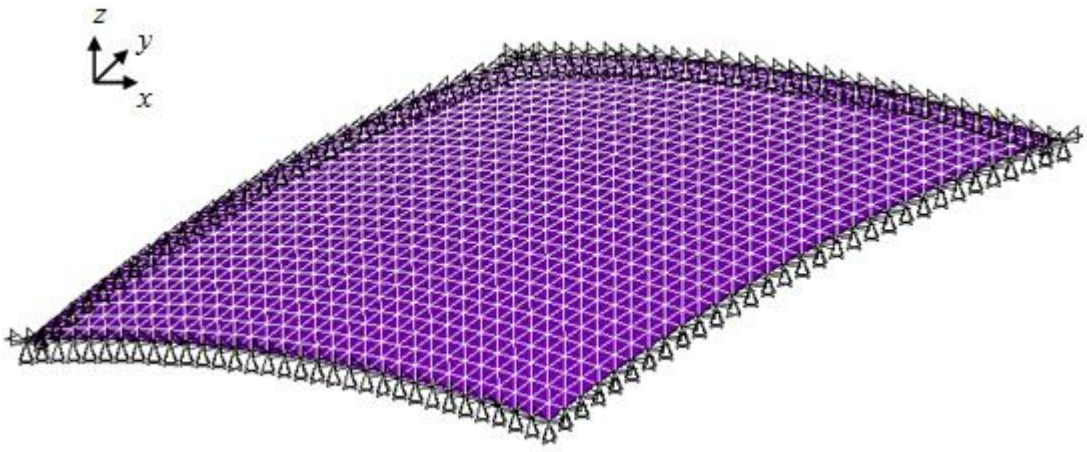

Figure 3.4 – Finite element model of the doubly-curved rectangular panel when z_c = 4 mm.

In the analytical models derived in Chapter 2, the out-of-plane displacement was calculated at the centre of each element. In order to retrieve out-of-plane nodal displacements that would correspond to the same positions from ANSYS, the elemental

resolution had to be quadrupled such that nodes would be created for those exact points ($N_e = 960$). As the mode shapes derived in the analytical models are assumed to remain unaffected by the changes in curvature, the mode shapes obtained from the FEM of curved panels will be studied to assess the importance of this simplification in the analytical models.

3.3 Modal Analysis

This section will present the data analysis performed in order to compare and validate the results from numerical and analytical models of the doubly-curved panel. The first part of this section will explain the process of organising and sorting the data obtained from the FEMs through statistical methods. The second part will discuss the obtained results and compare the two approaches.

3.3.1 Modal Assurance Criterion (MAC Analysis)

One method of comparing the two models would be to directly compare the natural frequencies of the two models for different levels of curvature. Even though this method allows the detection of possible errors in the models and a first assessment of the degree of correlation between each mode, the model verification should not be solely based on this comparison, because it does not confirm the ordering of each plotted mode in ANSYS with respect to its equivalent mode in the analytical models. Furthermore, the above approach would only allow the detection of discrepancies at the modelling and material properties levels of the simulation and would not verify the presence of errors such as the occurrence of degenerate modes.

The one-by-one comparison of mode orders can be performed by a method of analysis referred to as the ‘Modal Assurance Criterion’ (MAC). The MAC number is a scalar value that provides the degree of correlation between two mode shapes as [105]

$$MAC(A_i, X_j) = \frac{\left| \int_0^{l_x} \int_0^{l_y} \phi_{X,j}(x,y) \phi_{A,j}^*(x,y) dy dx \right|^2}{\left(\int_0^{l_x} \int_0^{l_y} \phi_{X,j}(x,y) \phi_{X,j}^*(x,y) dy dx \right) \left(\int_0^{l_x} \int_0^{l_y} \phi_{A,j}(x,y) \phi_{A,j}^*(x,y) dy dx \right)}, \tag{3.4}$$

where indices *A* and *X* refer to numerical values from ANSYS and analytical values respectively, and $\phi_{A,j}(x,y)$ and $\phi_{X,j}(x,y)$ are the numerical and analytical mode shapes respectively.

In practice the modal assurance criterion is calculated using a finite summation over the elemental points from the finite element analysis rather than an integral over all positions, such that

$$MAC\left(A_i, X_j\right) = \frac{\left| \boldsymbol{\phi}_{\mathbf{X_j}}^{\mathbf{H}} \boldsymbol{\phi}_{\mathbf{A_i}} \right|^2}{\left(\boldsymbol{\phi}_{\mathbf{X_j}}^{\mathbf{H}} \boldsymbol{\phi}_{\mathbf{X_j}} \right) \left(\boldsymbol{\phi}_{\mathbf{A_i}}^{\mathbf{H}} \boldsymbol{\phi}_{\mathbf{A_i}} \right)}, \tag{3.5}$$

where $\boldsymbol{\phi}_{\mathbf{A_i}}$ and $\boldsymbol{\phi}_{\mathbf{X_j}}$ are the vectors of the numerical and analytical mode shapes respectively. As both analytical models described in the previous chapter followed the hypothesis that the mode shape was not affected by curvature, the MAC percentages were only calculated between the ANSYS FEM and Warburton's modes. The results for four modelled panels of increasing curvature are shown in Figure 3.5.

For the analytical model based on Warburton's theory, the calculated mode shapes, which are those of a simply-supported flat panel, have been arranged in terms of ascending mode order, while in ANSYS, the mode shapes are sorted in terms of increasing natural frequencies. This organisation difference can be seen in the MAC percentage graphs in the form of location mismatch between some pairs of modes. For a flat or lightly-curved panel, all of the modes except 2 or 3 pairs are strongly correlated (90% and above) and lie on the regression line.

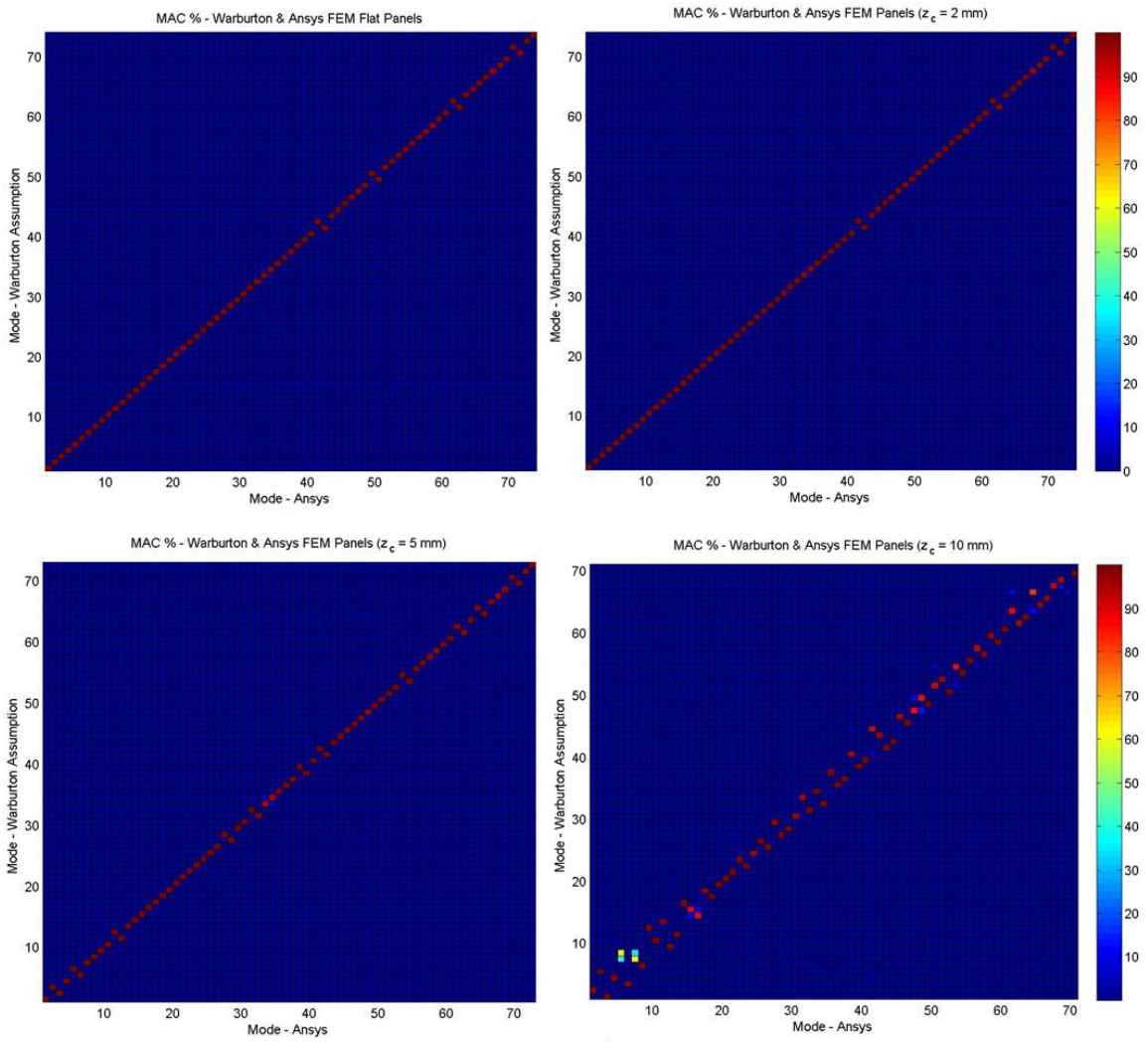

Figure 3.5 – MAC analysis between the analytical model based on Warburton's approach (vertical axis) and numerical FEM model (horizontal axis) for no curvature z_c = 0 mm (top left), light curvature z_c = 2 mm (top right), medium curvature z_c = 5 mm (bottom left) and strong curvature z_c = 10 mm (bottom right).

The calculation of the MAC percentage for mid to higher levels of curvature, corresponding to $5mm \le z_c \le 10mm$, reveals more recurring differences in mode location, especially for low order modes. For example, for a rise of $z_c = 5mm$, the modal correlation still remains above 90%, but for the highest curvature level corresponding to $z_c = 10mm$, the modes are more scattered despite still being strongly correlated. Additionally, the 5th and 7th modes display correlations of both 60% and 40% between the two models. The 5th ANSYS FEM mode is weakly correlated with the 5th Warburton analytical mode (40% correlation), but is better correlated with the 7th Warburton analytical mode (60% correlation). The 7th ANSYS FEM mode is better

correlated with the 5th analytical mode, rather than with the 7th analytical mode. The poorly correlated modes are caused by the occurrence of coupled modes in the FEM. These modes occur at a region of crossing between two closely-spaced modes, as shown in Figure 2.9 and Figure 2.10, and become more frequent with increasing curvature because of the occurrence of modal clusters, as explained in the previous chapter.

3.3.2 Mode Shapes and Natural Frequency Comparisons over Increasing Curvature

In the analytical approaches based on Warburton's theory and derived in Chapter 2 with and without the contribution of in-plane motion, the mode shapes were assumed to remain unchanged because the levels of surface curvature for a shallow shell are relatively low in comparison to the length and the width of the structure. In ANSYS, the nodal displacements in longitudinal and transverse directions are calculated for all of the elements. In order to verify whether the assumption made in the analytical model derivation was correct, the analytical mode shapes were compared to the numerical mode shapes obtained for different levels of curvature. The contour plots for the first 9 analytical modes are shown in Figure 3.6.

The same mode shapes obtained from the finite element models have been plotted for light curvature (Figure 3.7), medium curvature (Figure 3.8) and strong curvature (Figure 3.9). The numerical mode shapes from the FEM of the flat panel have not been shown as they are identical to the analytical mode shapes displayed in Figure 3.6.

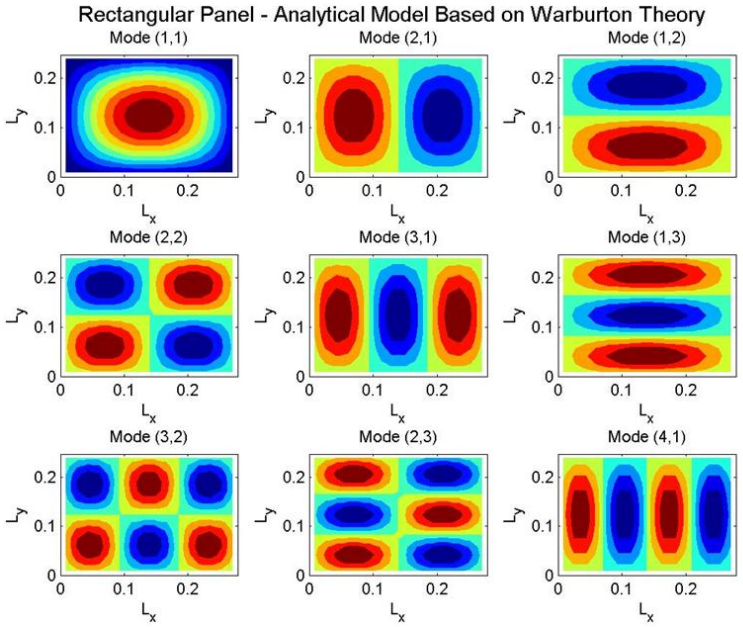

Figure 3.6 – First 9 analytical mode shapes assumed in Warburton's theory, in which their shapes is assumed to remained unchanged over increasing curvature.

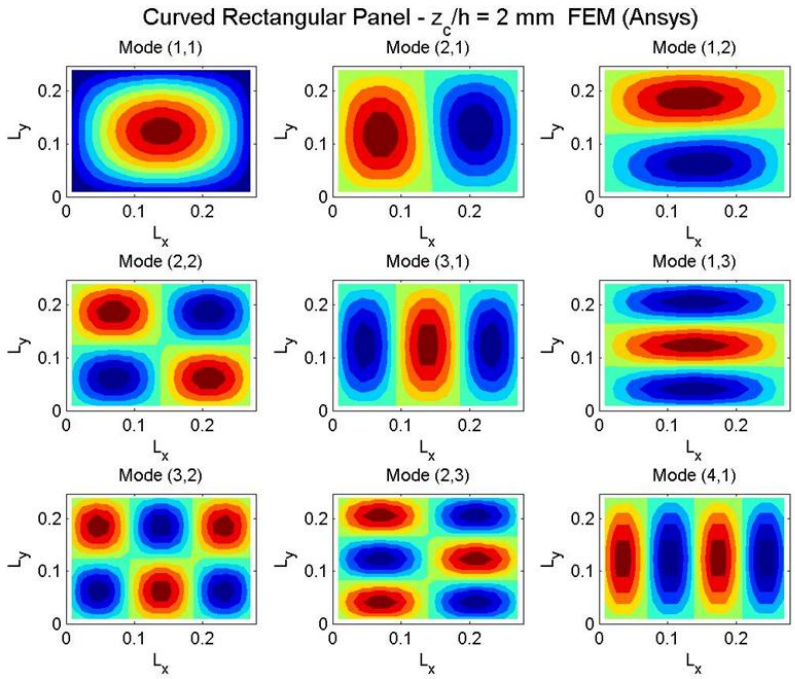

Figure 3.7 – Numerical mode shapes obtained from the FEM of a lightly-curved rectangular panel (corresponding to a rise from the centre z_c = 2 mm).

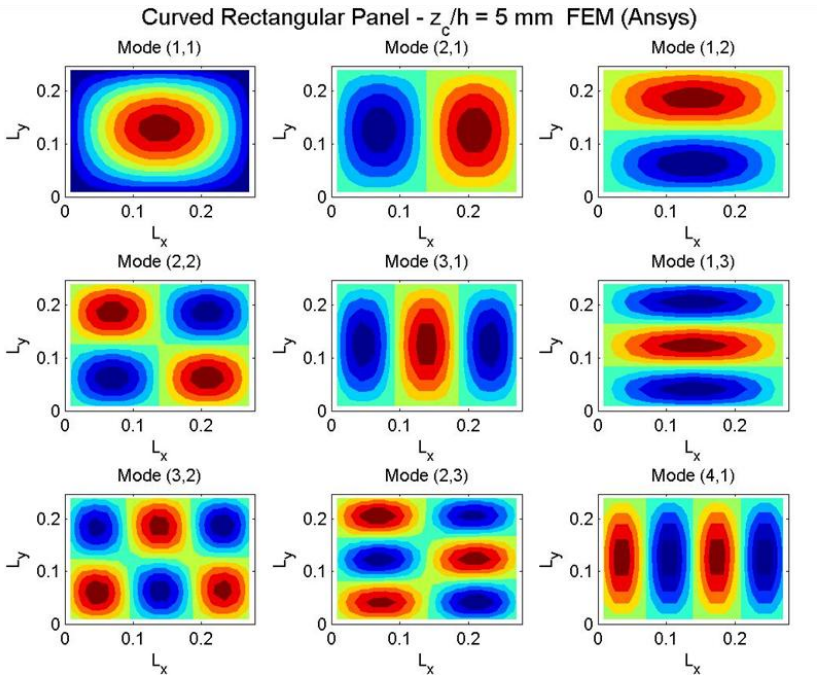

Figure 3.8 – Numerical mode shapes obtained from the FEM of a doubly-curved panel with a medium level of curvature (corresponding to z_c = 5 mm).

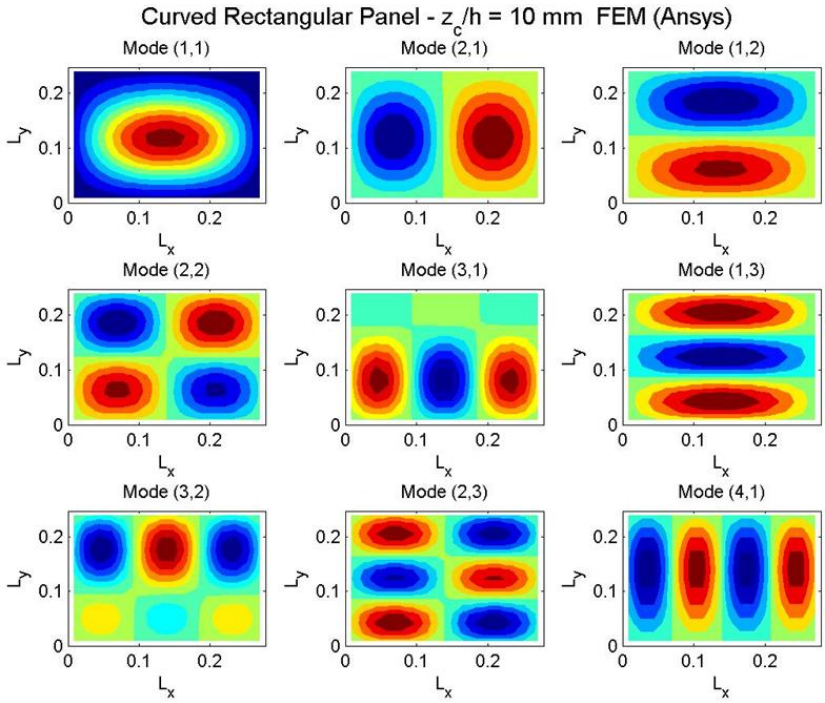

Figure 3.9 – Numerical mode shapes obtained from the FEM of a strongly-curved panel (corresponding to z_c = 10 mm).

In the above figures, the effect of curvature increase on the mode shapes is not noticeable up to medium levels of curvature. However, the mode shapes of the strongly-curved panel shown in Figure 3.9 show that Modes (3,1) and (3.2) include the

contribution of other modes that are very closely-spaced due to the mode clustering at high levels of curvature, as seen in Figure 2.11 of Chapter 2. Furthermore, an overall comparison between the mode shapes of Figure 3.6 and Figure 3.9 also reveals that the displacement amplitudes in the modes of the strongly-curved panel are noticeably smaller than in those of the flat panel. This is due to the stiffening effect also caused by curvature increase and modal clustering.

The natural frequencies of the two analytical models and the FEM model were also plotted over increasing curvature, in order to observe the differences between the three models and especially assess the contribution of in-plane bending. Figure 3.10 displays the first 10 modes plotted over increasing rise-to-thickness ratio $\frac{z_c}{h} = 0,1,...,10$ for the numerical model and the analytical model based on Warburton's theory. Both graphs show a similar overall trend: with the gradual deflection of the panel, the natural frequency of each mode is significantly increased over $\frac{z_c}{h}$ and a cluster of modes can be seen near the highest curvature.

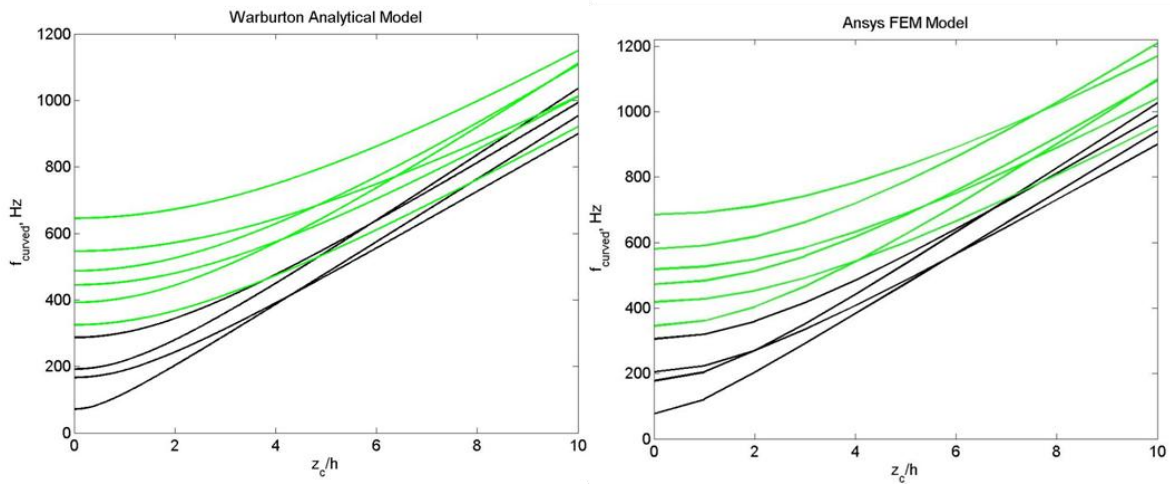

Figure 3.10 – Behaviour of the first ten modes over increasing curvature: Analytical results based on Warburton's approach (left) and numerical results from FEM (right). The first 4 modes are plotted in black and the rest in green in order to improve clarity.

For lower order modes, the increase in natural frequency is more pronounced, while for higher order modes, the difference between the natural frequencies without curvature and with strong curvature is not as significant. For example, the last mode calculated in both analytical and finite element models (not displayed in the figure) has a natural

frequency of 3.7 kHz when the panel is flat, and a natural frequency of 3.9 kHz when the panel is strongly curved $\left(\frac{z_c}{h}=10\right)$.

The mode shapes of both the analytical and the numerical models plotted in Figure 3.10 also reveal that the curves for the natural frequencies of the higher order modes, such as modes (1,2) and (2,2), intersect with the lower order modes (1,1) and (2,1). This can be explained by the different bow in the structure in the *x* and *y* directions, such that $R_x \neq R_y$, as mentioned in the previous chapter. If the modelled panel were square, the natural frequencies of all the modes would have gradually increased in a consecutive order. However, the deflections at which these intersections occur are different between the numerical model and the analytical model based on Warburton's theory in which the contribution of in-plane motion has been neglected. For example, in this analytical model, modes (1,1) and (2,1) cross each other near $z_c/h=5$, when in the FEM results, the same intersection occurs at $z_c/h=6$. There is also an additional intersection between modes (2,1) and (1,2) in the FEM results at $z_c/h=2$, which does not occur in the same modes of the analytical Warburton model. In order to examine the differences between the two models more closely, the natural frequencies of the individual modes for both models were plotted together in the same graph. The (1,1) and (2,2) modes, i.e. modes for which $m = n$, are presented in Figure 3.11, and the (1,2), (2,1), (1,3) and (3,1) modes, i.e. modes for which $m \neq n$, are shown in Figure 3.12.

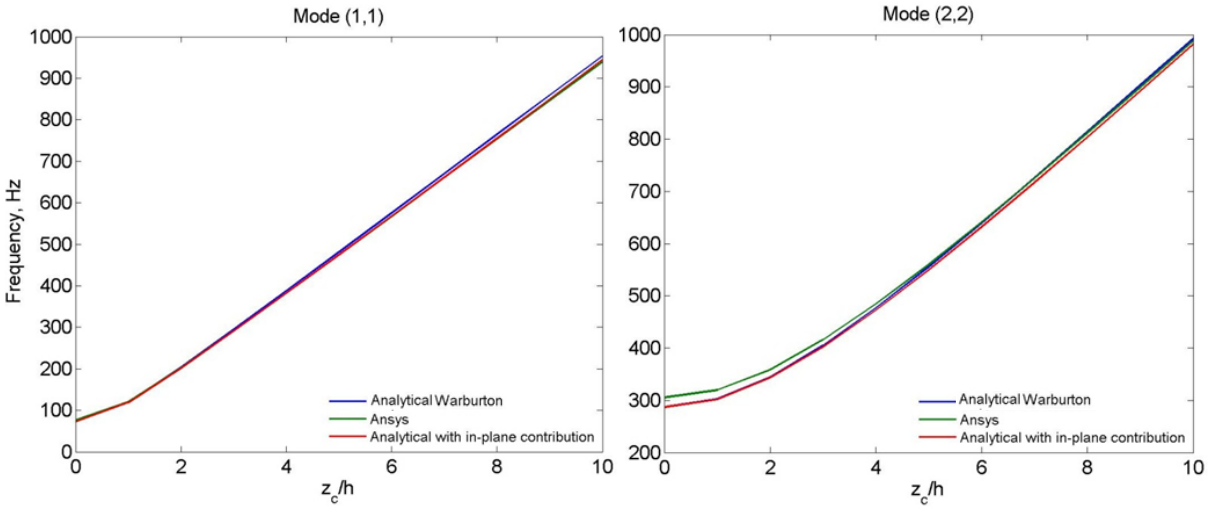

Figure 3.11 – Modes (1,1) and (2,2) plotted over increasing curvature for the numerical ANSYS model (green curve), analytical model based on Warburton's theory (blue curve) and analytical model with in-plane inertia contribution (red curve).

The curves plotted in Figure 3.11 show that the changes in the natural frequencies for these two modes are almost identical over increasing $\frac{z_c}{h}$ for all three models. For higher order modes where $m = n$, the numerical ANSYS model gives higher natural frequencies in the low $\frac{z_c}{h}$ region because of the way the boundary conditions are defined, which causes an increase in the stiffness of the structure.

The same agreements between the three models cannot be seen in the graphs of Figure 3.12. The natural frequencies of the FEM and the analytical model with in-plane inertia contribution are in very close agreement with each other. The natural frequencies of the analytical model based on Warburton's theory only follow the two other curves for very low levels of curvature ($\frac{z_c}{h} = 1$). Also, based on the analytical results, it was initially expected that modes such as the (1,2) and the (2,1) modes, where $m \neq n$, would be evolving in a similar manner over increasing curvature, with mode (1,2) starting at a slightly higher natural frequency in the absence of curvature and then gradually converging toward mode (2,1) for the maximum level of $\frac{z_c}{h}$. However, according to Figure 3.12, from the results of the FEM it can be seen that mode (1,2) ends up at a much lower natural frequency for $\frac{z_c}{h} = 10$, which explains why the two modes intersect

each other in the overall mode shape behaviour graph (presented in Figure 3.10). This difference is again caused by the rectangular shape of the surface, making the wavelength larger on the edges that are oriented in the *x*-axis direction.

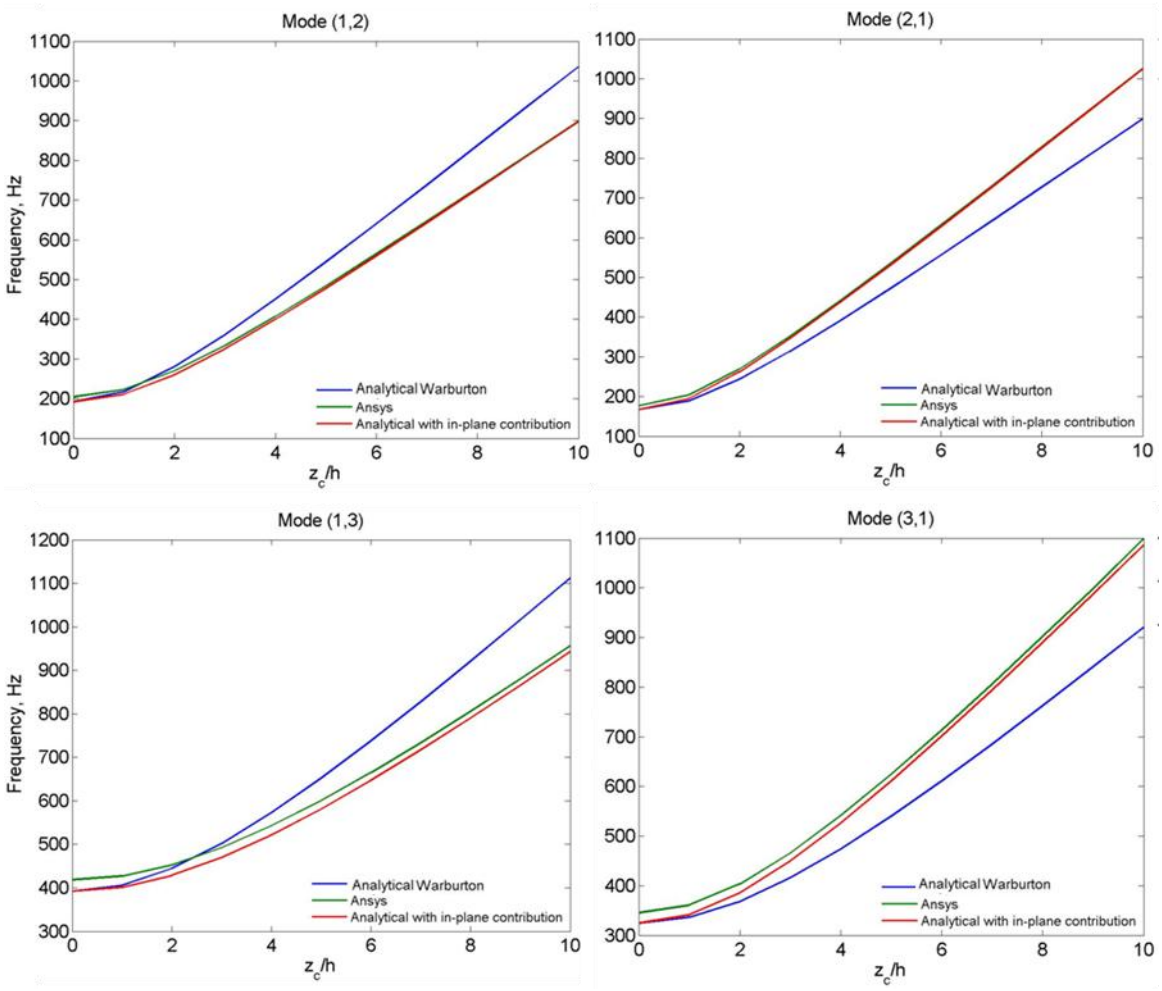

Figure 3.12 – Modes (1,2), (2,1), (1,3) and (3,1) plotted over increasing curvature for the numerical ANSYS model (green curve), analytical model based on Warburton's theory (blue curve) and analytical model with in-plane inertia contribution (red curve).

The comparison of Warburton's analytical model results with those of the FEM reveals that the results of the modes where $m = n$ are similar, while those for modes where $m \neq n$ behave differently between the two models. The difference arises from the fact that the contribution of in-plane inertia is neglected in the analytical model based on Warburton's theory. When the displacement of the surface is pre-dominantly due to the transverse component of motion, i.e. for modes where $m = n$, such as the (1,1) and the (2,2) modes, the absence of the in-plane contributions does not affect the mode shape. Therefore, the results obtained from the FEM and Warburton's analytical model are

similar. However, in modes where $m \neq n$, such as (1,2), (2,1), (1,3) and (3,1) modes, the in-plane component of displacement has more influence on the behaviour of the structure, consequently, neglecting their contribution in the analytical model derivation leads to different results.

3.4 Summary

In this chapter, analytical and numerical finite element models of a homogeneous aluminium rectangular panel were created. The panel was assumed to be supported by shear diaphragms along all four edges. The mesh and FEM of the panel were generated in ANSYS for different levels of curvature corresponding to those defined for the analytical models, and modal analysis was performed over increasing curvature. The results from the FEMs were re-arranged and validated against the analytical models using the Modal Assurance Criterion (MAC). The results of the MAC analysis showed some differences between the numerical and analytical models in the appearance of the modes, because the analytical mode shapes were calculated and arranged in terms of increasing mode order, while the ANSYS numerical mode shapes were sorted in terms of increasing natural frequencies. Further comparisons of the results obtained from the MAC analysis indicated that while for flat and lightly-curved panels, the majority of the numerical and analytical modes were strongly correlated, for medium to high levels of curvature, the percentage correlation decreased for some of the higher-order modes and the modes were generally more scattered. This was caused by the modal clustering and coupling between modes in the numerical model.

In the analytical models, the maximum level of curvature in the surface of the shell was assumed to be low enough in comparison to the other dimensions for the mode shapes to remain unchanged. In order to verify this assumption, the analytical and numerical mode shapes were compared. The effect of curvature increase on the mode shapes was noticeable for medium to high levels of curvature. The modal displacement amplitudes for strong curvature were noticeably smaller in the FEM mode shapes, as a result of the stiffening effect due to curvature increase and modal clustering. This could not be seen in the analytical mode shapes as they were assumed to remain unchanged for all levels of curvature. Therefore, in order to increase the accuracy of the analytical model,

especially at higher levels of curvature, it will be necessary to model the mode shapes such that these changes are accounted for.

Finally, the natural frequencies of the numerical and analytical modes were compared with increasing curvature, in order to assess the importance of the contribution of in-plane inertia. This was achieved by comparing the natural frequencies estimated from: (1) the analytical model based on Warburton's theory in which in-plane inertia is not taken into account, (2) the analytical model with in-plane inertia contribution, (3) the ANSYS FEM. All three showed a similar trend in terms of increasing natural frequency with respect to increasing curvature and occurrence of modal clustering for strong curvature. However, while the natural frequencies of modes where $m = n$ were practically identical across all three models, the other modes of the model, i.e. where $m \neq n$, derived from Warburton's theory in which in-plane inertia was not accounted for, only agreed with the other two models for light curvature and the natural frequencies of the mode was significantly different from the other two models for strong curvature.

In conclusion, even though Warburton's approach does help to gain a better understanding of the influence of two-dimensional curvature on the free vibrations of shallow shells and provided a good baseline for analytical models, the absence of the contribution of in-plane inertia in the model does not provide an accurate representation of the vibrational behaviour for more general cases.

4. Simulations of Active Vibration Control on Curved Panels

In this chapter, the effects of velocity feedback control will be investigated on the structural response and radiated sound power for the rectangular panel modelled in the previous chapter. It is assumed that the panel is simply-supported along its four edges and baffled. The excitation on the surface of the structure is assumed to be time harmonic with an angular frequency of ω rad/s. The acoustic plane wave exciting the panel has an azimuthal angle ϕ in the xy-plane taken from the x-axis and an angle of incidence θ from the normal to the surface in the z-direction. Both angles are set to 45° in these simulations, in order to approximate an excitation due to a diffuse sound field, which allows an even distribution of the excitation on the surface of the panel and for all the structural modes to be efficiently excited [17]. Figure 4.1 shows the arrangement of the panel, along with the incident harmonic acoustic wave and the resulting radiated sound.

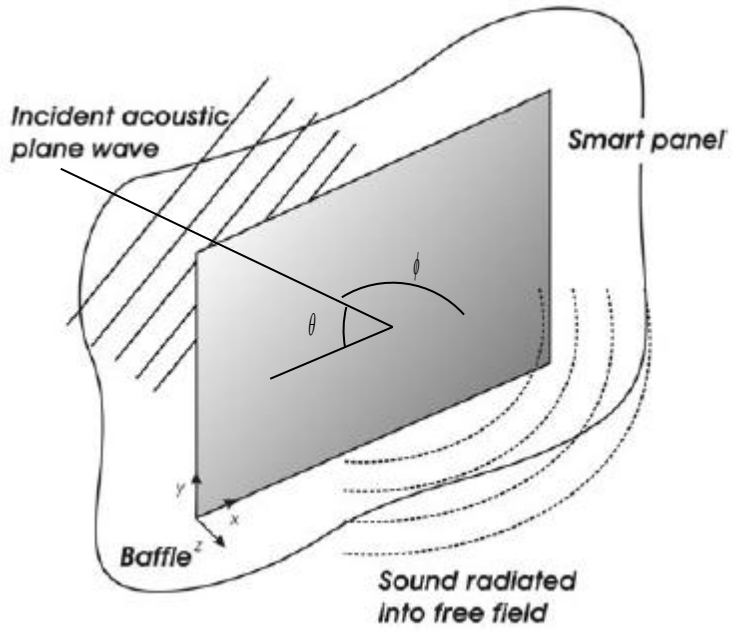

Figure 4.1 – Diagram of the modelled panel when it is excited by an acoustic plane wave incident at θ = 45° and φ= 45° [106].

The sound pressure field due to the harmonic excitation, defined as a function of position and time, is obtained from the real part of the counter clockwise rotating complex vector as [98] [106]

$$p_i(x,y,t) = \mathrm{Re}\left\{ p_i(\omega) e^{j(\omega t - k_x x - k_y y)} \right\}, \tag{4.1}$$

where $p_i(\omega)$ is the complex pressure phasors, $j = \sqrt{-1}$, and k_x and k_y are the wavenumbers in the *x* and *y* direction respectively defined in terms of the acoustic wavenumber k_0 and the angle of incidence and the azimuthal angle as

$$k_x(\omega) = k_0(\omega)\sin(\theta)\cos(\phi) \tag{4.2}$$

$$k_y(\omega) = k_0(\omega)\sin(\theta)\sin(\phi), \tag{4.3}$$

where $k_0 = \frac{\omega}{c_0}$ and the speed of sound in air $c_0 = 343 ms^{-1}$. Similarly, the time-harmonic force and velocity functions at a single point on the panel are also defined as the real part of their complex force and velocity phasors

$$f(t) = \mathrm{Re}\left\{ F(\omega) e^{j\omega t} \right\} \tag{4.4}$$

$$\dot{w}(t) = \mathrm{Re}\left\{ \dot{W}(\omega) e^{j\omega t} \right\}, \tag{4.5}$$

where $f(t)$ and $\dot{w}(t)$ refer to the time-harmonic force and velocity respectively, $F(\omega)$ and $\dot{W}(\omega)$ are the complex frequency-dependent force and velocity phasors. Throughout this chapter, the force and velocity will be expressed in the frequency domain and the complex exponential term $e^{j\omega t}$ will be omitted for simplification.

In the first section, it will be assumed that the feedback controller consists of an ideal point force collocated with a velocity error sensor. The effect of position and number of control forces on the performance of the system will be discussed. In the second section, the effect of using inertial actuators instead of point forces on the stability and performance of the control system will be investigated. The velocity feedback system with the ideal force actuator is unconditionally stable, but that with the inertial actuator

is only conditionally stable, i.e. only stable up to a maximum feedback gain. The third section of the chapter will assess the effect of increasing the curvature of the structure on the performance and stability of the control system. In this section, the simulations will be performed using the mode shapes and natural frequencies calculated in the analytical model of Section 2.5.2 of Chapter 2, where the contribution of in-plane inertia has been accounted for.

Throughout this chapter single-channel and decentralised multi-channel direct velocity feedback control systems will be simulated. The basis of the work described in Sections 4.1 and 4.2 has been based on [2] [17] [27] [98] [107]. The last section, Section 4.3, presents the work done towards the 2nd contribution of the thesis.

4.1 Formulation of Ideal Feedback Control of a Panel

The excitation on the surface of the panel consists of the sum of two contributions: the sound pressure incident on the structure and the control forces generated by the feedback controller at the points of control. The rectangular panel modelled in Chapter 3 has been divided into a grid of N_e elements and the harmonic excitation on the surface of the panel is assumed to be evenly distributed in terms of point forces and their corresponding velocities at the centre of each element. At this stage, it is assumed that an ideal velocity feedback control system consisting of ideal actuators generating secondary point forces and collocated error sensors measuring the velocity of the structure are positioned on the panel. The elemental representation of the modelled panel with the location of excitation forces, control force and the resulting panel and control velocities along with a lumped-parameter representation of one of the controllers is shown in Figure 4.2.

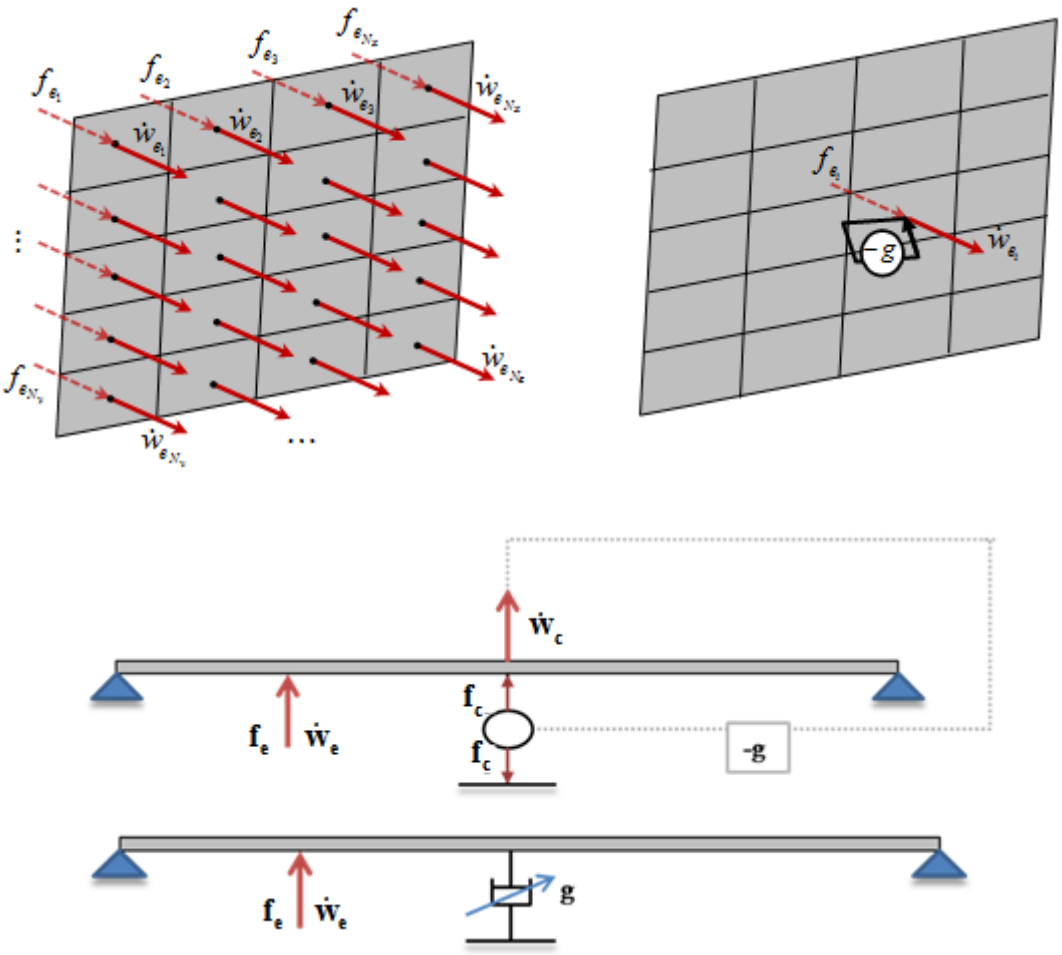

Figure 4.2 – Top, left: Elemental model of the panel showing distributed excitation and resulting complex velocity at the centre of each element. f_e refers to the velocity of at the centre of an element on the panel and $\dot{w}_e$ is the corresponding velocity of the panel at this point. Top, right: Representation of an ideal feedback controller with adjustable gain g on the panel surface. Bottom: Lumped parameter model of a controller implemented on the surface of the panel. f_c refers to the secondary control point force and $\dot{w}_c$ is the resulting control velocity at this point.

The harmonic excitation force on the surface of the panel defined in Equation (4.4) and the resulting velocity defined in Equation (4.5) can be alternatively expressed as a vector $\mathbf{f_e}(\omega)$ of point forces applied at the centre of each of the elements, and a vector $\dot{\mathbf{w}}_\mathbf{e}(\omega)$ of the resulting complex velocities at the same locations [2] [17] [106]

$$\mathbf{f_e}(\omega) = \left\{ f_{e_1}(\omega) \quad f_{e_2}(\omega) \quad \cdots \quad f_{e_{N_e}}(\omega) \right\}^T, \tag{4.6}$$

$$\dot{\mathbf{w}}_{\mathbf{e}}(\omega) = \left\{ \dot{w}_{e_1}(\omega) \quad \dot{w}_{e_2}(\omega) \quad \cdots \quad \dot{w}_{e_{N_e}}(\omega) \right\}^T, \tag{4.7}$$

where $f_{e_1}(\omega), f_{e_2}(\omega), ..., f_{e_{Ne}}(\omega)$ correspond to the point forces applied at the centre of each element of the panel grid and $\dot{w}_{e_1}(\omega), \dot{w}_{e_2}(\omega), ..., \dot{w}_{e_{Ne}}(\omega)$ are the resulting complex velocities at the same locations. The dimensions of the vectors defined in Equations (4.6) and (4.7) are $\left[N_e \times 1\right]$.

The i[th] element of the force vector $\mathbf{f}_{\mathbf{e}}(\omega)$ can be expressed in terms of the pressure excitation $p_i(\omega)$ as

$$\begin{aligned} f_{e_i}(\omega) &= A_e \left[2 p_i(\omega)\right] e^{-j(k_x x_i + k_y y_i)} \\ &= 2 A_e p_i(\omega) e^{-j(k_x x_i + k_y y_i)}, \end{aligned} \tag{4.8}$$

where A_e is the area of each element and $p_i(\omega)$ is the complex pressure amplitude of the incident sound wave. The factor of 2 in the above equation refers to the blocked force assumption on the rigid surface of the panel leading to a doubling in pressure [17]. In the simulations, the fluid medium in which the modelled panel is assumed to be located is air and therefore, the medium parameters used here are those of air, for example the density and the specific impedance of the medium are $\rho_{medium} = \rho_{air} = \rho_0 = 1.21 kgm^{-3}$ and $Z_{medium} = Z_{air} = Z_0 = 415 Nsm^{-3}$ respectively. The amplitude of the pressure was set to $p_i = 1$Pa [2] [98].

The control point forces and resulting complex control velocities generated by the feedback controllers can be defined in a similar manner to the primary excitation point forces and velocities of the panel as vectors $\mathbf{f}_{\mathbf{c}}$ and $\dot{\mathbf{w}}_{\mathbf{c}}$ respectively, such that

$$\mathbf{f}_{\mathbf{c}} = \left\{ f_{c_1} \quad f_{c_2} \quad \cdots \quad f_{c_{N_c}} \right\}^T \tag{4.9}$$

$$\dot{\mathbf{w}}_{\mathbf{c}} = \left\{ \dot{w}_{c_1} \quad \dot{w}_{c_2} \quad \cdots \quad \dot{w}_{c_{N_c}} \right\}^T, \tag{4.10}$$

where the terms $f_{c_1}, f_{c_2}, ..., f_{c_{N_c}}$ are the control point forces at the location of the controller and the terms $\dot{w}_{c_1}, \dot{w}_{c_2}, ..., \dot{w}_{c_{N_c}}$ are the resulting complex control velocities. The

dimensions of both vectors are $[N_c \times 1]$ [2] [17] [106]. For a single channel feedback control system Equations (4.9) and (4.10) are reduced to scalar values.

For a proportional or direct velocity feedback control system, the output of the velocity error sensor is fed back to the actuator with a negative gain which for consistency with the previous equations can be defined here as a diagonal matrix $\mathbf{H}$ containing the gains g of the control system. The system is therefore, directly governed by the gain of the feedback loop. Consequently, based on the definition of direct velocity feedback control, the control force $\mathbf{f_c}$ can be expressed in terms of the complex velocity as

$$\mathbf{f_c} = -\mathbf{H}\dot{\mathbf{w}}_\mathbf{c}, \tag{4.11}$$

where $\mathbf{H} = \begin{bmatrix} g & 0 & \cdots & 0 \\ 0 & g & \cdots & 0 \\ \vdots & \vdots & \ddots & \vdots \\ 0 & 0 & \cdots & g \end{bmatrix}$.

In order to make the understanding of the following equations easier for the reader, a diagram of the modelled panel with a decentralised multi-channel velocity feedback control system and the equivalent diagram, taken from [2], are displayed in Figure 4.3. In the block diagram, the terms $\mathbf{Y_{ee}}$ and $\mathbf{Y_{cc}}$ refer to the matrices of point and transfer mobilities at the centre of the elements and control points respectively, and $\mathbf{Y_{ec}}$ and $\mathbf{Y_{ce}}$ are the matrices of transfer mobilities between the centre of the elements and the control points. The dimensions of $\mathbf{Y_{ee}}$, $\mathbf{Y_{cc}}$, $\mathbf{Y_{ce}}$ and $\mathbf{Y_{ec}}$ are $[N_e \times N_e], [N_c \times N_c], [N_c \times N_e]$ and $[N_e \times N_c]$ respectively. For a single channel feedback control system $\mathbf{Y_{cc}}$ is reduced to a single scalar value, and $\mathbf{Y_{ce}}$ and $\mathbf{Y_{ec}}$ are reduced to $[1 \times N_e]$ and $[N_e \times 1]$ vectors.

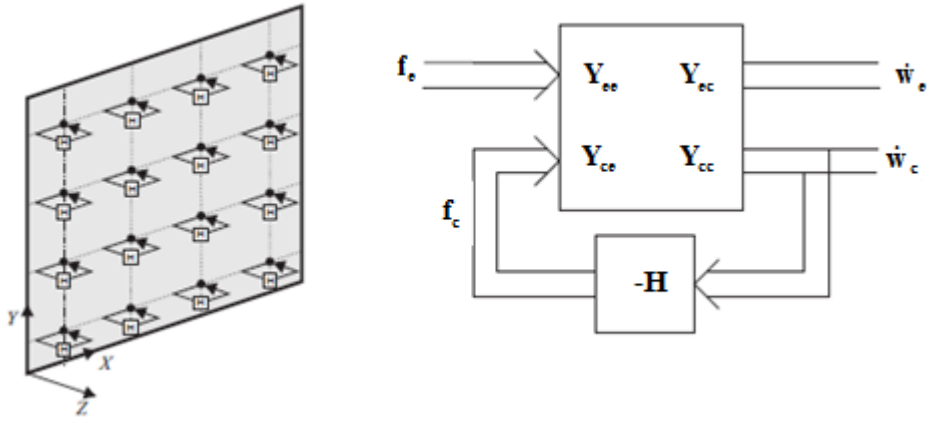

Figure 4.3 – Diagram of a multi-channel decentralised velocity feedback control system (left) and equivalent block diagram (right) [2].

Based on the block diagram provided in Figure 4.3, in the absence of control $\left(\mathbf{H}=0,\ \mathbf{f_c}=0\right)$, the elemental point and transfer mobilities can be defined as the complex velocity per unit excitation force at the centre of each element, or the complex velocity at the centre of each element can be defined as the product of the element point and transfer mobilities and the elemental forces

$$\dot{\mathbf{w}}_\mathbf{e} = \mathbf{Y}_{\mathbf{ee}}\mathbf{f}_\mathbf{e}. \tag{4.12}$$

The above equation can be further expanded in order to show the elements of the matrices and the vectors as

$$\begin{Bmatrix} \dot{w}_{e_1} \\ \dot{w}_{e_2} \\ \vdots \\ \dot{w}_{e_{N_e}} \end{Bmatrix} = \begin{bmatrix} Y_{ee_{11}} & Y_{ee_{12}} & \cdots & Y_{ee_{1N_e}} \\ Y_{ee_{21}} & \ddots & & Y_{ee_{2N_e}} \\ \vdots & & \ddots & \vdots \\ Y_{ee_{N_e1}} & Y_{ee_{N_e2}} & \cdots & Y_{ee_{N_eN_e}} \end{bmatrix} \begin{Bmatrix} f_{e_1} \\ f_{e_2} \\ \vdots \\ f_{e_{N_e}} \end{Bmatrix} \tag{4.13}$$

The $(i,j)^{\text{th}}$ term $Y_{ee_{ij}}$ of the mobility matrix $\mathbf{Y_{ee}}$, which is the mobility at the i^{th} element due to the excitation point force exerted at the centre of the j^{th} element, is calculated from the finite modal expansion approach explained in [17] [106], over the first N modes of the panel, using

$$Y_{ee_{ij}} = \frac{\dot{w}_{e_i}}{f_{e_j}} = j\omega \sum_{n=1}^{N} \frac{\phi_n(x_{e_i}, y_{e_i})\phi_n(x_{e_j}, y_{e_j})}{M\left[\omega_n^2(1+j2\zeta_n)-\omega^2\right]}, \tag{4.14}$$

where $\dot{w}_{e_i}$ is the complex velocity at the i[th] element, f_{e_j} is the point force acting at the centre of the j[th] element, $j=\sqrt{-1}$, $\phi_n(x_{e_i}, y_{e_i})$ and $\phi_n(x_{e_j}, y_{e_j})$ are the natural modes at the coordinates of the centres of the i[th] and j[th] elements respectively, $M=\rho l_x l_y h$ is the mass of the aluminium plate in kg, ω_n is the natural frequency of the panel in rad/s calculated using Equation (A.1) in Appendix A, and finally ζ_n is the modal damping ratio. The properties of the panel listed in Table 3.1 have been used for the damping ratio and for calculating the mass and the natural frequencies of the panel. The natural modes $\phi_n(x_{e_i}, y_{e_i})$ and $\phi_n(x_{e_j}, y_{e_j})$ can be calculated using Equation (2.32c) of Chapter 2 for the mode shapes in the out-of-plane direction, when the panel is simply-supported. Equation (4.14) can alternatively be expressed in terms of the elemental mobility matrix $\mathbf{Y_{ee}}$ and the matrix $\boldsymbol{\phi}_\mathbf{e}$ of the first N natural modes of the panel with dimensions $\left[N_e \times N\right]$ as

$$\mathbf{Y_{ee}} = \boldsymbol{\phi}_\mathbf{e}\boldsymbol{\Omega}\boldsymbol{\phi}_\mathbf{e}^\mathbf{T}, \tag{4.15}$$

where $\boldsymbol{\phi}_\mathbf{e} = \begin{bmatrix} \phi_1(x_{e_1}, y_{e_1}) & \phi_2(x_{e_1}, y_{e_1}) & \cdots & \phi_N(x_{e_1}, y_{e_1}) \\ \phi_1(x_{e_2}, y_{e_2}) & \phi_2(x_{e_2}, y_{e_2}) & \cdots & \phi_N(x_{e_2}, y_{e_2}) \\ \vdots & \vdots & \ddots & \vdots \\ \phi_1(x_{e_{N_e}}, y_{e_{N_e}}) & \phi_2(x_{e_{N_e}}, y_{e_{N_e}}) & \cdots & \phi_N(x_{e_{N_e}}, y_{e_{N_e}}) \end{bmatrix}$, and $\boldsymbol{\Omega}$ is a diagonal matrix defined as $\begin{bmatrix} \Omega & 0 & \cdots & 0 \\ 0 & \Omega & \cdots & 0 \\ \vdots & \vdots & \ddots & \vdots \\ 0 & 0 & \cdots & \Omega \end{bmatrix}$ of dimensions $\left[N_e \times N_e\right]$ in which

$$\Omega = \frac{j\omega}{M\left[\omega_n^2(1+j2\zeta_n)-\omega^2\right]}. \tag{4.16}$$

As already mentioned in the previous chapter, in order to have an accurate representation of the overall response of the modelled panel the contribution of higher

order residual modes needs to be taken into account. There are two ways of including this contribution into the calculations. One way consists of setting the dynamic frequency range – the range over which the modal summation of Equation (4.14) is calculated – well beyond the frequency range of observation, for example up to 50 times greater than the upper limit of the observation range as shown in [106]. However, depending on how large the frequency range of observation is, this method becomes very computationally demanding. The alternative method is to calculate the panel mobility due to these higher order residual modes using the modal expansion shown in Equation (4.14) and simplifying to only include the stiffness and damping terms, as these higher order residual modes are dominated by the stiffness and damping over the observation frequency range. Consequently, Equation (4.14) can be more generally expressed as [17] [41]

$$Y_{ee_{ij}} = Y_{ee_{ij}} + Y_{ee_{ij,res}} = \frac{\dot{w}_{e_i}}{f_{e_j}} + \frac{\dot{w}_{e_{i,res}}}{f_{e_j}}, \tag{4.17}$$

$$Y_{ee_{ij}} = j\omega \sum_{n=1}^{N} \frac{\phi_n(x_{e_i}, y_{e_i})\phi_n(x_{e_j}, y_{e_j})}{M\left[\omega_n^2(1+j2\zeta_n) - \omega^2\right]} + j\omega \sum_{n=N+1}^{N_{res}} \frac{\phi_n(x_{e_i}, y_{e_i})\phi_n(x_{e_j}, y_{e_j})}{M\omega_n^2(1+j2\zeta_n)}, \tag{4.18}$$

where $Y_{ee_{ij,res}}$ and $\dot{w}_{e_{i,res}}$ are the panel mobility and complex velocity respectively due to the residual modes, and N_{res} is the number of included residual modes.

When the feedback loop is closed and a control force is applied to the panel at the location of each controller, based on the block diagram of Figure 4.3, the equation for the complex velocities at the centre of each element changes to reflect the contribution of the control forces, such that

$$\dot{\mathbf{w}}_\mathbf{e} = \mathbf{Y}_{\mathbf{ee}}\mathbf{f}_\mathbf{e} + \mathbf{Y}_{\mathbf{ec}}\mathbf{f}_\mathbf{c}. \tag{4.19}$$

The complex velocities at the points of control can also be similarly expressed in terms of the structural mobilities, primary excitation and secondary control forces as

$$\dot{\mathbf{w}}_\mathbf{c} = \mathbf{Y}_{\mathbf{cc}}\mathbf{f}_\mathbf{c} + \mathbf{Y}_{\mathbf{ce}}\mathbf{f}_\mathbf{e}. \tag{4.20}$$

Equations (4.19) and (4.20) can be expanded in order to show the elements of the matrices and vectors as

$$\begin{Bmatrix} \dot{w}_{e1} \\ \dot{w}_{e2} \\ \vdots \\ \dot{w}_{eN_e} \end{Bmatrix} = \begin{bmatrix} Y_{ee11} & Y_{ee12} & \cdots & Y_{ee1N_e} \\ Y_{ee21} & \ddots & & Y_{ee2N_e} \\ \vdots & & \ddots & \vdots \\ Y_{eeN_e1} & Y_{eeN_e2} & \cdots & Y_{eeN_eN_e} \end{bmatrix} \begin{Bmatrix} f_{e1} \\ f_{e2} \\ \vdots \\ f_{eN_e} \end{Bmatrix} + \begin{bmatrix} Y_{ec11} & Y_{ec12} & \cdots & Y_{ec1N_c} \\ Y_{ec21} & \ddots & & Y_{ec2N_c} \\ \vdots & & \ddots & \vdots \\ Y_{ecN_e1} & Y_{ecN_e2} & \cdots & Y_{ecN_eN_c} \end{bmatrix} \begin{Bmatrix} f_{c1} \\ f_{c2} \\ \vdots \\ f_{cN_c} \end{Bmatrix} \tag{4.21}$$

$$\begin{Bmatrix} \dot{w}_{c1} \\ \dot{w}_{c2} \\ \vdots \\ \dot{w}_{cN_c} \end{Bmatrix} = \begin{bmatrix} Y_{cc11} & Y_{cc12} & \cdots & Y_{cc1N_c} \\ Y_{cc21} & \ddots & & Y_{cc2N_c} \\ \vdots & & \ddots & \vdots \\ Y_{ccN_c1} & Y_{ccN_c2} & \cdots & Y_{ccN_cN_c} \end{bmatrix} \begin{Bmatrix} f_{c1} \\ f_{c2} \\ \vdots \\ f_{cN_c} \end{Bmatrix} + \begin{bmatrix} Y_{ce11} & Y_{ce12} & \cdots & Y_{ce1N_e} \\ Y_{ce21} & \ddots & & Y_{ce2N_e} \\ \vdots & & \ddots & \vdots \\ Y_{ceN_c1} & Y_{ceN_c2} & \cdots & Y_{ceN_cNe} \end{bmatrix} \begin{Bmatrix} f_{e1} \\ f_{e2} \\ \vdots \\ f_{eN_e} \end{Bmatrix} \tag{4.22}$$

The $(i,j)^{\text{th}}$ terms of the mobility matrices $\mathbf{Y_{cc}}$, $\mathbf{Y_{ec}}$ and $\mathbf{Y_{ce}}$ were calculated using the modal expansion technique of Equation (4.15)

$$Y_{cc_{ij}} = \frac{\dot{w}_{c_i}}{f_{c_j}} = j\omega \sum_{n=1}^{N} \frac{\phi_n(x_{c_i}, y_{c_i})\phi_n(x_{c_j}, y_{c_j})}{M\left[\omega_n^2(1+j2\zeta_n) - \omega^2\right]}, \tag{4.23}$$

$$Y_{ec_{ij}} = \frac{\dot{w}_{e_i}}{f_{c_j}} = j\omega \sum_{n=1}^{N} \frac{\phi_n(x_{e_i}, y_{e_i})\phi_n(x_{c_j}, y_{c_j})}{M\left[\omega_n^2(1+j2\zeta_n) - \omega^2\right]}, \tag{4.24}$$

$$Y_{ce_{ij}} = \frac{\dot{w}_{c_i}}{f_{e_j}} = j\omega \sum_{n=1}^{N} \frac{\phi_n(x_{c_i}, y_{c_i})\phi_n(x_{e_j}, y_{e_j})}{M\left[\omega_n^2(1+j2\zeta_n) - \omega^2\right]}. \tag{4.25}$$

Finally, by substituting Equation (4.11) into Equations (4.19) and (4.20) for complex velocities $\dot{\mathbf{w}}_\mathbf{e}$ and $\dot{\mathbf{w}}_\mathbf{c}$ and with further simplifications, both Equations can be formulated in terms of the excitation force $\mathbf{f_e}$ as

$$\dot{\mathbf{w}}_\mathbf{e} = \left[\mathbf{Y_{ee}} - \mathbf{Y_{ec}}\mathbf{H}(\mathbf{I} + \mathbf{Y_{cc}}\mathbf{H})^{-1}\mathbf{Y_{ce}}\right]\mathbf{f_e} \tag{4.26}$$

$$\dot{\mathbf{w}}_\mathbf{c} = (\mathbf{I} + \mathbf{Y_{cc}}\mathbf{H})^{-1}\mathbf{Y_{ce}}\mathbf{f_e} \tag{4.27}$$

Equation (4.26) will be used in the next subsection for the estimation of the structural response and radiated sound power of the panel.

4.1.1 Panel Structural Response and Total Radiated Sound Power

The overall structural response of the panel can be estimated through the calculation of the total kinetic energy. The time-averaged kinetic energy of the panel is defined by the integration over the panel surface of the product of panel mass and the squared panel velocity due to the harmonic excitation as [17] [106]

$$\begin{aligned} E_k(\omega) &= \frac{1}{4}\iint_A \rho h \left|\dot{w}(x,y,\omega)\right|^2 dA \\ &= \frac{\rho h}{4}\int_0^{l_x}\int_0^{l_y} \left|\dot{w}(x,y,\omega)\right|^2 dydx, \end{aligned} \tag{4.28}$$

where ρ and h are the density and thickness of the panel respectively with values listed in Table 3.1, $\dot{w}(x,y,\omega)$ is the complex transverse velocity at the surface of the panel due to the harmonic excitation and A is the area of the panel. The additional factor of ½ has been introduced in the above equation for converting peak to rms values. Equation (4.28) can be formulated in terms of its elemental equivalent representation as a summation over the panel elemental grid of the product of the elemental masses and the squared complex velocities at the centre of each element [106]

$$E_k(\omega) = \frac{1}{4}\sum_{i=1}^{N_e} M_e \left|\dot{w}_{e_i}(\omega)\right|^2, \tag{4.29}$$

where $M_e = \dfrac{M}{N_e}$ is the mass of each element. Alternatively, the vector denotation of the above equation can be expressed as the product of the complex velocity vector $\dot{\mathbf{w}}_\mathbf{e}$ and its Hermitian or conjugate transpose $\dot{\mathbf{w}}_\mathbf{e}^\mathbf{H}$

$$E_k = \frac{M_e}{4}\dot{\mathbf{w}}_\mathbf{e}^\mathbf{H}\dot{\mathbf{w}}_\mathbf{e} \tag{4.30}$$

$$E_k = \frac{M_e}{4}\left\{\dot{w}_{e_1}^* \quad \dot{w}_{e_2}^* \quad \dots \quad \dot{w}_{e_{N_e}}^*\right\}\begin{Bmatrix}\dot{w}_{e_1}\\ \dot{w}_{e_2}\\ \vdots\\ \dot{w}_{e_{N_e}}\end{Bmatrix}. \tag{4.31}$$

The total time-averaged radiated sound power level is obtained from the integration over the surface of the panel of the product of the near field sound pressure radiated from the panel and the panel transverse velocity [106]

$$\begin{aligned} P_{\mathbf{rad}}(\omega) &= \frac{1}{2}\iint_A \mathrm{Re}\left\{\dot{w}^*(x,y,\omega)\, p_o(x,y,\omega)\right\} dA \\ &= \frac{1}{2}\int_0^{l_x}\int_0^{l_y} \mathrm{Re}\left\{\dot{w}^*(x,y,\omega)\, p_o(x,y,\omega)\right\} dydx, \end{aligned} \tag{4.32}$$

where $p_0(x,y,\omega)$ is the near field sound pressure and the factor of ½ is due to the peak to rms conversion. The near field acoustic pressure can be expressed in terms of the panel velocity with the Rayleigh integral as [17]

$$p_o(x,y,\omega) = \frac{j\omega\rho_0}{2\pi}\int_0^{l_x}\int_0^{l_y} \dot{w}(x',y',\omega)\frac{e^{-jk_0 r}}{r} dy'dx', \tag{4.33}$$

where ρ_0 is the density of air and r is the distance between the coordinates of the sound pressure and the panel velocity located respectively at (x',y') and (x,y) found from $r = \sqrt{(x-x')^2 + (y-y')^2}$ [106]. The substitution of Equation (4.33) into Equation (4.32) leads to the following quadruple integral for the radiated sound power [17]

$$P_{rad}(\omega) = \frac{1}{2}\mathrm{Re}\left\{\frac{j\omega\rho_0}{2\pi}\int_0^{l_x}\int_0^{l_y}\int_0^{l_x}\int_0^{l_y} \dot{w}^*(x,y,\omega)\dot{w}(x',y',\omega)\frac{e^{-jk_0 r}}{r} dy'dx'dydx\right\}. \tag{4.34}$$

Since $e^{-jk_0 r} = \cos k_0 r - j\sin k_0 r,$

$$\mathrm{Re}\left\{\frac{je^{-jk_0 r}}{r}\right\} = \mathrm{Re}\left\{\frac{j(\cos k_0 r - j\sin k_0 r)}{r}\right\} = \frac{\sin k_0 r}{r}.$$

Consequently, Equation (4.34) can be further simplified and rewritten as

$$P_{rad}(\omega)=\frac{\omega\rho_0}{4\pi}\int_0^{l_x}\int_0^{l_y}\int_0^{l_x}\int_0^{l_y}\dot{w}^*(x,y,\omega)\dot{w}(x',y',\omega)\frac{\sin k_0 r}{r}dy'dx'dydx. \tag{4.35}$$

For the elemental approach, the above integral can be formulated in terms of the sum of the radiated power of each element as [17]

$$P_{rad}(\omega)=\frac{1}{2}\sum_{i=1}^{N_e}\sum_{j=1}^{N_e}A_e\,\mathrm{Re}\left\{\dot{w}_{e_i}^*(x_{e_i},y_{e_i},\omega)\,p_{e_j}(x_{e_j},y_{e_j},\omega)\right\}, \tag{4.36}$$

which can be alternatively written in terms of the complex velocity vector $\dot{\mathbf{w}}_\mathbf{e}$ and its Hermitian $\dot{\mathbf{w}}_\mathbf{e}^\mathbf{H}$ as

$$P_{rad}=\dot{\mathbf{w}}_\mathbf{e}^\mathbf{H}\mathbf{R}_\mathbf{rad}\dot{\mathbf{w}}_\mathbf{e}, \tag{4.37}$$

where $\mathbf{R}_\mathbf{rad}$ is referred to as the radiation resistance matrix of dimensions $\left[N_e\times N_e\right]$ defined as [17]

$$\mathbf{R}_\mathbf{rad}=\begin{bmatrix} R_{11} & R_{12} & \cdots & R_{1j} & \cdots & R_{1N_e} \\ R_{21} & R_{22} & & & & R_{2N_e} \\ \vdots & & \ddots & & & \vdots \\ R_{i1} & & & R_{ij} & & R_{iN_e} \\ \vdots & & & & \ddots & \vdots \\ R_{N_e1} & & \cdots & R_{N_ej} & \cdots & R_{N_eN_e} \end{bmatrix}. \tag{4.38}$$

Assuming that the panel is radiating into the free field and has an infinite baffle, the $(i,j)^{\text{th}}$ element of the above matrix can be written as [17]

$$R_{ij}=\frac{\omega^2\rho_e A_e^2}{4\pi c_0}\frac{\sin(k_0 r_{ij})}{k_0 r_{ij}}, \tag{4.39}$$

where $\rho_e=\dfrac{\rho}{N_e}$ is the density of each element of the panel and r_{ij} is the $(i,j)^{\text{th}}$ distance between the i$^{\text{th}}$ elemental velocity and the j$^{\text{th}}$ elemental sound pressure.

The structural response and radiated sound power expressions defined here for the elemental approach will be used in the next sections of this chapter to assess the performance of velocity feedback control on the modelled aluminium panel.

4.1.2 Simulations of Structural Response and Sound Radiation

Simulations of direct velocity feedback were performed with the initial assumption that one ideal point force actuator was positioned at the centre of the rectangular aluminium panel, as shown in Figure 4.4. For the simulations, up to 40 frequency-independent gain levels, ranging from 10^{-3} to 10^{6}, were chosen for the feedback loop gain, in order to observe the effect of extreme gain variations on the dynamic performance of the panel. The observed frequency range was set to 1.5 kHz but the contribution of the higher order residual modes was taken into account through the calculation of the mobilities using Equation (4.18).

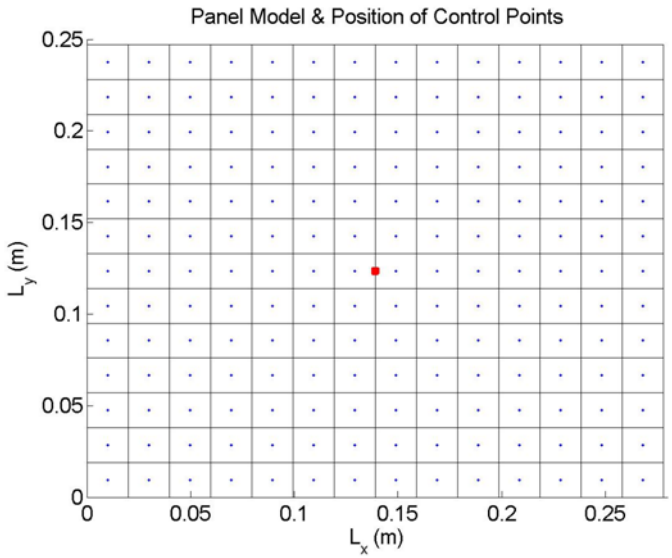

Figure 4.4 – Elemental panel model with the location of the ideal point force controller marked as a red point in the centre of the panel.

The performance, as a measure of the overall structural response, of the simulated control system was first assessed by plotting the frequency response of the kinetic energy and radiated sound power over the observed frequency range, when the panel is simply-supported and subjected to a diffuse field excitation $\left(\phi = \theta = 45^{\circ}\right)$, before and

after closing the feedback loop. 25 different gain levels were used in the spectra displayed in Figure 4.5. The uncontrolled structural response and radiated sound power spectra show well separated modes for the low frequencies. The first resonance of the panel associated with Mode (1,1) occurs at 71.7 Hz and dominates the spectrum in both graphs. This is due to the fact that volumetric modes such as Mode (1,1) are strongly radiating modes. After that, the amplitude of the modes monotonically decreases such that, for example, at the mode occurring at 1.5 kHz, the amplitude reaches -60 dB which is 48 dB less than the amplitude of Mode (1,1). The occurrence of a pair of low-amplitude and identical resonance peaks can be seen in both structural response and radiated sound power graphs at 166.7 Hz and 192 Hz. These resonances belong to the (2,1) and (1,2) structural modes which have a negligible influence on the radiated sound power due to their poor radiation efficiency.

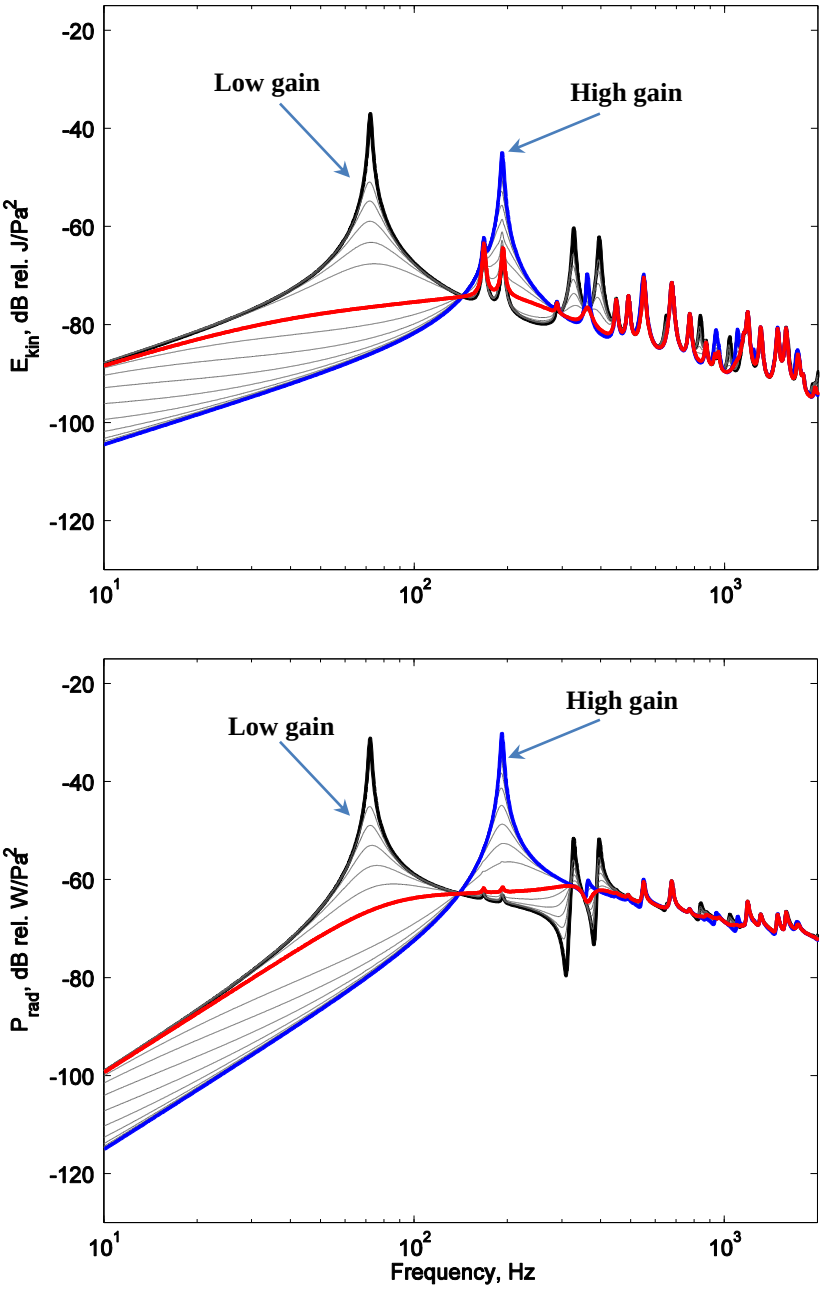

Figure 4.5 – Overall structural response (top) and total radiated sound power (bottom) graphs of the modelled aluminium panel when a feedback controller with an ideal point force actuator is assumed to be positioned at the centre of the panel. The response and radiated sound power with no feedback gain are shown in black, with increasing gain in grey, with optimal gain in red, and with high gain in blue.

When the feedback loop is closed and feedback gain is increased, the structural response and radiated sound power are both gradually attenuated, due to active damping. The lower-frequency resonances are more heavily damped while towards higher frequencies, the contribution of residual modes does not allow efficient control due to the resulting spillover effect. Both the structural response and the radiated sound power of the panel

are initially attenuated with increasing gain. But then, further increases in the gain level causes a large increase in the control force, which is a result of the controller actively pinning the panel. Due to the pinning effect, a new additional boundary condition is created at the location of control force, which causes the occurrence of new resonance peaks and a shift in the resonances toward higher frequencies but no additional damping [17]. The first new resonance peak can be observed at 200 Hz in both spectra. The amplitude of this resonance peak is lower than the panel's initial first resonance in the absence of control because the pinning of the controller in the centre of the panel increases the stiffness of the structure. For the case of the radiated sound power, this new resonance peak has higher amplitude than that initial first resonance of the uncontrolled panel, because the increase in natural frequency allows this mode to radiate more efficiently than before.

This effect has been demonstrated by Gardonio and Elliott in [108] where theoretical studies of direct velocity feedback have been conducted on a beam, first with an ideal point force controller then with a modelled piezoelectric patch actuator.

4.1.3 Stability and Gain Analysis

The use of an ideal controller for the simulations of velocity feedback control causes the system to be unconditionally stable for all gain levels. As explained in Chapter 1, this is due to the fact that the real-part of the frequency response between the ideal point force actuator and the error sensor –the plant response – is positive, i.e. the Nyquist plot of the plant response will always remain on the right-hand side or positive part of the real axis. As can be seen in the bottom diagram of Figure 4.2, the actuator is only modelled as an ideal point force and has no dynamic properties that could influence the plant, therefore, in theory, an ideal controller synthesises a passive system, which is always stable.

The gain value corresponding to optimal control, for which the maximum reduction in the structural response is achieved, can be estimated through the integration of the total kinetic energy of the panel over the control bandwidth frequency, and plotting the result over increasing feedback gain. The optimal gain value for achieving maximum attenuation in radiated sound power can also be estimated using the same approach. The estimation of the optimal gain level can help to avoid the use of high gain levels for which the controller pins the structure. The resulting graphs are displayed in Figure 4.6.

The minimum points in both graphs correspond to the optimal gain values for which the structural response and radiated sound power are attenuated the most. These optimal values are 41.2 and 24.2 for the structural response and the radiated sound power, respectively, and the amplification of the feedback controller by these values result in attenuations of 13.6 dB and 7 dB in the structural response and radiated sound power, respectively.

The gain amplitude required to minimise the radiated sound power level is almost half the amplitude needed for minimising the kinetic energy. This phenomenon can be explained by the occurrence of the new lightly-damped resonance peaks at high gain levels, which occur due to the pinning effect and radiate sound more efficiently. This mean that at high levels of gain the total radiated sound power is increased by up to 5 dB compared to the total radiated sound power in the absence of control. Conversely, at high levels of gain the total kinetic energy is still reduced by almost 4 dB due to the efficient dissipation of the energy by these new structural modes.

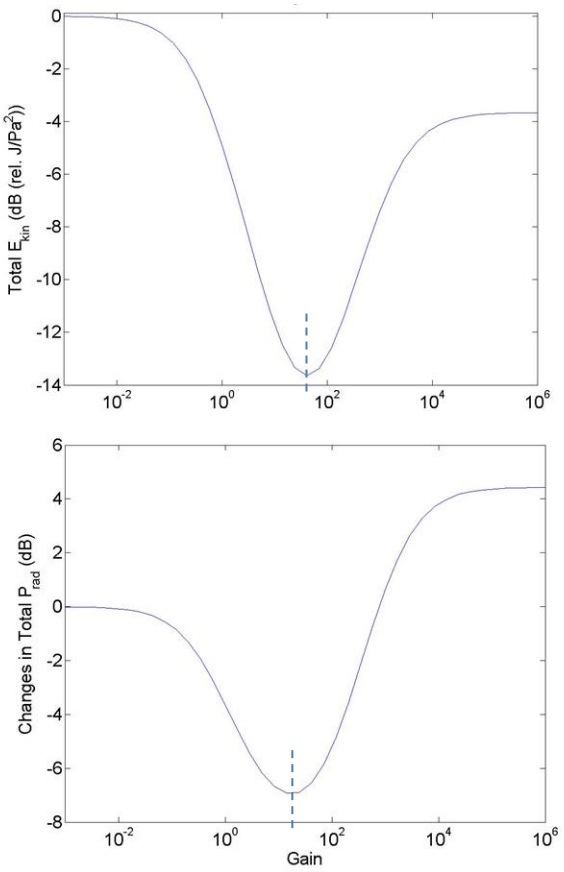

Figure 4.6 – Estimation of the optimal gain value for a single feedback controller through the plot of the total changes in kinetic energy (top) and radiated sound power (bottom) over increasing gain.

4.1.4 Effect of Actuators Number and Positioning on Feedback Control Performance

Another factor that significantly influences optimal control conditions is the position of the controllers on the structure. For example, in the case of a single controller, locating the device at the centre of the panel provides the most efficient control. For a multi-channel control system, the use of a symmetrical arrangement of actuators allows a more efficient coupling with several panel modes, while using lower gain levels than a single centred actuator. Achieving similar overall attenuation with a single actuator positioned in the centre of the panel will not be possible, as the gain will have to be increased to amplitudes which will cause the panel to be pinned at the location of the actuator. The pinning of the panel at the point of control will lead to a change in the boundary conditions of the panel, and the actuator will then be positioned on a node, resulting in no control.

In the next step of the investigation, the number of controllers was increased to four and then five. The 4 feedback controllers were placed on the diagonals of the rectangular panel, 10 cm away – about one third of the diagonal length – from the edges. The aim of this arrangement was to keep the positions symmetrical and attempt to cover the largest surface on the panel without being too close to the edges. The simulation using an arrangement of 5 point force actuators was a combination of the arrangements with a single actuator at the centre of the panel and with the 4 actuators. The excitation and control points' coordinates have been listed in Table 4.1. Figure 4.7 displays the panel model for 4 and 5 feedback controllers, with the controllers situated in the positions which produce maximum attenuation. All the controllers were assumed to have the same feedback gain.

Table 4.1 – Coordinates of the positions of the ideal point force actuators on the panel

Parameter	value	units
Position of excitation forces f_{ei}	x_{ei}, y_{ei}	m
Position of control point 1	$x_{c1} = l_x/2$, $y_{c1} = l_y/2$	m
Position of control point 2	$x_{c2} = 0.0927$, $y_{c2} = 0.1647$	m
Position of control point 3	$x_{c3} = 0.1853$, $yc_3 = 0.1647$	m
Position of control point 4	$x_{c4} = 0.0927$, $y_{c4} = 0.0823$	m
Position of control point 5	$x_{c5} = 0.1853$, $y_{c5} = 0.0823$	m

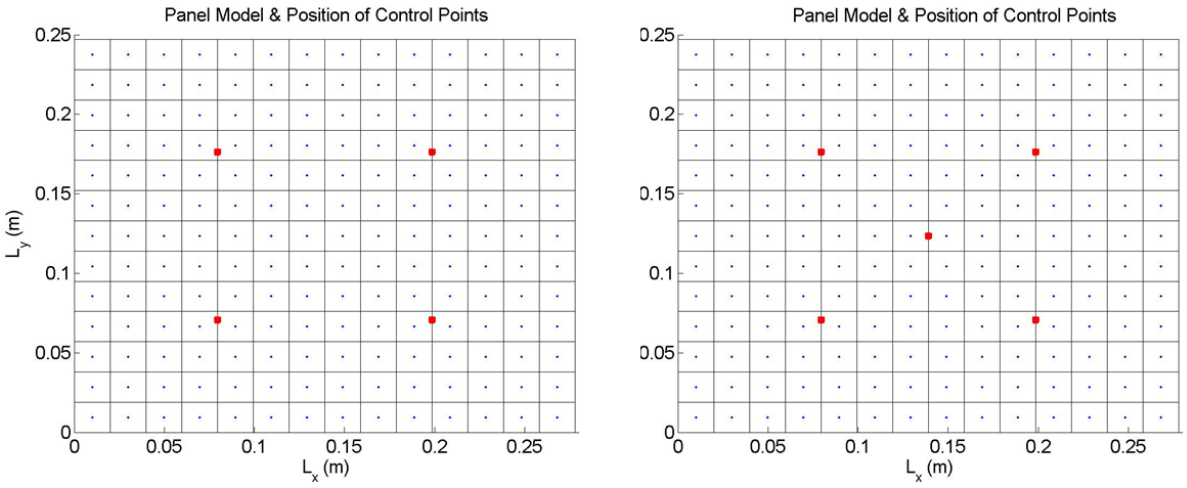

Figure 4.7 – Arrangement of 4 and 5 actuators shown on the panel elemental model (red squares).

Table 4.2 – Optimal gain values and resulting attenuations in total kinetic energy (KE) and radiated sound power (P_{rad}) for arrangements of single, four and five ideal point force actuators on the surface of the modelled panel.

Number of controllers	Optimal Feedback gain (KE)	Resulting attenuation in total KE	Optimal feedback gain (P_{rad})	Resulting attenuations in total P_{rad}
1	41.2	13.6	24.2	7
4	41.2	16.2	14.25	7.5
5	41.2	18.3	14.25	7.8

Based on the above results, the optimal gain for maximum attenuation in total kinetic energy is similar for all three arrangements. In the case of the radiated sound power, the optimal gain for the 4 and 5 controller arrangements is nearly half the optimal gain for the single controller system. The use of 5 controllers has the best attenuation levels in comparison with the single and four controller set-ups, and it provides almost 5 dB more attenuation in the kinetic energy than the single controller. All three configurations provide similar attenuation levels for the radiated sound power, because the radiated sound power is dominated by the (1,1) mode, which only takes a single force to control.

The comparison of the 3 different arrangements of actuators reveals that even though the use of 4 actuators results in more attenuation than the single controller set-up, it only provides an additional reduction of 2.6 dB in the kinetic energy and only 0.5 dB additional reduction in the total radiated sound power. The difference between the three

arrangements is small enough to conclude that for a flat panel, positioning a single controller in the centre of the plate provides the best practical choice for controlling both the structural modes of vibration and sound and energy levels. The choice of a single controller versus five controllers for active feedback control is also interesting, in terms of space, weight and cost minimisation, as the practical implementation of a multi-channel feedback control system might encounter space, weight and budget limitations.

After selecting the single feedback controller setup, it was important to investigate the extent to which the accuracy of the placement of the controller at the centre of the panel would affect the levels of attenuation. The controller was moved from the centre of the panel along the diagonal at increments of 3.5% of the length of the diagonal to observe the changes in the optimal gain and the resulting attenuation levels. The attenuation levels achieved for the different controller position with respect to the centre of the panel can be found in Table 4.3. Figure 4.8 shows a plot of the total kinetic energy attenuation levels plotted over an increasing distance from the centre of the panel for the actuator.

Table 4.3 – Ranges of kinetic energy (KE) and radiated sound power (Prad) attenuation levels for different ranges in distance from the centre of the panel for an ideal feedback control with a single actuator.

Distance from centre (m)	Attenuation in E_{kin} (dB)	Attenuation in total P_{rad} (dB)
0 - 0.01	13.6 - 14.7	7
0.01 - 0.03	14.7 - 14.2	7 to 7.1
0.03 - 0.04	14.2 - 13.1	7.1 to 7
0.04 - 0.05	13.1 - 11.4	7 to 6.2
0.05 - 0.07	11.4 - 10.5	6.2 to 5.8
0.07 - 0.08	10.5 - 10.6	5.8 to 6.1
0.08 - 0.09	10.6 - 10	6.1

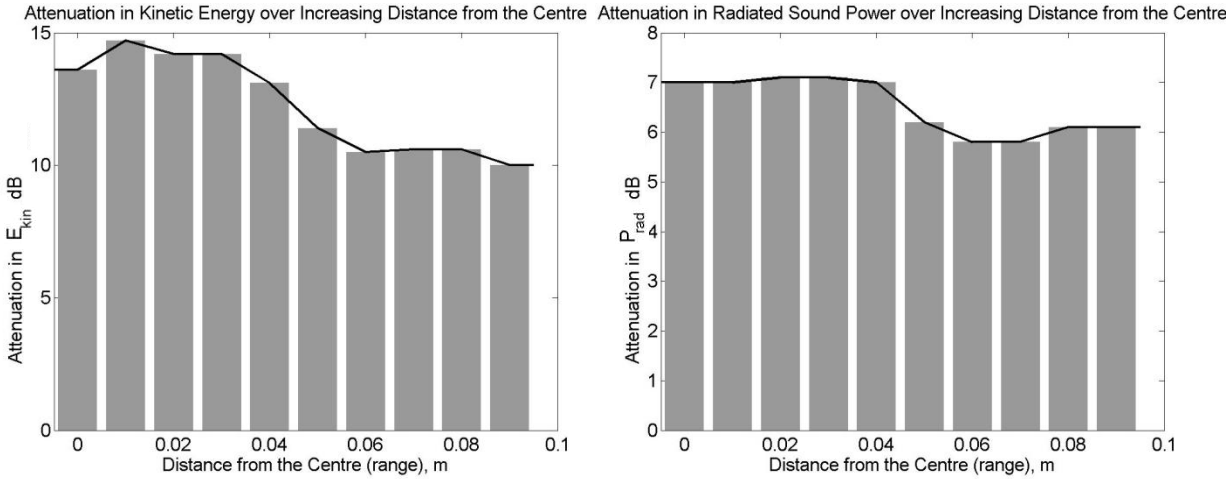

Figure 4.8 – Variations of total kinetic energy (left) and total radiated sound power (right) attenuation levels over increasing distance from the centre for the actuator.

Up to 4 cm away from the centre of the panel, the radiated sound power attenuation levels do not seem to be significantly affected by the positioning of the actuator. However, a further reduction of 1 dB can be observed in the kinetic energy attenuation, 1 to 3 cm away from the centre. This can be explained by the ability of a slightly off-centre controller to couple with more modes. This outcome could be useful later for applications with limitations on the choice of controller locations or structures with slight curvature or deformation.

4.2 Feedback Control of a Panel Using Inertial Actuators

Inertial actuators offer an attractive solution for multi-channel vibration control systems because of the low cost of mass production and ease of implementation in comparison with other transducers. As mentioned in the first chapter, they can also generate high amplitude control forces with a low electrical power requirement. Therefore, these actuators will be used in the following investigations.

An electrodynamic inertial actuator is composed of a suspended mass-spring system and an electromagnetic arrangement for dynamic and magnetic coupling. The lumped-parameter model of a proof-mass electrodynamic actuator is illustrated in Figure 4.9

[107]. It is assumed that a velocity feedback control system consisting of an error sensor measuring the velocity of the structure and an actuator generating reactive forces between the mass and the base of the controller is implemented on the panel.

The amplitude and phase of the blocked force response T_B of the actuator, per input voltage and per input current, are shown in the graphs of Figure 4.9. The natural frequency of the actuator corresponds to the resonance peak observed in upper subplot of Figure 4.9. The associated 180-degree phase-lag can be seen in the lower subplot. The fundamental resonance of the mass-spring system influences the stability of the control system. For frequencies above the natural frequency of the spring-mass system, the structure is subjected to a sky-hook damping effect during negative velocity feedback control, since the base force is almost equal to the mass-spring reactive force. For frequencies lower than the natural frequency of the mass-spring system, however, a negative damping effect can be observed, caused by the base force being out of phase with the reactive force of the system. Consequently, instabilities can arise in the control system. Therefore, in order to achieve good control, it is necessary to use an actuation mechanism with a natural frequency much lower than the one of the vibrating structure, and high damping at the resonance frequency [109].

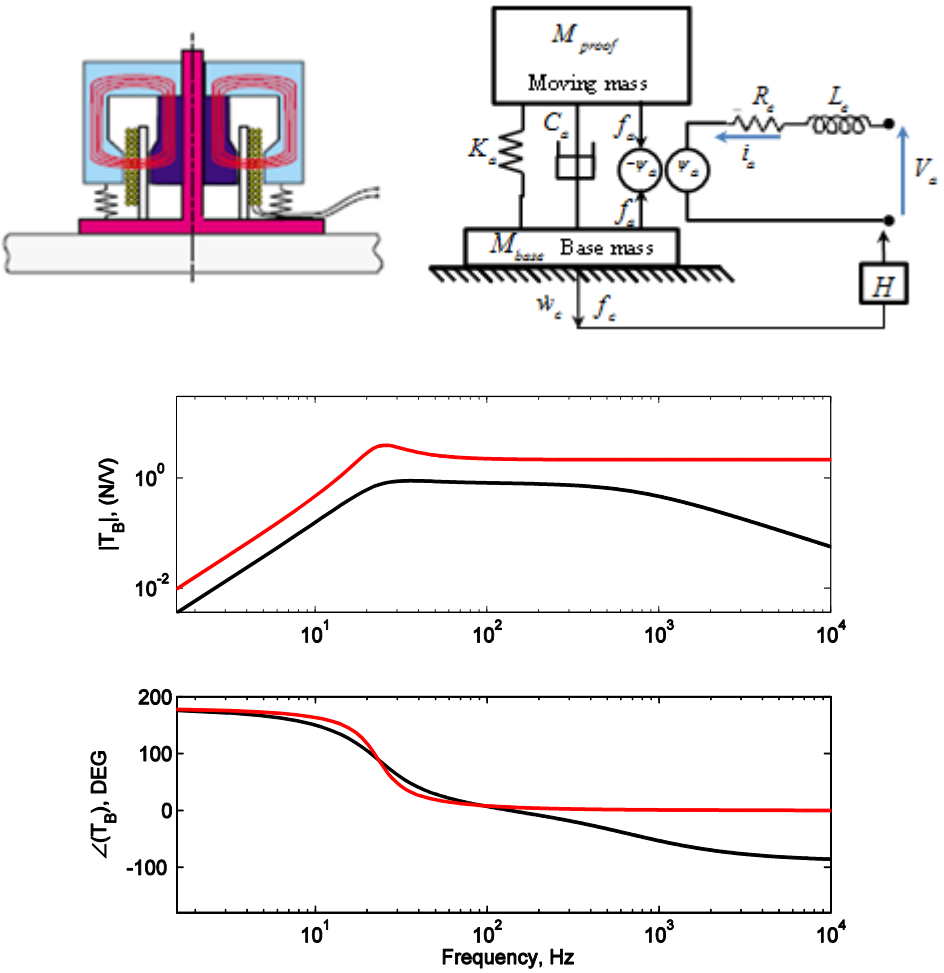

Figure 4.9 – Lumped-parameter diagram (left) and internal view of a particular electrodynamic actuator (right) [107], together with the blocked force response calculated from the lumped parameter model.

Considering the lumped-parameter model of the actuator displayed in Figure 4.9, the complex velocity vector of the moving masses for a multi-channel feedback control system can be defined as

$$\dot{\mathbf{w}}_{\mathbf{M}_{\text{proof}}} = \mathbf{Y}_{\mathbf{M}_{\text{proof}}} \mathbf{f}_{\mathbf{M}_{\text{proof}}}, \tag{4.40}$$

where $\mathbf{Y}_{\mathbf{M}_{\text{proof}}}$ is the mobility of the mass defined as a diagonal matrix with elements $Y_{M_{proofi}} = \dfrac{1}{j\omega M_{proof}}$ on the diagonal, M_{proof} is the proof mass, and $\mathbf{f}_{\mathbf{M}_{\text{proof}}}$ is the vector of the forces exerted by the magnet or moving mass of the actuator to the coil shown in Figure 4.9. The vector of the actuation force $\mathbf{f}_{\mathbf{a}}$ due to the vector of the current $\mathbf{i}_{\mathbf{a}}$ in the coil is found from

$$\mathbf{f_a} = \psi_a \mathbf{i_a}, \tag{4.41}$$

where ψ_a is the transducer coefficient of the actuator's coil and $\mathbf{i_a}$ is proportional to the complex velocity at the point of the control such that

$$\mathbf{i_a} = -g\dot{\mathbf{w}}_\mathbf{c}, \tag{4.42}$$

where g is the feedback loop gain defined as a scalar value for a single-channel feedback control system and $\dot{\mathbf{w}}_\mathbf{c}$ is the complex velocity vector at the locations of the actuator. The resultant force exerted on the panel due to the actuation force and the force of the inertial mass can be written in terms of the complex control velocity and complex velocity of the inertial mass as

$$\mathbf{f_c} = \mathbf{Z_a}\dot{\mathbf{w}}_\mathbf{c} - \mathbf{Z_a}\dot{\mathbf{w}}_{\mathbf{M_{proof}}} - \mathbf{f_a} \tag{4.43}$$

where $\mathbf{Z_a}$ is the impedance of the spring-damper system defined as a diagonal matrix with the elements $Z_{a,i} = \frac{K_a}{j\omega} + C_a$ on the diagonal. The inertial actuator parameters have been listed in Table 4.4. The inertial effects of the base mass and the coil have been omitted at this stage, but will be included later in the thesis.

Table 4.4 – Inertial actuator parameters

Parameter	value	units
Proof mass	M_{proof} = 0.024	kg
Suspension stiffness	K_a = 511	N m^{-1}
Suspension damping coefficient	C_a = 1.99	Ns m^{-1}
Voice coil coefficient	ψ_a = 2.16	NA^{-1}
Modal Damping Ratio	ξ_n = 0.28	
Natural frequency	f_{na} = 23.2	Hz

Equations (4.40)-(4.42) can be combined and substituted into Equation (4.43) to formulate the control force in terms of the complex control velocity and the current as

$$\mathbf{f}_c = \mathbf{Z}_{cc}\dot{\mathbf{w}}_c + \mathbf{Z}_{ca}\mathbf{i}_a \tag{4.44}$$

where $\mathbf{Z}_{cc} = \mathbf{Z}_{Mech} = \left[\mathbf{I} + \mathbf{Z}_a\mathbf{Y}_{M_{proof}}\right]^{-1}\mathbf{Z}_a$ is the mechanical impedance of the actuator, $\mathbf{Z}_{ca} = \psi_a\left[\mathbf{I} + \mathbf{Z}_a\mathbf{Y}_{M_{proof}}\right]^{-1}$ and $\mathbf{I}$ is the identity matrix. With the use of the aluminium panel as the base structure and application of the elemental approach, the same general equations as for the ideal feedback controller can be used for the complex velocities $\dot{\mathbf{w}}_e$ and $\dot{\mathbf{w}}_c$ (Equations 4.26 and 4.27). The substitution of $\mathbf{f}_c$ into these equations leads to

$$\dot{\mathbf{w}}_c = \mathbf{Y}_{cc}\mathbf{Z}_{ca}\left(\mathbf{I} + \mathbf{Y}_{cc}\mathbf{Z}_{cc}\right)^{-1}\mathbf{i}_a + \mathbf{Y}_{ce}\left(\mathbf{I} + \mathbf{Y}_{cc}\mathbf{Z}_{cc}\right)^{-1}\mathbf{f}_e \tag{4.45}$$

$$\dot{\mathbf{w}}_e = \left[\mathbf{Y}_{ee} - \left[\mathbf{I} + \mathbf{Y}_{cc}\left(\mathbf{Z}_{cc} + \mathbf{Z}_{ca}\mathbf{H}\right)\right]^{-1}\mathbf{Y}_{ec}\mathbf{Y}_{ce}\left(\mathbf{Z}_{cc} + \mathbf{Z}_{ca}\mathbf{H}\right)\right]\mathbf{f}_e \tag{4.46}$$

For the kinetic energy and the total radiated sound power level calculations, the same equations as for the ideal feedback controller can be used (Equations 4.30 and 4.37).

4.2.1 Structural Response and Sound Radiation Analysis

The structural response and radiated sound power were calculated for 25 different gains ranging from 10^{-3} to 10^{6} in a similar manner to Section 4.1.2, when a single inertial actuator was assumed to be positioned at the centre of the panel. The observed frequency range was set to 1.5 kHz. The corresponding frequency responses of the overall structural response and total radiated sound power are shown in Figure 4.10 for increasing feedback gain.

As the loading effects of the actuator have been omitted in the calculations, its contribution to the structural response and radiated sound power can only be observed in Figure 4.10, when the feedback loop is closed. In the absence of control, both structural response and radiated sound power are identical to those for a simply-supported panel without any actuators added to the structure. The resonance peak observed at 23.2 Hz corresponds to the natural frequency of the inertial actuator. The

first resonance of the structure, mode (1,1), occurs at 71.7 Hz. Both spectra were plotted over the range of feedback gain values for which the system remained stable. High levels of feedback gain cause enhancement in the resonance of the actuator.

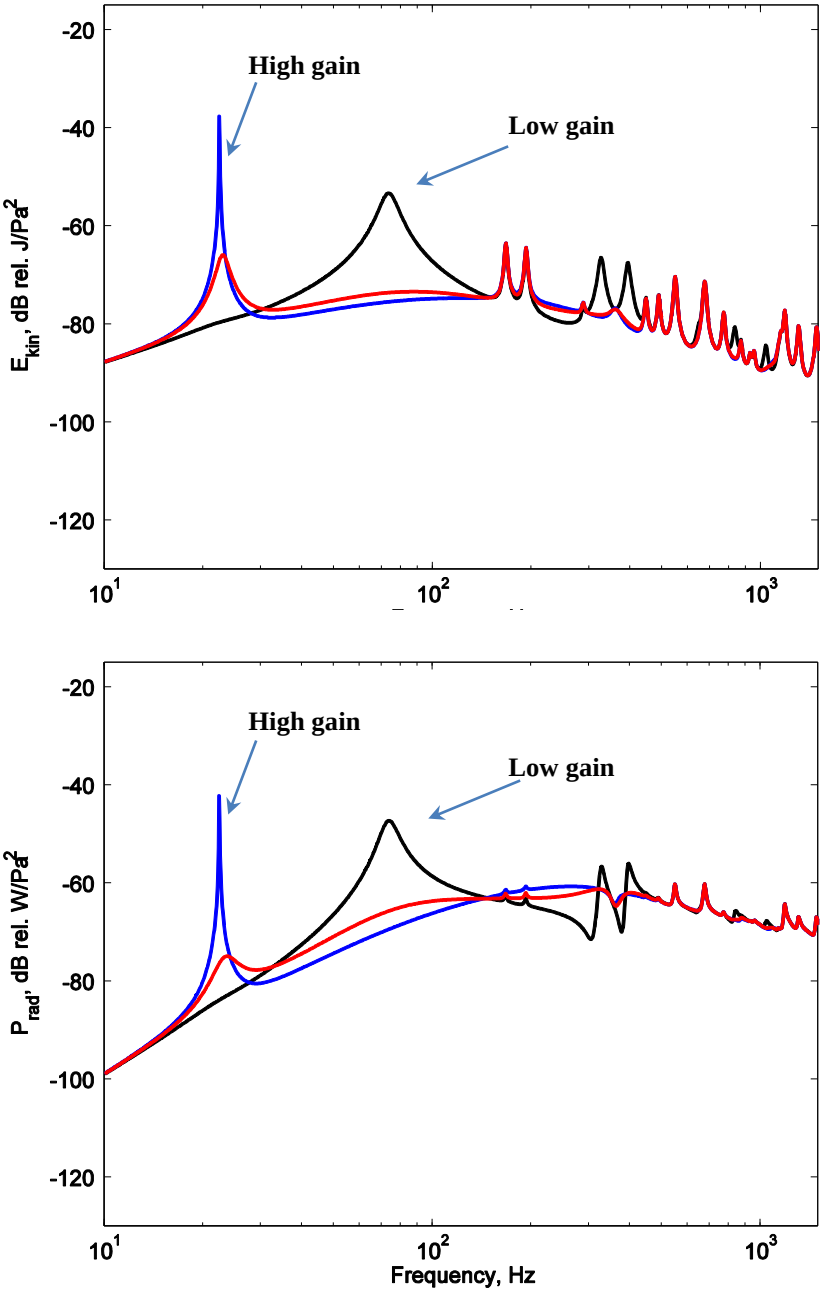

Figure 4.10 – Overall structural response and total radiated sound power of the aluminium panel, when a single proof-mass actuator is located at the centre of the panel, for increasing feedback gain. The overall structural response and total radiated sound power are shown in black for no control, red for optimal feedback gain and blue for high feedback gain.

4.2.2 Stability and Gain Analysis

When an inertial actuator is implemented on the structure, the control system is no longer unconditionally stable. The internal dynamics of the actuator, such as the resonance and phase shift associated with the moving mass, impose a limit on the stability of the system. The plant response, as defined in Chapter 1, now includes the dynamic effects of the actuator and is formulated as

$$\mathbf{G}_{ca} = \mathbf{Y}_{cc}\mathbf{Z}_{ca}(\mathbf{I} + \mathbf{Y}_{cc}\mathbf{Z}_{cc})^{-1}, \tag{4.49}$$

where $\mathbf{Y}_{cc}$ is the point mobility at the location of the actuator and is calculated from Equation 4.23. The Bode and Nyquist plots of the plant can be viewed in Figure 4.11 and Figure 4.12, respectively.

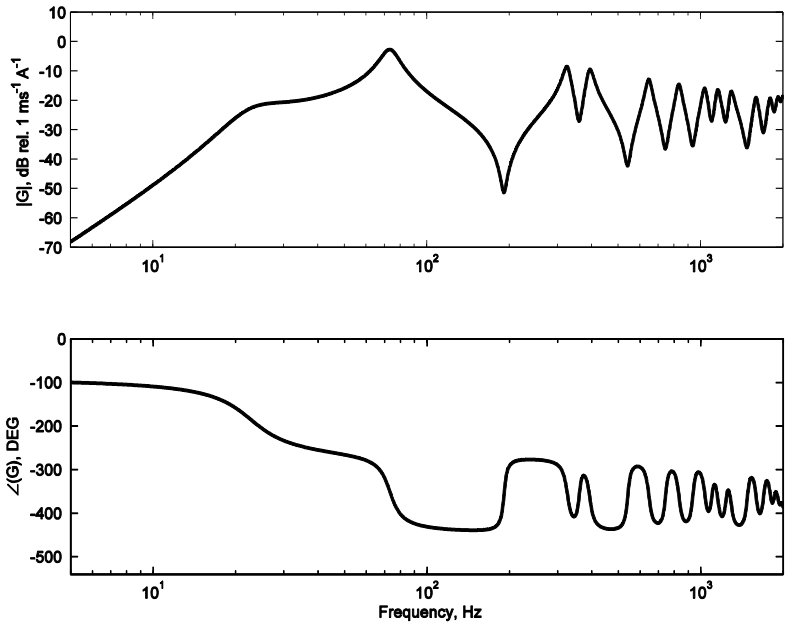

Figure 4.11 – Bode plot of the amplitude (top) and phase (bottom) of the plant response of the feedback control system with an inertial actuator.

In the above figure, the damped resonance observed at 23.2 Hz is the natural frequency of the actuator which introduces a 180° phase shift into the plant response. This can be seen as the change in the phase from -90° to -270° that occurs at frequencies below the first panel resonance. At higher frequencies, the phase response is related to the structural resonances of the panel, with each resonance introducing a 180° phase shift between -270° and -450° is due to unwrapping of the phase response.

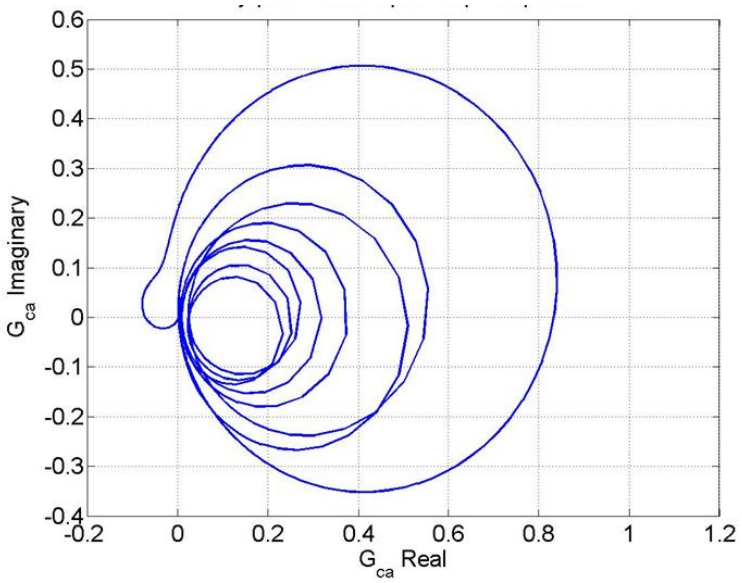

Figure 4.12 – Nyquist plot of the plant response.

Figure 4.12 shows the Nyquist plot of the plant response. The response in the two left-hand quadrants of the Nyquist plot is due to the contribution of the natural frequency of the inertial actuator. In the right-hand side of the Nyquist plot, the response is caused by the resonances of the aluminium panel. Consequently, the system is only stable for gain levels at which the graph does not cross the point of instability, -1. The boundary of the stability region can be found through the calculation of the maximum gain which corresponds to the point $(-g_c,0)$, where the Nyquist plot intersects the negative-real axis. The maximum feedback gain was found to be 14 for these simulations, the feedback gain that provides a 6-dB gain margin is half of this value.

The total changes in kinetic energy and radiated sound power level integrated over the control bandwidth, were plotted over increasing gain up to limit of stability and are displayed in Figure 4.13. The optimal feedback gain values for which maximum attenuations in structural response and sound power can be achieved were estimated by finding the minima in the graphs, and were $g_{optimal} = 11$ for minimising the kinetic energy and $g_{optimal} = 7$ for minimising the radiated sound power.

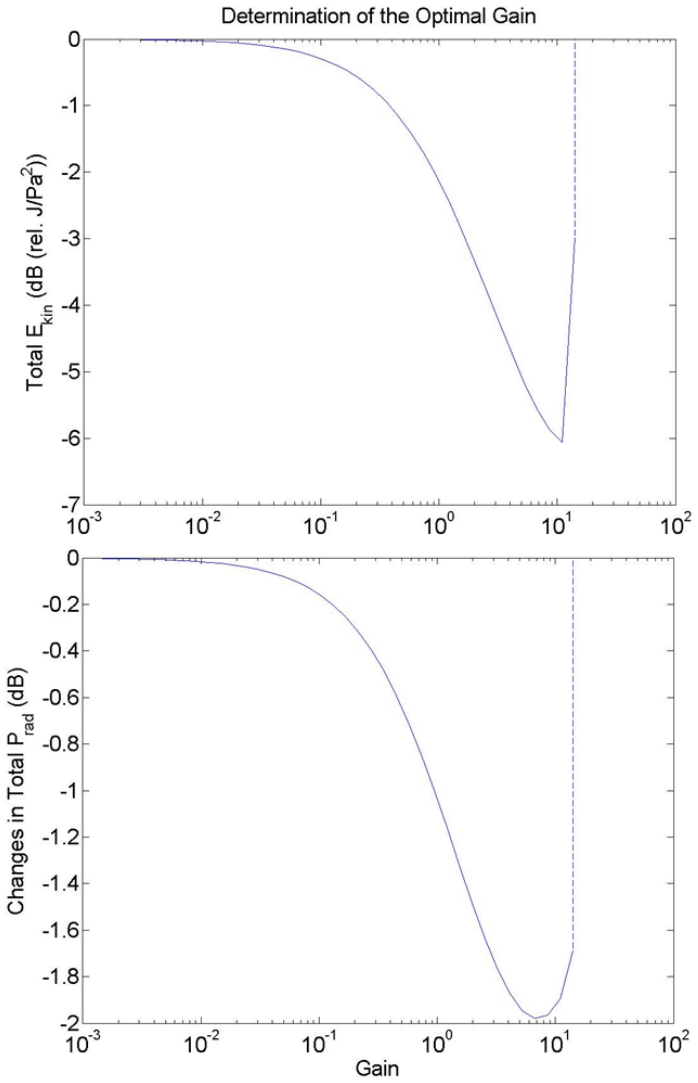

Figure 4.13 – Variations in total kinetic energy (top) and radiated sound power (bottom) plotted over increasing feedback gain up to the 6-dB gain margin when a single actuator with a natural frequency of 23.2 Hz is assumed to be positioned at the centre of the panel. The minimum point in both graphs corresponds to the gain value for which maximum attenuation in structural response and radiated sound power is achieved.

The optimal gain value to minimise the overall structural response in this case is just below the unstable value, making the system very sensitive, but the optimal gain value for minimising the radiated sound power is only about half of this almost unstable value.

4.2.3 Effects of Modifying the Actuator Natural Frequency

As stated in the previous section, the natural frequency of the actuator and the amplitude of the resonance peak have a crucial role in maintaining the stability of the system and

providing efficient active damping. The lower the resonance frequency of the inertial actuator and the further away it is from the first resonance of the structure, the more possible it is to achieve optimal control conditions. One way to decrease the natural frequency of the actuator is to reduce its stiffness, which would be the equivalent of using softer springs in the proof mass suspension system. In practice, in order to decrease the stiffness, the actuator's suspension must be softened and this results in a larger static displacement of the proof mass. This large static displacement means that the proof mass is more liable to hit the end stops of the actuator, which would generate nonlinearities and affect the stability of the control system [110]. Another alternative that would result in the attenuation of the resonance peak amplitude consist in increasing the damping of the actuator [38]. The reduction in the apparent natural frequency of the actuator using an electrical compensator is also discussed in Chapter 6.

In the first step, the stiffness of the actuator, K_a, was reduced by a factor of 4 $\left(K_a = 127.75\, Nm^{-1}\right)$, to lower the actuator resonance frequency to 11.6 Hz, while C_a remained constant, and the kinetic energy and sound power level were calculated over 25 gain levels. The boundaries of the stability region were calculated again using the Nyquist plot. The plant response of the actuator is shown in Figure 4.14, and the Nyquist plot of the plant response is displayed in Figure 4.15. The point of intersection between the Nyquist plot and the real-negative axis is now further from the limit of the stability indicating that a higher feedback gain can be used. The point of intersection of the real-negative axis is -0.016 corresponding to a maximum stable gain of about 60 which is significantly larger than that obtained in the Section 4.2.2.

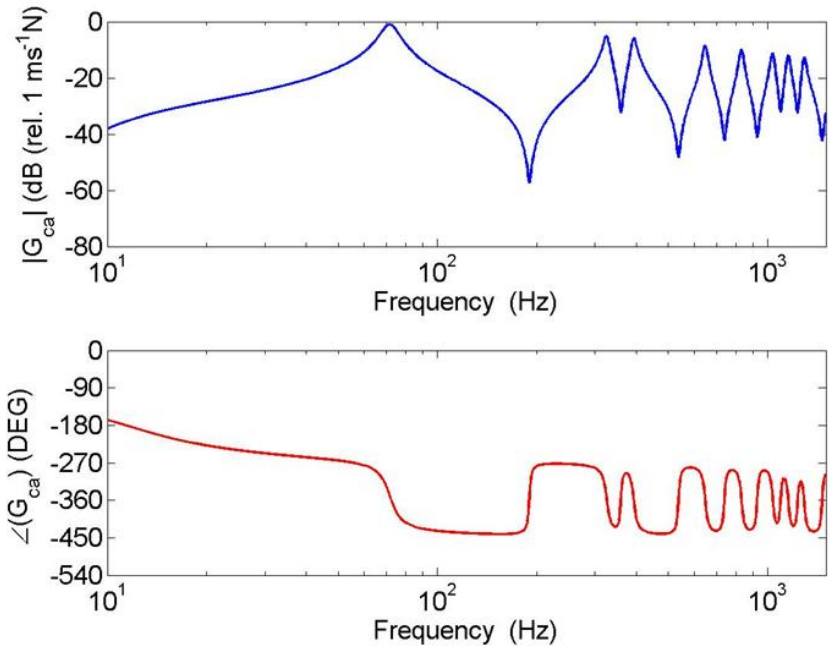

Figure 4.14 – Plant response of the control system when a single actuator with a reduced stiffness is modelled at the centre of the structure.

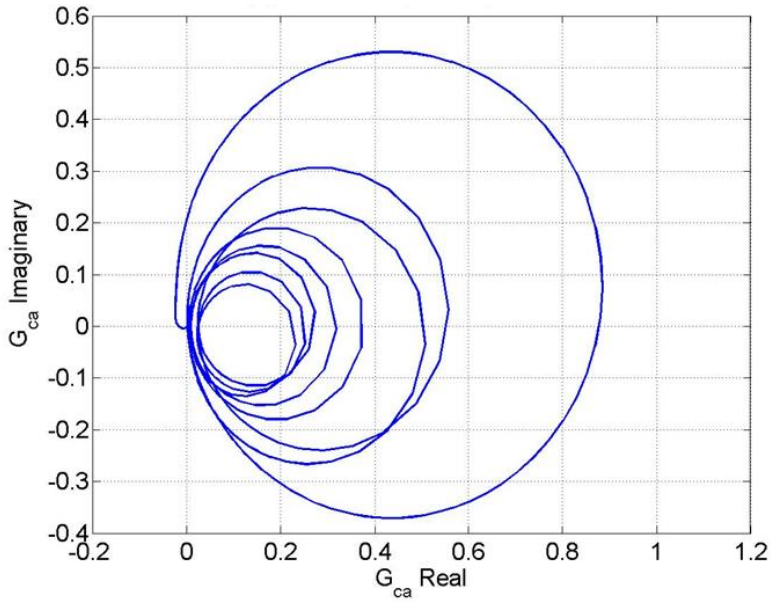

Figure 4.15 – Nyquist plot of the plant response for a feedback gain of unity when the modelled actuator's stiffness is reduced.

The frequency response of the structural response and sound power level of the panel for the modelled actuator with reduced stiffness are shown in Figure 4.16.

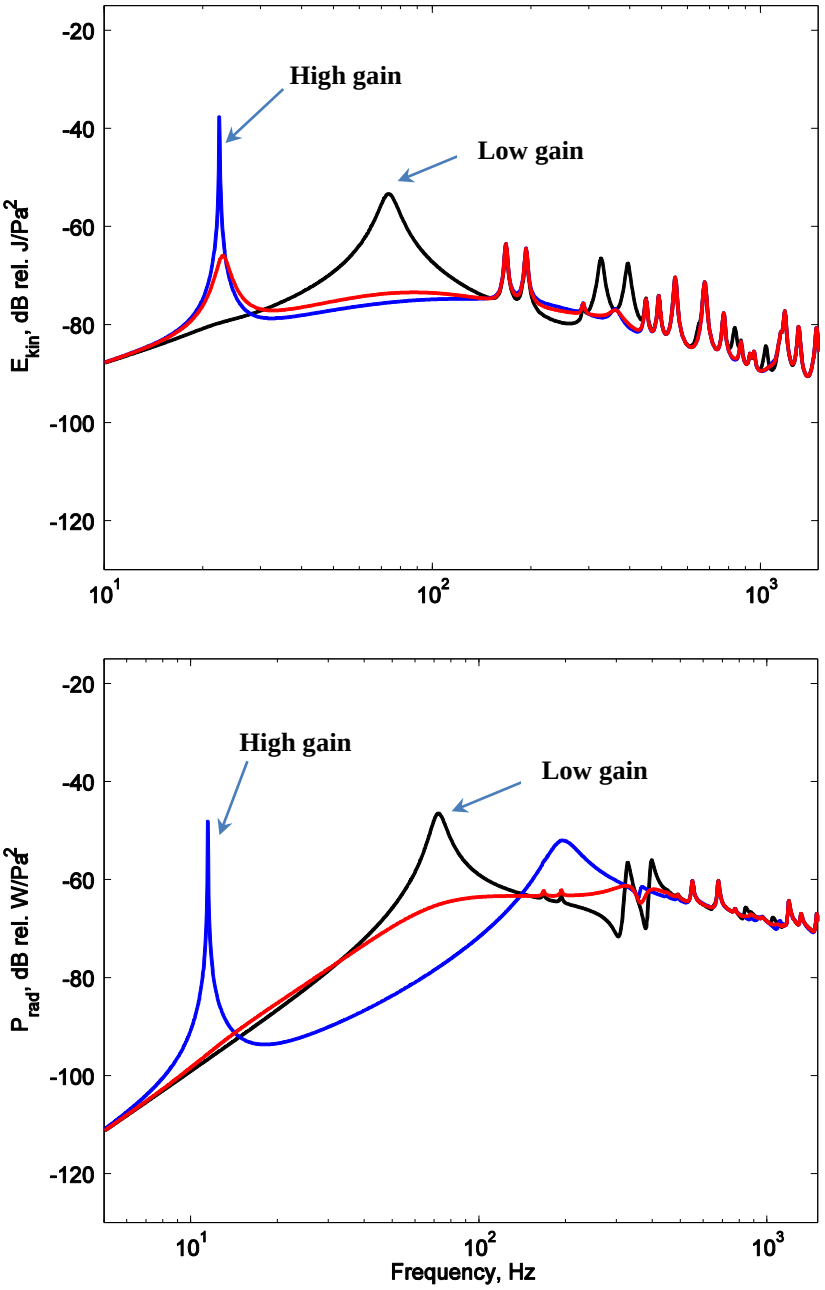

Figure 4.16 – Overall structural response and total radiated sound power of the aluminium panel, when the stiffness of the actuator is reduced, for increasing feedback gain. The overall structural response and total radiated sound power are shown in black for no control, red for optimal feedback gain and blue for high feedback gain.

Figure 4.17 shows the total kinetic energy and sound power level plotted over increasing gain and the resulting optimal gains. With the increase in the stability of the system, the optimal gains for both the kinetic energy and the sound power level are increased to 19.2 and 8.3 respectively, providing slightly higher attenuations of 7 and 2dB respectively. Most importantly, however, both of these optimal values are well

below the maximum stable gain, of about 60, providing a good gain margin for the control system.

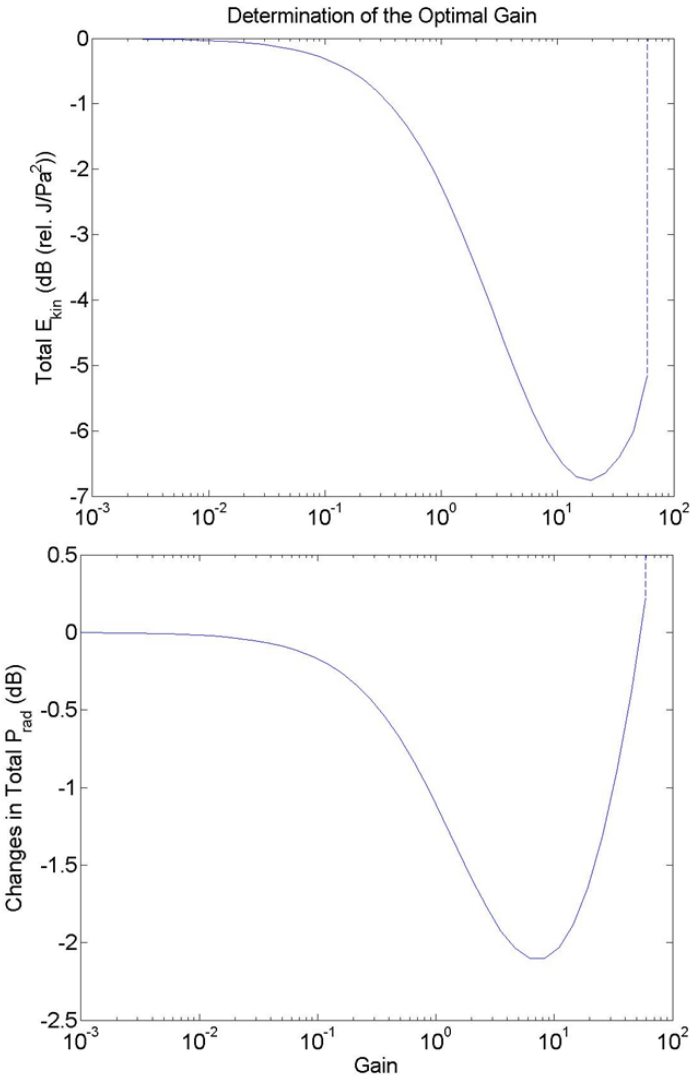

Figure 4.17 – Variations in the total kinetic energy (top) and the total radiated sound power (bottom) plotted for increasing feedback gain up to the 6-dB gain margin, when a single actuator with a natural frequency of 11.6 Hz is assumed to be positioned at the centre of the panel. The minimum point in both graphs corresponds to the gain value for which maximum attenuation in structural response and radiated sound power is achieved.

4.3 Effects of Curvature Increase on the Performance of the Control System using an Inertial Actuator

The effect on control has been investigated of increasing the curvature of the modelled panel in both *x* and *y* directions. The natural frequencies and modes calculated in Chapter 2 over increasing curvature were used in the calculation of the elemental and control mobilities with the modal decomposition of Equation 4.14. An inertial actuator having the parameters shown in Table 4.4 and a natural frequency of 23.2 Hz was assumed to be positioned in the centre of the panel. The structural response and radiated sound power were estimated for broadband disturbances both in the absence and presence of velocity feedback control, over different levels of curvature corresponding to a deflection at the centre of the panel z_c ranging from 0 to 10 mm. It was assumed that a single inertial actuator was positioned at the centre of the panel. For the simulations, the observed and dynamic frequency ranges were set to 2 kHz and 4 kHz respectively. The frequency responses of the structural response and radiated sound power level for no curvature $(z_c = 0mm)$, low curvature $(z_c = 2mm)$, medium curvature $(z_c = 5mm)$ and strong curvature $(z_c = 10mm)$ have been plotted as a function of frequency for increasing feedback gain in Figure 4.18 - Figure 4.21.

In comparison to the sound power level of Figure 4.18 where the panel has no curvature, where the panel is lightly curved, as in Figure 4.19, the natural frequency of the first panel mode is increased, so that the sound power in the absence of control has higher amplitude for the first structural mode.

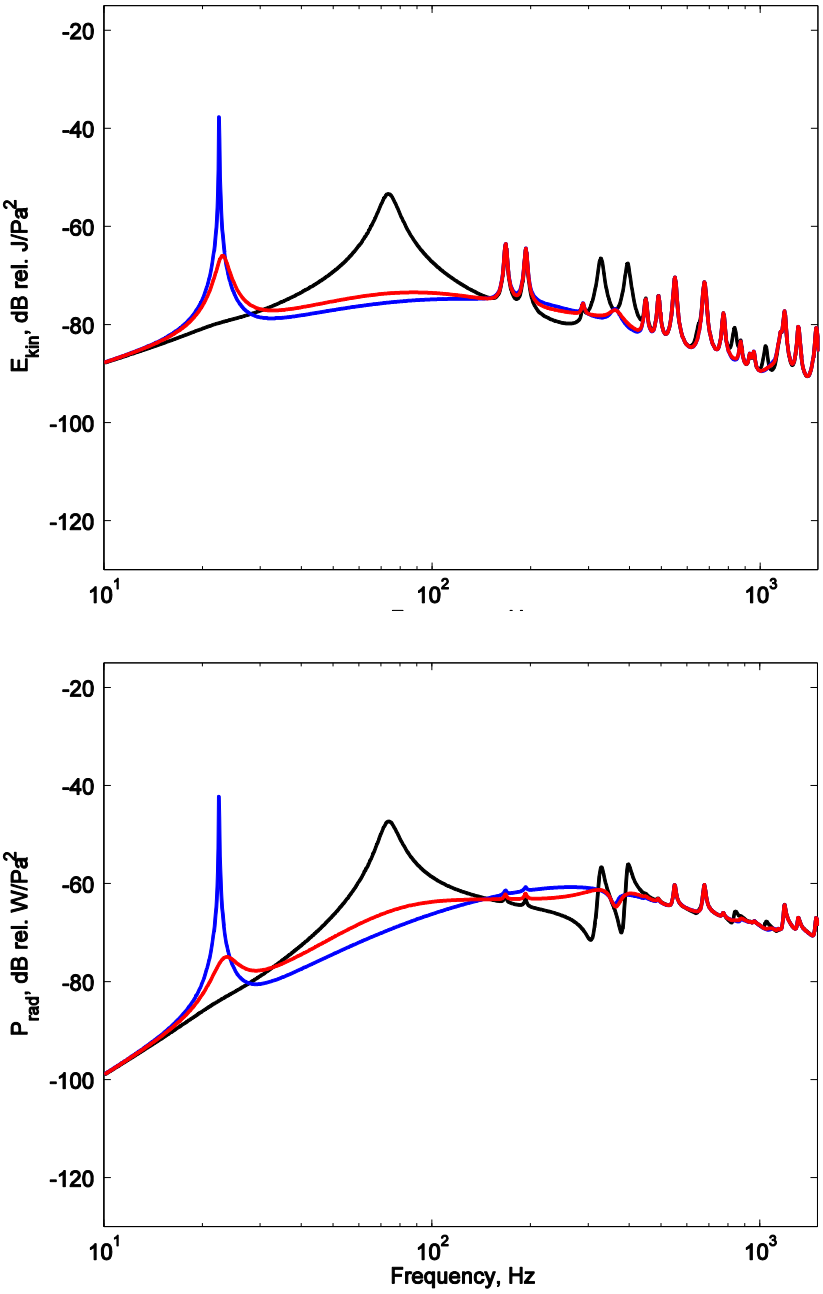

Figure 4.18 – Overall structural response and total radiated sound power of a flat aluminium panel, when a single proof-mass actuator is located at the centre of the panel, for increasing feedback gain. The overall structural response and total radiated sound power are shown in black for no control, red for optimal feedback gain, g_{max} = 14, and blue for high feedback gain.

The maximum value of the feedback gain increases with the level of curvature, from $g_{\max} = 14$ for the flat panel, to $g_{\max} = 65, 174$ and 376 for $z_c = 2, 5, 10\, mm$, since the first panel resonance moves further away from the actuator resonance. The optimal gain values calculated as in the previous section are well below the maximum stable gains for higher levels of curvature. The level of performance achieved by the control system

is, however, reduced by the clustering of the modes for higher levels of curvature, since the single actuator cannot independently control all the modes that cluster about the first panel resonance frequency in this case.

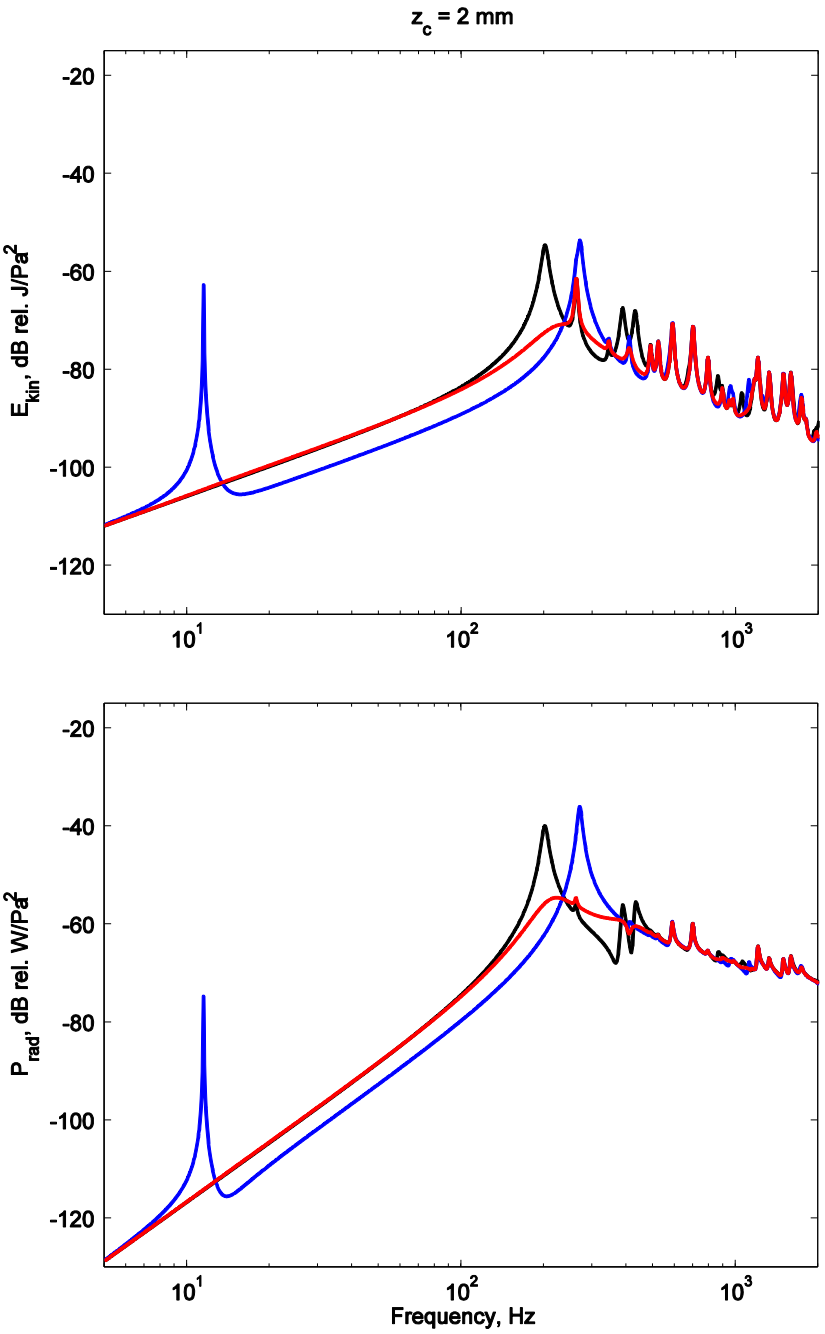

Figure 4.19 – Overall structural response and total radiated sound power of a lightly-curved aluminium panel, when a single proof-mass actuator is located at the centre of the panel, for increasing feedback gain. The overall structural response and total radiated sound power are shown in black for no control, red for optimal feedback gain, g_{max} = 65, and blue for high feedback gain.

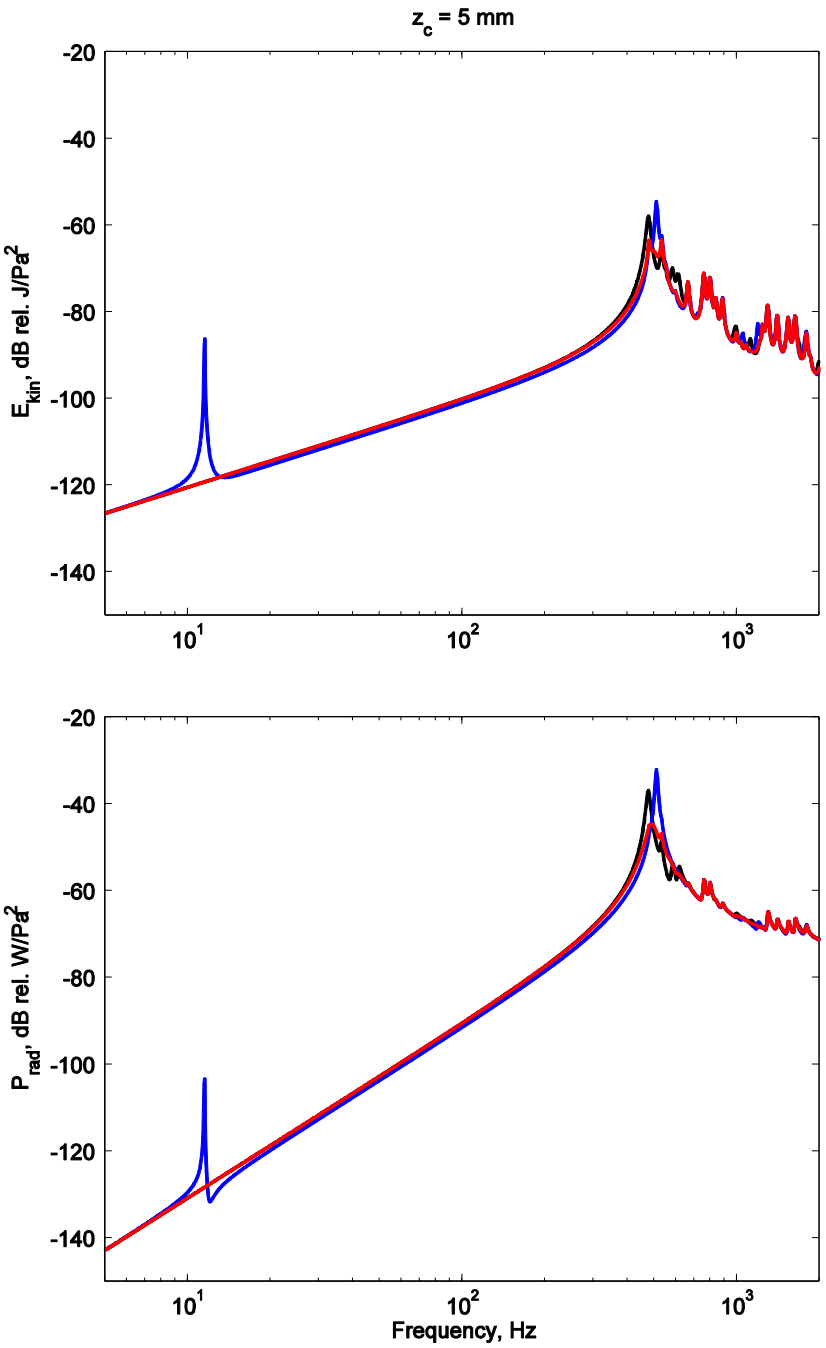

Figure 4.20 – Overall structural response and total radiated sound power of an aluminium panel with medium curvature, when a single proof-mass actuator is located at the centre of the panel, for increasing feedback gain. The overall structural response and total radiated sound power are shown in black for no control, red for optimal feedback gain gain, g_{max} = 174, and blue for high feedback gain.

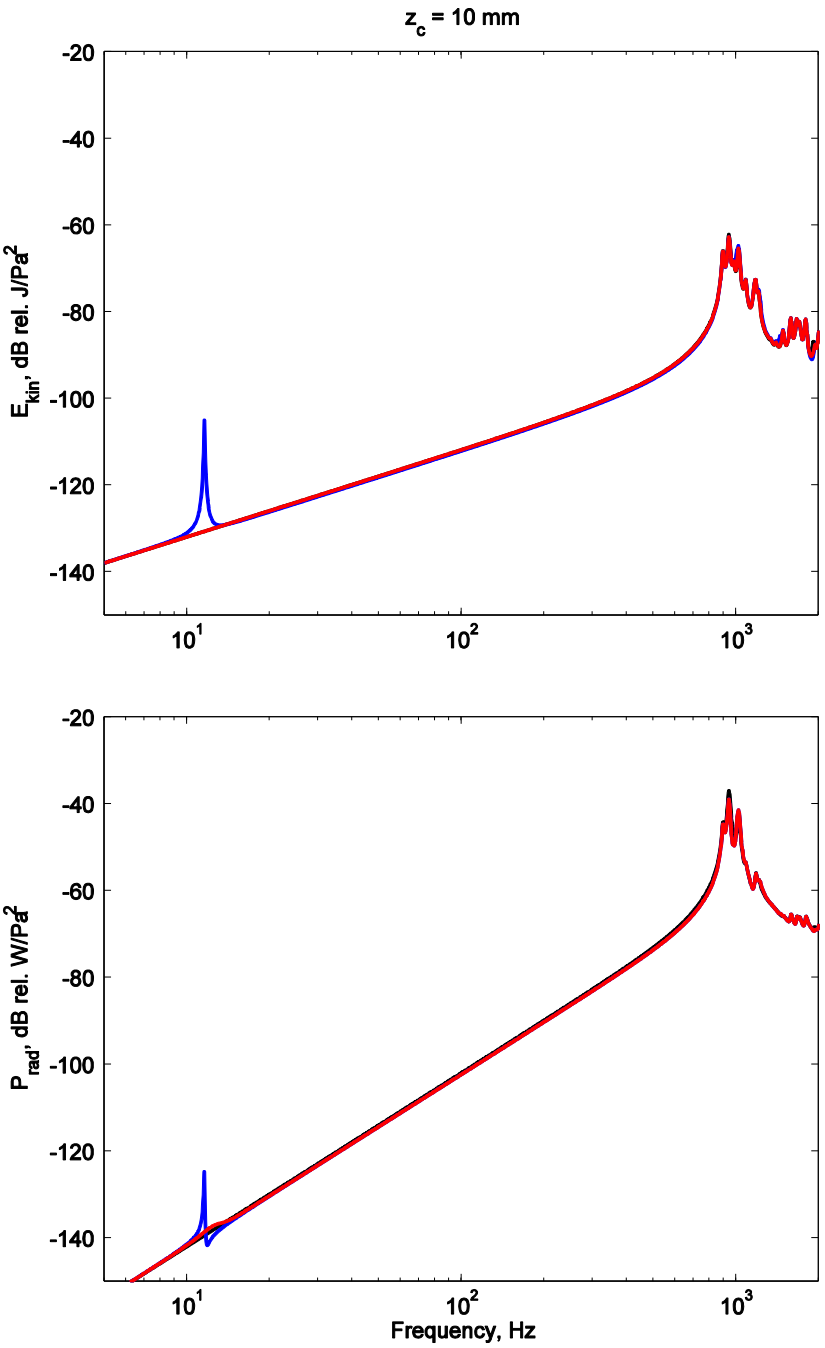

Figure 4.21 – Overall structural response and total radiated sound power of a strongly-curved aluminium panel, when a single proof-mass actuator is located at the centre of the panel, for increasing feedback gain. The overall structural response and total radiated sound power are shown in black for no control, red for optimal feedback gain, g_{max} = 376, and blue for high feedback gain.

The frequency responses of the structural response and the radiated sound power are shown in Figure 4.22 as a function of frequency for the 4 levels of curvature in the same graph, in the absence and presence of control with optimised gain, in order to observe

the effect of curvature on the performance. In all cases, an inertial actuator is assumed to be positioned in the centre of the panel.

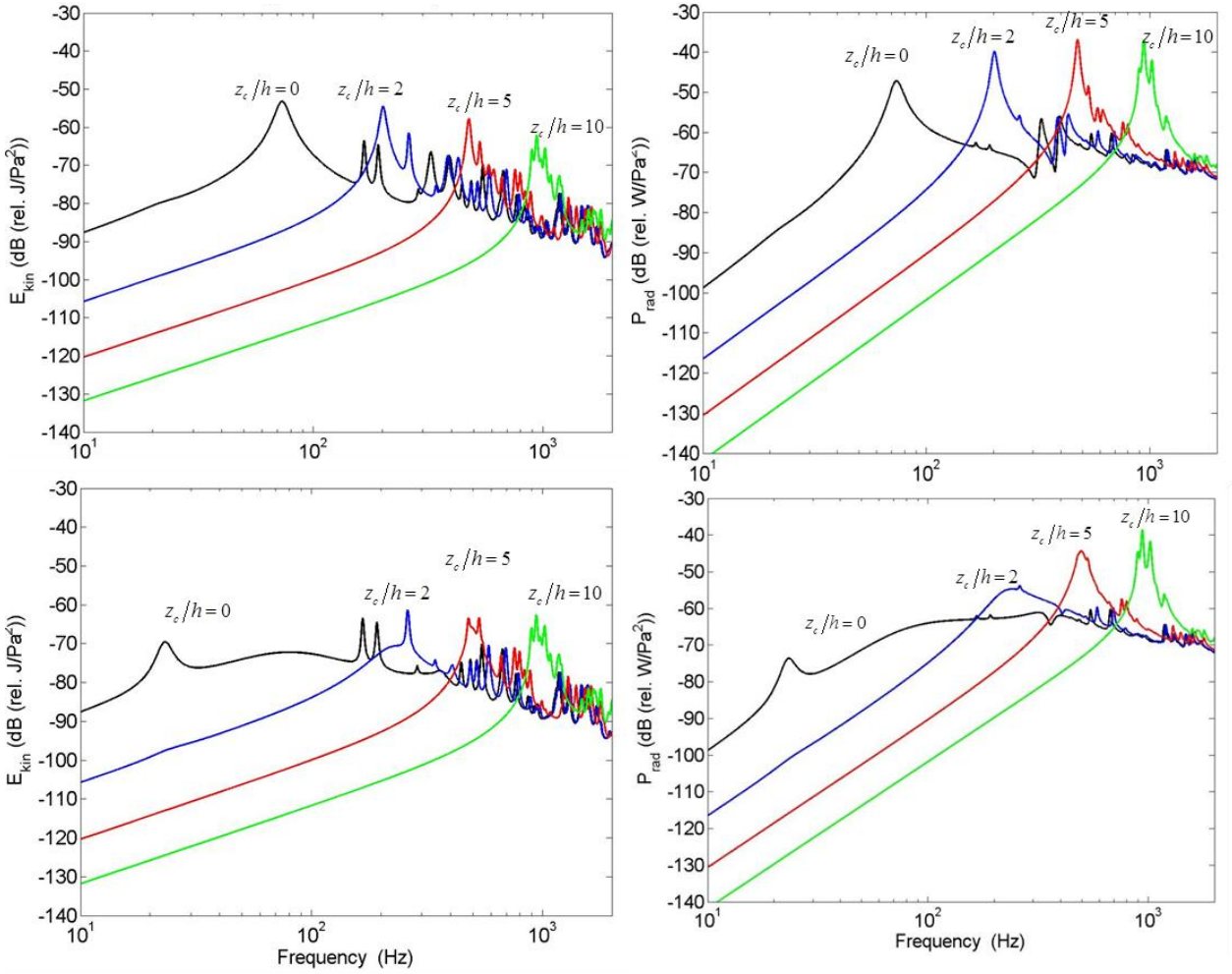

Figure 4.22 – Left: Overall structural response for 5 different curvatures without (top) and with an optimised feedback gain (bottom), Right: Total radiated sound power level for 5 different curvatures plotted without (top) and with optimised feedback gain (bottom). A single inertial actuator is assumed to be positioned at the centre of the panel.

With the increase in the curvature of the panel, the natural frequencies of the system are shifted toward the higher end of the frequency range, such that for the strongly-curved panel $(z_c/h=10)$, the first natural frequency occurs near 1 kHz rather than at 70 Hz for the panel with no curvature, which reiterates the results observed in Chapters 2 and 3. In the absence of control, the amplitudes of the low frequency resonance peaks in the kinetic energy are gradually decreased over the range of curvature corresponding to $0 \le z_c/h \le 5$, because the introduction of curvature increases the stiffness of the panel

and acts as passive control that attenuates the structural response. In the opposite, the sound power level graphs of Figure 4.22 show resonance peaks with increasing amplitudes in the absence of control, due to the increase in radiation efficiency over increasing curvature. When active control with optimal gain is applied to the structure, the increase in curvature limits the performance of the feedback controller, such that in the range of curvature corresponding to $5 \le z_c/h \le 10$, both the kinetic energy and sound power level graphs display no attenuation and closely resemble the curves with no control. Additionally, with the increase in curvature, the fundamental response of the actuator that can be seen near 23 Hz in the structural response and sound power level of the flat panel gradually disappears due to the stiffening of the panel with the increase in curvature. Due to the clustering of modes and the overlap of several modes in regions with higher z_c/h (observed in graphs of Figure 2.9 and Figure 3.10), it was suspected that not only the individual response for the structural modes would be overlapping for high levels of curvature, but also the response of some higher order modes will occur at frequencies lower than those of lower modes.

Based on the assumption of the presence of modal clustering, the individual structural response and sound power level were calculated for each mode. Unlike earlier calculations where a plane wave was assumed to excite the structure, a stochastic model was chosen to create a 'rain on the roof' random excitation. The main reason for choosing the stochastic model was its higher accuracy for simulating acoustic diffuse fields (ADF) encountered in real-life problems [98]. Despite the fact that all the structural modes were excited by the complex pressure excitation defined earlier in the chapter, all the points on the panel were not equally excited and the contribution of the modes that were situated on a nodal line was ignored. The individual responses of these modes under the deterministic model displayed both resonance and anti-resonance peaks that cancelled each other in the overall response.

For the stochastic model, kinetic energy and sound power level are calculated in terms of spectral density and spatial correlation functions. The spectral density for the total kinetic energy and the power spectral density of the sound power level are respectively

$$\mathbf{S}_{\mathbf{EE}}(\omega) = \frac{M_e}{2} \mathrm{tr}\left[\mathbf{G}_{\mathbf{ee}}^{\mathbf{H}} \mathbf{S}_{\mathbf{ff}} \mathbf{G}_{\mathbf{ee}}\right], \tag{4.50}$$

$$\mathbf{S_{PP}}(\omega) = 2\mathrm{tr}\left[(\mathbf{G_{ee}^{H}S_{ff}G_{ee}})\mathbf{R_{rad}}\right], \tag{4.51}$$

where $\mathbf{S_{ff}}$ is the matrix of power and cross-spectral density of the forces exciting each element, M_e is the elemental mass and $\mathbf{G_{ee}}$ is the matrix containing the point and transfer mobility functions for all the elements of the panel. Both matrices have dimensions of $\left[N_e \times N_e\right]$. $\mathbf{G_{ee}}$ can be expressed in terms of the vector of the forces $\mathbf{f_e}$ exerted at the centre of each element and their resulting vector of complex velocities $\dot{\mathbf{w}}_\mathbf{e}$ as

$$\dot{\mathbf{w}}_\mathbf{e} = \mathbf{G_{ee}f_e} \tag{4.52}$$

By substituting the equations for control force and velocity defined earlier in the chapter, $\mathbf{G_{ee}}$ can also be formulated to include the effects of the feedback loop as

$$\mathbf{G_{ee}} = \mathbf{Y_{ee}} - \mathbf{Y_{ec}}\left(\mathbf{Z_{cc}} + \mathbf{Z_{ca}H}\right)\left[\mathbf{I} + \mathbf{Y_{cc}}\left(\mathbf{Z_{cc}} + \mathbf{Z_{ca}H}\right)\right]^{-1}\mathbf{Y_{ce}} \tag{4.53}$$

The structural response and sound power level of the first 5 modes were plotted both in the absence and presence of control for a modelled panel with a deflection of $z_c = 5h = 5mm$ from the centre of the panel. Figure 4.23 – Comparison displays the frequency response of the structural response when no control is applied to the panel versus when the feedback loop is closed with an optimal gain value of 50. In both graphs, the overall response was plotted in a black thick line over the individual responses. Because the panel is bowed differently in the *x* and *y* direction $\left(R_x \neq R_y\right)$, it was suspected that not only the individual response for the structural modes would be overlapping for high levels of curvature, but the responses of some higher order modes would occur at lower frequencies than some of the lower order modes.

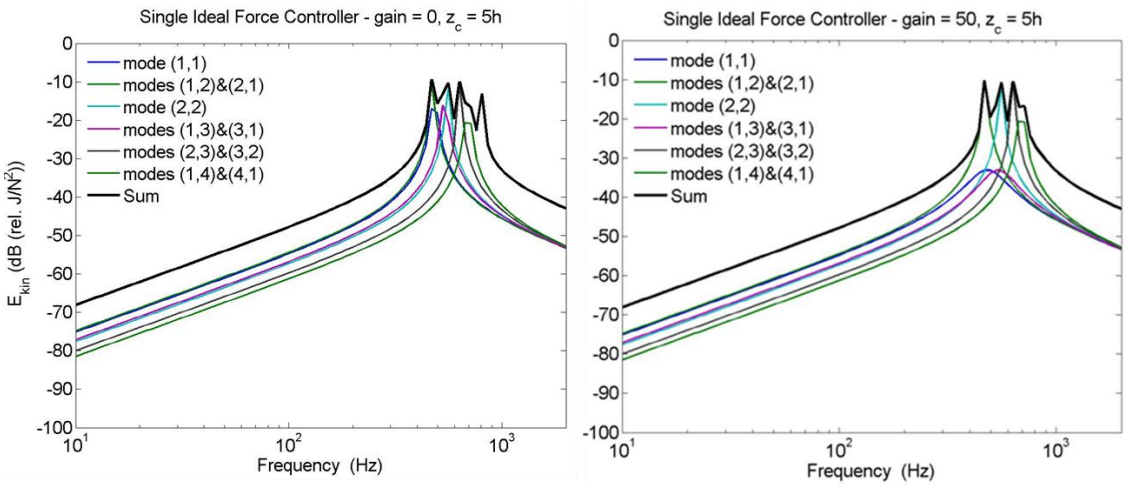

Figure 4.23 – Comparison of the individual structural response of the 5 first modes for a panel with medium curvature ($z_c = 5h$ = 5 mm). Left: No control, Right: Feedback control with an optimal gain of 50. The overall response is indicated with a black solid line.

The optimal gain causes an attenuation of 15 dB in Mode (1,1) and 20 dB in Mode (1,3) while Modes (1,2), (2,1) and (2,2) remain unaffected. The comparison of the overall response of the 5 modes with and without control show very little difference and no attenuation is observed. The bandwidth of the overall response is reduced when control is applied to the structure, because of the attenuation in 2 out of the 5 modes. The radiated sound power level of the same modes can be viewed in Figure 4.24. The overall response again remains unaffected due to the contribution of 3 out of 5 modes which are not controlled and efficiently radiate sound power.

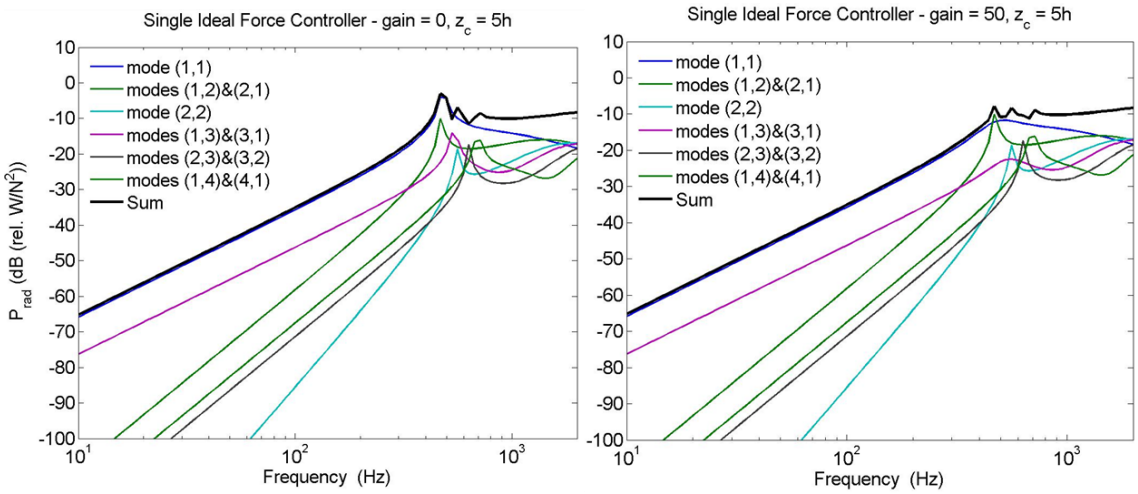

Figure 4.24 – Comparison of the individual radiated sound power of the 5 first modes for a panel with medium curvature ($z_c = 5h$ = 5 mm). Left: No control, Right: Feedback control with an optimal gain of 50. The overall radiated sound power is indicated with a black solid line.

The simulation was repeated for $z_c = 10h$ and the individual frequency responses for structural response and radiated sound power are displayed in Figure 4.25 and Figure 4.26. The increase in the curvature of the panel causes the modes to be more closely grouped. As a result, the individual responses in these Figures overlap causing an overall response with a single sharp peak. This overlap causes the overall control to be less efficient than for lower amount of curvature. The overall kinetic energy and sound power level remain without attenuation, even though the response and radiation of modes (1,1) and (1,3) are reduced.

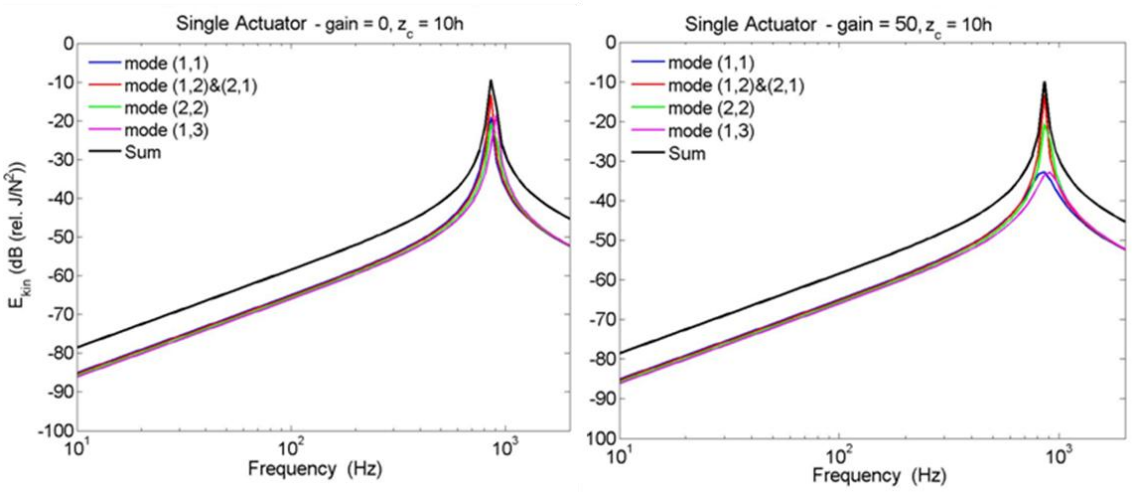

Figure 4.25 – Comparison of the individual structural response of the 5 first modes for a panel with high curvature (z_c = 10h = 10 mm). Left: No control, Right: Feedback control with an optimal gain of 50. The overall response is indicated with a black solid line.

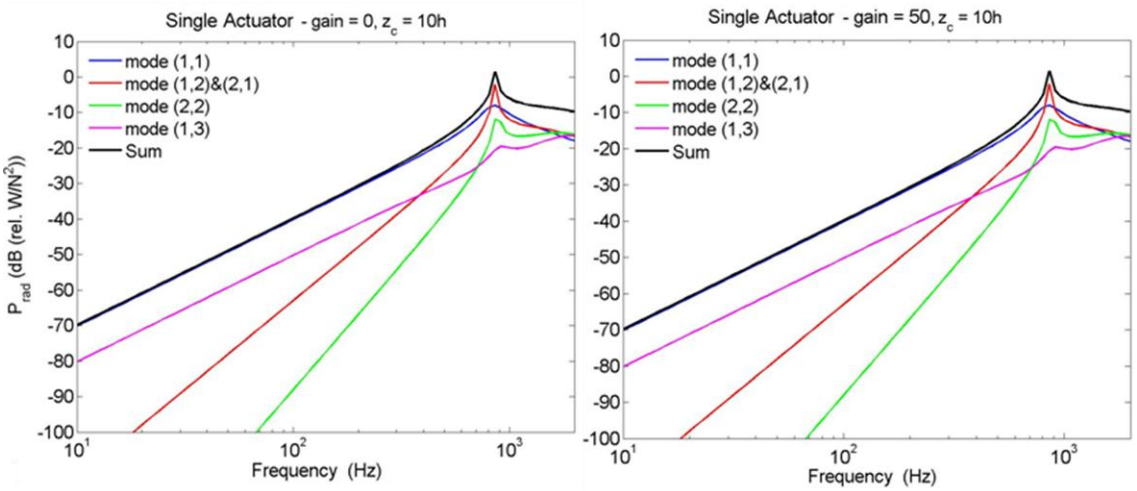

Figure 4.26 – Comparison of the individual radiated sound power of the 5 first modes for a panel with high curvature (z_c = 10h = 10 mm). Left: No control, Right: Feedback control with an optimal gain of 50. The overall radiated sound power is indicated with a black solid line.

In the simulations conducted for medium and strong curvatures corresponding to $z_c = 5h$ and $z_c = 10h$ respectively, the actuator was assumed to be positioned in the centre of the panel. Even though this position was concluded to be the most efficient at controlling the structural response and radiation of flat panels, due the mode clustering caused by the increasing curvature of the panel, the actuator hardly provides overall attenuation when placed at the centre. For this reason, the effect of the actuator positioning was investigated through simulations of feedback control at different positions on the panel in order to assess whether more efficient control and greater attenuation could be achieved at a distance away from the centre of the panel, on all modes.

The position of the actuator was changed along the diagonal of the panel, moving away from the centre at increments of 20% of the diagonal length. With each increment, the individual response and radiated sound power level of more modes were attenuated. However, after a distance of 10 cm from the centre of panel, the response and sound power level of the first structural modes started increasing again. For the 10 first structural modes of the panel, the actuator achieved the best overall attenuation when it was placed 10 – 11 cm from the centre, along the diagonal. The attenuation levels for both kinetic energy and sound power level have been listed in Table 4.5 for this actuator position when $z_c = 5mm$. The attenuation levels for Modes (1,1), (1,4) and (4,1) are much lower than other modes as the actuator has less effect on these modes away from

the centre of the panel. On the other hand, other modes, such as Mode (2,2), reveal the highest level of attenuation, indicating that the actuator is positioned on the resonance peak.

Table 4.5 – Attenuation levels in kinetic energy (KE) and radiated sound power (P_{rad}) for individual structural modes when the feedback loop has an optimal gain value and the deflection at the centre of the panel is 5 mm.

Mode Number	Attenuation in KE, dB	Attenuation in total P_{rad}, dB
(1,1)	4	1.8
(1,2) & (2,1)	10	5
(2,2)	18	9
(1,3) & (3,1)	14	7
(2,3) & (3,2)	17	8
(1,4) & (4,1)	4	2

Figure 4.27 and Figure 4.28 display respectively the frequency responses of the structural response and radiated sound power of these first 10 modes, when the actuator is placed 11 cm away from the centre of the panel. This distance was chosen in order to control even modes also. The maximum overall attenuations under these conditions were 7 dB for the kinetic energy and 3 dB for the sound power level.

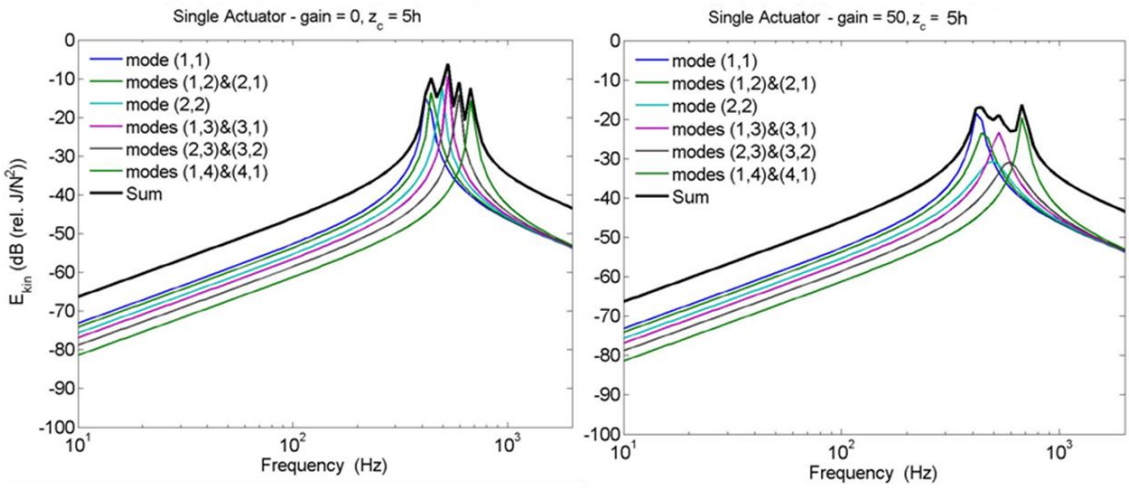

Figure 4.27 – Individual structural responses of the first 10 modes when the actuator is placed 11 cm away from the centre of the panel (zc = 5 mm), without control (top) and with a control gain of 50 (bottom). The overall response is indicated with a black solid line.

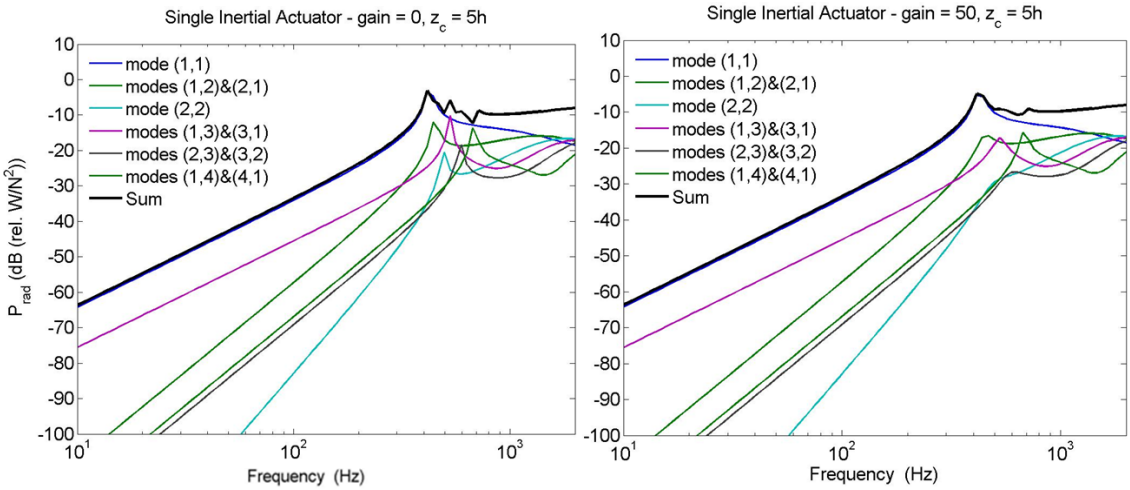

Figure 4.28 – Individual radiated sound power of the first 10 modes when the actuator is placed 11 cm away from the centre of the panel (zc = 5 mm), without control (top) and with a control gain of 50 (bottom). The overall radiate sound power is indicated with a black solid line.

In order to get a better understanding of the structural response and radiated sound power level for higher levels of curvature, the kinetic energy and sound power level were calculated over increasing gain for each of the 11 levels of curvature in the range $0 \leq z_c / h \leq 10$. The limit of the system stability and the maximum attenuations for optimal gain were estimated for each case and displayed in Figure 4.29.

The increase in the curvature of the panel results in a more stable system as shown by the increase in the maximum gain for which the system remains stable. The level of attenuation in the kinetic energy increases slightly, by 0.3dB, from no curvature to $\frac{z_c}{h} = 1$, but then decreases due to modal clustering. A significant increase can be seen in the attenuation of the sound power level, from about 2 dB to 4 dB, as the curvature increases from 0 to $\frac{z_c}{h} = 2$. However, beyond $\frac{z_c}{h} = 5$, the spacing between the modes is too small to allow them to be controlled efficiently. Therefore, a trade-off can be observed between the stability of the system and the increase in curvature. The increased curvature provides an increase in the limit of stability and the maximum stable feedback gain; however, further increases in curvature then result in an increase in the modal density of the panel, which has a detrimental effect on the overall control performance.

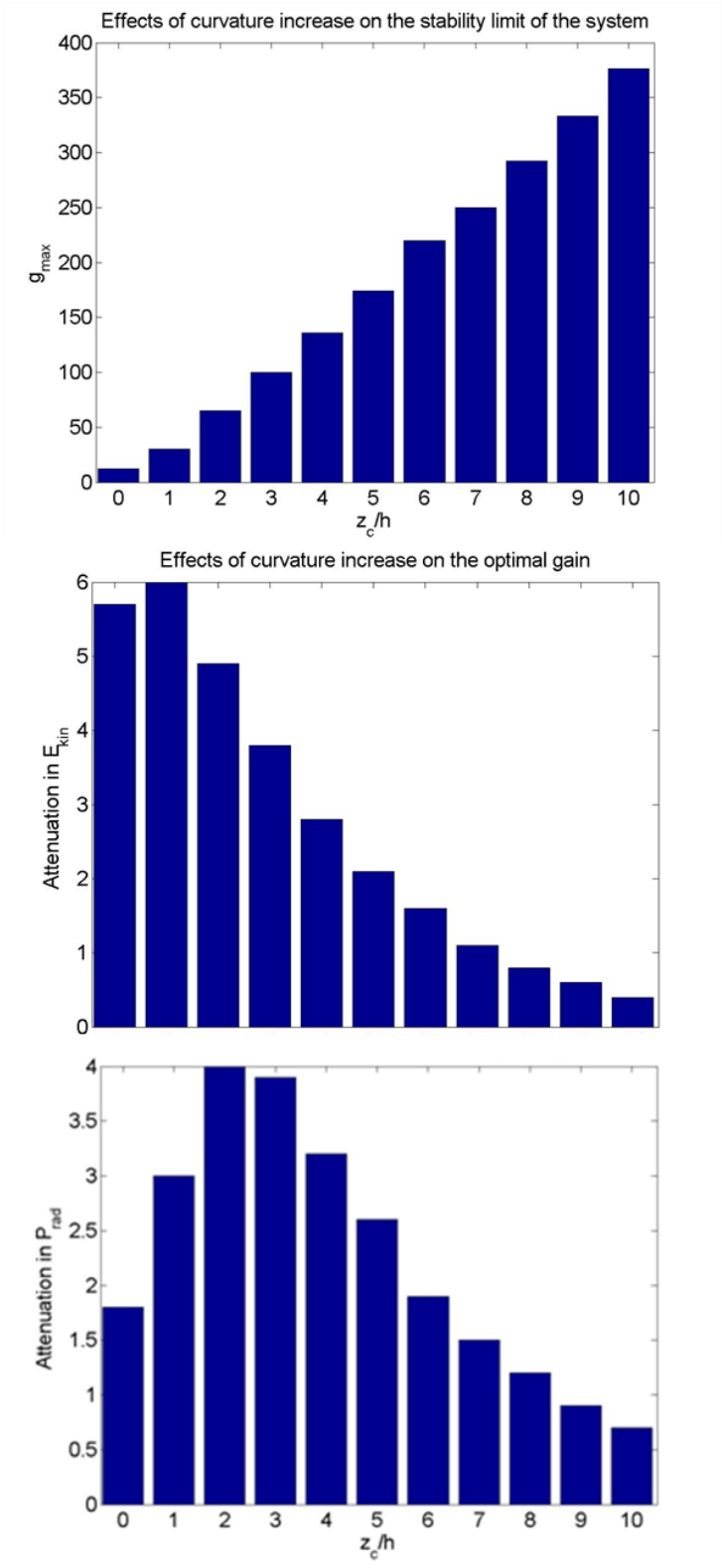

Figure 4.29 – (Top) Effect of curvature increase on the maximum gain and on the optimal gain for maximum attenuations in kinetic energy (Middle) and radiated sound power (Bottom).

4.4 Summary

The aim of this chapter was to investigate the main aspects of active vibration control using velocity feedback control on flat and curved aluminium panels. The elemental approach was used to formulate the dynamic behaviour and sound radiation of the excited structure.

Ideal feedback controllers were initially used to study the effects of the number of controllers and their locations on the panel. The effects of different negative feedback gains were also observed on the kinetic energy and radiated sound power level spectra. The estimation of the optimal gain and determination of maximum attenuation for different numbers of actuators lead to the conclusion that the use of a single controller placed at or near to centre of the plate provided good control and seemed to be the best solution for practical active control designs with space and budget limitations.

The next part of the investigation involved the use of an inertial actuator in the centre of the panel. In this case, in addition to the structural response and radiated sound power of the panel, other characteristics such as the modal contribution of the actuator and the spill-over effect were studied. The stability analysis of the system, using Nyquist plots of the open-loop system response, allowed the calculation of the boundaries for the stability region. It was seen how changes in the properties of the actuator, such as decrease in stiffness and natural frequency, directly influenced the efficiency of active control and the stability of the system.

The third and final part of the study concentrated on the application of active control to curved panels. Initially, a small curvature stiffened the panel and this attenuated the structural response and radiated sound power of some of the modes. However, larger curvature of the panel resulted in a clustering of modes and the inability of the controller to attenuate the overall response and sound power level.

5. Vibration Analysis of a Car Roof Panel and Decentralised Control

In this chapter, a feasibility study is presented of the practical implementation of velocity feedback control of a car roof panel. In a car, the roof panel is one of the components responsible for structure-borne sound radiation to the passenger compartment. The use of active vibration control techniques on this structure could help in reducing the low frequency content of interior cabin noise by attenuating the vibrations propagating through the structure. The aim of this chapter is to gain a better understanding of the dynamic behaviour of a car roof panel and assess the possibility of implementing such a control system. Passive NVH techniques such as damping treatments cannot reduce these low frequency vibrations without adding significant weight to the vehicle, which can lead to an increase in cost and a decrease in fuel efficiency due to the increase in the vehicle weight. Therefore, the successful application of active control technologies presents an appealing solution to the automotive industry.

The analytical and numerical simulations presented and discussed in the previous chapters will be used here to assess the feasibility of active control in this real-life problem. The first part of this chapter provides a description of the experimental procedure used for the modal analysis and the estimation of the structural response of the roof panel. Numerical modelling of the roof panel through finite element models is also discussed when it is subjected to different boundary conditions. The experimental and numerical mode shapes, natural frequencies and frequency response functions (FRFs) are compared and discussed and the experimental data are used for validating the numerical results obtained from the FEMs. Finally, the last part of the chapter deals with the study of the feasibility of implementing a decentralised feedback control system for supressing the vibrations of the roof panel, through offline simulations of feedback control based on measured roof panel responses.

5.1 Vibration Analysis of a Roof Panel

In this section, the experimental and finite element methods used to identify the structural modes of the roof panel are first discussed. The results from the two methods are then compared.

5.1.1 Experimental Modal Analysis

Experimental Modal Analysis (EMA) was performed on the roof panel, when the structure was clamped along the two edges corresponding to the windshield and the rear window side and left free along the two other edges. Clamping of the two edges was achieved by fixing them to blocks of wood of the same length which were fixed to a large plywood sheet.

The surface of the panel was divided into a grid of 35 points (7 rows and 5 columns) in order to measure the response at different points on the surface and to be able to obtain the mode shapes and the overall structural response. The source of excitation was continuous random noise which was used to provide a force with an LDS type V201 electro-dynamic shaker. The shaker was connected to the roof panel with a stinger and positioned near one of the corners of the panel in order to excite the majority of the modes. The excitation was detected by a piezoelectric B&K Type 8001 force transducer and the acceleration of the panel was measured via 5 low-mass piezoelectric PCB Type A352C67 accelerometers, one row of the grid at a time. The force transducer and accelerometers were connected to a 16–channel sensor signal conditioner set to a gain of 1. A picture of the rig and the experimental arrangement is displayed in Figure 5.1. A diagram of the experimental set-up is shown in Figure 5.2. The list of equipment used in this chapter has been provided in Appendix E.

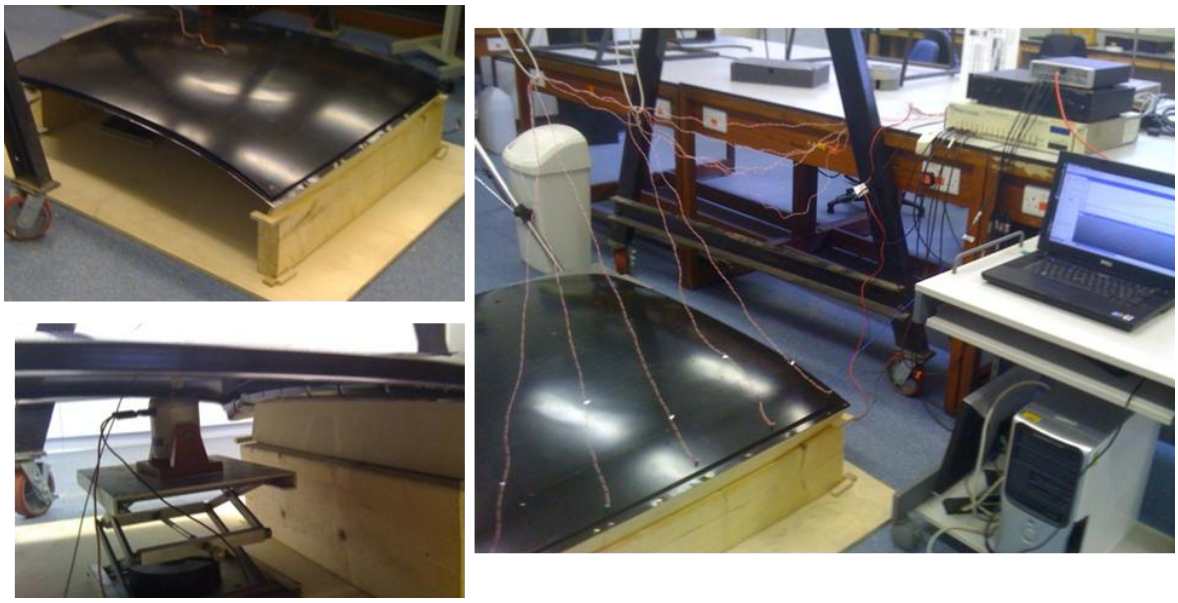

Figure 5.1 – Picture of the rig and the arrangement of accelerometers and shaker.

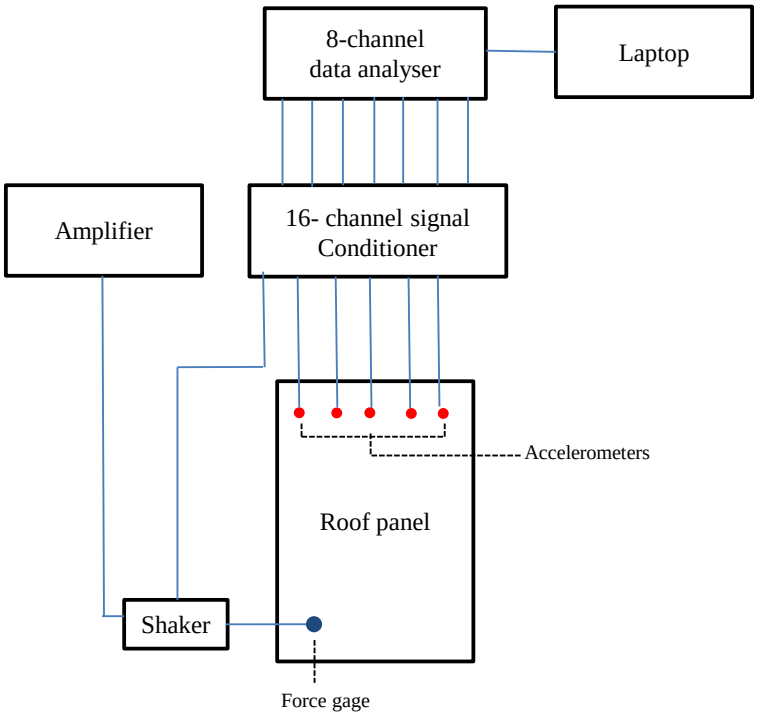

Figure 5.2 – Block diagram of the experimental set-up.

The FRF of the acceleration per unit input excitation force was measured at all the points of the defined grid. This was done with five accelerometers which covered one row of the grid at a time. The measured FRFs were acquired using an LMS Scadas Mobile 8-channel data analyser up to 512 Hz. The reason for choosing this frequency range is because in a car, the structure-borne noise frequency content rolls off rapidly

beyond this range [1]. A Hanning window was applied to the data with 50% overlap and 10 averages per acquisition. The results were exported into MATLAB files for further data analysis.

5.1.2 Modal Analysis through Numerical Modelling

A numerical model of the roof panel based on the properties and dimensions provided in Table 5.1 was created in ANSYS. The properties of the roof panel were based on the 1030 carbon steel commonly used in car bodies.

Table 5.1 – Dimensions and physical properties of the road vehicle roof panel

Parameter	Value	units
Dimensions	$l_x = 0.95$ $l_y = 1.22$	m m
Rise from centre of the panel	$_{zc} = 0.05$	m
Thickness	$h = 2$	mm
Density	$\rho_{plate} = 7800$	kg m^{-3}
Young's Modulus	$E = 2\times10^{11}$	N m^{-2}
Poisson's Ratio	$\nu_{plate} = 0.28$	
Modal Damping Ratio	$\xi_n = 0.0016$	

The triangular SHELL63 elastic shell element used in the FEMs of Chapter 3 was used for generating the mesh of the roof panel. The mesh of the roof panel was first generated with the assumption that it was a trapezoidal section on the surface of a torus, in a similar manner to the FEMs in Chapter 3. The geometry of the mesh was then further modified to reflect the different elevations of the roof panel edges and corners, and to more accurately represent the structure. The frequency range for modal analysis was set to 1500 Hz. The mode shapes of the finite element model and the out-of-plane nodal displacements of the points corresponding to the experimental grid were calculated and exported from ANSYS for further data analysis and comparison with experimental data. A FEM of the roof panel with the points corresponding to the experimental grid has been shown in Figure 5.3.

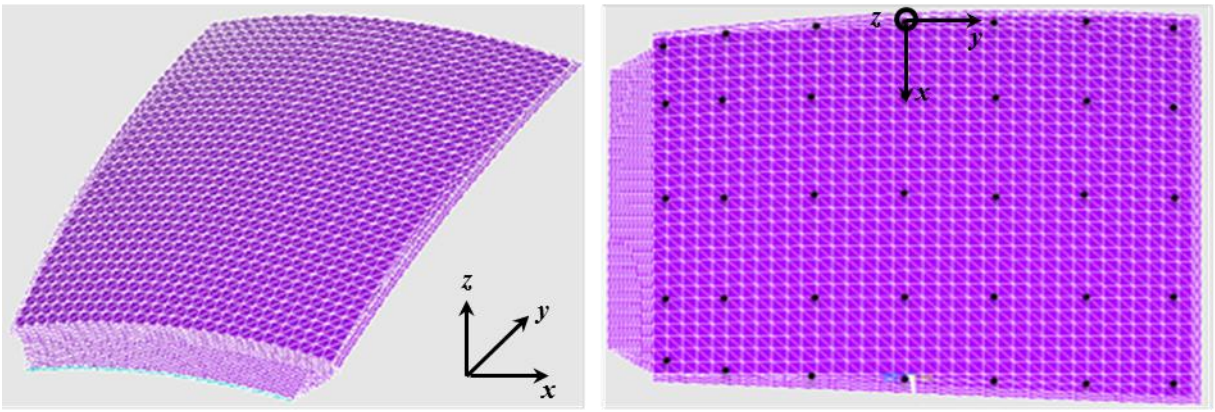

Figure 5.3 – FEM of the road vehicle roof panel. The location of the 35 points corresponding to the experimental grid has been marked with black dots.

Different boundary conditions were applied to the finite element model in order to obtain results that would be comparable with the experimental measurements. In the most accurate configuration, displacement and rotational constraints were applied at the location of the screws, which were used to fix the ends of the roof panel, in the *x* and *z* direction, leaving the panel flexible in the *y* direction to imitate the small lateral motion and rotation about the wooden support. The rest of the nodes of the surfaces in contact with the wooden blocks – where the roof would be mounted on the car body – were subjected to simply supported constraints (i.e. z constrained).

5.1.3 Experimental and Numerical Results Comparison

The natural frequencies measured for the modes of the roof panel were calculated and retrieved from the LMS SCADAS data analyser. The first 25 resonances have been listed in Table 5.2, along with the natural frequencies of the FEM for the boundary conditions above.

Table 5.2 – Natural frequencies of the structural modes of the roof panel obtained from measurements and finite element models.

	Frequency (Hz)	
Mode #	Experimental	FEM - distributed constraint
1	19.8	21.2
2	26.7	26.1
3	65.5	109.7
4	76	113.1
5	96.1	148.3
6	109.4	242.8
7	121.2	244
8	123	269.7
9	125.6	272
10	140	281.6
11	154	281.8
12	157.5	286
13	159.4	286.5
14	172.6	290.6
15	175.9	297.7
16	181.6	299.3

It can be seen from the above table that the FEM and experimental results only seem to accurately match for the two first modes of the system. The natural frequencies calculated in the numerical ANSYS model increase at a faster rate than those of the experimental and several modes appear to be missing. The simulated and experimental mode shapes were plotted for further comparison and the first 9 mode shapes of the roof panel are shown in Figure 5.4.

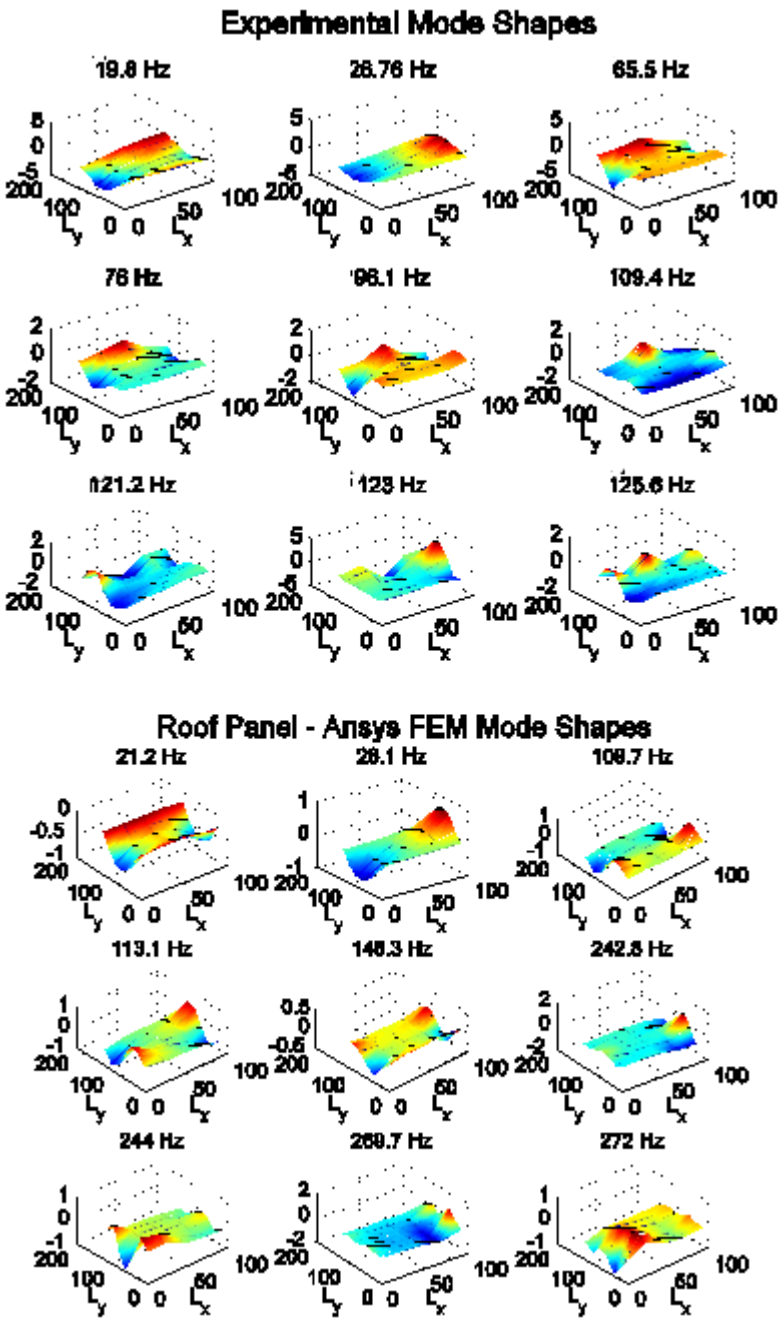

Figure 5.4 – The first 9 mode shapes of the roof panel obtained from measurements (top) and FEM (bottom).

In order to help sort and validate the results obtained from the FEM and modal testing experiments, a one-by-one comparison of the mode orders was performed via MAC analysis (Modal Assurance Criterion) in order to determine the degree of correlation between the two sets of data. The resulting correlation percentages for the first 16 natural frequencies have been shown in Figure 5.5.

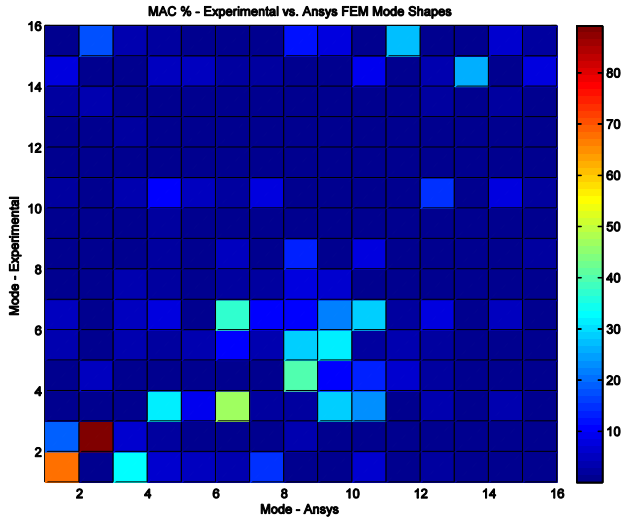

Figure 5.5 - MAC Analysis between experimental modes and numerical modes on the roof panel.

A poor correlation can be observed for the majority of the modes and only the two first mode orders can be confirmed through the MAC analysis. The overall response of the roof panel was calculated from the sum of the squared experimental and numerical velocities over the 35 points on the grid. In the FEM of the roof panel, the disturbance was modelled as a point force. During experimental work, an electrodynamic shaker was used and positioned at the same points as those chosen in the FEM. A comparative plot of the two can be viewed in Figure 5.6.

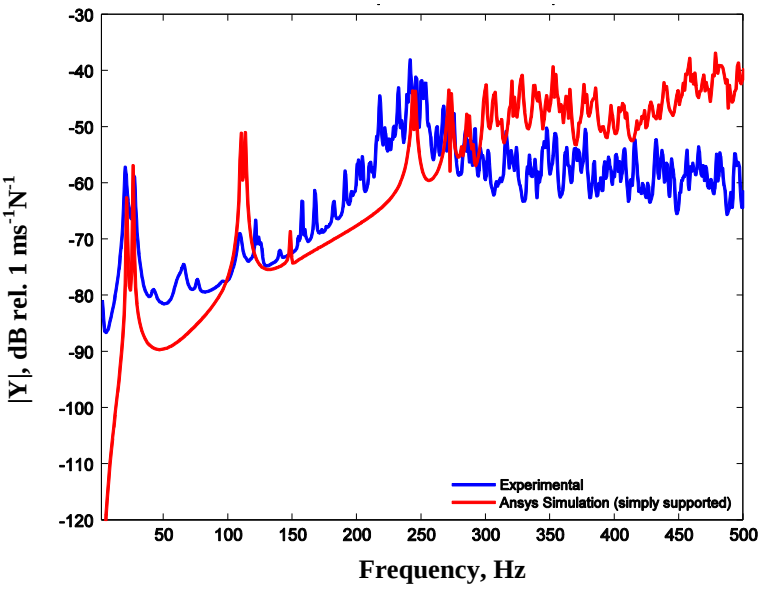

Figure 5.6 – Overall structural response of the roof panel, measured experimentally (blue line) and calculated from the FEM analysis (red line).

Overall, both responses display a similar dynamic range but, limited agreement exists between the modelled and experimental responses. As expected from the mode shape results, the overall response obtained from the finite element model lacks many of the resonances observed in the experimental response in the 0-260 Hz frequency range. Modal clustering is visible in both responses, even though in the case of the FEM, the overlap starts occurring after 260 Hz, as opposed to 120 Hz in the experimental results. Additionally, a closer study of the experimental mode shapes reveals that some of the resonances observed in the lower frequency range are rigid body modes or are associated with the supporting panel.

Due to the complex three-dimensional shape of the roof structure, the creation of a finite element model with accurate structural mode shapes can become complicated. The difference in stiffness due to the welding of parts of the structure together and the introduction of strain in the surface during manufacturing creates further limitations in the accurate representation of the system.

Future work will be based on data obtained from the actual roof as the structure is already available. However, in an industrial development this might not be possible, due to cost restrictions and unavailability of the structure, and therefore, more time and effort might be dedicated to the generation of accurate finite element models.

5.2 Simulation of Feedback Control on the Roof Panel

In this section, simulations of velocity feedback control with an ideal point force are performed using the simulated responses of the road vehicle roof panel. Since the finite element model of the roof panel clearly demonstrates the main features of the measured structural response, this will now be used to investigate the effect of active control. The aim of the simulations was to achieve optimal control of the first four modes of the system using up to 4 control forces.

Figure 5.7 shows the positions of the modelled control forces on the surface of the roof panel, based on the modelled mode shapes at 26 Hz and 108 Hz (second and third

modes). Simulations of feedback control were conducted using 2 and 4 ideal point forces, because it was not possible to model an actuator with a natural frequency low enough to be well separated from the structure's first resonance and avoid compromising the stability of the control system. The gains of each control system were optimised in order to minimise the overall response of the modelled structure.

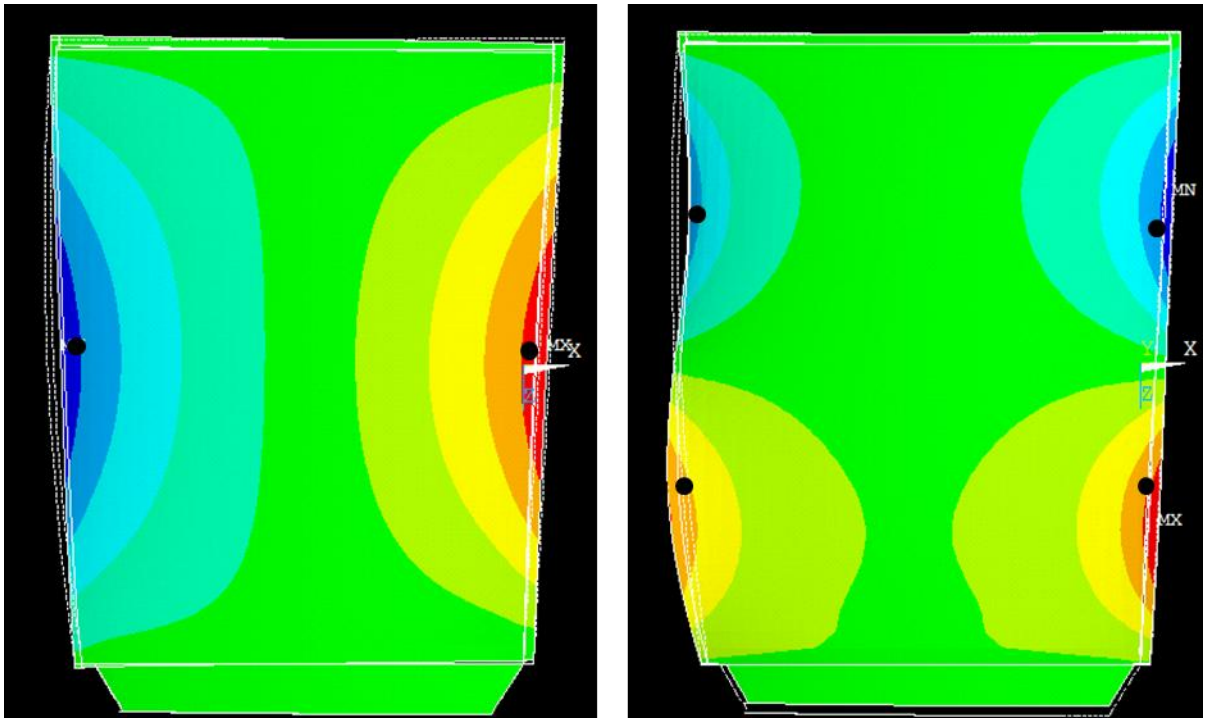

Figure 5.7 – Positions of the Control points on the surface of the roof panel based on the second (26 Hz) and third modes (108 Hz) of the system.

The overall response of the panel before and after active control is shown in Figure 5.8 for two control points and for four control points. The response has been plotted for the 0-500 Hz frequency range.

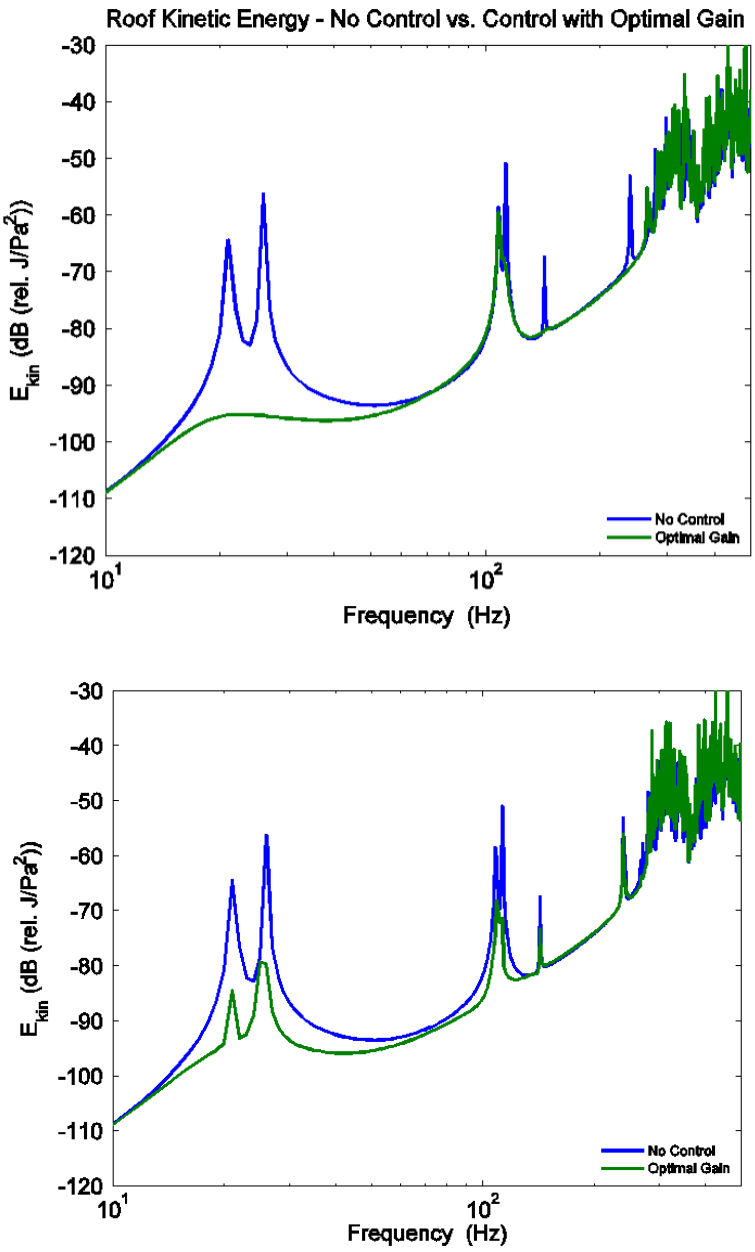

Figure 5.8 – Roof panel response in the absence and presence of active control with optimal gain, when two controllers are assumed to be positioned on the surface of the roof (top), when four controllers are assumed to be positioned on the surface of the roof (bottom).

Both graphs of Figure 5.8 show an attenuation of the response for the first two modes of the system. The 2-controller arrangement displayed in the top graph of Figure 5.8 shows a significant attenuation for the first two resonance peaks of the system and some attenuation for the 4^{th} and 5^{th} modes. Although the addition of 2 more control points, in the bottom graph of Figure 5.8, improves the performance of the feedback control system somewhat between 100 Hz and 150 Hz, the levels of attenuation in the first two mode is far less than for the 2-controller arrangement. This is caused by the positioning

of the 4 controllers, which as can be seen in the left picture of Figure 5.7, cannot couple as efficiently with the 2nd mode of the roof panel as the 2-controller arrangement. In both cases, the cluster of mode observed above 200 Hz remains unaffected by the control system.

The outcome of this simulation suggests that it is not feasible to use a small number of feedback control systems to practically control the vibration of the roof panel. Even though the simulations show that the first modes of the system can be significantly attenuated, the response of the structure in the frequency range of interest, 100Hz – 300Hz, that contributes to the interior noise cannot be controlled. The first two modes of the roof occur at 20 and 26 Hz and are therefore too low in the frequency range to significantly influence the interior noise levels in the passenger compartment. Furthermore, considering how low these natural frequencies are, the design of an inertial actuator with a low enough natural frequency may not be practical within reasonable size and weight constraints, even with the addition of a compensating filter.

5.3 Summary

It can be deduced from the above results that the practical application of velocity feedback control on the roof panel of the road vehicle is not economically feasible. Based on the results obtained from the study of active control of doubly-curved panels in Chapter 4, this conclusion came as no surprise, because the dimensions and curvature level of the roof panel place it in the strongly-curved category of shallow shells (i.e. $\frac{z_c}{h} = 50$). In order to achieve any substantial reduction in the response level in the 100-300 Hz frequency range, it would be necessary to install a large number of sensor-actuator pairs, because of the cluster of local modes present in this region. However, this solution would not be economically efficient. In addition, even though the choice of other types of actuators such as PVDF patches may help the performance of the control system, it would still be difficult to ensure that the control system remains stable under all conditions, for example, for different types of driving or road surfaces.

Despite the lack of success in controlling the response of strongly curved panels such as the vehicle roof, the outcomes of Chapter 4 remain promising for shallow shells having low levels of curvature. The initial introduction of bow in the structure of a flat panel increased the attenuation level of both the structural response and radiated sound power levels, and also the stability of the control system. These results can be promising for the applications of feedback control systems on surfaces with low levels of curvature, such as the fuselage panels in aircraft, which are deformed due to pressurisation. As the fuselage tends to slightly bow during these processes, a small section of the body can then be considered as a doubly-curved panel of small curvature. This application is investigated using an experimental arrangement described in Chapter 6.

6. Velocity Feedback Control on a Pressurised Enclosure

The previous chapters of the thesis have concentrated on the study of the structural behaviour of an isolated panel and its sound radiation into free space. This is not an accurate representation of practical systems however, in which the structure is usually part of an enclosure, for example part of a car body, an airplane fuselage or a submarine hull, and therefore, the sound radiated from the vibrating/excited structure can be influenced by the acoustic properties of the enclosure. An example of such interactions occurs in road vehicles where the coupling between structural vibrations from the engine and interior noise results in a low-frequency structure-borne booming noise. In the case of an aircraft, the structural-acoustic coupling between the vibrations of the flexible panels of the fuselage, caused by engine or wind turbulence excitation, with the acoustic properties of the cabin interior results in low-frequency interior noise.

Such problems could be addressed by changes and optimisation in the design of the structure but this is often difficult or unfeasible to modify. Decentralised velocity feedback control can be a robust solution for the control of vibrations in flexible structures such as an aircraft fuselage. This chapter presents the results of experimental studies on the effect of changes in curvature on the performance of a velocity feedback control system.

In the first part of the chapter, the experimental rig will be described and the control unit used in the experiments will be discussed. The second part will describe the results of offline simulations of active control based on measured data. The effects of adding a simulated compensator filter on the robustness of the system will be investigated. Finally the last section of the chapter will focus on real-time experiments of active control for increasing curvature and assess the performance and robustness of the system. The importance of using the compensator filter in maintaining the robustness of the control system is emphasised in both simulated and real-time results.

6.1 Experimental Set-up

6.1.1 Experimental Rig

The experimental rig consists of a rigid-walled enclosure on which the panel is mounted, whose curvature can be changed through the variation of the internal pressure in the enclosure. A thin homogeneous aluminium panel of 1 mm thickness is mounted and clamped along its four edges on a rigid frame fixed on top of the rectangular enclosure. The enclosure walls are made of 3-cm thick panels of Plexiglas to provide approximate rigid-wall acoustic boundary conditions and ensure that sound is only radiated by the panel. The dimensions of the free area of the panel are $414 \times 314 \times 1 mm^3$ and the inner dimensions of the Perspex box are $414 \times 314 \times 385 mm^3$. The enclosure was made airtight in order to prevent any air leaking during pressurisation. The changes in the interior static pressure are achieved with a pressure compressor and a pressure regulator to control the air flow into the enclosure. In order to measure the static deflection of the aluminium panel, a dial indicator was mounted on the top frame of the enclosure and positioned at its centre. A block diagram and photograph of the set-up are provided in Figure 6.1.

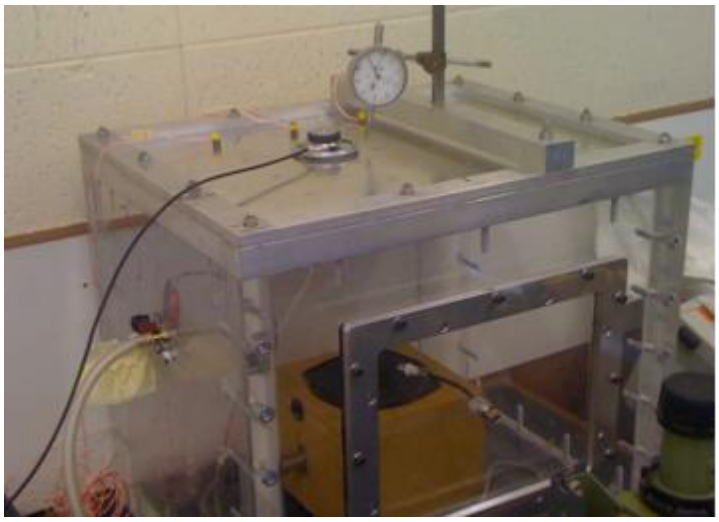

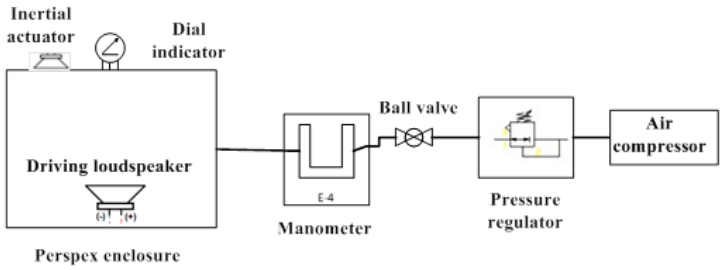

Figure 6.1 – Experimental set-up and diagram of the pressurised enclosure.

The source used in this experiment for the primary disturbance was acoustic, and to achieve a given volume velocity was composed of two loudspeakers fixed face-to-face to each other, as shown in Figure 6.2. This configuration, known as the Salava source, is composed of a driving loudspeaker and a sensor loudspeaker and allows to measure the volume velocity per unit voltage of the source [111]. The sensitivity of the source, which has been calculated in [111], is $S_q = 1.1 \times 10^{-4} m^3 s^{-1} V^{-1}$. The volume velocity per unit voltage was measured at the output of the sensor loudspeaker and the transfer response can be viewed in Figure 6.2. Because of the use of two loudspeakers in the source, two resonance peaks occur in the transfer response. In comparison to a single loudspeaker baffled source, the additional resonance increases the efficiency of the source at higher frequencies [111].

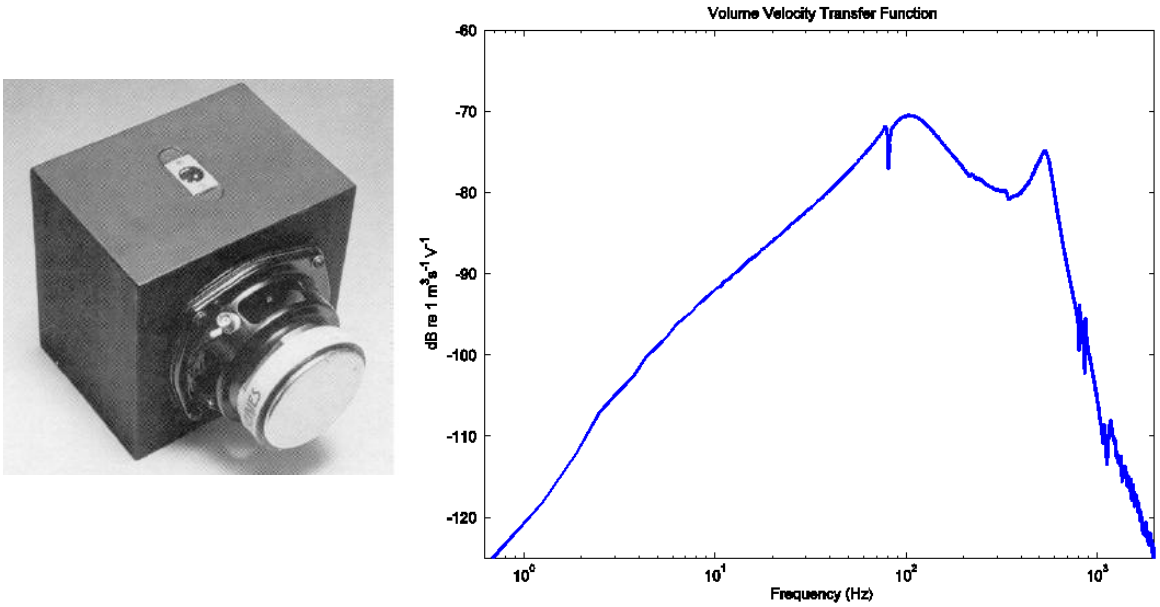

Figure 6.2 – Salava source implemented by Anthony and Elliott in [111] and used for the current experiments (left), Measured volume velocity frequency response per unit driving voltage for the source (Right).

In order to obtain a maximum static deflection of 2mm in the centre of the panel, the interior pressure of the enclosure needed to be increased to 715 Pa. This pressure was calculated at the design stage, in order to get safety approval for enclosure pressurisation during experiments, using Timoshenko's equation of deflection for the case of a distributed load on a clamped-clamped surface, formulated as [112]

$$z_c = \frac{0.00191q\left[Min(l_x, l_y)\right]^4}{D} = \frac{0.00191ql_y^4}{D}, \tag{6.1}$$

where q is the intensity of the distributed load and D is the bending stiffness of the panel calculated from $D = \frac{Eh^3}{12\left(1-v^2\right)}$.

The maximum stress applied at the centre along the *x*-direction can be obtained from Timoshenko's equations of bending moment

$$\sigma_{\max} = \frac{6M_x}{h^2}, \tag{6.2}$$

where M_x is the moment along the *x*-axis. The maximum stress $\sigma_{\max}$ for a 2-mm deflection at the centre of the panel was found to be 28.2 MPa. The yield and ultimate strength of aluminium were also found from the physical properties of aluminium 6061-T6 to be 275 MPa and 310 MPa respectively, which are both well above the maximum stress caused at the centre of the panel by a 2-mm deflection.

Based on the dimensions of the enclosure, the first natural frequency of the acoustic modes in the cavity is not expected until a frequency of 410 Hz and so these are not expected to play an important role in the frequency range of interest here. The calculated natural frequencies of the cavity and the extent to which they couple with the structural modes of the aluminium panel can be found in Appendix C.

6.1.2 Control Unit

The control unit used in this study consists of a proof-mass electrodynamic actuator collocated with a lightweight accelerometer for measuring the error signal, a signal conditioner and a power amplifier. The main criteria in actuator selection were size, weight and natural frequency. As the structure in question was a thin lightweight aluminium panel, it was required to choose an actuator that was small and relatively light in order to minimise the changes in the properties of the panel and the deflection in the surface of the panel due to the weight of the actuator. The other requirement was to choose an actuator which had a natural frequency low enough to be below the first natural frequency of the panel, and therefore avoid compromising the stability of the control system. The combination of the low weight and low natural frequency requirements brought in limitations in the selection process because the natural frequency is inversely proportional to the square root of the mass, for a given suspension stiffness. Finally, the other important limiting factor in the choice of actuator was the cost of the unit which must be taken into account for the practical implementation of the system to real-life problems, especially when more than one actuator is needed.

The transducer unit used as a proof-mass electrodynamic actuator is a 60-mm diameter cone loudspeaker, Type S066M, manufactured by Pro Signal. These loudspeakers are mass-produced and commercially available at a very low cost. They are lightweight and their high cone stiffness makes them fairly robust. Therefore, they are suitable for modification to act as inertial actuators in a lightweight and cost effective velocity feedback control system. The unit is used here in an unconventional way compared with when it is used as a loudspeaker, with the diaphragm attached to the structure and the mass free to move. The loudspeaker unit is composed of a Mylar diaphragm attached to a voice coil suspended in a constant magnetic field. The magnetic field is provided by a permanent magnet which in the arrangement used here, also acts as the proof mass in this modified arrangement. Pictures and a diagram of the actuator are shown in Figure 6.3.

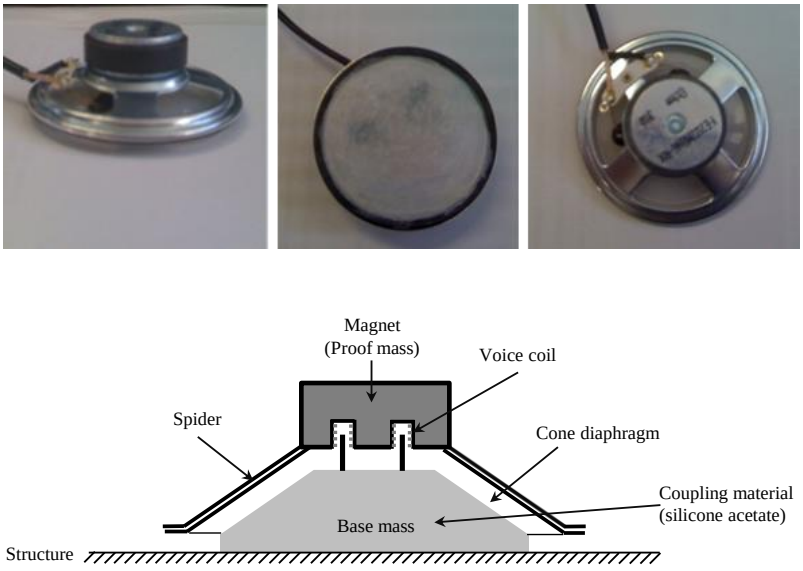

Figure 6.3 – Pro Signal Type S066M actuator unit and diagram of the actuator.

Various methods were investigated in order to achieve efficient coupling between the loudspeaker cone and the vibrating surface. Finally, it was found that the most effective method was to fill the cone of the loudspeaker with silicone acetate sealant and fix a thin plastic disk on this filling to ensure a level and smooth contact surface onto the panel. The silicone acetate was chosen because of its light weight, ease of application and flexibility. These properties allow the loudspeaker diaphragm to move freely and react against the surface when being driven. The measured mechanical and electrical properties of the unit when used in this way have been listed in Table 6.1.

Table 6.1 – Inertial actuator parameters

Parameter	value	units
Proof mass	$M_{proof} = 60\times10^{-3}$	kg
Base mass	$M_{base} = 2.3\times10^{-3}$	kg
Suspension stiffness	$K_a = 6700$	Nm^{-1}
Suspension damping coefficient	$C_a = 2$	Nsm^{-1}
Voice coil coefficient	$\psi_a = 0.018$	NA^{-1}
Modal Damping Ratio	$\zeta_a = 0.05$	
Actuator natural frequency	$f_{n_a} = 53.1$	Hz
Coil electrical resistance	$R_e = 8$	Ω
Coil inductance	$L_e = 88.1\times10^{-6}$	H

To characterise the designed actuator, blocked force measurements were performed up to 10 kHz when the actuator was mounted on a heavy rigid steel block acting as the blocked base. The blocked force response was measured between an input voltage to the actuator and the resulting acceleration measured by an accelerometer fixed on the top of the actuator. The acceleration was then multiplied by the moving mass to give the applied force and this, divided by the applied voltage is shown in Figure 6.4, where the simulated blocked force response has also been plotted in blue. The simulated blocked force response for a voltage-driven actuator was calculated using the actuator's parameters listed in Table 6.1, and can be written as [2]

$$T_{blocked} = \frac{\psi_a}{Z_{eb}}\left[\frac{Z_{M_{proof}}}{Z_{M_{proof}} + Z_a + \left(\psi_a^2 / Z_{eb}\right)}\right], \tag{6.3}$$

where $Z_{M_{base}} = j\omega M_{base}$ and $Z_{M_{proof}} = j\omega M_{proof}$ are the impedance of the base mass and the proof mass respectively and $Z_a = \frac{K_a}{j\omega} + C_a$ is the impedance of the spring-damper system, Z_{eb} is the blocked electrical impedance of the actuator and $Z_{eb} = R_e + j\omega L_e$, where R_e and L_e are the coil electrical resistance and inductance respectively and ψ_a is the voice coil coefficient. The substitution of the above mechanical impedances into Equation (6.3) leads to the following equation for the blocked force response of the voltage-driven actuator

$$T_{blocked} = \frac{\psi_a}{Z_{eb}} \left[\frac{-\omega^2}{\omega_a^2 + j\left(2\zeta_a \omega_a + \frac{\psi_a^2}{Z_{eb} M_{proof}} \right) \omega - \omega^2} \right], \tag{6.4}$$

where ω_a and ζ_a are the natural frequency and the modal damping ratio of the actuator respectively. For a current-driven actuator, Equation (6.4) reduces to

$$T_{blocked,current} = \psi_a \frac{-\omega^2}{\omega_a^2 + j2\zeta_a \omega_a \omega - \omega^2}. \tag{6.5}$$

The details of the calculations for the simulated actuator will be covered in the next section of the chapter.

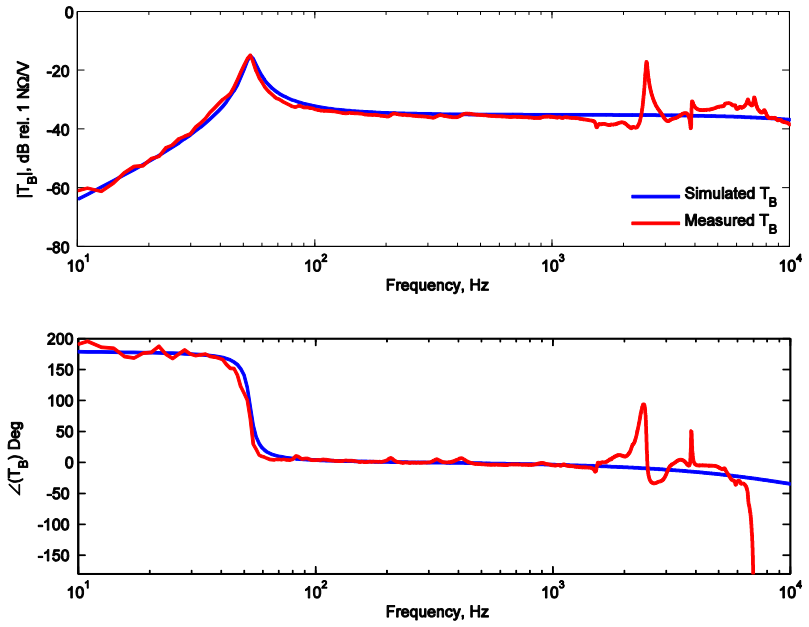

Figure 6.4 – Blocked force transfer response, normalised to the voice coil electrical resistance R_e, when the actuator is voltage driven: Measured response (blue), Simulated response (red).

In the above figure, the natural frequency of the actuator corresponds to the 53 Hz lightly-damped resonance peak observed in both of the measured and simulated transfer response plots. The associated 180-degree phase-lag can be seen in the lower subplot. The damping ratio of this resonance is about 4.8%. For frequencies above the natural frequency of the actuator, the response drops until it becomes flat up to an excitation frequency of 2 kHz, above which the unit has internal resonances, which do not occur in the simulated response as the contribution of these internal dynamics at higher frequencies has been neglected. The phase of this actuator does not go beyond the ±90° limit that would cause stability problems until about 7 kHz. By this frequency, the panel response has fallen sufficiently for this not to be a problem.

As discussed in Chapter 4, the fundamental resonance of the actuator influences the stability of the feedback control system. At frequencies above the natural frequency of the spring-mass system, the structure is subjected to a sky-hook damping effect, which is due to a base force being equal to the mass-spring reactive force. At frequencies lower than the natural frequency of the actuator, a negative damping effect occurs, caused by the base force being out of phase with the reactive force of the system, which may lead to instabilities in the feedback control system. Therefore, in order to achieve optimal control, the actuator should have a natural frequency which is much lower than

the first mode of the vibrating structure under control, and high damping at the resonance [41] [113].

Based on simulations of velocity feedback control performed using an actuator modelled with the parameters listed in Table 6.1, although the resonance of the actuator is below the natural frequency of the first structural mode, the spacing between the two is not sufficient to ensure a stable control system.

In order to overcome these limitations for the actuator used in this study, a second order compensator filter was added in the feedback loop. The compensator, which reduces the apparent natural frequency of the actuator, was based on the design proposed by Elliott et al. in [114] and is described by the following equation:

$$C(\omega) = \frac{2j\hat{\zeta}_a\hat{\omega}_a\omega + \hat{\omega}_a^2 - \omega^2}{2j\zeta_c\omega_c\omega + \omega_c^2 - \omega^2}, \tag{6.6}$$

where $\hat{\zeta}_a$ and $\hat{\omega}_a$ are estimates of the damping ratio and the natural frequency of the actuator respectively, and ζ_c and ω_c, respectively, refer to the damping ratio and natural frequency of the compensator. Assuming that the actuator natural frequency and damping ratio are correctly identified such that $\hat{\omega}_a = \omega_a$ and $\hat{\zeta}_a = \zeta_a$, the filter compensates for the actuators dynamics in Equations (6.2) and (6.3), and introduces a new resonance with a frequency of ω_c and a damping ratio of ζ_c. In this study, the new natural frequency is chosen to be $\frac{\omega_c}{2\pi} = 10.6\,\text{Hz}$ and is critically damped $(\zeta_c = 1)$ in order to reduce the natural frequency of the actuator by a factor of 5 and completely flatten the actuator's resonance peak.

The frequency response of the simulated compensator, the uncompensated and compensated blocked force frequency responses, all plotted up to 10 kHz, are shown in Figure 6.5 and Figure 6.6 respectively. In the graphs of Figure 6.5, the frequency response of the compensator displays an anti-resonance and a phase lead of 180° at the natural frequency of the actuator. This results in the cancellation of the actuator resonance peak and makes up for the 180° phase lag (Figure 6.6). However, the compensated blocked force response graph of Figure 6.6 also reveals that the addition of the compensator results in up to 20 dB enhancement below 40 Hz. This enhancement

may be detrimental to the stability of the feedback loop as it results in an amplification of the low frequency noise in the measurements. This low-frequency noise amplification may result in force/stroke saturation of the actuator which occurs when the actuator is driven with a large force and results in the proof mass hitting the casing of the actuator. Displacement saturation occurs causing an impulse to be transmitted to the structure, which in turn when detected by the error sensor can introduce additional phase shifts in the feedback loop and cause spillover and instability [115].

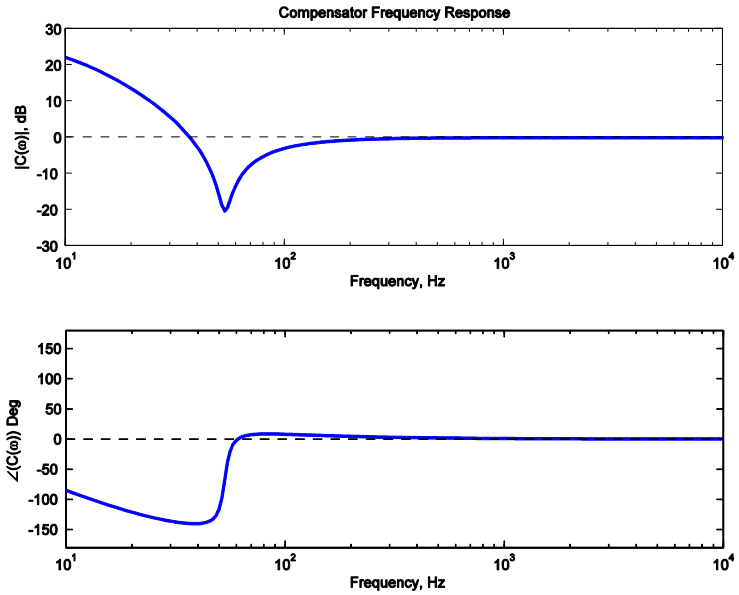

Figure 6.5 – Frequency response of the compensator: magnitude (top), phase (bottom).

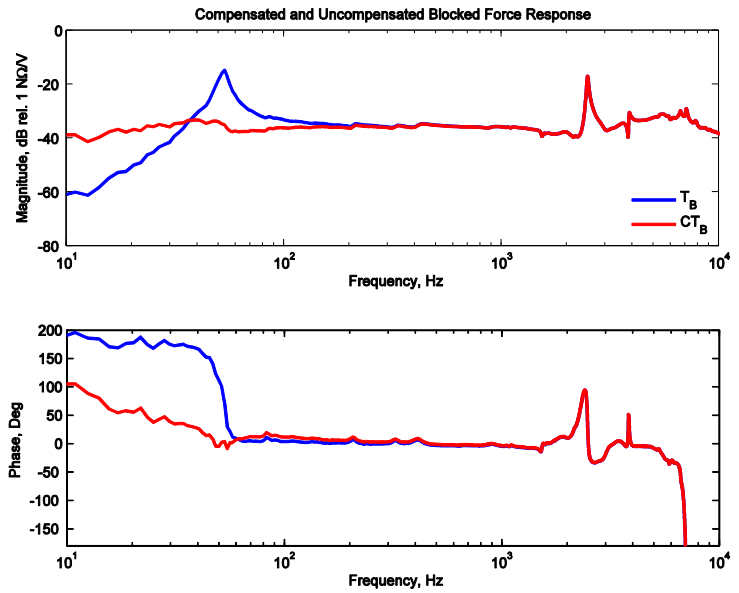

Figure 6.6 – Blocked force frequency response of the actuator: uncompensated (blue curve), compensated (red curve).

Consequently, the degree to which the natural frequency can be lowered is limited by the amount of low frequency gain that can be used in the compensator. The main disadvantage of using such a compensator is thus the enhancement of the low-frequency range below the control unit natural frequency by nearly 20 dB which could cause potential problems in the practical implementation of the feedback control system, as the slightest further enhancement picked up by the error sensor could induce saturation in the actuator and potential stability issues may arise.

Another danger in this actuator design is that additional phase shifts will be introduced into the open-loop response if the assumed natural frequency and damping of the actuator are not equal to the true values. This could occur if these parameters are not correctly identified, if they change over time or with temperature, or if a single design of compensator is used for a number of different actuators with a range of natural frequency and damping values. The robustness of the compensator has been studied by Rohlfing et al. in [116], who showed that the compensator phase response is not significantly affected by quite large changes in the actuator damping, from 0.03 to 0.06, but to maintain the compensated phase change to below $\pm 90°$, the natural frequency must be estimated to about $\pm 5\,\mathrm{Hz}$ for the damping ratio range here.

The actuator was mounted on the surface of the panel at a position $(x_c, y_c) = (0.38l_x, 0.53l_y)$ and the corresponding accelerometer sensor was positioned directly underneath the actuator. As described in Chapter 4, this slightly off-centre position of the actuator-sensor pair on the panel is optimal for controlling more modes when there is only one controller. The robustness of the control system unit in the presence and absence of the compensator filter will be further assessed in the next sections through offline simulations and real-time experiments of velocity feedback control on the pressurised enclosure.

6.2 Offline Simulations of Active Control

In order to predict the performance and stability of the feedback control system for increasing levels of curvature, offline simulations of active control were performed using measured data. For this purpose, the panel was divided into a grid of 4×4 points and the transfer mobility between the primary disturbance and the grid of 16 points (acceleration measured by accelerometers per unit volume velocity of the source), the transfer mobility between the actuator (secondary source) and the grid of 16 points (acceleration measured by accelerometers per unit input voltage to the actuator) and the open-loop response (acceleration measured by the error sensor per unit input voltage to the actuator) were measured. These measurements were performed for 11 different curvature levels corresponding to elevations in the centre of the panel $z_c = 0, 0.2, 0.4, ..., 2$ mm. This was achieved by pressurising the air inside the enclosure. The closed-loop response of the system was then simulated offline using the above data and the effect of adding a compensator in the feedback loop was investigated. The results for different curvature levels are provided in the upcoming subsections. An elemental model of the enclosure has also been derived in Appendix D, for which the results of simulated of velocity feedback control are shown for different curvature levels.

6.2.1 Open-Loop Response

The actuator which was positioned slightly off-centre at the position given at the beginning of the chapter, was driven by a voltage source to excite the panel. The open-loop or plant response was measured between the voltage input to the actuator and the acceleration measured by the error sensor over increasing curvature. Figure 6.7 shows the positioning of the actuator on the surface of the panel during the open-loop response measurements. The stability of the control system over increasing curvature was assessed through the Nyquist and bode plots of the plant frequency response function (FRF).

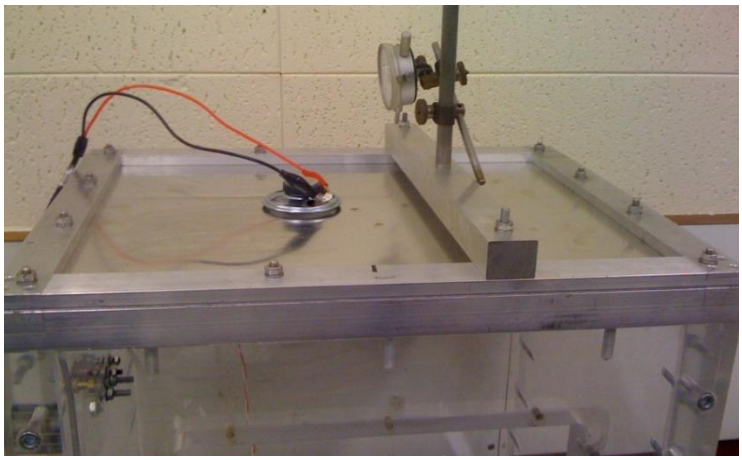

Figure 6.7 – Picture of the actuator set-up on the surface of the panel during open-loop FRF measurements.

Figure 6.8 shows the Bode plots of the open-loop response with increasing levels of curvature. The plots show the coupled interactions between the actuator and the panel. In both flat and curved panel open-loop FRFs, the first peak which occurs near 40 Hz, corresponds to the coupled response where the actuator dominates. The actuator's blocked natural frequency, of 53 Hz, is lowered to near 40 Hz, because of the decrease in the effective suspension stiffness which is due to the compliance of the panel. The frequency of this peak increases from 40 Hz to about 45 Hz as the panel stiffens when the enclosure is pressurised. A low-amplitude dip can also be seen in the Bode plot near 50 Hz, which corresponds to the passive effect at the natural frequency of the mass-spring system in the actuator.

In the case of the curved panel, the second peak which is due to the first panel mode, is shifted towards higher frequencies, such that although it is near 88 Hz for the flat panel, it increases to 140 Hz for $z_c = 2\,mm$. This is caused by the stiffening effect of the curvature, as explained in Chapters 2-4.

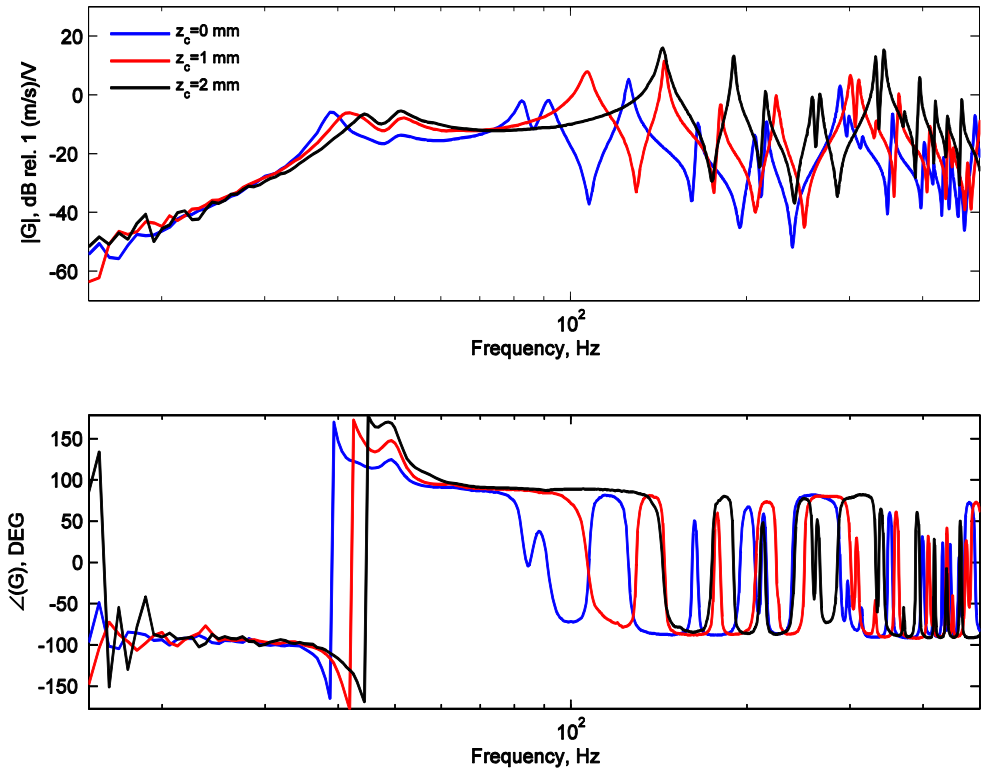

Figure 6.8 – Bode plot of the open-loop response of the control system with increasing curvature: flat panel (blue curve), doubly-curved panel with a deflection of zc = 1 mm (red curve), doubly-curved panel with a deflection zc = 2 mm (black curve).

The effect of adding the compensator on the open-loop frequency response, and hence on the stability of the system can be seen in the Nyquist and Bode plots of Figure 6.9. In both cases, the results have been plotted for a gain level corresponding to the 6-dB gain margin of the uncompensated control system, in order to give an idea of the scale, as the 6-dB gain margin of the compensated system is significantly higher.

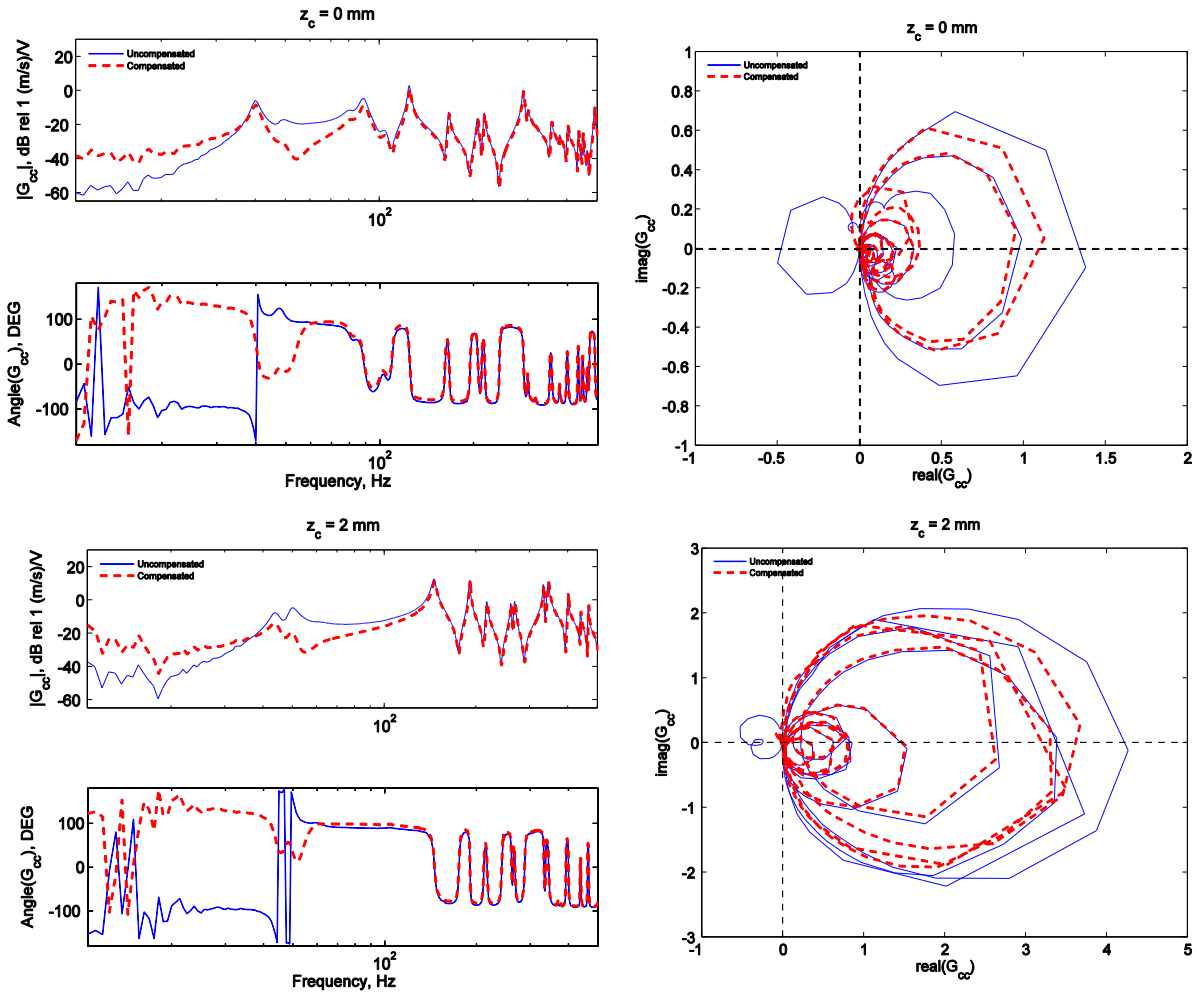

Figure 6.9 – Bode plots (left) and Nyquist plot (right) of the open-loop frequency response for the flat and doubly-curved panels, z_c = 2mm, before and after compensation.

For the uncompensated system, the natural frequency of the actuator appears on the left-hand side of the Nyquist plots, while the lobes on the right-hand side are due to the resonances of the panel. The stability and performance of the control system can be assessed by the ratio of the size of the right-hand side lobe to the left-hand side lobe [107]. The larger this ratio, the greater is the distance between the natural frequency of the actuator and the 1st mode of the panel. It can be seen from the uncompensated Nyquist plots, that this ratio is much larger in the case of the curved panel than the flat panel. As demonstrated in the simulations of Chapters 4 and Appendix D, it can be deducted that the introduction of curvature in the structure may improve the stability of the uncompensated system.

When the compensator is added in the feedback loop, a dip occurs at the location of the actuator's resonance or compensator's anti-resonance and a phase lag is introduced to

the system at this frequency. Consequently, the lobe corresponding to the actuator natural frequency is shifted to the right-hand side in the Nyquist plot, which corresponds to a significant increase in the stability of the system and allows the implementation of feedback control at higher gain levels. The Nyquist plot of the curved panel still shows a larger ratio of right-hand lobe to left-hand lobe size after compensation, showing that the actuator-compensator system is robust to changes in curvature.

6.2.2 Panel Structural Response

The transfer mobility between the primary disturbance and the grid of 16 points defined on the panel was measured for 11 levels of curvature corresponding to a deflection in the centre of the panel $z_c = 0, 0.2, 0.4, ..., 10$ mm. The averaged structural response was calculated from the sum of the squared velocities over the 16 points of the grid. Figure 6.10 shows the structural response as the enclosure is pressurised and the panel curvature increases.

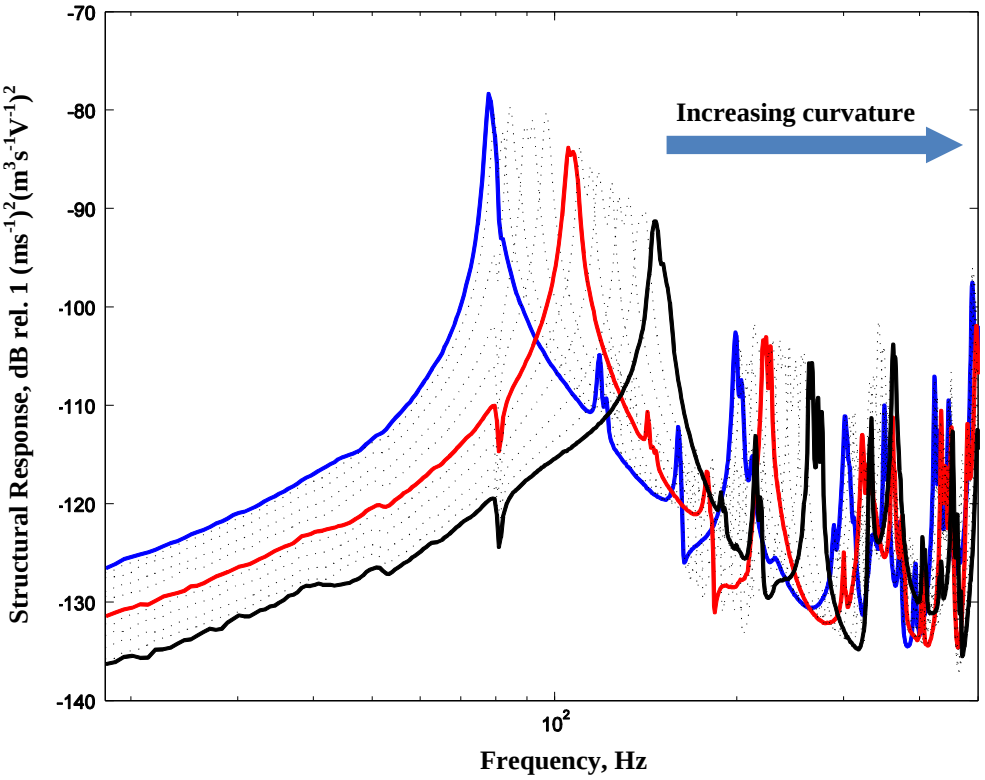

Figure 6.10 – Effect of curvature increase on the overall structural response of the panel before the actuator is attached: flat (blue curve), curved with z_c = 1 mm (red curve), curved with z_c = 2 mm (black curve). The dotted curves between the graphs show the progression of the structural response over increasing curvature.

With the increase in the internal pressure of the enclosure, a shift in the panel modes towards higher frequencies can be observed in the above figure. These experimental results confirm the results obtained from the analytical models described in the previous chapters. For example, the natural frequency of the first mode of the panel which occurs around 70 Hz when the panel is flat, more than doubles when the deflection in the centre of the panel is increased to 2 mm and can be seen to be near 150 Hz. The increase in curvature also reduces the amplitude of the lower natural frequencies such that the magnitude of the first mode is reduced by 13 dB. This is due to the increase in the stiffness of the panel as the stiffness-controlled region is extended to higher frequencies, which passively controls the panels' lower modes.

When the actuator is positioned on the surface of the panel slightly off-centre at the location specified at the beginning of the chapter, the structural response changes due to the influence of the mechanical properties of the actuator. Figure 6.11 shows the loaded averaged structural response of the panel with increasing curvature.

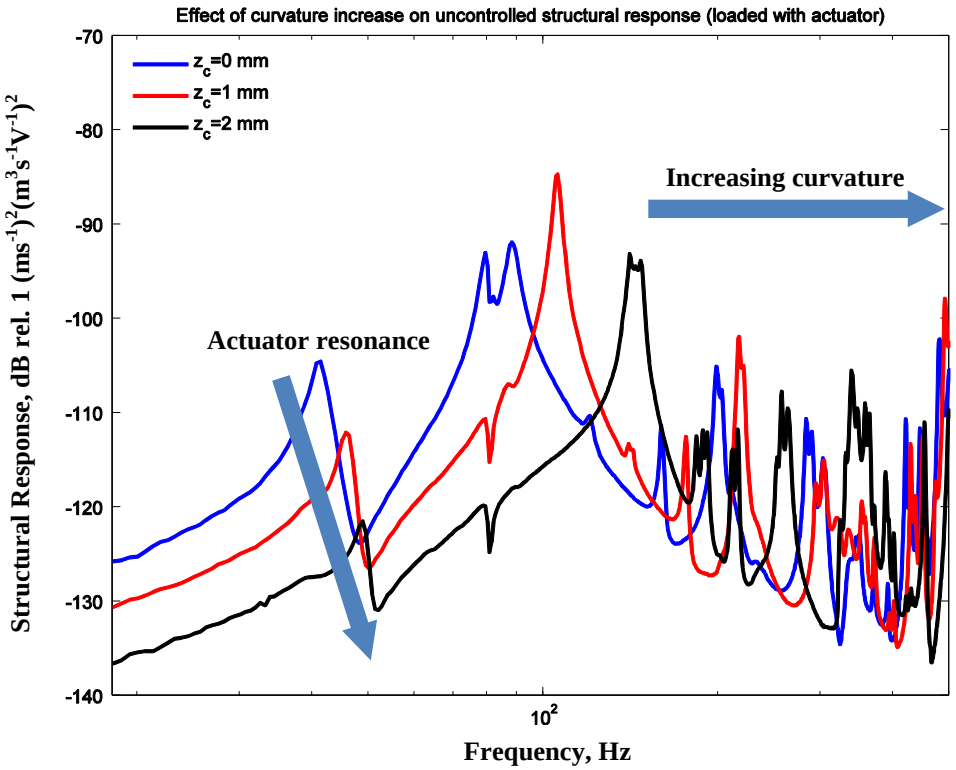

Figure 6.11 – Effect of curvature increase on the overall structural response of the panel, when it is loaded with the actuator: flat (blue curve), curved with z_c = 1 mm (red curve), curved with z_c = 2 mm (black curve).

Two low frequency resonance peaks are now seen, near 40 Hz and 78 Hz, and correspond to the coupled actuator resonance and the coupled first resonance of the panel, instead of a single dominant peak. While the natural frequency of the first mode of the panel is significantly increased with the enclosure pressurisation, the actuator resonance is only shifted by a few Hz, as its mechanical properties such as the proof mass and the stiffness of the coil, are not significantly affected by the changes in curvature. Furthermore, the amplitude of the actuator resonance is significantly attenuated with the increase in the stiffness of the panel over increasing curvature which acts as passive control on the actuator and allows the implementation of higher feedback gain without causing enhancements at the natural frequency of the actuator. The trend in the natural frequency of the actuator-panel resonance and the first 3 modes of the panel over the increasing curvature due to pressurisation is shown in Figure 6.12.

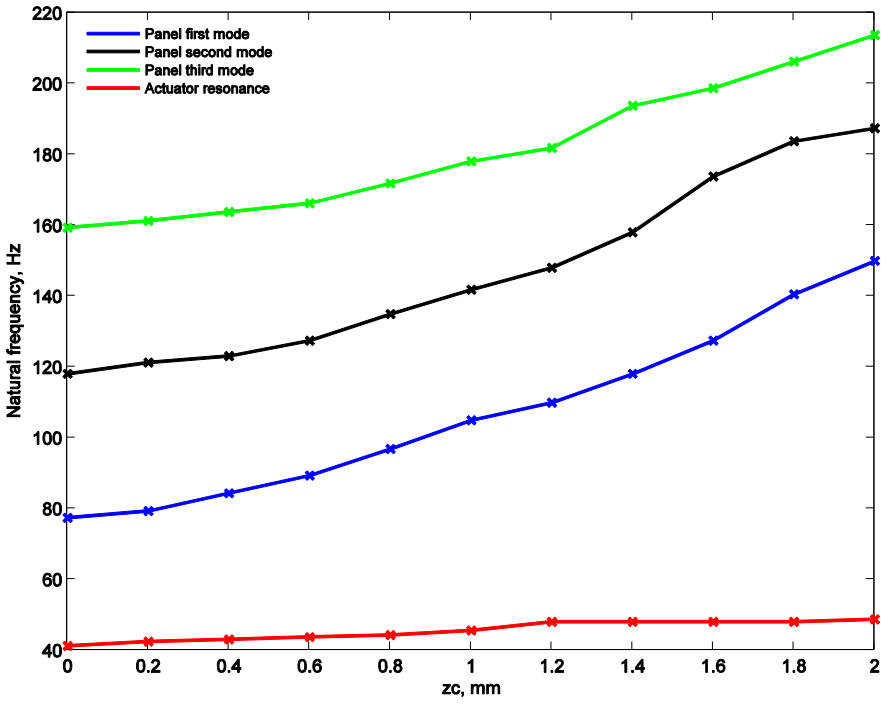

Figure 6.12 – Natural frequencies of the first 3 modes of the panel plotted along with the natural frequency of the actuator over increasing deflection in the centre of the panel.

This figure shows that while the difference between the actuator natural frequency and the panel mode increases, which improves control performance, the increasing curvature brings the natural frequencies of the panel closer together. As shown in simulations of active control of Chapter 4, modal clustering is detrimental to the performance of the control system. Consequently, there are two effects that curvature has on control

performance. While the stability of the system is increased due to the increasing difference between the actuator and the panel first resonances, worse control is achieved due to the decrease in the difference between the natural frequencies of the panel's modes. This trade-off is demonstrated in the simulations of active control based on measured responses in the following subsections.

6.3 Simulations of Open-Loop Response including the Loading Effects of the Actuator

When a control system is implemented on a structure the coupled velocity changes to include the effects of this secondary source. In the simulations of feedback control of Chapter 4, the loading effects of the actuator on the panel were neglected in order to simplify the equations. In this section, the open-loop response of a SISO feedback control system will be simulated while the loading effect of the base and coil mass of the actuator are included.

The control system modelled in this section consists of an inertial actuator collocated with an ideal velocity sensor measuring the velocity of the panel at the point of control. A lumped-parameter model of the electromechanical system of the actuator, modelled as a single degree of freedom (SDOF) system, is shown in Figure 6.13. The inertial actuator modelled here is based on the actuator used in the experiments described in this chapter. The parameters and physical properties of the actuator are the same as those listed in Table 6.1.

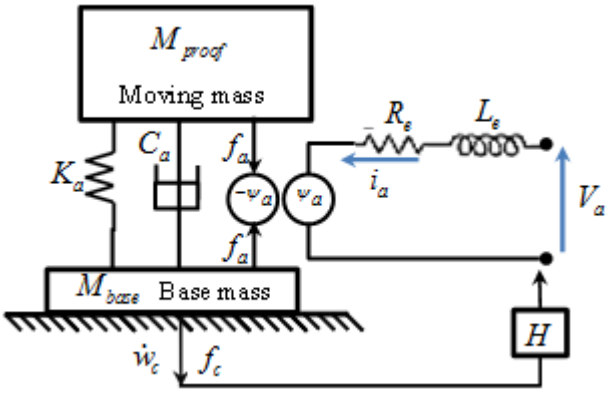

Figure 6.13 - Lumped parameter model of the actuator with a base mass.

The inertial actuator both supplies a force to the panel and modifies its passive dynamic behaviour. If the force generated by the actuator is as a result of feedback from the panel's velocity, the effect of the feedback can also be modelled as a modification to the plate dynamics. The overall effects of the actuator can be defined in terms of both active and passive contribution as

$$Z_c = Z_{mech} + Z_{active}, \tag{6.7}$$

where Z_{mech} is the passive or open-circuit mechanical impedance and Z_{active} is the active impedance. The mechanical impedance is calculated from the equivalent impedances of the SDOF system of Figure 6.13 as

$$Z_{mech} = Z_{M_{base}} + \frac{Z_{M_{proof}} Z_a}{Z_{M_{proof}} + Z_a}, \tag{6.8}$$

where $Z_{M_{base}} = j\omega M_{base}$ and $Z_{M_{proof}} = j\omega M_{proof}$ are the impedance of the base mass and the proof mass respectively and $Z_a = \frac{K_a}{j\omega} + C_a$ is the impedance of the spring-damper system.

If a velocity feedback loop is used to drive the actuator with a voltage source, the equation for the active impedance of the actuator can be determined using the two-port network method discussed in [117], such that the voltage of the electrical circuit in Figure 6.13 can be written in terms of the complex control velocity and the control force can be expressed in terms of the current, leading to the set of equations

$$V_a = Z_{eb} i_a + T_{em} \dot{w}_c \tag{6.9a}$$

$$f_c = T_{me} V_a + Z_{mech} \dot{w}_c, \tag{6.9b}$$

where V_a is the voltage across the electrical inputs to the transducer, i_a is the current, T_{em} is the transduction coefficient. For an anti-reciprocal transducer such as a moving coil transducer, $T_{em} = -T_{me}$. The transduction coefficient T_{em} is the blocked force response of the actuator, which is the maximum force per unit input voltage and can be measured when the actuator is fixed on a solid block, such that the velocity of the

moving mass is 0 and the actuator cannot couple with the structure. For a voltage-driven source, the blocked force response is obtained from Equation (6.3) defined in Section 6.1.2.

The control velocity on the panel can be expressed in terms of the point mobility $Y_{cc,coupled}$ of the panel at the location of control, and the control force f_c, as

$$\dot{w}_c = -Y_{cc,coupled} f_c, \tag{6.10}$$

where unlike the point mobility Y_{cc} defined in Chapter 4, $Y_{cc,coupled}$ includes the passive effects of the actuator and is defined as

$$Y_{cc,coupled} = \left[Z_c\right]^{-1} = \left[Z_{mech} + Z_{active}\right]^{-1}. \tag{6.11}$$

Alternatively, the control force can be written in terms of the impedance at the point of control and the complex control velocity as

$$f_c = -Z_c \dot{w}_c, \tag{6.12}$$

where the negative sign in the above equation is due to the direction of the force in Figure 6.13 being in the opposite direction of the sign convention. The substitution of Equations (6.3) and (6.11) in Equations (6.9a-b) and the combination of the two equations lead to the equation for the active impedance of the actuator

$$f_c = T_{blocked} V_a - Z_{mech} Y_{cc,coupled} f_c$$

$$f_c = \frac{1}{1 + Z_{mech} Y_{cc,coupled}} T_{blocked} V_a$$

$$T_a = \frac{f_c}{V_a} = \frac{T_{blocked}}{1 + Z_{mech} Y_{cc,coupled}} \tag{6.13}$$

$$Z_{active} = H T_a, \tag{6.14}$$

where H is the feedback loop gain which for a single channel control system is a frequency-independent value, $H = g$. Finally the open-loop response or plant response of the actuator is expressed in terms of the active impedance T_a and the structural point mobility of the panel Y_{cc} at the point of control as

$$G = HY_{cc,coupled}T_a. \tag{6.15}$$

The bode plot of the simulated open-loop response of the control system is shown in Figure 6.14 before and after including the loading effect of the actuator. The effect of the actuator base mass which was omitted in the simulations of Chapter 4, have also been taken into account here.

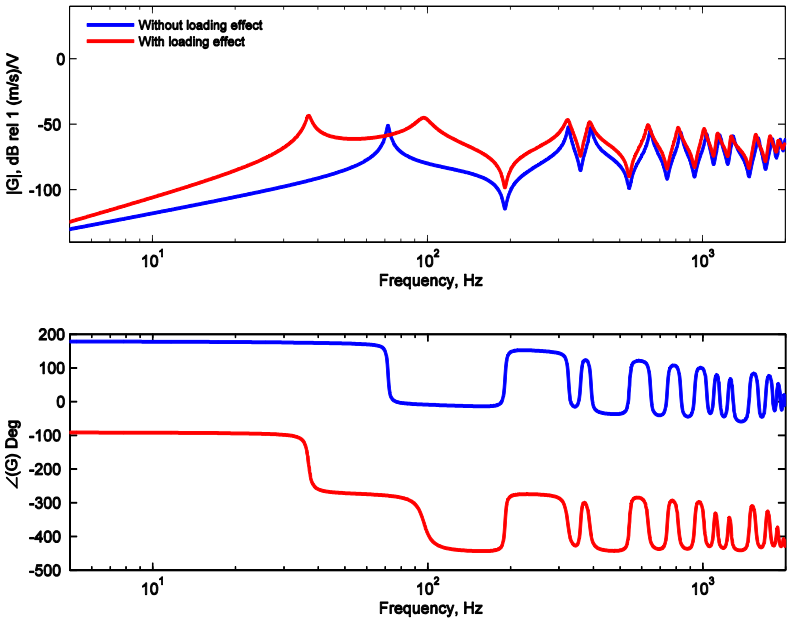

Figure 6.14 – Bode plot of the simulated open-loop response of the SISO feedback control system: without the loading effect of the actuator (blue curve), with the loading effect of the actuator included (red curve).

As shown in the blue curve of Figure 6.14, when the loading effects of the actuator are not taken into account, the open-loop response does not reflect the coupling interactions between the actuator and the panel. Therefore, the response resembles the one of a control system with an ideal point force actuator. In this case, the first resonance peak corresponds to the panel's first structural mode. However, when these loading effects are included in the model, the simulated open-loop response shown by the red curve in Figure 6.14 closely resembles the measured open-loop response shown in the Bode

plots of Figure 6.8. The first resonance which is caused by the inertial effect of the actuator's mass and coil on the panel and is known to occur around 40 Hz from measurements, can be seen in the red response curve. Simulating the loading effect of the actuator on the structure is an important factor to consider in the actuator selection, especially in applications where weight is an important factor

6.4 Control Performance

The control performance and robustness of the system were assessed through offline simulations based on the measured open-loop responses, the measured transfer mobility between the actuator and the grid of 16 points on the panel and the measured transfer mobility between the primary disturbance and the grid of 16 points. A fixed compensator was assumed for all experiments, regardless of the curvature level of the panel.

In order to assess the control performance, the average structural response which is the sum of the squared velocities over the grid of 16 points on the panel, was calculated up to 500 Hz both with and without compensator. Figure 6.15 shows the averaged structural response and optimal gain graphs for both flat and curved panel. The increase in the natural frequency of the first panel mode with pressurization, from 88 Hz to 150 Hz, is clear from the comparison of the two figures. The optimal gain value is the feedback gain value for which maximum attenuations in the overall frequency response levels can be achieved. This value can be estimated using the graphical approach discussed in Chapter 4 and the corresponding graphs are shown on the right-hand plots of Figure 6.15.

The changes in kinetic energy level with feedback gain for the uncompensated system give an indication of its low gain margin. Because of the low gain margin of the controller and the lack of sufficient distance between the optimal gain and the maximum stable gain, most of the attenuation in the structural response is due to the loading effect of the actuator rather than the feedback controller. However, when the compensator is added to the feedback loop, the maximum stable gain and the gain margin are both

significantly increased. The optimal feedback gain is also at least a factor of 10 away from the limit of instability.

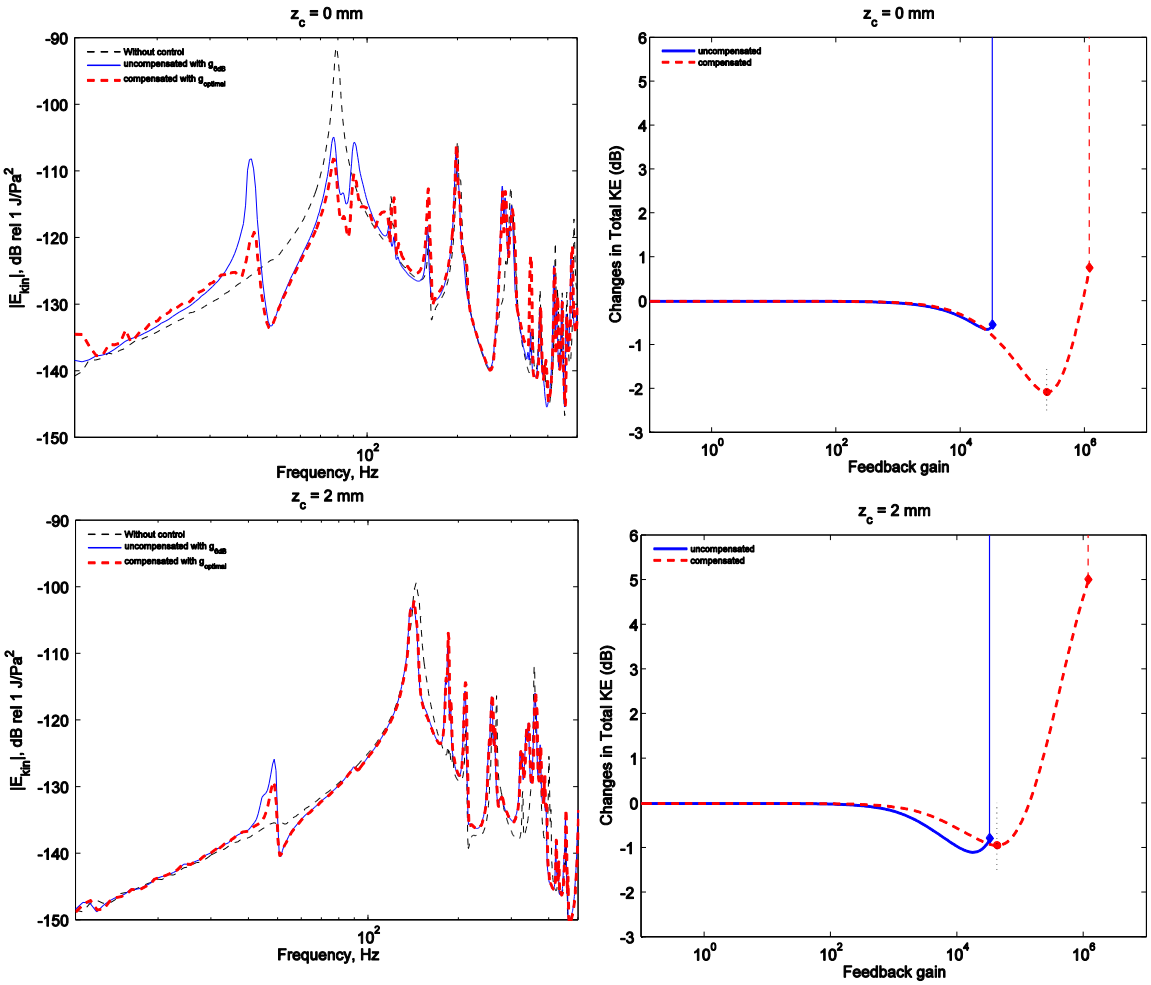

Figure 6.15 – Kinetic energy (left) and optimal gain plots (right) for the uncompensated and compensated control loops for both flat (top) and curved (bottom) panels: maximum stable gain (diamond) and optimal gain (circle).

For the flat panel, the attenuation level of the first few modes is significant and the first peak is reduced by 20 dB. For the curved panel, even though the overall attenuation is not as significant as for the flat panel and the first peaks only show a 2 dB reduction, the optimal feedback gain is well below the maximum stable gain. Despite the change in curvature, the stability of the feedback system is not compromised and the controller with the compensator-actuator pair remains robust to the changes in the surface shape due to pressurisation. This is because the compensator has been designed to only modify the physical properties of the actuator without needing to account for the dynamics of

the panel. The optimal gain of the compensated system also does not seem to be very sensitive to the increase in curvature and is similar in both flat and curved panel cases.

The uncompensated and compensated velocity FRFs at the location of the actuator for an enclosure with a flat panel are shown in the graphs of Figure 6.16, both plotted before control, when the feedback loop is closed with a 6-dB gain margin and when the feedback loop is closed with an optimal feedback gain. The same results for the case of a curved panel are shown in Figure 6.17.

In the absence of the compensator, when the feedback loop is closed, the level of control is very limited. The uncompensated system has a low gain that cannot be increased without pushing the system towards instability and despite the low gain level up to 10 dB enhancement occurs at the 40-Hz resonance peak. However, when the compensator is introduced in the feedback loop, the control system can more successfully attenuate the response.

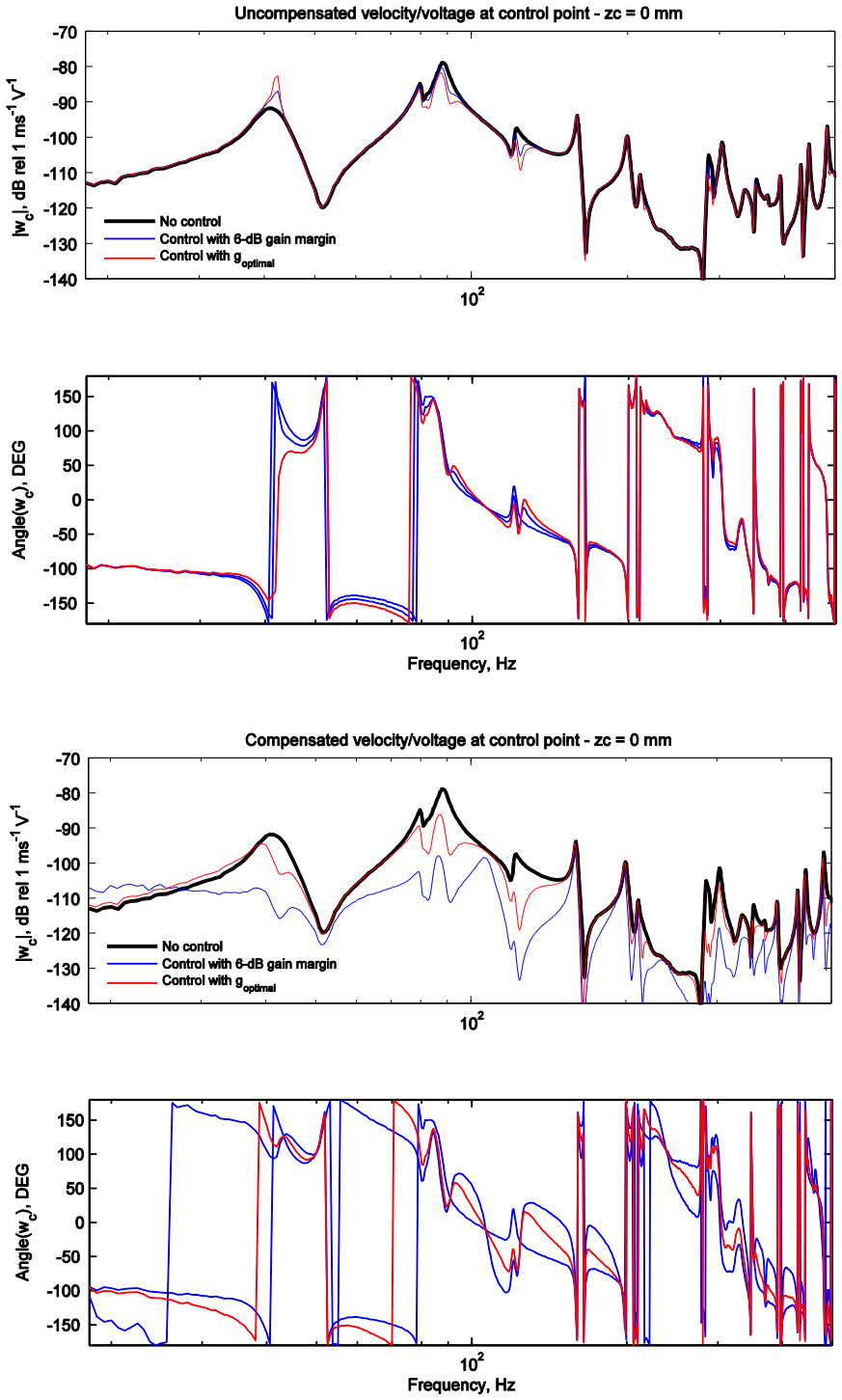

Figure 6.16 – Bode plots of the uncompensated (top) and compensated (bottom) panel velocity at the location of the actuator, for a flat panel.

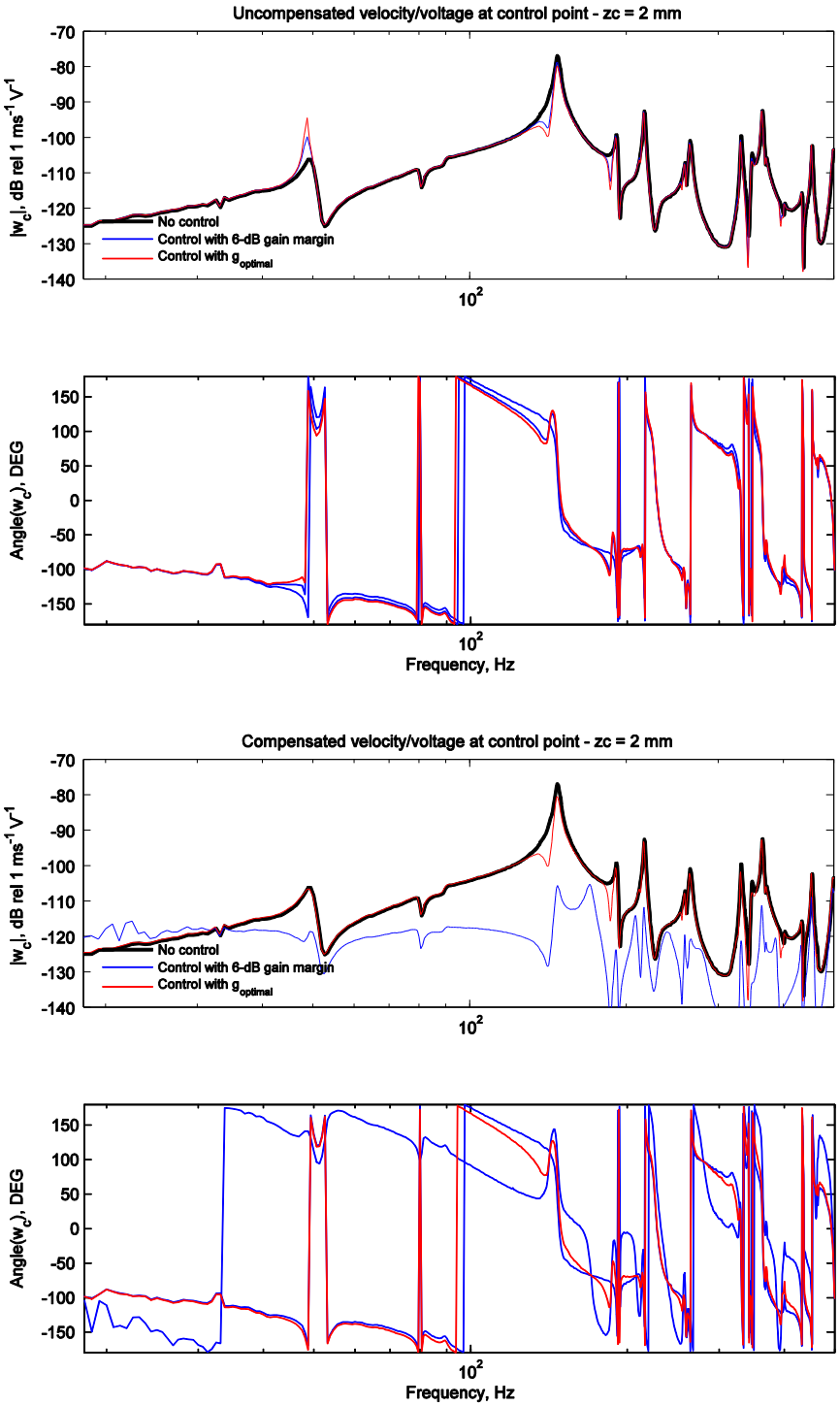

Figure 6.17 – Bode plots of the uncompensated (top) and compensated (bottom) panel velocity at the location of the actuator, for a curved panel, z_c = 2 mm.

The comparison of the graphs of Figure 6.16 and Figure 6.17 indicates that even though the increase in curvature may reduce the attenuation levels for an optimal feedback gain value, in comparison with the flat panel, the curved panel is still controlled and no spill-over or noticeable enhancement occurs. When the feedback loop gain is set to the

optimal gain value, the local attenuations in the panel velocity, especially below 200 Hz, is significantly less than when the 6-dB gain margin is applied. This is due to the fact that the optimal feedback loop gain corresponds to the maximum attenuation in the global response over the frequency of control, rather than local attenuations at the point of control. However, the use of the optimal gain value allows a better global attenuation and unlike the 6-dB gain margin prevents enhancements at low frequencies.

The maximum attenuation level in kinetic energy resulting from the optimal feedback loop gain value was plotted over increasing curvature, before and after the introduction of the compensator in the feedback loop. These plots have been shown in Figure 6.18. This was done to assess the effect of curvature increase on the maximum overall attenuation in kinetic energy levels, both in the absence and presence of the compensator. It was expected that the control performance would be initially improved for lower levels of curvature before being degraded by larger deflections. Not only does Figure 6.18 confirm and validate the simulation results, but the compensated result show attenuation levels twice as high as the uncompensated attenuations. The further increase in curvature reduces the performance of the controller, as predicted, and the uncompensated and compensated plots converge to the same value for the maximum panel deflection $z_c = 2\,mm$. The addition of the compensator does, however, maintain the stability of the system despite the lack of overall attenuations for higher levels of curvature.

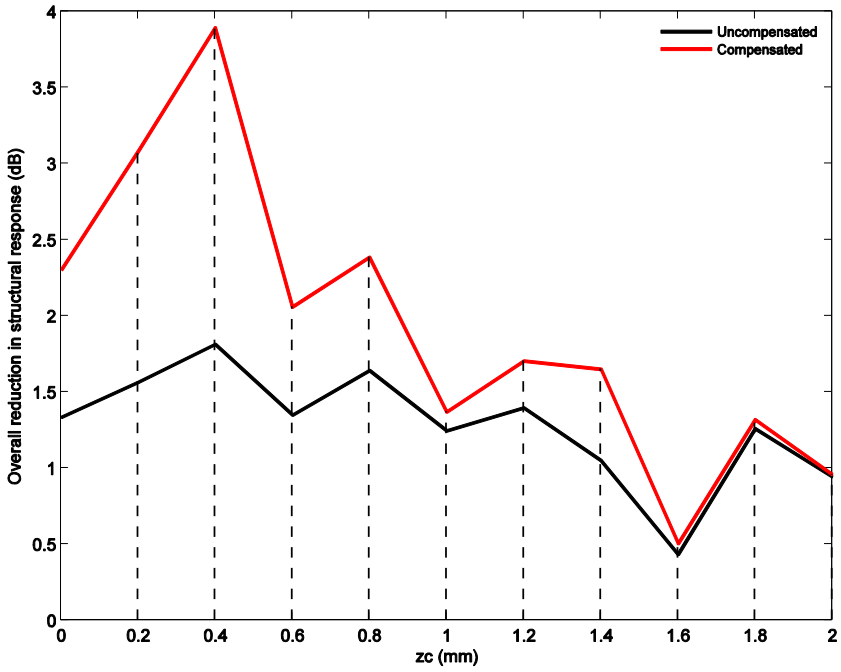

Figure 6.18 – Maximum reduction in overall kinetic energy plotted over increasing curvature, uncompensated (red) and compensated (black).

The outcomes of the offline simulations discussed in this section will be verified against real-time implementation of active control on the experimental rig.

6.5 Real-Time Experiments of Active Control

This section discusses the results obtained from the real-time implementation of the single-channel feedback control system on the experimental rig. The actuator was mounted on the panel slightly off centre, as above, and a lightweight accelerometer was again mounted under it inside the enclosure. An integrator was used to convert acceleration to velocity and obtain proportional velocity feedback control. A second order analogue compensator designed to reduce the natural frequency of the actuator by a factor of 5 was also implemented into the feedback loop. A high-pass filter with a cut-on frequency of 15 Hz was also added to the control system in order to filter out low frequency noise. The diagrams of the compensator and high-pass filter taken from [116] can be found in Appendix E. Although the use of the high-pass filter reduces the stability margin of the system due to the introduction of delay in the system, it also

prevents the system from being overloaded due to sudden amplifications of low frequency background noise.

Three additional accelerometers were mounted on the surface of the panel in order to measure the acceleration at points other than the actuator location and assess the performance at points further away from the location of control. The primary source described in the previous sections was placed in the enclosure to excite the panel. The spectra of the accelerations at these points were measured before and after closing the feedback loop. The location of the additional accelerometers and the diagram of the feedback control system is shown in Figure 6.19.

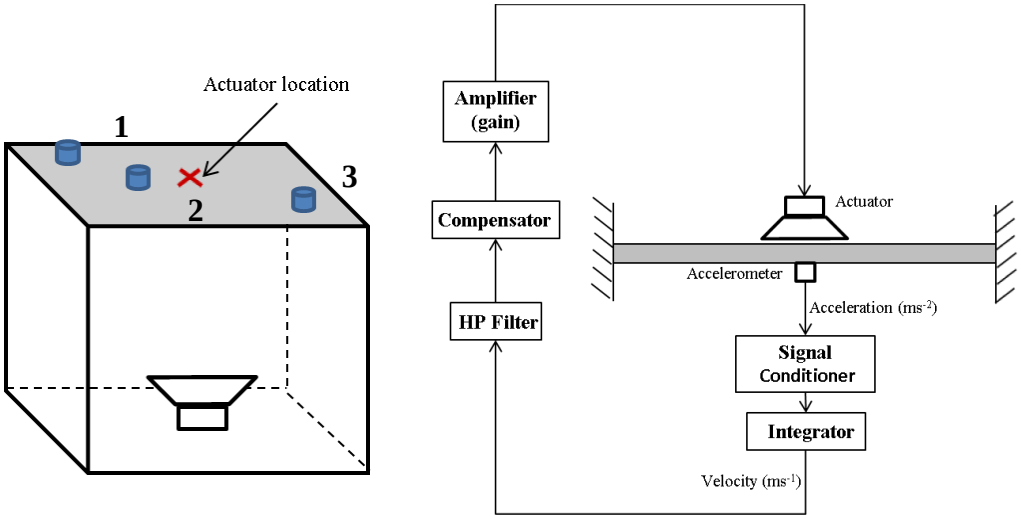

Figure 6.19 – Experimental set-up and block diagram of the feedback control system. The location of the accelerometers has been indicated on the panel.

The enclosure on which the panel was clamped was pressurised in order to change the deflection of the panel and perform measurements for the three levels of curvature corresponding to a deflection of 0 mm, 1 mm and 2 mm in the centre of the panel. In the first stage, the 6-dB gain margin was determined by the measurement and real-time amplification of the open-loop response when only the actuator was exciting the panel. Defining this limit was important in order to adjust the input voltage into the actuator such that spillover and instabilities could be avoided during real-time control experiments. Then the feedback loop was closed and real-time feedback control was performed. The measured open-loop response amplified to the feedback gain to the 6-dB gain margin is shown in the Nyquist and Bode plots of Figure 6.20 for the three levels of curvature.

The open-loop response FRF of the flat panel is again characterised by two resonance peaks under 100 Hz, corresponding to the actuator's coupled natural frequency and the panel's coupled first natural frequency. These peaks correspond to the left-side lobe and the right-side circles of the Nyquist plot respectively. With the increase in curvature, the modes of the panel are shifted towards higher frequencies which results in an increase in distance between the actuator resonance and the panel's first mode resonance. The resonance peak of the actuator is attenuated by the panel stiffening with the introduction of curvature. This behaviour is translated in the Nyquist plot of the open-loop response through the gradual reduction of the left-side lobe. As discussed previously, all these factors contribute to an improvement in the feedback loop stability. Although the compensator largely removes the left-hand lobe in the Nyquist plots for larger curvatures, it can be seen in the results with no curvature due to the effects of the high-pass filter.

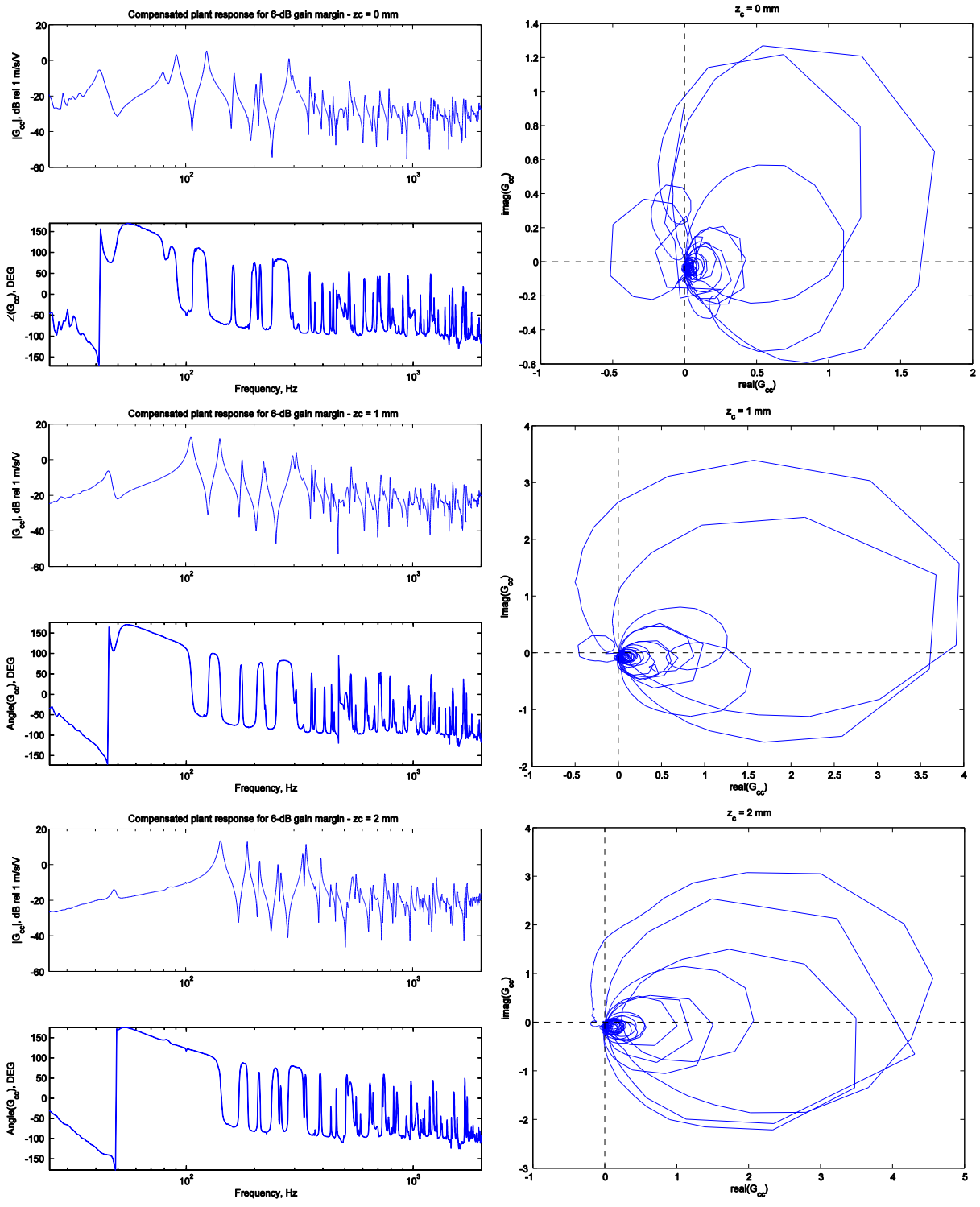

Figure 6.20 – Bode (left) and Nyquist plots of the open-loop response for a 6-dB gain margin, for increasing curvature.

Real-time feedback control was performed for the three levels of curvature shown above corresponding to a deflection of 0 mm, 1 mm and 2 mm in the centre of the panel. Before the feedback loop was closed, the gain was adjusted to the 6-dB gain margin

level defined during open-loop measurements. The voltage output of the collocated accelerometer was continuously monitored via the oscilloscope in order to reduce the gain if needed and avoid instability and damage to the actuator.

In order to assess the performance of the controller over increasing curvature, the squared velocity of the panel, measured at the location of the actuator and near the corner of the panel (position 3 in Figure 6.19), were compared with the uncontrolled squared velocity at those locations. Figure 6.21, Figure 6.22 and Figure 6.23 show these graphs for the three levels of curvature. As seen in the Bode plots of Figure 6.20 and the plots of the previous section, the implementation of the actuator on the panel results in coupling interactions between the two. The actuator also acts similarly to a tuned-mass absorber on the panel's first resonance which, for the flat panel, contributes to significant passive reductions.

However, the increase in the curvature of the panel is detrimental to the passive control of the actuator and as it can be observed from the graphs of Figure 6.22 and Figure 6.23, the loaded velocity of the panel looks like the unloaded one. On the other hand, the increase in curvature improves the local performance of the control system such that the panel's first resonance which is the dominating peak in the response is attenuated by up to 20 dB and the enhancement at the actuator's resonance is completely reduced for a panel deflection of $z_c = 2\,mm$. The stability of the system is also maintained with the use of the compensator. However, very little attenuation can be seen in the overall spectra. This is expected since a single-channel system can only effectively control a couple of modes and is not efficient at global control.

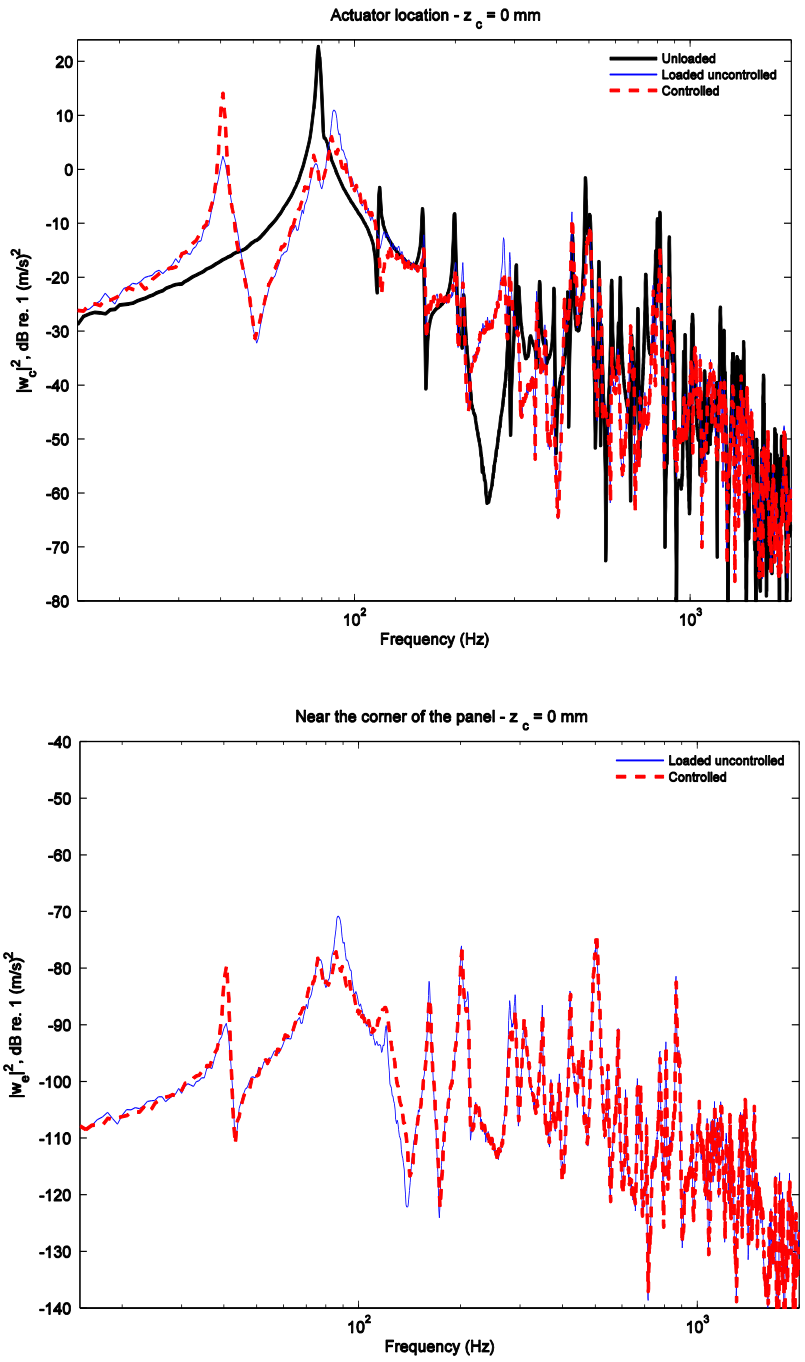

Figure 6.21 – Spectrum of the control velocity at the location of the actuator, w_c, (top) and near the corner of the panel away from the actuator, w_e (bottom) for a flat panel. The response of the panel before mounting the actuator, with the actuator mounted but undriven, and with feedback control with a 6-dB gain margin are shown by the different curves.

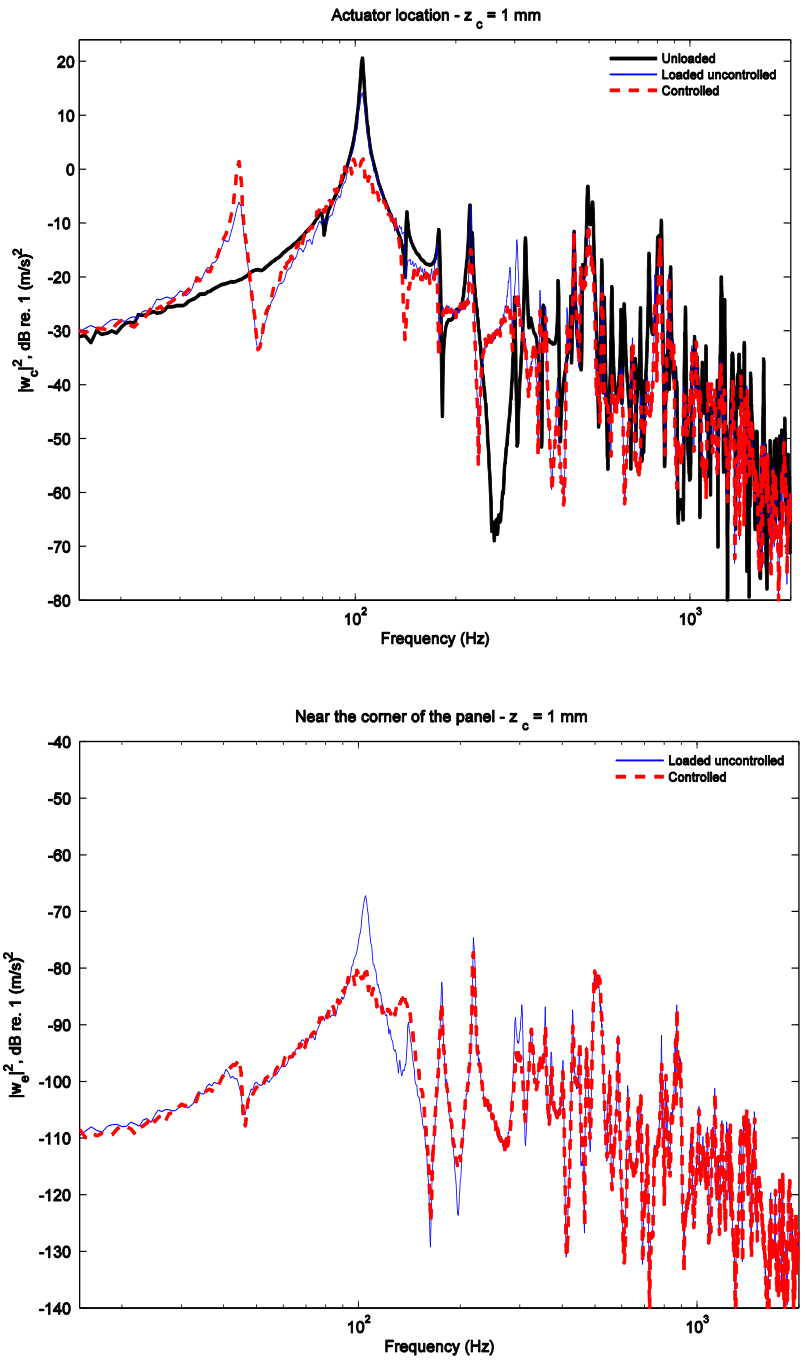

Figure 6.22 –Spectrum of the control velocity at the location of the actuator, w_c, (top) and near the corner of the panel away from the actuator, w_e (bottom) for a curved panel with z_c = 1 mm. The response of the panel before mounting the actuator, with the actuator mounted but undriven, and with feedback control with a 6-dB gain margin are shown by the different curves.

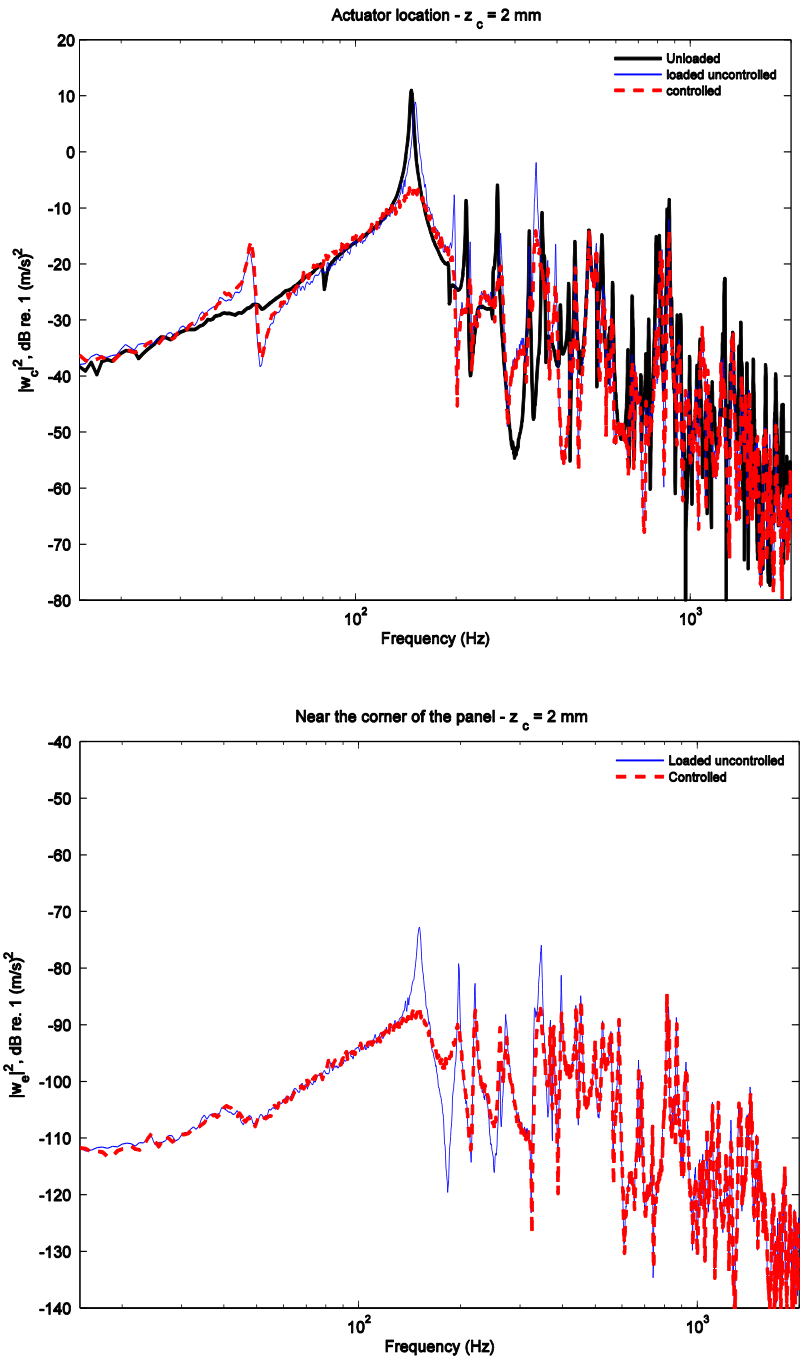

Figure 6.23 – Spectrum of the control velocity at the location of the actuator, $w_{c,}$ (top) and near the corner of the panel away from the actuator, w_e (bottom) for a curved panel with z_c = 2 mm. The response of the panel before mounting the actuator, with the actuator mounted but undriven, and with feedback control with a 6-dB gain margin are shown by the different curves.

The measured velocities spectra at the corner of the panel away from the actuator also show that the attenuation levels are not as good as when the accelerometer is collocated with the actuator. However, except for some of the mode near 150 Hz, no enhancement can be seen at higher frequencies.

6.6 Summary

In this chapter, the real-time implementation of velocity feedback control on an experimental rig was investigated. The rig consisted of an aluminium panel clamped on top of an airtight Perspex enclosure. The air inside the enclosure was pressurised in order to control the deflection in the panel. The actuator was positioned slightly off-centre in order to allow it to couple with more modes.

First, offline simulations of velocity feedback control were performed based on measured transfer responses and the effects of adding a compensator filter in the feedback loop were assessed. The results indicated that the addition of the compensator increased the gain margin and improved the stability of the system. Higher attenuation levels were also achieved in comparison to the uncompensated results. The increase in the curvature of the panel also improved the stability of the control system, pushing the gain margin further away from the optimal gain for which maximum attenuation in the overall response could be achieved. This outcome confirmed the results obtained from simulations in previous chapters. In addition, after an initial improvement in control performance as expected based on previous simulations, the attenuation levels in the response decreased with the increase in curvature. The addition of the compensator to the feedback loop did not significantly affect the optimal gain for which maximum attenuation in the overall response could be achieved.

Despite the changes in curvature, the real-time experiments showed that the stability of the system was not compromised and the compensator-actuator pair remained robust to the changes in the surface shape due to pressurisation. The results from these experiments confirmed the outcomes of the offline simulations and analytical models of the previous chapters.

7. Conclusions and Future Work

7.1 Conclusions

This thesis consisted of two parts. In the first part of the thesis, the effects of curvature on the performance of a velocity feedback control system were investigated when the system was implemented on a rectangular panel. This was done through analytical, numerical and experimental work.

First, a comprehensive study of doubly-curved shell theory was provided in Chapter 2 through the formulation of analytical models of rectangular shells for two different boundary conditions. The analysis of the mode shapes of the shell with increasing curvature showed an increase in the natural frequency of each mode. However, this increase was not uniform for all modes; the lower order modes showed a more pronounced increase, while the natural frequency of the higher order modes did not significantly change with curvature. As a result, at some of the curvature levels, regions of intersection between the modes could be observed, indicating that at those curvature levels, more than one mode could occur at a single frequency or very nearby. Furthermore, towards the highest level of curvature in the defined range, with the difference in the rate of increase for lower-order and higher order modes, all the modes formed a cluster, which is believed to be near the ring frequency of the shell.

As a continuation to the investigations of Chapter 2, in the third chapter, three analytical and numerical finite element models of a homogeneous aluminium rectangular panel were created for different curvatures: 1) the analytical model based on Warburton's theory in which in-plane inertia is not taken into account, (2) the analytical model with in-plane inertia contribution, (3) the ANSYS FEM. The panel was assumed to be supported by shear diaphragms along all four edges.

The effect of curvature increase on the mode shapes was noticeable for medium to high levels of curvature. The modal displacement amplitudes for strong curvature were noticeably smaller in the FEM mode shapes, as a result of the stiffening effect due to curvature increase and modal clustering. This could not be seen in the analytical mode shapes as they were assumed to remain unchanged for all levels of curvature. Therefore,

in order to increase the accuracy of the analytical model, especially at higher levels of curvature, it will be necessary to model the mode shapes such that these changes are accounted for.

Finally, the natural frequencies of the numerical and analytical models were compared with increasing curvature, in order to assess the importance of the contribution of in-plane inertia. All three models showed a similar trend in terms of increasing natural frequency with respect to increasing curvature and occurrence of modal clustering for strong curvature. However, while the natural frequencies of modes where $m = n$ were practically identical across all three models, the other modes of the model derived from Warburton's theory in which in-plane inertia was not accounted for, only agreed with the other two models for light curvature and the natural frequencies of the mode was significantly different from the other two models for strong curvature. Thus, even though Warburton's approach does help to gain a better understanding of the influence of two-dimensional curvature on the free vibrations of shallow shells and provided a good baseline for analytical models, the absence of the contribution of in-plane inertia in the model does not provide an accurate representation of the vibrational behaviour for more general cases.

The outcomes of these two chapters demonstrated the occurrence of modal clustering for increasing curvature. Previous investigations of active vibration control have shown successful results in the attenuation of the low-frequency structural excitations when there are a small number of modes and there is separation between them. It was concluded that this modal clustering could have a detrimental effect on the performance of an active vibration control system installed on the structure.

These effects were assessed in Chapter 4. The results of simulations of velocity feedback control on a modelled simply-supported rectangular panel were shown for increasing curvature. The positive conclusion of this investigation was that the increase in curvature of the panel improved the stability of the system and allowed a larger gain margin in the controller. This is caused by the increase in the stiffness of the panel due to curvature increase. For strong curvatures, the contribution of the actuator dynamics becomes less important. Initially, the increase in curvature improves the performance of the control system. For the panel modelled in this chapter based on given dimensions and physical properties, the performance of the control system was improved up to a

curvature level corresponding to a deflection of 2 mm at the centre of the panel. More generally, for structures where the deflection from the centre is up to 0.8% of their length and width dimensions, efficient attenuations can be achieved when the controller or controllers are positioned in a non-symmetrical arrangement on the structure. Beyond this level of curvature, however, the clustering of the modes tended to reduce the effect of active control.

Chapter 5 looked into the implementation of velocity feedback control through a case study on a vehicle roof panel. While there was limited agreement between the results from experiments and finite element analysis, they both showed the occurrence of modal clusters after 200 Hz. The difficulty in identifying the accurate boundary conditions for the FEM of the roof panel did not allow the validation of the model over the whole frequency range of observation.

In the second part of the chapter, simulations of feedback control based on numerical and measured results were performed for arrangements of 2 and 4 ideal controllers positioned in an attempt to cancel the first two modes of the roof. The outcomes of this simulation presented a great concern for the successful implementation of a feedback control system on the roof panel of the car. Even though the first two modes of the system were significantly attenuated, based on the results obtained from the FEM, the response of the structure in the frequency range of interest that contributes to the interior noise cannot be controlled. The first two modes of the roof occurred at frequencies that were too low to allow the selection and design of an appropriate actuator with internal dynamics that would not compromise the stability of the control system without introducing significant changes in the mass and stiffness of the actuator that would be unreasonable for the size and weight constraints.

Despite the lack of success in controlling the response of strongly-curved panels such as the vehicle roof, the outcomes of Chapter 4 remain promising for shallow shells of low levels of curvature. These results can be promising for the applications of feedback control systems on surfaces with low levels of curvature such as the fuselage of airplanes because of the structural deformation that it undergoes during pressurisation/depressurisation. As the fuselage tends to slightly bow during these processes, a small section of the body can then be considered as a doubly-curved panel of small curvature fitted on an enclosure.

For this purpose, the orientation of this thesis moved away from the application of feedback control to panels, and in the second part of the thesis, the performance of the control system was assessed over increasing curvature when the structure was assumed to be part of an otherwise rigid enclosure. The effects of curvature on structural-acoustic coupling and sound transmission into the enclosure were studied before and after closing the feedback loop.

The last chapter of the thesis presented the real-time implementation of velocity feedback control on an experimental rig. In the first part of the chapter, offline simulations of velocity feedback control were performed based on measured transfer responses and the effects of adding a compensator in the feedback loop were assessed.

The results indicated that the addition of the compensator increased the gain margin and improved the stability of the system. Higher attenuation levels were also achieved in comparison to the uncompensated results. The increase in the curvature of the panel also improved the stability of the control system, pushing the gain margin further away from the optimal gain for which maximum attenuation in the overall response could be achieved. This outcome confirmed the results obtained from simulations in previous chapters. In addition, after an initial improvement in control performance as expected based on previous simulations, the attenuation levels in the response decreased with the increase in curvature. The addition of the compensator to the feedback loop did not significantly affect the optimal gain for which maximum attenuation in the overall response could be achieved. Despite the changes in curvature, the real-time experiments showed that the stability of the system was not compromised and the compensator-actuator pair remained robust to the changes in the surface shape.

7.2 Future Work

The outcomes of this thesis have identified several areas in which further work could be done towards achieving a successful practical implementation of velocity feedback control on curved structures.

- The analytical model can be further improved to cover more general cases, such as medium and thick shells and also varying rather than uniform curvature.

- Now that a better understanding of the effect of curvature on the performance of an active control system has been gained, the control algorithm could be improved in the next step, for example, through the implementation of a frequency-dependent gain filter, rather than a constant gain. The single-channel feedback control system with compensator shows promising results for the implementation of a robust control system and the increase curvature further improves the stability of the control system. In real-life systems, such as an aircraft fuselage, the curvature varies with the changes in the pressure at different altitudes. Therefore, in the next step, the possibility of self-tuning the control system to adapt to changes in curvature for further stability and better performance could be investigated, using the method cited in [15] [118].

- The results of Chapter 6 also demonstrated that the stability of the control system is maintained without significant changes in the optimal gain. Therefore, future multi-channel implementation of this system could be investigated. In addition, self-tuning of the decentralised multiple-channel feedback control system should also be considered [15] [118]. This will allow more efficient control of the cluster of modes on a curve structure.

- Another potential area of future work is the investigation of different types of actuator. This could be in continuation to the work done by [119], where the application of PVDF actuators has been investigated for doubly-curved structures. These actuators might be more suitable for the application of control to curved structures, because their distributed force, rather than point force, would allow a better coupling with the dominant in-plane modes that cannot be controlled with inertial actuators. One challenge in this area is the choice of collocated and dual sensor, since Elliott et al and Gardonio et al have shown in [27] [120] that using a similar distributed sensor leads to large plant response at high frequencies because of the coupling via in-plane modes.

Appendices

Appendix A. Natural Frequencies and Mode Shapes of Rectangular Panels

For any given boundary condition, the natural frequencies of a rectangular panel can be formulated as [121] [97]

$$\omega_{mn} = \sqrt{\frac{Eh^2}{12\left(1-\nu^2\right)}}\left(\frac{\pi}{l_x}\right)^2 q_{mn}, \tag{A.1}$$

where q_{mn} is calculated from

$$q_{mn} = \sqrt{G_x^4(m)+G_y^4(n)\left(\frac{l_x}{l_y}\right)^4 + 2\left(\frac{l_x}{l_y}\right)^2\left[\nu H_x(m)H_y(n)+\left(1-\nu\right)J_x(m)J_y(n)\right]}, \tag{A.2}$$

and $G_x(m), G_y(n), H_x(m), H_y(n), J_x(m)$ and $J_y(n)$ are constants defined in Table A. 1 for all sides clamped (C-C-C-C).

Table A. 1 - Values for the constants G_x, H_x and J_x for clamped boundary conditions along the y-direction. The constant G_y, H_y and J_y for boundary conditions along the x-directions have the same values [117] [93].

Boundary Conditions	m	G_x	H_x	J_x
$C-C-C-C$ $W(0)=0,\ W'(0)=0$ $W(l)=0,\ W''(l)=0$	1 $2,3,4,\ldots$	1.506 $m+\frac{1}{2}$	1.248 $\left(m+\frac{1}{2}\right)^2\left[1-\frac{4}{(2m+1)\pi}\right]$	

The mode shape functions or natural modes $\phi_{mn}(x,y)$ of the panel are calculated from the product of the beam functions $\varphi_m(x)$ and $\varphi_n(y)$, such that

$$\phi_{mn}(x,y) = \varphi_m(x)\varphi_n(y). \tag{A.3}$$

The beam functions for all sides clamped boundary conditions are given in Table A. 2.

Table A. 2 – Beam functions for clamped boundary conditions in the *x*-direction [117] [93]. The beam functions in the *y*-direction are formulated using the same equations.

Boundary Conditions	$\varphi_m(x)$ for $m = 1,3,5,...$ and $i = \frac{(m+1)}{2}$	$\varphi_m(x)$ for $m = 2,4,6,...$ and $j = \frac{m}{2}$
CCCC $W(0) = 0,$ $W'(0) = 0,$ $W(l) = 0,$ $W''(l) = 0,$	$\varphi_m(x) = \sqrt{2}\left\{\cos\gamma_i\left(\frac{x}{l_x}-\frac{1}{2}\right)+\kappa_m\cosh\gamma_i\left(\frac{x}{l_x}-\frac{1}{2}\right)\right\}$ $\kappa_m = \frac{\sin\frac{\gamma_i}{2}}{\sinh\frac{\gamma_i}{2}}$, with $\tan\frac{\gamma_i}{2}+\tanh\frac{\gamma_i}{2}=0$	$\varphi_m(x) = \sqrt{2}\left\{\sin\gamma_j\left(\frac{x}{l_x}-\frac{1}{2}\right)+\kappa_m\sinh\gamma_j\left(\frac{x}{l_x}-\frac{1}{2}\right)\right\}$ $\kappa_m = -\frac{\sin\frac{\gamma_j}{2}}{\sinh\frac{\gamma_j}{2}}$, with $\tan\frac{\gamma_j}{2}-\tanh\frac{\gamma_j}{2}=0$

The zeros of the gamma functions γ_i and γ_j can be found in Table A. 3.

Table A. 3 – Zeros of the gamma functions defined in Table A. 2 [117] [93].

m	$\tan\frac{\gamma_i}{2}+\tanh\frac{\gamma_i}{2}=0$	$\tan\frac{\gamma_j}{2}-\tanh\frac{\gamma_j}{2}=0$
1	4.73004	7.8532
2	10.9956	14.13716
3	17.27876	20.4204
4	23.5620	26.7036
5	29.8452	32.9868
6, 7, 8, ...	$\frac{(4i-1)\pi}{2}$	$\frac{(4j+1)\pi}{2}$

Appendix B. Natural Frequencies of a Doubly-Curved Rectangular Panel Clamped along all four edges

For a C-C-C-C (all sides clamped) doubly-curved shallow shell with a rectangular base projection of dimensions $l_x \times l_y \times h$, based on the difference between the odd and even modal indices, four different equations are used for defining the out-of-plane mode shapes. The equations for each of the four cases are given in Table B. 1.

Table B. 1 – Equations for the transverse mode shapes of a clamped rectangular panel

Modal indices (*m*,*n*)	Transverse Mode shapes
m and *n* both odd	$w = w(t)\left(\cos\gamma_{m,i}\left(\frac{x}{l_x}-\frac{1}{2}\right)+\kappa_m\cosh\gamma_{m,i}\left(\frac{x}{l_x}-\frac{1}{2}\right)\right)\left(\cos\gamma_{n,i}\left(\frac{y}{l_y}-\frac{1}{2}\right)+\kappa_n\cosh\gamma_{n,i}\left(\frac{y}{l_y}-\frac{1}{2}\right)\right),$
m odd and *n* even	$w = w(t)\left(\cos\gamma_{m,i}\left(\frac{x}{l_x}-\frac{1}{2}\right)+\kappa_m\cosh\gamma_{m,i}\left(\frac{x}{l_x}-\frac{1}{2}\right)\right)\left(\sin\gamma_{n,j}\left(\frac{y}{l_y}-\frac{1}{2}\right)+\kappa_n\sinh\gamma_{n,j}\left(\frac{y}{l_y}-\frac{1}{2}\right)\right),$
m even and *n* odd	$w = w(t)\left(\sin\gamma_{m,j}\left(\frac{x}{l_x}-\frac{1}{2}\right)+\kappa_m\sinh\gamma_{m,j}\left(\frac{x}{l_x}-\frac{1}{2}\right)\right)\left(\cos\gamma_{n,i}\left(\frac{y}{l_y}-\frac{1}{2}\right)+\kappa_n\cosh\gamma_{n,i}\left(\frac{y}{l_y}-\frac{1}{2}\right)\right),$
m and *n* both even	$w = w(t)\left(\sin\gamma_{m,j}\left(\frac{x}{l_x}-\frac{1}{2}\right)+\kappa_m\sinh\gamma_{m,j}\left(\frac{x}{l_x}-\frac{1}{2}\right)\right)\left(\sin\gamma_{n,j}\left(\frac{y}{l_y}-\frac{1}{2}\right)+\kappa_n\sinh\gamma_{n,j}\left(\frac{y}{l_y}-\frac{1}{2}\right)\right).$

The in-plane mode shapes for the shell model described in Chapter 2 are defined using cross sliding-cross sliding boundary conditions as [121] [97]

$$u = U(t)\cos\left(\lambda_x x\right)\sin\left(\lambda_y y\right), \tag{B.1a}$$

$$\upsilon = V(t)\sin\left(\lambda_x x\right)\cos\left(\lambda_y y\right), \tag{B.1b}$$

where $\lambda_x = \frac{m\pi}{l_x}$ and $\lambda_y = \frac{n\pi}{l_y}$.

In order to estimate the natural frequencies for each of the above four cases, the Rayleigh-Ritz method was used with the general expressions for kinetic and strain energy stated in Equations (2.50) and (2.51). Assuming harmonic motion in all three directions, the Lagrange equation was then applied in order to obtain the equations of motion for *u*, υ and *w*. The general equation for the natural frequencies can then be formulated as the Eigenvalue problem

$$\begin{bmatrix} L_{11} & L_{12} & L_{13} \\ L_{21} & L_{22} & L_{23} \\ L_{31} & L_{32} & L_{33} \end{bmatrix} \begin{bmatrix} U \\ V \\ W \end{bmatrix} = -\begin{bmatrix} \ddot{U} \\ \ddot{V} \\ \ddot{W} \end{bmatrix} = \omega^2 \begin{bmatrix} U \\ V \\ W \end{bmatrix}. \tag{B.2}$$

The elements of the above matrix for each of the four different transverse mode shapes are defined in the following subsection.

1. m and n both odd:

$$L_{11} = \frac{E}{\rho\left(1-\nu^2\right)}\left[\lambda_x^2 + \frac{1-\nu}{2}\lambda_y^2\right] \tag{B.3a}$$

$$L_{12} = \frac{E}{\rho\left(1-\nu^2\right)}\lambda_x\lambda_y\left[\nu + \frac{1-\nu}{2}\right] \tag{B.3b}$$

$$L_{13} = \frac{-4E}{\rho\left(1-\nu^2\right)} \frac{4mn\pi^2\lambda_x}{\left(\gamma_{m,i}^4 - m^4\pi^4\right)\left(\gamma_{n,i}^4 - n^4\pi^4\right)} \left(\frac{1}{R_x} + \frac{\nu}{R_y}\right) \left[\kappa_m\left(\gamma_{m,i}^2 - m^2\pi^2\right)\cosh\frac{\gamma_{m,i}}{2}\sin^2\left(\frac{m\pi}{2}\right) - \left(\gamma_{m,i}^2 + m^2\pi^2\right)\cos\frac{\gamma_{m,i}}{2}\sin^2\left(\frac{m\pi}{2}\right)\right] \left[\kappa_n\left(\gamma_{n,i}^2 - n^2\pi^2\right)\cosh\frac{\gamma_{n,i}}{2}\sin^2\left(\frac{n\pi}{2}\right) - \left(\gamma_{n,i}^2 + n^2\pi^2\right)\cos\frac{\gamma_{n,i}}{2}\sin^2\left(\frac{n\pi}{2}\right)\right] \tag{B.3c}$$

$$L_{21} = \frac{E}{\rho\left(1-\nu^2\right)}\lambda_x\lambda_y\left[\nu + \frac{1-\nu}{2}\right] \tag{B.3d}$$

$$L_{22} = \frac{E}{\rho\left(1-\nu^2\right)}\left[\lambda_y^2 + \frac{1-\nu}{2}\lambda_x^2\right] \tag{B.3e}$$

$$L_{23} = \frac{-4E}{\rho\left(1-\nu^2\right)} \frac{4mn\pi^2\lambda_y}{\left(\gamma_{m,i}^4 - m^4\pi^4\right)\left(\gamma_{n,i}^4 - n^4\pi^4\right)} \left(\frac{1}{R_y} + \frac{\nu}{R_x}\right) \left[\kappa_m\left(\gamma_{m,i}^2 - m^2\pi^2\right)\cosh\frac{\gamma_{m,i}}{2}\sin^2\left(\frac{m\pi}{2}\right) - \left(\gamma_{m,i}^2 + m^2\pi^2\right)\cos\frac{\gamma_{m,i}}{2}\sin^2\left(\frac{m\pi}{2}\right)\right] \left[\kappa_n\left(\gamma_{n,i}^2 - n^2\pi^2\right)\cosh\frac{\gamma_{n,i}}{2}\sin^2\left(\frac{n\pi}{2}\right) - \left(\gamma_{n,i}^2 + n^2\pi^2\right)\cos\frac{\gamma_{n,i}}{2}\sin^2\left(\frac{n\pi}{2}\right)\right] \tag{B.3f}$$

$$L_{31} = \frac{4E}{\rho\left(1-\nu^2\right)} \frac{-4mn\pi^2\lambda_x\gamma_{m,i}\gamma_{n,i}}{\left(\gamma_{m,i}^4 - m^4\pi^4\right)\left(\gamma_{n,i}^4 - n^4\pi^4\right)} \left(\frac{1}{R_x} + \frac{\nu}{R_y}\right) \frac{\left[\kappa_m\left(\gamma_{m,i}^2 - m^2\pi^2\right)\cosh\frac{\gamma_{m,i}}{2}\sin^2\left(\frac{m\pi}{2}\right) - \left(\gamma_{m,i}^2 + m^2\pi^2\right)\cos\frac{\gamma_{m,i}}{2}\sin^2\left(\frac{m\pi}{2}\right)\right]}{\left[\gamma_{m,i} + \gamma_{m,i}\kappa_m^2 + \sin\gamma_{m,i} + \kappa_m\left(4\cosh\frac{\gamma_{m,i}}{2}\sin\frac{\gamma_{m,i}}{2} + 4\cos\frac{\gamma_{m,i}}{2}\sinh\frac{\gamma_{m,i}}{2} + \kappa_m\sinh\gamma_{m,i}\right)\right]} \frac{\left[\kappa_n\left(\gamma_{n,i}^2 - n^2\pi^2\right)\cosh\frac{\gamma_{n,i}}{2}\sin^2\left(\frac{n\pi}{2}\right) - \left(\gamma_{n,i}^2 + n^2\pi^2\right)\cos\frac{\gamma_{n,i}}{2}\sin^2\left(\frac{n\pi}{2}\right)\right]}{\left[\gamma_{n,i} + \gamma_{n,i}\kappa_n^2 + \sin\gamma_{n,i} + \kappa_n\left(4\cosh\frac{\gamma_{n,i}}{2}\sin\frac{\gamma_{n,i}}{2} + 4\cos\frac{\gamma_{n,i}}{2}\sinh\frac{\gamma_{n,i}}{2} + \kappa_n\sinh\gamma_{n,i}\right)\right]} \tag{B.3g}$$

$$L_{32}=\frac{-4E}{\rho\left(1-\nu^2\right)}\frac{4mn\pi^2\lambda_y\gamma_{m,i}\gamma_{n,i}}{\left(\gamma_{m,i}^4-m^4\pi^4\right)\left(\gamma_{n,i}^4-n^4\pi^4\right)}\left(\frac{1}{R_y}+\frac{\nu}{R_x}\right) \tag{B.3h}$$

$$\frac{\left[\kappa_m\left(\gamma_{m,i}^2-m^2\pi^2\right)\cosh\frac{\gamma_{m,i}}{2}\sin^2\left(\frac{m\pi}{2}\right)-\left(\gamma_{m,i}^2+m^2\pi^2\right)\cos\frac{\gamma_{m,i}}{2}\sin^2\left(\frac{m\pi}{2}\right)\right]}{\left[\gamma_{m,i}+\gamma_{m,i}\kappa_m^2+\sin\gamma_{m,i}+\kappa_m\left(4\cosh\frac{\gamma_{m,i}}{2}\sin\frac{\gamma_{m,i}}{2}+4\cos\frac{\gamma_{m,i}}{2}\sinh\frac{\gamma_{m,i}}{2}+\kappa_m\sinh\gamma_{m,i}\right)\right]}$$

$$\frac{\left[\kappa_n\left(\gamma_{n,i}^2-n^2\pi^2\right)\cosh\frac{\gamma_{n,i}}{2}\sin^2\left(\frac{n\pi}{2}\right)-\left(\gamma_{n,i}^2+n^2\pi^2\right)\cos\frac{\gamma_{n,i}}{2}\sin^2\left(\frac{n\pi}{2}\right)\right]}{\left[\gamma_{n,i}+\gamma_{n,i}\kappa_n^2+\sin\gamma_{n,i}+\kappa_n\left(4\cosh\frac{\gamma_{n,i}}{2}\sin\frac{\gamma_{n,i}}{2}+4\cos\frac{\gamma_{n,i}}{2}\sinh\frac{\gamma_{n,i}}{2}+\kappa_n\sinh\gamma_{n,i}\right)\right]}$$

$$L_{33}=\frac{E}{\rho\left(1-\nu^2\right)}\frac{h^2}{12}\times\ldots \tag{B.3i}$$

$$\left\{\frac{12}{h^2}\left(\frac{1}{R_x^2}+\frac{1}{R_y^2}+\frac{2\nu}{R_xR_y}\right)+\ldots\right.$$

$$\left(\frac{\gamma_{m,i}}{l_x}\right)^4\frac{\left[\gamma_{m,i}+\gamma_{m,i}\kappa_m^2+\sin\gamma_{m,i}+\kappa_m\left(\kappa_m\sinh\gamma_{m,i}-(2-2i)\left[\sin\gamma_{m,i}\left(\frac{1}{2}+\frac{i}{2}\right)+\sinh\gamma_{m,i}\left(\frac{1}{2}+\frac{i}{2}\right)\right]\right)\right]}{\left[\gamma_{m,i}+\gamma_{m,i}\kappa_m^2+\sin\gamma_{m,i}+\kappa_m\left(4\cosh\frac{\gamma_{m,i}}{2}\sin\frac{\gamma_{m,i}}{2}+4\cos\frac{\gamma_{m,i}}{2}\sinh\frac{\gamma_{m,i}}{2}+\kappa_m\sinh\gamma_{m,i}\right)\right]}+\ldots$$

$$\left(\frac{\gamma_{n,i}}{l_y}\right)^4\frac{\left[\gamma_{n,i}+\gamma_{n,i}\kappa_n^2+\sin\gamma_{n,i}+\kappa_n\left(\kappa_n\sinh\gamma_{n,i}-(2-2i)\left[\sin\gamma_{n,i}\left(\frac{1}{2}+\frac{i}{2}\right)+\sinh\gamma_{n,i}\left(\frac{1}{2}+\frac{i}{2}\right)\right]\right)\right]}{\left[\gamma_{n,i}+\gamma_{n,i}\kappa_n^2+\sin\gamma_{n,i}+\kappa_n\left(4\cosh\frac{\gamma_{n,i}}{2}\sin\frac{\gamma_{n,i}}{2}+4\cos\frac{\gamma_{n,i}}{2}\sinh\frac{\gamma_{n,i}}{2}+\kappa_n\sinh\gamma_{n,i}\right)\right]}+\ldots.$$

$$\left(\frac{\gamma_{m,i}\gamma_{n,i}}{l_xl_y}\right)^2\frac{1}{\left[\gamma_{m,i}+\gamma_{m,i}\kappa_m^2+\sin\gamma_{m,i}+\kappa_m\left(4\cosh\frac{\gamma_{m,i}}{2}\sin\frac{\gamma_{m,i}}{2}+4\cos\frac{\gamma_{m,i}}{2}\sinh\frac{\gamma_{m,i}}{2}+\kappa_m\sinh\gamma_{m,i}\right)\right]}$$

$$\frac{1}{\left[\gamma_{n,i}+\gamma_{n,i}\kappa_n^2+\sin\gamma_{n,i}+\kappa_n\left(4\cosh\frac{\gamma_{n,i}}{2}\sin\frac{\gamma_{n,i}}{2}+4\cos\frac{\gamma_{n,i}}{2}\sinh\frac{\gamma_{n,i}}{2}+\kappa_n\sinh\gamma_{n,i}\right)\right]}$$

$$\left\{2\nu\left[\gamma_{m,i}\left(-1+\kappa_m^2\right)-\sin\gamma_{m,i}+\kappa_m^2\sinh\gamma_{m,i}\right]\left[\gamma_{n,i}\left(-1+\kappa_n^2\right)-\sin\gamma_{n,i}+\kappa_n^2\sinh\gamma_{n,i}\right]+\ldots\right.$$

$$2(1-\nu)\left[\gamma_{m,i}\left(1-\kappa_m^2\right)-\sin\gamma_{m,i}+\kappa_m\left(-4\cosh\frac{\gamma_{m,i}}{2}\sin\frac{\gamma_{m,i}}{2}+4\cos\frac{\gamma_{m,i}}{2}\sinh\frac{\gamma_{m,i}}{2}+\kappa_m\sinh\gamma_{m,i}\right)\right]$$

$$\left.\left.\left[\gamma_{n,i}\left(1-\kappa_n^2\right)-\sin\gamma_{n,i}+\kappa_n\left(-4\cosh\frac{\gamma_{n,i}}{2}\sin\frac{\gamma_{n,i}}{2}+4\cos\frac{\gamma_{n,i}}{2}\sinh\frac{\gamma_{n,i}}{2}+\kappa_n\sinh\gamma_{n,i}\right)\right]\right]\right\}$$

2. m odd and n even:

$$L_{11}=\frac{E}{\rho\left(1-\nu^2\right)}\left[\lambda_x^2+\frac{1-\nu}{2}\lambda_y^2\right] \tag{B.4a}$$

$$L_{12}=\frac{E}{\rho\left(1-\nu^2\right)}\lambda_x\lambda_y\left[\nu+\frac{1-\nu}{2}\right] \tag{B.4b}$$

$$\begin{aligned}L_{13}=&\frac{4E}{\rho\left(1-\nu^2\right)}\frac{4mn\pi^2\lambda_x}{\left(\gamma_i^4-m^4\pi^4\right)\left(\gamma_j^4-n^4\pi^4\right)}\left(\frac{1}{R_x}+\frac{\nu}{R_y}\right)\\&\left[\kappa_{m,i}\left(\gamma_i^2-m^2\pi^2\right)\cosh\frac{\gamma_i}{2}\sin^2\left(\frac{m\pi}{2}\right)-\left(\gamma_i^2+m^2\pi^2\right)\cos\frac{\gamma_i}{2}\sin^2\left(\frac{m\pi}{2}\right)\right]...\\&\left[\kappa_{n,j}\left(\gamma_j^2-n^2\pi^2\right)\cos^2\left(\frac{n\pi}{2}\right)\sinh\frac{\gamma_j}{2}-\left(\gamma_j^2+n^2\pi^2\right)\cos^2\left(\frac{n\pi}{2}\right)\sin\frac{\gamma_j}{2}\right]\end{aligned} \tag{B.4c}$$

$$L_{21}=\frac{E}{\rho\left(1-\nu^2\right)}\lambda_x\lambda_y\left[\nu+\frac{1-\nu}{2}\right] \tag{B.4d}$$

$$L_{22}=\frac{E}{\rho\left(1-\nu^2\right)}\left[\lambda_y^2+\frac{1-\nu}{2}\lambda_x^2\right] \tag{B.4e}$$

$$\begin{aligned}L_{23}=&\frac{4E}{\rho\left(1-\nu^2\right)}\frac{4mn\pi^2\lambda_y}{\left(\gamma_i^4-m^4\pi^4\right)\left(\gamma_j^4-n^4\pi^4\right)}\left(\frac{1}{R_y}+\frac{\nu}{R_x}\right)\\&\left[\kappa_{m,i}\left(\gamma_i^2-m^2\pi^2\right)\cosh\frac{\gamma_i}{2}\sin^2\left(\frac{m\pi}{2}\right)-\left(\gamma_i^2+m^2\pi^2\right)\cos\frac{\gamma_i}{2}\sin^2\left(\frac{m\pi}{2}\right)\right]\\&\left[\kappa_{n,j}\left(\gamma_j^2-n^2\pi^2\right)\cos^2\left(\frac{n\pi}{2}\right)\sinh\frac{\gamma_j}{2}-\left(\gamma_j^2+n^2\pi^2\right)\cos^2\left(\frac{n\pi}{2}\right)\sin\frac{\gamma_j}{2}\right]\end{aligned} \tag{B.4f}$$

$$\begin{aligned}L_{31}=&\frac{4E}{\rho\left(1-\nu^2\right)}\frac{4mn\pi^2\lambda_x\gamma_i\gamma_j}{\left(\gamma_i^4-m^4\pi^4\right)\left(\gamma_j^4-n^4\pi^4\right)}\left(\frac{1}{R_x}+\frac{\nu}{R_y}\right)\\&\frac{\left[\kappa_{m,i}\left(\gamma_i^2-m^2\pi^2\right)\cosh\frac{\gamma_i}{2}\sin^2\left(\frac{m\pi}{2}\right)-\left(\gamma_i^2+m^2\pi^2\right)\cos\frac{\gamma_i}{2}\sin^2\left(\frac{m\pi}{2}\right)\right]}{\left[\gamma_i\left(1+\kappa_{m,i}^2\right)+\sin\gamma_i+\kappa_{m,i}\left(4\cosh\frac{\gamma_i}{2}\sin\frac{\gamma_i}{2}+4\cos\frac{\gamma_i}{2}\sinh\frac{\gamma_i}{2}+\kappa_{m,i}\sinh\gamma_i\right)\right]}\\&\frac{\left[\kappa_{n,j}\left(\gamma_j^2-n^2\pi^2\right)\cos^2\left(\frac{n\pi}{2}\right)\sinh\frac{\gamma_j}{2}-\left(\gamma_j^2+n^2\pi^2\right)\cos^2\left(\frac{n\pi}{2}\right)\sin\frac{\gamma_j}{2}\right]}{\left[\gamma_j\left(1-\kappa_{n,j}^2\right)-\sin\gamma_j+\kappa_{n,j}\left(4\cosh\frac{\gamma_j}{2}\sin\frac{\gamma_j}{2}-4\cos\frac{\gamma_j}{2}\sinh\frac{\gamma_j}{2}+\kappa_{n,j}\sinh\gamma_j\right)\right]}\end{aligned} \tag{B.4g}$$

$$L_{32}=\frac{4E}{\rho\left(1-\nu^2\right)}\frac{4mn\pi^2\lambda_y\gamma_i\gamma_j}{\left(\gamma_i^4-m^4\pi^4\right)\left(\gamma_j^4-n^4\pi^4\right)}\left(\frac{1}{R_y}+\frac{\nu}{R_x}\right)$$
$$\frac{\left[\kappa_{m,i}\left(\gamma_i^2-m^2\pi^2\right)\cosh\frac{\gamma_i}{2}\sin^2\left(\frac{m\pi}{2}\right)-\left(\gamma_i^2+m^2\pi^2\right)\cos\frac{\gamma_i}{2}\sin^2\left(\frac{m\pi}{2}\right)\right]}{\left[\gamma_i\left(1+\kappa_{m,i}^2\right)+\sin\gamma_i+\kappa_{m,i}\left(4\cosh\frac{\gamma_i}{2}\sin\frac{\gamma_i}{2}+4\cos\frac{\gamma_i}{2}\sinh\frac{\gamma_i}{2}+\kappa_{m,i}\sinh\gamma_i\right)\right]}$$
$$\frac{\left[\kappa_{n,j}\left(\gamma_j^2-n^2\pi^2\right)\cos^2\left(\frac{n\pi}{2}\right)\sinh\frac{\gamma_j}{2}-\left(\gamma_j^2+n^2\pi^2\right)\cos^2\left(\frac{n\pi}{2}\right)\sin\frac{\gamma_j}{2}\right]}{\left[\gamma_j\left(1-\kappa_{n,j}^2\right)-\sin\gamma_j+\kappa_{n,j}\left(4\cosh\frac{\gamma_j}{2}\sin\frac{\gamma_j}{2}-4\cos\frac{\gamma_j}{2}\sinh\frac{\gamma_j}{2}+\kappa_{n,j}\sinh\gamma_j\right)\right]} \qquad \text{(B.4h)}$$

$$L_{33}=\frac{E}{\rho\left(1-\nu^2\right)}\frac{h^2}{12}\times\left\{\frac{12}{h^2}\left(\frac{1}{R_x^2}+\frac{1}{R_y^2}+\frac{2\nu}{R_xR_y}\right)+\ldots\right.$$
$$\left(\frac{\gamma_i}{l_x}\right)^4\frac{\left[\gamma_i\left(1+\kappa_{m,i}^2\right)+\sin\gamma_i+\kappa_{m,i}\left(\kappa_{m,i}\sinh\left(\gamma_i\right)-\left(2-2i\right)\left[\sin\gamma_i\left(\frac{1}{2}+\frac{i}{2}\right)-\sinh\gamma_i\left(\frac{1}{2}+\frac{i}{2}\right)\right]\right)\right]}{\left[\gamma_i\left(1+\kappa_{m,i}^2\right)+\sin\gamma_i+\kappa_{m,i}\left(4\cosh\frac{\gamma_i}{2}\sin\frac{\gamma_i}{2}+4\cos\frac{\gamma_i}{2}\sinh\frac{\gamma_i}{2}+\kappa_{m,i}\sinh\gamma_i\right)\right]}+\ldots$$
$$\left(\frac{\gamma_j}{l_y}\right)^4\frac{\left[\gamma_j\left(1-\kappa_{n,j}^2\right)-\sin\gamma_j+\kappa_{n,j}\left(-4\cosh\frac{\gamma_j}{2}\sin\frac{\gamma_j}{2}+4\cos\frac{\gamma_j}{2}\sinh\frac{\gamma_j}{2}+\kappa_{n,j}\sinh\gamma_j\right)\right]}{\left[\gamma_j\left(1-\kappa_{n,j}^2\right)-\sin\gamma_j+\kappa_{n,j}\left(4\cosh\frac{\gamma_j}{2}\sin\frac{\gamma_j}{2}-4\cos\frac{\gamma_j}{2}\sinh\frac{\gamma_j}{2}+\kappa_{n,j}\sinh\gamma_j\right)\right]}+\ldots$$
$$\left(\frac{\gamma_i\gamma_j}{l_xl_y}\right)^2\frac{1}{\left[\gamma_i\left(1+\kappa_{m,i}^2\right)+\sin\gamma_i+\kappa_{m,i}\left(4\cosh\frac{\gamma_i}{2}\sin\frac{\gamma_i}{2}+4\cos\frac{\gamma_i}{2}\sinh\frac{\gamma_i}{2}+\kappa_{n,i}\sinh\gamma_i\right)\right]}$$
$$\frac{1}{\left[\gamma_j\left(1-\kappa_{n,j}^2\right)-\sin\gamma_j+\kappa_{n,j}\left(4\cosh\frac{\gamma_j}{2}\sin\frac{\gamma_j}{2}-4\cos\frac{\gamma_j}{2}\sinh\frac{\gamma_j}{2}+\kappa_{n,j}\sinh\gamma_j\right)\right]}$$
$$\left\{-2\nu\left[\gamma_i\left(-1+\kappa_{m,i}^2\right)-\sin\gamma_i+\kappa_{m,i}^2\sinh\gamma_i\right]\left[\gamma_j\left(1+\kappa_{n,j}^2\right)-\sin\gamma_j-\kappa_{n,j}^2\sinh\gamma_j\right]+\ldots\right.$$
$$2\left(1-\nu\right)\left[\gamma_i\left(1-\kappa_{m,i}^2\right)-\sin\gamma_i+\kappa_{m,i}\left(-4\cosh\frac{\gamma_i}{2}\sin\frac{\gamma_i}{2}+4\cos\frac{\gamma_i}{2}\sinh\frac{\gamma_i}{2}+\kappa_{m,i}\sinh\gamma_i\right)\right]\ldots$$
$$\left.\left.\left[\gamma_j+\gamma_j\kappa_{n,j}^2+\sin\gamma_j+\kappa_{n,j}\left(4\cosh\frac{\gamma_j}{2}\sin\frac{\gamma_j}{2}+4\cos\frac{\gamma_j}{2}\sinh\frac{\gamma_j}{2}+\kappa_{n,j}\sinh\gamma_j\right)\right]\right\}\right\} \qquad \text{(B.4i)}$$

3. m even and n odd:

$$L_{11}=\frac{E}{\rho\left(1-\nu^2\right)}\left[\lambda_x^2+\frac{1-\nu}{2}\lambda_y^2\right] \tag{B.5a}$$

$$L_{12}=\frac{E}{\rho\left(1-\nu^2\right)}\lambda_x\lambda_y\left[\nu+\frac{1-\nu}{2}\right] \tag{B.5b}$$

$$\begin{aligned}L_{13}=&\frac{4E}{\rho\left(1-\nu^2\right)}\frac{4mn\pi^2\lambda_x}{\left(\gamma_{m,j}^4-m^4\pi^4\right)\left(\gamma_{n,i}^4-n^4\pi^4\right)}\left(\frac{1}{R_x}+\frac{\nu}{R_y}\right)\\&\left[\kappa_n\left(\gamma_{n,i}^2-n^2\pi^2\right)\cosh\frac{\gamma_{n,i}}{2}\sin^2\left(\frac{n\pi}{2}\right)-\left(\gamma_{n,i}^2+n^2\pi^2\right)\cos\frac{\gamma_{n,i}}{2}\sin^2\left(\frac{n\pi}{2}\right)\right]\\&\left[\kappa_m\left(\gamma_{m,j}^2-m^2\pi^2\right)\cos^2\left(\frac{m\pi}{2}\right)\sinh\frac{\gamma_{m,j}}{2}-\left(\gamma_{m,j}^2+m^2\pi^2\right)\cos^2\left(\frac{m\pi}{2}\right)\sin\frac{\gamma_{m,j}}{2}\right]\end{aligned} \tag{B.5c}$$

$$L_{21}=\frac{E}{\rho\left(1-\nu^2\right)}\lambda_x\lambda_y\left[\nu+\frac{1-\nu}{2}\right] \tag{B.5d}$$

$$L_{22}=\frac{E}{\rho\left(1-\nu^2\right)}\left[\lambda_y^2+\frac{1-\nu}{2}\lambda_x^2\right] \tag{B.5e}$$

$$\begin{aligned}L_{23}=&\frac{4E}{\rho\left(1-\nu^2\right)}\frac{4mn\pi^2\lambda_y}{\left(\gamma_{m,j}^4-m^4\pi^4\right)\left(\gamma_{n,i}^4-n^4\pi^4\right)}\left(\frac{1}{R_y}+\frac{\nu}{R_x}\right)\\&\left[\kappa_n\left(\gamma_{n,i}^2-n^2\pi^2\right)\cosh\frac{\gamma_{n,i}}{2}\sin^2\left(\frac{n\pi}{2}\right)-\left(\gamma_{n,i}^2+n^2\pi^2\right)\cos\frac{\gamma_{n,i}}{2}\sin^2\left(\frac{n\pi}{2}\right)\right]\\&\left[\kappa_m\left(\gamma_{m,j}^2-m^2\pi^2\right)\cos^2\left(\frac{m\pi}{2}\right)\sinh\frac{\gamma_{m,j}}{2}-\left(\gamma_{m,j}^2+m^2\pi^2\right)\cos^2\left(\frac{m\pi}{2}\right)\sin\frac{\gamma_{m,j}}{2}\right]\end{aligned} \tag{B.5f}$$

$$\begin{aligned}L_{31}=&\frac{4E}{\rho\left(1-\nu^2\right)}\frac{4mn\pi^2\lambda_x\gamma_{n,i}\gamma_{m,j}}{\left(\gamma_{m,j}^4-m^4\pi^4\right)\left(\gamma_{n,i}^4-n^4\pi^4\right)}\left(\frac{1}{R_x}+\frac{\nu}{R_y}\right)\\&\frac{\left[\kappa_n\left(\gamma_{n,i}^2-n^2\pi^2\right)\cosh\frac{\gamma_{n,i}}{2}\sin^2\left(\frac{n\pi}{2}\right)-\left(\gamma_{n,i}^2+n^2\pi^2\right)\cos\frac{\gamma_{n,i}}{2}\sin^2\left(\frac{n\pi}{2}\right)\right]}{\left[\gamma_{n,i}+\gamma_{n,i}\kappa_n^2+\sin\gamma_{n,i}+\kappa_n\left(4\cosh\frac{\gamma_{n,i}}{2}\sin\frac{\gamma_{n,i}}{2}+4\cos\frac{\gamma_{n,i}}{2}\sinh\frac{\gamma_{n,i}}{2}+\kappa_n\sinh\gamma_{n,i}\right)\right]}\\&\frac{\left[\kappa_m\left(\gamma_{m,j}^2-m^2\pi^2\right)\cos^2\left(\frac{m\pi}{2}\right)\sinh\frac{\gamma_{m,j}}{2}-\left(\gamma_{m,j}^2+m^2\pi^2\right)\cos^2\left(\frac{m\pi}{2}\right)\sin\frac{\gamma_{m,j}}{2}\right]}{\left[\gamma_{m,j}-\gamma_{m,j}\kappa_m^2-\sin\gamma_{m,j}+\kappa_m\left(4\cosh\frac{\gamma_{m,j}}{2}\sin\frac{\gamma_{m,j}}{2}-4\cos\frac{\gamma_{m,j}}{2}\sinh\frac{\gamma_{m,j}}{2}+\kappa_m\sinh\gamma_{m,j}\right)\right]}\end{aligned} \tag{B.5g}$$

$$L_{32}=\frac{4E}{\rho\left(1-\nu^2\right)}\frac{4mn\pi^2\lambda_y\gamma_{n,i}\gamma_{m,j}}{\left(\gamma_{m,j}^4-m^4\pi^4\right)\left(\gamma_{n,i}^4-n^4\pi^4\right)}\left(\frac{1}{R_y}+\frac{\nu}{R_x}\right)$$
$$\frac{\left[\kappa_n\left(\gamma_{n,i}^2-n^2\pi^2\right)\cosh\frac{\gamma_{n,i}}{2}\sin^2\left(\frac{n\pi}{2}\right)-\left(\gamma_{n,i}^2+n^2\pi^2\right)\cos\frac{\gamma_{n,i}}{2}\sin^2\left(\frac{n\pi}{2}\right)\right]}{\left[\gamma_{n,i}+\gamma_{n,i}\kappa_n^2+\sin\gamma_{n,i}+\kappa_n\left(4\cosh\frac{\gamma_{n,i}}{2}\sin\frac{\gamma_{n,i}}{2}+4\cos\frac{\gamma_{n,i}}{2}\sinh\frac{\gamma_{n,i}}{2}+\kappa_n\sinh\gamma_{n,i}\right)\right]}$$
$$\frac{\left[\kappa_m\left(\gamma_{m,j}^2-m^2\pi^2\right)\cos^2\left(\frac{m\pi}{2}\right)\sinh\frac{\gamma_{m,j}}{2}-\left(\gamma_{m,j}^2+m^2\pi^2\right)\cos^2\left(\frac{m\pi}{2}\right)\sin\frac{\gamma_{m,j}}{2}\right]}{\left[\gamma_{m,j}-\gamma_{m,j}\kappa_m^2-\sin\gamma_{m,j}+\kappa_m\left(4\cosh\frac{\gamma_{m,j}}{2}\sin\frac{\gamma_{m,j}}{2}-4\cos\frac{\gamma_{m,j}}{2}\sinh\frac{\gamma_{m,j}}{2}+\kappa_m\sinh\gamma_{m,j}\right)\right]} \quad \text{(B.5h)}$$

$$L_{33}=\frac{E}{\rho\left(1-\nu^2\right)}\frac{h^2}{12}$$
$$\left\{\frac{12}{h^2}\left(\frac{1}{R_x^2}+\frac{1}{R_y^2}+\frac{2\nu}{R_xR_y}\right)+\ldots\right.$$
$$\left(\frac{\gamma_{m,j}}{l_x}\right)^4\frac{\left[\gamma_{m,j}-\gamma_{m,j}\kappa_m^2-\sin\gamma_{m,j}+\kappa_m\left(-4\cosh\frac{\gamma_{m,j}}{2}\sin\frac{\gamma_{m,j}}{2}+4\cos\frac{\gamma_{m,j}}{2}\sinh\frac{\gamma_{m,j}}{2}+\kappa_m\sinh\gamma_{m,j}\right)\right]}{\left[\gamma_{m,j}-\gamma_{m,j}\kappa_m^2-\sin\gamma_{m,j}+\kappa_m\left(4\cosh\frac{\gamma_{m,j}}{2}\sin\frac{\gamma_{m,j}}{2}-4\cos\frac{\gamma_{m,j}}{2}\sinh\frac{\gamma_{m,j}}{2}+\kappa_m\sinh\gamma_{m,j}\right)\right]}+\ldots$$
$$\left(\frac{\gamma_{n,j}}{l_y}\right)^4\frac{\left[\gamma_{n,i}+\gamma_{n,i}\kappa_n^2+\sin\gamma_{n,i}+\kappa_n\left(-(2-2i)\left[\sin\gamma_{n,i}\left(\frac{1}{2}+\frac{i}{2}\right)+\sinh\gamma_{n,i}\left(\frac{1}{2}+\frac{i}{2}\right)\right]+\kappa_n\sinh\left(\gamma_{n,i}\right)\right)\right]}{\left[\gamma_{n,i}+\gamma_{n,i}\kappa_n^2+\sin\gamma_{n,i}+\kappa_n\left(4\cosh\frac{\gamma_{n,i}}{2}\sin\frac{\gamma_{n,i}}{2}+4\cos\frac{\gamma_{n,i}}{2}\sinh\frac{\gamma_{n,i}}{2}+\kappa_n\sinh\gamma_{n,i}\right)\right]}+\ldots$$
$$\left(\frac{\gamma_{n,i}\gamma_{m,j}}{l_xl_y}\right)^2\frac{1}{\left[\gamma_{n,i}+\gamma_{n,i}\kappa_n^2+\sin\gamma_{n,i}+\kappa_n\left(4\cosh\frac{\gamma_{n,i}}{2}\sin\frac{\gamma_{n,i}}{2}+4\cos\frac{\gamma_{n,i}}{2}\sinh\frac{\gamma_{n,i}}{2}+\kappa_n\sinh\gamma_{n,i}\right)\right]}$$
$$\frac{1}{\left[\gamma_{m,j}-\gamma_{m,j}\kappa_m^2-\sin\gamma_{m,j}+\kappa_m\left(4\cosh\frac{\gamma_{m,j}}{2}\sin\frac{\gamma_{m,j}}{2}-4\cos\frac{\gamma_{m,j}}{2}\sinh\frac{\gamma_{m,j}}{2}+\kappa_m\sinh\gamma_{m,j}\right)\right]}$$
$$\left\{-2\nu\left[\gamma_{n,i}\left(-1+\kappa_n^2\right)-\sin\gamma_{n,i}+\kappa_n^2\sinh\gamma_{n,i}\right]\left[\gamma_{m,j}+\gamma_{m,j}\kappa_m^2-\sin\gamma_{m,j}-\kappa_m^2\sinh\gamma_{m,j}\right]+\ldots\right.$$
$$2(1-\nu)\left[\gamma_{n,i}\left(1-\kappa_n^2\right)-\sin\gamma_{n,i}+\kappa_n\left(-4\cosh\frac{\gamma_{n,i}}{2}\sin\frac{\gamma_{n,i}}{2}+4\cos\frac{\gamma_{n,i}}{2}\sinh\frac{\gamma_{n,i}}{2}+\kappa_n\sinh\gamma_{n,i}\right)\right]$$
$$\left.\left.\left[\gamma_{m,j}\left(1+\kappa_m^2\right)+\sin\gamma_{m,j}+\kappa_m\left(4\cosh\frac{\gamma_{m,j}}{2}\sin\frac{\gamma_{m,j}}{2}+4\cos\frac{\gamma_{m,j}}{2}\sinh\frac{\gamma_{m,j}}{2}+\kappa_m\sinh\gamma_{m,j}\right)\right]\right\}\right\} \quad \text{(B.5i)}$$

4. m and n both even:

$$L_{11} = \frac{E}{\rho\left(1-\nu^2\right)}\left[\lambda_x^2 + \frac{1-\nu}{2}\lambda_y^2\right] \tag{B.6a}$$

$$L_{12} = \frac{E}{\rho\left(1-\nu^2\right)}\lambda_x\lambda_y\left[\nu + \frac{1-\nu}{2}\right] \tag{B.6b}$$

$$L_{13} = \frac{-4E}{\rho\left(1-\nu^2\right)}\frac{4mn\pi^2\lambda_x}{\left(\gamma_{m,j}^4 - m^4\pi^4\right)\left(\gamma_{n,j}^4 - n^4\pi^4\right)}\left(\frac{1}{R_x} + \frac{\nu}{R_y}\right)$$
$$\left[\kappa_m\left(\gamma_{m,j}^2 - m^2\pi^2\right)\cos^2\left(\frac{m\pi}{2}\right)\sinh\frac{\gamma_{m,j}}{2} - \left(\gamma_{m,j}^2 + m^2\pi^2\right)\cos^2\left(\frac{m\pi}{2}\right)\sin\frac{\gamma_{m,j}}{2}\right]$$
$$\left[\kappa_n\left(\gamma_{n,j}^2 - n^2\pi^2\right)\cos^2\left(\frac{n\pi}{2}\right)\sinh\frac{\gamma_{n,j}}{2} - \left(\gamma_j^2 + n^2\pi^2\right)\cos^2\left(\frac{n\pi}{2}\right)\sin\frac{\gamma_{n,j}}{2}\right] \tag{B.6c}$$

$$L_{21} = \frac{E}{4\rho\left(1-\nu^2\right)}\lambda_x\lambda_y\left[\nu + \frac{1-\nu}{2}\right] \tag{B.6d}$$

$$L_{22} = \frac{E}{\rho\left(1-\nu^2\right)}\left[\lambda_y^2 + \frac{1-\nu}{2}\lambda_x^2\right] \tag{B.6e}$$

$$L_{23} = \frac{-4E}{\rho\left(1-\nu^2\right)}\frac{4mn\pi^2\lambda_y}{\left(\gamma_{m,j}^4 - m^4\pi^4\right)\left(\gamma_{n,j}^4 - n^4\pi^4\right)}\left(\frac{1}{R_y} + \frac{\nu}{R_x}\right)$$
$$\left[\kappa_m\left(\gamma_{m,j}^2 - m^2\pi^2\right)\cos^2\left(\frac{m\pi}{2}\right)\sinh\frac{\gamma_{m,j}}{2} - \left(\gamma_{m,j}^2 + m^2\pi^2\right)\cos^2\left(\frac{m\pi}{2}\right)\sin\frac{\gamma_{m,j}}{2}\right]$$
$$\left[\kappa_n\left(\gamma_{n,j}^2 - n^2\pi^2\right)\cos^2\left(\frac{n\pi}{2}\right)\sinh\frac{\gamma_{n,j}}{2} - \left(\gamma_{n,j}^2 + n^2\pi^2\right)\cos^2\left(\frac{n\pi}{2}\right)\sin\frac{\gamma_{n,j}}{2}\right] \tag{B.6f}$$

$$L_{31} = \frac{-4E}{\rho\left(1-\nu^2\right)}\frac{4mn\pi^2\lambda_x\gamma_{m,j}\gamma_{n,j}}{\left(\gamma_{m,j}^4 - m^4\pi^4\right)\left(\gamma_{n,j}^4 - n^4\pi^4\right)}\left(\frac{1}{R_x} + \frac{\nu}{R_y}\right)$$
$$\frac{\left[\kappa_m\left(\gamma_{m,j}^2 - m^2\pi^2\right)\cos^2\left(\frac{m\pi}{2}\right)\sinh\frac{\gamma_{m,j}}{2} - \left(\gamma_{m,j}^2 + m^2\pi^2\right)\cos^2\left(\frac{m\pi}{2}\right)\sin\frac{\gamma_{m,j}}{2}\right]}{\left[\gamma_{m,j}\left(-1+\kappa_m^2\right) + \sin\gamma_{m,j} - \kappa_m\left(4\cosh\frac{\gamma_{m,j}}{2}\sin\frac{\gamma_{m,j}}{2} - 4\cos\frac{\gamma_{m,j}}{2}\sinh\frac{\gamma_{m,j}}{2} + \kappa_m\sinh\gamma_{m,j}\right)\right]}$$
$$\frac{\left[\kappa_n\left(\gamma_{n,j}^2 - n^2\pi^2\right)\cos^2\left(\frac{n\pi}{2}\right)\sinh\frac{\gamma_{n,j}}{2} - \left(\gamma_j^2 + n^2\pi^2\right)\cos^2\left(\frac{n\pi}{2}\right)\sin\frac{\gamma_{n,j}}{2}\right]}{\left[\gamma_{n,j}\left(-1+\kappa_n^2\right) + \sin\gamma_{n,j} - \kappa_n\left(4\cosh\frac{\gamma_{n,j}}{2}\sin\frac{\gamma_{n,j}}{2} - 4\cos\frac{\gamma_{n,j}}{2}\sinh\frac{\gamma_{n,j}}{2} + \kappa_n\sinh\gamma_{n,j}\right)\right]} \tag{B.6g}$$

$$L_{32}=\frac{4E}{\rho\left(1-\nu^2\right)}\frac{4mn\pi^2\lambda_y\gamma_{n,i}\gamma_{m,j}}{\left(\gamma_{m,j}^4-m^4\pi^4\right)\left(\gamma_{n,i}^4-n^4\pi^4\right)}\left(\frac{1}{R_y}+\frac{\nu}{R_x}\right) \tag{B.6h}$$

$$\frac{\left[\kappa_n\left(\gamma_{n,i}^2-n^2\pi^2\right)\cosh\frac{\gamma_{n,i}}{2}\sin^2\left(\frac{n\pi}{2}\right)-\left(\gamma_{n,i}^2+n^2\pi^2\right)\cos\frac{\gamma_{n,i}}{2}\sin^2\left(\frac{n\pi}{2}\right)\right]}{\left[\gamma_{n,i}+\gamma_{n,i}\kappa_n^2+\sin\gamma_{n,i}+\kappa_n\left(4\cosh\frac{\gamma_{n,i}}{2}\sin\frac{\gamma_{n,i}}{2}+4\cos\frac{\gamma_{n,i}}{2}\sinh\frac{\gamma_{n,i}}{2}+\kappa_n\sinh\gamma_{n,i}\right)\right]}$$

$$\frac{\left[\kappa_m\left(\gamma_{m,j}^2-m^2\pi^2\right)\cos^2\left(\frac{m\pi}{2}\right)\sinh\frac{\gamma_{m,j}}{2}-\left(\gamma_{m,j}^2+m^2\pi^2\right)\cos^2\left(\frac{m\pi}{2}\right)\sin\frac{\gamma_{m,j}}{2}\right]}{\left[\gamma_{m,j}-\gamma_{m,j}\kappa_m^2-\sin\gamma_{m,j}+\kappa_m\left(4\cosh\frac{\gamma_{m,j}}{2}\sin\frac{\gamma_{m,j}}{2}-4\cos\frac{\gamma_{m,j}}{2}\sinh\frac{\gamma_{m,j}}{2}+\kappa_m\sinh\gamma_{m,j}\right)\right]}$$

$$L_{33}=\frac{E}{\rho\left(1-\nu^2\right)}\frac{h^2}{12}\left\{\frac{12}{h^2}\left(\frac{1}{R_x^2}+\frac{1}{R_y^2}+\frac{2\nu}{R_xR_y}\right)+\ldots \right. \tag{B.6i}$$

$$\left(\frac{\gamma_{m,j}}{l_x}\right)^4\frac{\left[\gamma_{m,j}-\gamma_{m,j}\kappa_m^2-\sin\gamma_{m,j}+\kappa_m\left(-4\cosh\frac{\gamma_{m,j}}{2}\sin\frac{\gamma_{m,j}}{2}+4\cos\frac{\gamma_{m,j}}{2}\sinh\frac{\gamma_{m,j}}{2}+\kappa_m\sinh\gamma_{m,j}\right)\right]}{\left[\gamma_{m,j}\left(1-\kappa_m^2\right)-\sin\gamma_{m,j}+\kappa_m\left(4\cosh\frac{\gamma_{m,j}}{2}\sin\frac{\gamma_{m,j}}{2}-4\cos\frac{\gamma_{m,j}}{2}\sinh\frac{\gamma_{m,j}}{2}+\kappa_m\sinh\gamma_{m,j}\right)\right]}+\ldots$$

$$\left(\frac{\gamma_{n,j}}{l_y}\right)^4\frac{\left[\gamma_{n,j}-\gamma_{n,j}\kappa_n^2-\sin\gamma_{n,j}+\kappa_n\left(-4\cosh\frac{\gamma_{n,j}}{2}\sin\frac{\gamma_{n,j}}{2}+4\cos\frac{\gamma_{n,j}}{2}\sinh\frac{\gamma_{n,j}}{2}+\kappa_n\sinh\gamma_{n,j}\right)\right]}{\left[\gamma_{n,j}\left(1-\kappa_n^2\right)-\sin\gamma_{n,j}+\kappa_n\left(4\cosh\frac{\gamma_{n,j}}{2}\sin\frac{\gamma_{n,j}}{2}-4\cos\frac{\gamma_{n,j}}{2}\sinh\frac{\gamma_{n,j}}{2}+\kappa_n\sinh\gamma_{n,j}\right)\right]}+\ldots$$

$$\left(\frac{\gamma_{m,j}\gamma_{n,j}}{l_xl_y}\right)^2\frac{1}{\left[\gamma_{n,j}\left(1-\kappa_n^2\right)-\sin\gamma_{n,j}+\kappa_n\left(4\cosh\frac{\gamma_{n,j}}{2}\sin\frac{\gamma_{n,j}}{2}-4\cos\frac{\gamma_{n,j}}{2}\sinh\frac{\gamma_{n,j}}{2}+\kappa_n\sinh\gamma_{n,j}\right)\right]}$$

$$\frac{1}{\left[\gamma_{m,j}\left(1-\kappa_m^2\right)-\sin\gamma_{m,j}+\kappa_m\left(4\cosh\frac{\gamma_{m,j}}{2}\sin\frac{\gamma_{m,j}}{2}-4\cos\frac{\gamma_{m,j}}{2}\sinh\frac{\gamma_{m,j}}{2}+\kappa_m\sinh\gamma_{m,j}\right)\right]}$$

$$\left\{2\nu\left[\gamma_{n,j}+\gamma_{n,j}\kappa_n^2-\sin\gamma_{n,j}-\kappa_n^2\sinh\gamma_{n,j}\right]\left[\gamma_{m,j}+\gamma_{m,j}\kappa_m^2-\sin\gamma_{m,j}-\kappa_m^2\sinh\gamma_{m,j}\right]+\ldots\right.$$

$$2\left(1-\nu\right)\left[\gamma_{n,j}+\gamma_{n,j}\kappa_n^2+\sin\gamma_{n,j}+\kappa_n\left(4\cosh\frac{\gamma_{n,j}}{2}\sin\frac{\gamma_{n,j}}{2}+4\cos\frac{\gamma_{n,j}}{2}\sinh\frac{\gamma_{n,j}}{2}+\kappa_n\sinh\gamma_{n,j}\right)\right]$$

$$\left.\left.\left[\gamma_{m,j}+\gamma_{m,j}\kappa_m^2+\sin\gamma_{m,j}+\kappa_m\left(4\cosh\frac{\gamma_{m,j}}{2}\sin\frac{\gamma_{m,j}}{2}+4\cos\frac{\gamma_{m,j}}{2}\sinh\frac{\gamma_{m,j}}{2}+\kappa_m\sinh\gamma_{m,j}\right)\right]\right\}\right\}$$

Appendix C. Elemental Model of a Doubly-Curved Panel Mounted on a Rigid-Walled Enclosure

Comprehensive theoretical studies of the interactions between the vibrations of a flexible structure and the acoustic space of the enclosure it is part of have been presented in [118] [119] [120] [121] based on the initial theory derived by Dowell and Voss in [122]. These theoretical models formulate the coupled response of the system in terms of the uncoupled structural and acoustic modes. Other theoretical studies have concentrated on the matrix formulation of these coupled equations using elemental impedance and mobility approaches, such as [123] [124] [125] [126]. Finite element methods have also been used for the structural-acoustic coupling analysis of enclosures with complex shapes for the implementation of active noise and vibration control techniques, for example in applications to automotive NVH problems [42] [127] [128].

This appendix will present the theoretical elemental model of the experimental rig described in Chapter 6, where a thin aluminium panel is fixed on top of an otherwise rigid-walled enclosure. The effects and degree of coupling between the enclosure acoustic modes and the panel structural modes will be assessed.

C.1 Elemental Model of the system

The structural-acoustic coupled model considered in this section for the derivations of the coupled steady-steady response and study of the effects of the enclosure on the structural behaviour of the panel, is composed of a clamped aluminium panel which is fixed on top of a rectangular enclosure with otherwise rigid-walled boundary conditions. The dimensions and properties of the system can be found in Table C.1 which are based on the experimental rig presented in Chapter 6.

The fully-coupled fluid-structural system includes the enclosure's interior sound field and the vibration field in the aluminium panel, both generated by either an acoustic source located inside the enclosure, or by a force acting on the panel. The results shown here are based on an acoustic excitation which is assumed to be provided by a monopole source positioned in the centre of the bottom of the enclosure. Since the pressure on the

enclosure side of the panel, due to the acoustics of the enclosure, is significantly greater than that on the other side which is due to sound radiation into free space, the latter contribution can be ignored.

Table C. 1 – Dimensions and physical properties of the aluminium panel and the enclosure

Parameter	Value	Units
Panel Dimensions	$l_x = 278$	mm
	$l_y = 247$	mm
Panel Thickness	$h = 1$	mm
Enclosure Height	$l_z = 385$	mm
Panel Density	$\rho = 2700$	kgm^{-3}
Density of Air	$\rho_0 = 1.21$	kgm^{-3}
Speed of Air	$c_0 = 343$	ms^{-1}
Young's Modulus	$E = 7 \times 10^{10}$	Nm^{-2}
Poisson Ratio	$\nu = 0.33$	
Structural Modal Damping Ratio	$\zeta_m = 0.01$	
Acoustic Modal Damping Ratio	$\zeta_n = 0.01$	

The elemental method of Section 4.1 was used to model the system and derive the coupled responses. Figure C. 1 shows a diagram of the modelled enclosure with the location of the excitation source and the elemental grids used to define the volume of the enclosure and surface of the panel.

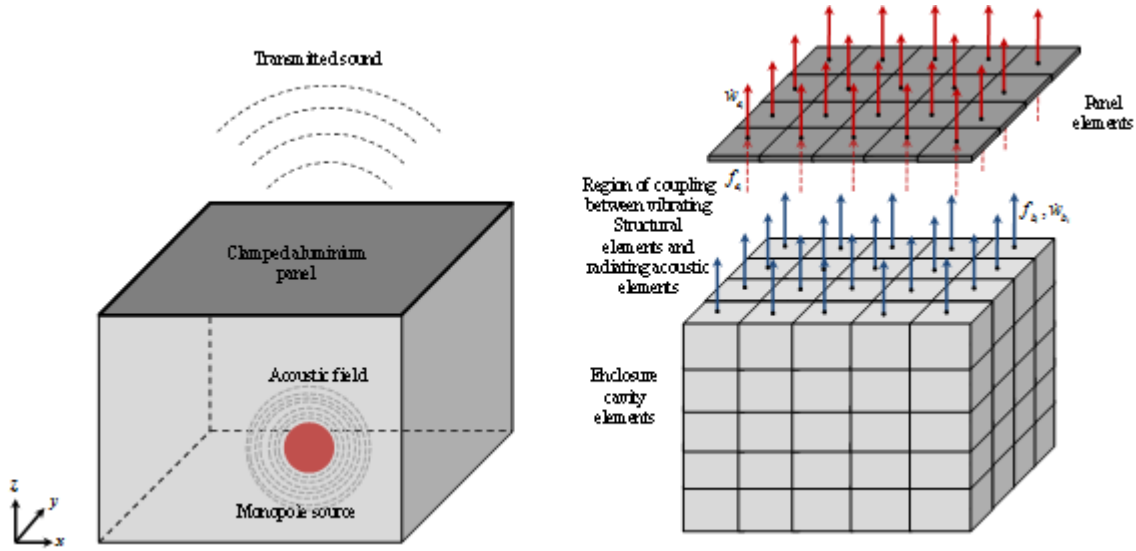

Figure C. 1 – Diagram of the coupled panel (left) and enclosure and elemental representation of the two subsystems (right). f_{ei} and $\dot{w}_{ei}$ refer to one of the panel elements force and complex velocity. f_{bi} and $\dot{w}_{bi}$ refer to one of the cavity elements force and complex velocity.

The elemental resolution of the modelled grid was determined using the approach discussed in Chapter 3, Section 3.1, for a minimum resolution of 4 elements per wavelength. The resulting elemental grid representing the surface of the panel consists of $N_e = N_x \times N_y = 432$ elements $\left(N_x = 24, N_y = 18\right)$. The top side of the enclosure cavity has the same elemental resolution as the panel grid. The height of the cavity is divided into $N_z = 22$ elements so that the total number of elements in the cavity model is $N_v = N_x \times N_y \times N_z = 9504$ elements. The modelled monopole source was assumed to be positioned at coordinates $(x_p, y_p, z_p) = \left(l_x/2, l_y/2, 0.005\right)$ inside the cavity. The volume velocity of the primary acoustic excitation provided by the monopole source which was assumed to be time-harmonic can be defined as

$$q_p(\omega) = \mathrm{Re}\left\{q_p(\omega)e^{j\omega t}\right\}. \tag{C.1}$$

The frequency range of observation was set to 2 kHz while the dynamic frequency range was defined for up to 4 kHz, in order to take into account the contribution of higher frequency acoustic and structural modes. The steady-state total kinetic and acoustic potential energies were calculated up to 2 kHz for various panel curvatures.

The equations describing the mathematical model of the system will be formulated in the two following subsections, in the absence and presence of control. The forces and velocities used in the next subsections will be taken to be the force and velocity phasors respectively, as in Chapter 4, which are the real parts of the counter clockwise rotating complex force and velocity vectors.

C.1.1 Elemental Model without the Actuator:

The acoustic excitation due to the monopole source in the enclosure generates a set of forces at the elements of the panel and the resulting panel velocity, which can be defined as vectors of transverse point forces and velocities at the centre of each element. These elemental force and elemental velocity vectors can be written as

$$\mathbf{f_e} = \left\{ f_{e_1}(\omega) \quad f_{e_2}(\omega) \quad \dots \quad f_{e_{N_e}}(\omega) \right\}^T \tag{C.2}$$

$$\dot{\mathbf{w}}_\mathbf{e} = \left\{ \dot{w}_{e_1}(\omega) \quad \dot{w}_{e_2}(\omega) \quad \dots \quad \dot{w}_{e_{N_e}}(\omega) \right\}^T, \tag{C.3}$$

where the index *e* refers to the elements of the model, $f_{e_1}(\omega), f_{e_2}(\omega), ..., f_{e_{Ne}}(\omega)$ of the force vector correspond to point forces at the centre of each element of the panel grid, and $\dot{w}_{e_1}(\omega), \dot{w}_{e_2}(\omega), ..., \dot{w}_{e_{Ne}}(\omega)$ of the velocity vector are the resulting complex velocities at the same location. The dimension of both vectors is $\left[N_e \times 1\right]$.

Before the panel and the cavity are assumed to be coupled, the uncoupled elemental velocity of the panel is the same as the elemental velocity calculated in Chapter 4 for the *in-vacuo* panel, such that

$$\dot{\mathbf{w}}_\mathbf{e} = \mathbf{Y_{ee}} \mathbf{f_e}, \tag{C.4}$$

where $\mathbf{Y_{ee}}$ is the mobility of the panel, and the vector of elemental forces $\mathbf{f_e}$ is due to the monopole source in the enclosure. The acoustic response of the enclosure due to the panel motion can be expressed in terms of the source strength and the acoustic transfer impedance between the excitation on the panel and the monopole source, and the acoustic transfer impedance between the excitation due to each element on the panel and the pressure at each element as

$$\mathbf{f_e} = \mathbf{z_{ep}} q_p - \mathbf{Z_A} \dot{\mathbf{w}}_\mathbf{e}, \tag{C.5}$$

where the negative sign reflects the fact that $\dot{\mathbf{w}}_\mathbf{e}$ is defined to be positive on the upper panel surface. Substituting Equation (C.5) into Equation (C.4) leads to

$$\dot{\mathbf{w}}_\mathbf{e} = \mathbf{Y_{ee}} \left[\mathbf{z_{ep}} q_p - \mathbf{Z_A} \dot{\mathbf{w}}_\mathbf{e} \right],$$

$$\dot{\mathbf{w}}_\mathbf{e} = \left[\mathbf{I} + \mathbf{Y_{ee}} \mathbf{Z_A} \right]^{-1} \mathbf{Y_{ee}} \mathbf{z_{ep}} q_p, \tag{C.6}$$

where $\mathbf{I}$ is the identity matrix of dimensions $\left[N_e \times N_e \right]$. The mobility matrix $\mathbf{Y_{ee}}$ has dimensions of $\left[N_e \times N_e \right]$ and is expressed as

$$\mathbf{Y_{ee}} = \begin{bmatrix} Y_{ee_{11}} & Y_{ee_{12}} & \cdots & Y_{ee_{1N_e}} \\ Y_{ee_{21}} & \ddots & & Y_{ee_{2N_e}} \\ \vdots & & \ddots & \vdots \\ Y_{ee_{N_e1}} & Y_{ee_{N_e2}} & \cdots & Y_{ee_{N_eN_e}} \end{bmatrix}, \tag{C.7}$$

where the $(i,j)^{\text{th}}$ term $Y_{ee_{ij}}$ of the mobility matrix $\mathbf{Y_{ee}}$, which is the mobility at the i$^{\text{th}}$ element due to the excitation point force exerted at the centre of the j$^{\text{th}}$ element, is calculated from the finite modal expansion approach, defined in Equation (4.15), over the first M structural modes of the panel, as

$$Y_{ee_{ij}} = \frac{\dot{w}_{e_i}}{f_{e_j}} = j\omega \sum_{m=1}^{M} \frac{\phi_m(x_{e_i}, y_{e_i}) \phi_m(x_{e_j}, y_{e_j})}{M_{panel} \left[\omega_m^2 (1 + j2\zeta_m) - \omega^2 \right]}, \tag{C.8}$$

where $\dot{w}_{e_i}$ is the complex velocity at the i$^{\text{th}}$ element, f_{e_j} is the point force acting at the centre of the j$^{\text{th}}$ element, $j = \sqrt{-1}$, $\phi_m(x_{e_i}, y_{e_i})$ and $\phi_m(x_{e_j}, y_{e_j})$ are the natural structural modes at the coordinates of the centres of the i$^{\text{th}}$ and j$^{\text{th}}$ elements respectively, $M_{panel} = \rho l_x l_y h$ is the mass of the aluminium plate in kg, ω_m is the natural frequency of the clamped panel in rad/s calculated based on the equations of Chapter 2, and finally ζ_m is the modal damping ratio of the structural modes which is set to 1% here. The values used for all the parameters can be found in Table C.1.

The acoustic transfer impedance vector $\mathbf{z_{ep}}$ between the primary excitation for the top layer of the cavity and the monopole source has dimensions of $[N_e \times 1]$ and the acoustic transfer impedance matrix $\mathbf{Z_A}$ between the excitation due to each element on the panel and the pressure at each element has dimensions of $[N_e \times N_e]$. These can both be written as

$$\mathbf{z_{ep}} = \begin{bmatrix} Z_{ep_1} \\ Z_{ep_2} \\ \vdots \\ Z_{ep_i} \\ \vdots \\ Z_{ep_{N_e}} \end{bmatrix}. \tag{C.13}$$

$$\mathbf{Z_A} = \begin{bmatrix} Z_{A_{11}} & Z_{A_{12}} & \cdots & Z_{A_{1N_e}} \\ Z_{A_{21}} & \ddots & & Z_{A_{2N_e}} \\ \vdots & & \ddots & \vdots \\ Z_{A_{N_e1}} & Z_{A_{N_e2}} & \cdots & Z_{A_{N_eN_e}} \end{bmatrix}. \tag{C.14}$$

The ith term Z_{ep_i} of the impedance vector $\mathbf{z_{ep}}$, which is the transfer impedance between the force at the ith element of the top layer of the cavity and the monopole excitation source located at (x_p, y_p, z_p) in the enclosure, is calculated from the following finite modal expansion approach, over the first *N* acoustic modes of the cavity, as

$$Z_{ep_i} = \frac{f_{e_i}}{q_p} = \omega \sum_{n=0}^{N} \frac{\rho_0 c_0^2 A_e}{V_{cavity}} \frac{\psi_n(x_{e_i}, y_{e_i}, l_z)\psi_n(x_p, y_p, z_p)}{2\zeta_n \omega_n \omega + j(\omega^2 - \omega_n^2)}, \tag{C.15}$$

where f_{e_i} is the force acting on the ith element, $\psi_n(x_{e_i}, y_{e_i}, l_z)$ and $\psi_n(x_p, y_p, z_p)$ are the natural acoustic modes at the coordinates of the centre of the ith element and the location of the monopole source respectively. For a rigid-walled rectangular enclosure, the mode shape found from [124]

$$\psi_n(x_e, y_e, z_e) = \sqrt{e_1 e_2 e_3}\cos\left(\frac{n_1 \pi x_e}{l_x}\right)\cos\left(\frac{n_2 \pi y_e}{l_y}\right)\cos\left(\frac{n_3 \pi z_e}{l_z}\right), \tag{C.16a}$$

$$z_e = l_z$$

$$\psi_n(x_p, y_p, z_p) = \sqrt{e_1 e_2 e_3}\cos\left(\frac{n_1 \pi x_p}{l_x}\right)\cos\left(\frac{n_2 \pi y_p}{l_y}\right)\cos\left(\frac{n_3 \pi z_p}{l_z}\right), \tag{C.16b}$$

where n_1, n_2 and n_3 are the acoustic modal integers, and e_1, e_2 and e_3 are the normalisation factors obtained from

$$e_i = \begin{cases} 1, & if\ n_i = 0 \\ 2, & if\ n_i \geq 1 \end{cases}, \tag{C.17}$$

$V_{cavity} = l_x l_y l_z$ is the volume of the cavity in m^3, ω_n is the natural frequency of the cavity in rad/s calculated from

$$\omega_n = \pi c_0 \sqrt{\left(\frac{n_1}{l_x}\right)^2 + \left(\frac{n_2}{l_y}\right)^2 + \left(\frac{n_3}{l_z}\right)^2}, \tag{C.18}$$

and finally ζ_n is the modal damping ratio of acoustic modes, which is also set to 1%. The values used for all the parameters can be found in Table C.1.

Similarly, the (i,j)th element of $\mathbf{Z_A}$, denoting the force on the ith element due to the vibration of the jth element, is calculated from the finite modal expansion over the first *N* acoustic modes

$$Z_{A_{i,j}} = \frac{f_{e_i}}{\dot{w}_{e_j}} = \omega \sum_{n=0}^{N} \frac{\rho_0 c_0^2 A_e^2}{V_{cavity}} \frac{\psi_n(x_{e_i}, y_{e_i}, l_z)\psi_n(x_{e_j}, y_{e_j}, l_z)}{2\zeta_n \omega_n \omega + j(\omega^2 - \omega_n^2)}. \tag{C.19}$$

The total coupled structural kinetic energy and the acoustic sound power radiated from the free side of the panel are found using Equations (4.30) and (4.37), defined in Chapter 4.

C.1.2 Mathematical Model with Actuator:

The inertial actuator modelled here is based on the actuator used in Chapter 6 for open-loop response simulations and real-time experiments of feedback control on the pressurised enclosure experimental rig.

The inertial actuator both supplies a force to the panel and modifies its passive dynamic behaviour. If the force generated by the actuator is as a result of feedback from the panel's velocity, the effect of the feedback can also be modelled as a modification to the plate dynamics. The vector of forces at the elemental points on the panel can thus be written as

$$\mathbf{f_e} = \mathbf{Z_{ee}}\dot{\mathbf{w}}_\mathbf{e} + \mathbf{Z_c}\dot{\mathbf{w}}_\mathbf{e}, \tag{C.20}$$

where $\mathbf{Z_{ee}}$ is the inverse of the matrix of mobility responses $\mathbf{Y_{ee}}$ of the panel, whose elements are given by Equation (C.8), and $\mathbf{Z_c}$ accounts for the overall effect of the actuator, both active and passive. The modified matrix of structural mobilities is thus

$$\mathbf{Y_s} = \left[\mathbf{Z_{ee}} + \mathbf{Z_c}\right]^{-1}. \tag{C.21}$$

When the feedback loop is closed, the complex elemental velocity $\dot{\mathbf{w}}_\mathbf{e}$ is expressed in terms of both the primary elemental force $\mathbf{f_e}$ and the control force f_c generated by the actuator, which for a single-channel control system can be written as

$$\dot{\mathbf{w}}_\mathbf{e} = \mathbf{Y_{ee}}\mathbf{f_e} + \mathbf{y_{ec}}\, f_c, \tag{C.22}$$

where $\mathbf{y_{ec}}$ is the transfer mobility vector between the elements of the panel and the control force. The control velocity on the panel can be expressed in terms of the point mobility Y_{cc} of the panel at the location of control, and the control force f_c, as

$$\dot{w}_c = -Y_{cc}\, f_c \tag{C.23}$$

Alternatively, the control force can be written in terms of the impedance at the point of control and the complex control velocity as

$$f_c = -Z_{cc}\dot{w}_c, \tag{C.24}$$

The substitution of Equation (C.24) into the above equation leads to

$$\dot{\mathbf{w}}_\mathbf{e} = \mathbf{Y}_{\mathbf{ee}}\mathbf{f}_\mathbf{e} - Z_c\mathbf{y}_{\mathbf{ec}}\dot{w}_c, \tag{C.25}$$

The velocity at the control point can be expressed in terms of the elemental velocity as

$$\dot{w}_c = \mathbf{a}^\mathbf{T}\dot{\mathbf{w}}_\mathbf{e}, \tag{C.26}$$

where $\mathbf{a}$ is a vector of the same dimensions as $\dot{\mathbf{w}}_\mathbf{e}$ in which all the elements are zero except for the element corresponding to the location of the actuator which is 1, such that $\mathbf{a} = \{0 \quad \ldots \quad 1 \quad 0 \quad \ldots \quad 0\}$.

As a result, Equation (C.25) can be rewritten as

$$\dot{\mathbf{w}}_\mathbf{e} = \mathbf{Y}_{\mathbf{ee}}\mathbf{f}_\mathbf{e} - Z_c\mathbf{y}_{\mathbf{ec}}\mathbf{a}^\mathbf{T}\dot{\mathbf{w}}_\mathbf{e}, \tag{C.27}$$

Finally, the combination of Equation (C.27) with Equation (C.5), leads to the general equation for the coupled elemental velocity as

$$\dot{\mathbf{w}}_\mathbf{e} = -\left[\mathbf{I} + \mathbf{Y}_{\mathbf{ee}}\mathbf{Z}_\mathbf{A} + Z_c\mathbf{y}_{\mathbf{ec}}\mathbf{a}^\mathbf{T}\right]^{-1}\mathbf{Y}_{\mathbf{ee}}\mathbf{z}_{\mathbf{ep}}q_p, \tag{C.28}$$

The total coupled kinetic energy and acoustic potential energy can be calculated using Equations (4.30) and (4.37) defined in Chapter 4.

C.2 Structural Response Analysis:

In this section, the effect of structural-acoustic coupling for a flexible panel that is part of an otherwise rigid-walled enclosure will be assessed through simulations of the total structural kinetic energy. This will be performed first for a flat flexible panel and will then progress to a doubly-curved flexible panel with gradually increasing curvature. The results will be compared for the same model, when the panel is weakly coupled with the

enclosure in order to gain a better understanding of the degree of coupling between the structural and acoustic modes. The volume velocity of the primary monopole source was assumed to be 10^{-5} m^3s^{-1}.

C.2.1 Effects of Structural-Acoustic Coupling on the Structural Response:

The total structural kinetic energy is shown in Figure C. 2 for a weakly coupled and a strongly coupled enclosure modelled based on the parameters and properties defined in the previous sections. It can be seen from the graph that with coupling, the natural frequency of the first mode is increased from 73.4 Hz to 82.5 Hz and the amplitude of some of the higher order modes, such as Mode (3,3) occurring near 445 Hz and Mode (7,1) occurring near 835 Hz, is reduced.

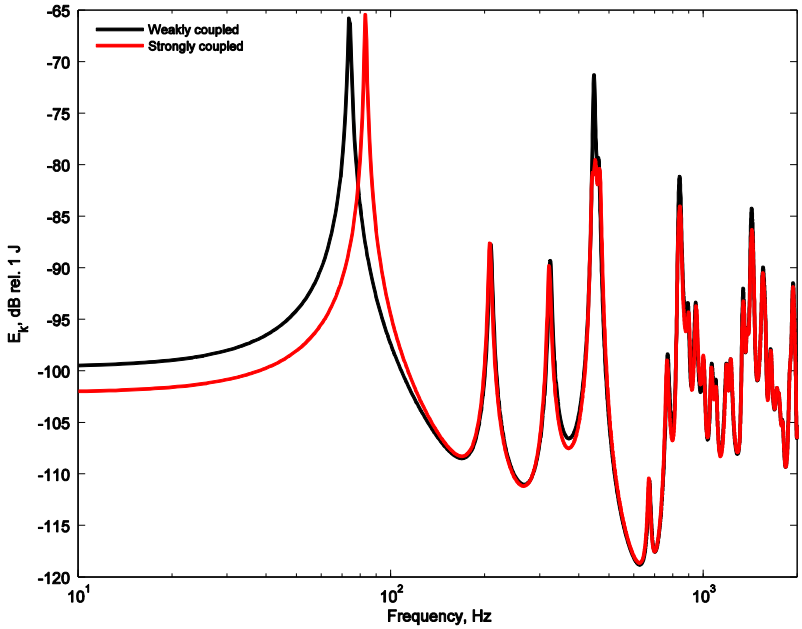

Figure C. 2 - Simulated structural kinetic energy and acoustic potential energy for a modelled system consisting of a flexible flat panel clamped on the top of a rigid-walled enclosure: strongly coupled (black curve) and weakly coupled (red curve). The primary excitation is provided by a modelled monopole source with a volume velocity of 10^{-5} m^3s^{-1}.

In order to assess the degree of coupling between different acoustic cavity modes and panel structural modes, the coupling coefficient is calculated from [125] as

$$C_{n,m} = \begin{cases} -1^{n_3} 2A\sqrt{e_1 e_2 e_3}\,\dfrac{mn\left(-1^{n_1+m}-1\right)\left(-1^{n_2+n}-1\right)}{\pi^2\left(n_1^2-m^2\right)\left(n_2^2-n^2\right)}, & n_1 \neq m,\ n_2 \neq n \\ 0, & \text{otherwise,} \end{cases} \tag{C.29}$$

where A is the area of the panel. The results are shown in Table C. 2 for the first 9 panel structural modes and the first ten cavity acoustic modes. It is important to note that the cavity acoustic modes start at much higher frequencies than the panel structural modes. The natural frequency of the second acoustic mode (1,0,0) is 414.25 Hz which is significantly higher than the natural frequency of the (1,1) panel mode.

Table C. 2 - The first 9 uncoupled structural modes and first 10 uncoupled acoustic modes, their natural frequencies and the coupling coefficient between each of the acoustic and structural modes.

Mode order		Panel	1	2	3	4	5	6	7	8	9
	Modes	Structural	(1,1)	(2,1)	(1,2)	(3,1)	(2,2)	(3,2)	(4,1)	(1,3)	(2,3)
Cavity	Acoustic	Frequency (Hz)	73.43	124.31	172.10	207.82	219.17	298.17	321.70	322.04	367.78
1	(0,0,0)	0	0.11	0	0	0.04	0	0	0	0.04	0
2	(1,0,0)	414.25	0	0.10	0	0	0	0	0.04	0	0.03
3	(0,0,1)	445.45	-0.15	0	0	-0.05	0	0	0	-0.05	0
4	(0,1,0)	546.18	0	0	0.10	0	0	0.03	0	0	0
5	(1,0,1)	608.30	0	-0.14	0	0	0	0	-0.06	0	-0.05
6	(1,1,0)	685.50	0	0	0	0	0.09	0	0	0	0
7	(0,1,1)	704.80	0	0	-0.14	0	0	-0.05	0	0	0
8	(1,1,1)	817.52	0	0	0	0	-0.13	0	0	0	0
9	(2,0,0)	828.50	-0.05	0	0	0.09	0	0	0	-0.02	0
10	(0,0,2)	890.91	0.15	0	0	0.05	0	0	0	0.05	0

The effect of the distance between the acoustic and structural modes on structural-acoustic coupling has been investigated in [129]. A coupling constant g_{nm} has been defined in terms of the coupling coefficient as

$$g_{nm} = \frac{C_{nm}^2\left(\Delta\omega_m\omega_n^2 + \Delta\omega_n\omega_m^2\right)}{\left(\omega_m^2-\omega_n^2\right)^2 + \left(\Delta\omega_m + \Delta\omega_n\right)\left(\Delta\omega_m\omega_n^2 + \Delta\omega_n\omega_m^2\right)}, \tag{C.30}$$

where ω_m and ω_n are the natural frequencies of the mth structural mode and the nth acoustic mode respectively, and $\Delta\omega_m$ and $\Delta\omega_n$ refer to the half-power bandwidth of the mth structural mode and the nth acoustic mode respectively. Equation (C.30) for the coupling constant can be further simplified based on the following conditions as

$$g_{nm} = \begin{cases} \dfrac{C_{nm}^2}{\left(\Delta\omega_m + \Delta\omega_n\right)}, & 2\left|\omega_m - \omega_n\right| < \left(\Delta\omega_m + \Delta\omega_n\right) \\ 0, & 2\left|\omega_m - \omega_n\right| > \left(\Delta\omega_m + \Delta\omega_n\right) \end{cases} \tag{C.31}$$

Structural and acoustic mode pairs for which the spacing between their natural frequencies are less than half of the sum of their half-power bandwidth – condition 1 in Equation (C.31) – are referred to as mode pairs with *proximate modal coupling* [129]. The difference between the natural frequency of the structural mode (1,1) and the acoustic mode (1,0,0) is far too large for this pair to fulfil the proximate modal coupling condition and as it can be seen in Table C. 2, the coupling coefficient of this mode pair is 0. Due to the large spacing between the acoustic and structural modes, even the non-zero coupling coefficients between different modes pair of Table C. 2 are low indicating a relatively weak coupling between acoustic and structural modes for the modelled enclosure.

Figure C. 3 shows the amplitude of the coupling coefficient for different pairs of structural and acoustic modes. Some of the highest coupling coefficients are for the 1st structural and first acoustic mode pair, the 1st structural and the 3rd acoustic mode pair, and the 1st structural and the 10th acoustic mode pair.

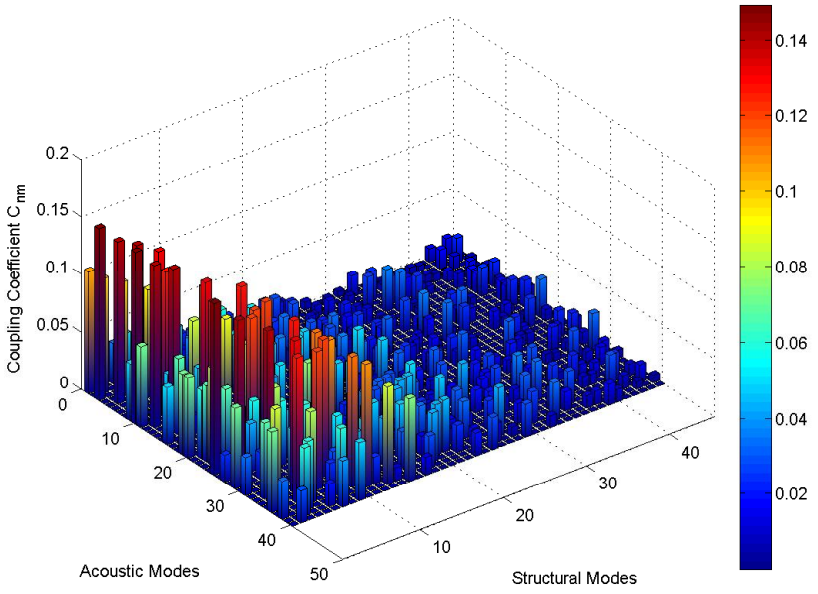

Figure C. 3 - Coupling coefficient plotted for different pairs of the first 50 structural and the first 40 acoustic modes.

Appendix D. List of Equipment

Vibration Analysis of the Car Roof Panel:

- PC running Matlab 2011b for data analysis.
- Laptop running LMS data acquisition and data analysis toolbox.
- 8-channel LMS Scadas Mobile SCM01 front-end.
- Cambridge Audio A1 integrated power Amplifier.
- 16-channel PCB Electronics type 481A03 signal conditioner.
- 5 PCB Piezotronics type A352C67 piezoelectric accelerometers.
- LDS V201 Permanent magnet electrodynamic shaker.
- PCB Piezotronics type 208C01 piezoelectric force transducer.

Experiments of Velocity Feedback Control on a Pressurised Enclosure:

- PC running Matlab 2011b for data analysis.
- PC running Data Physics SignalCalc data acquisition and data analysis toolbox.
- X-channel Data Physics SignalCalc data acquisition front end.
- Cambridge Audio A1 integrated power Amplifier.
- 16-channel PCB Electronics type 481A03 signal conditioner.
- 4 PCB electronics type A352C67 piezoelectric accelerometers.
- ‘Salava’ volume velocity source custom-built by the ISVR.
- Modified 66-mm diameter Pro Signal type S066M cone loudspeaker used as actuator.
- 2^{nd} order compensator filter custom-built by the ISVR and 15-V DC voltage supply.
- Kemo High-pass filter.

Appendix E. Equipment Specifications

Proof-mass Actuator:

Pro Signal S066M Mylar cone speaker:

Figure F. 1 – Picture of Pro Signal S066M loudspeaker.

- 66-mm external diameter.
- Maximum power: 3W.
- RMS Power rating: 1.5W.
- Impedance: 8Ω.
- Frequency response: 350 Hz-4.5 kHz.

  Weight: 60g

Compensator:

55-Hz 2nd order compensator filter:

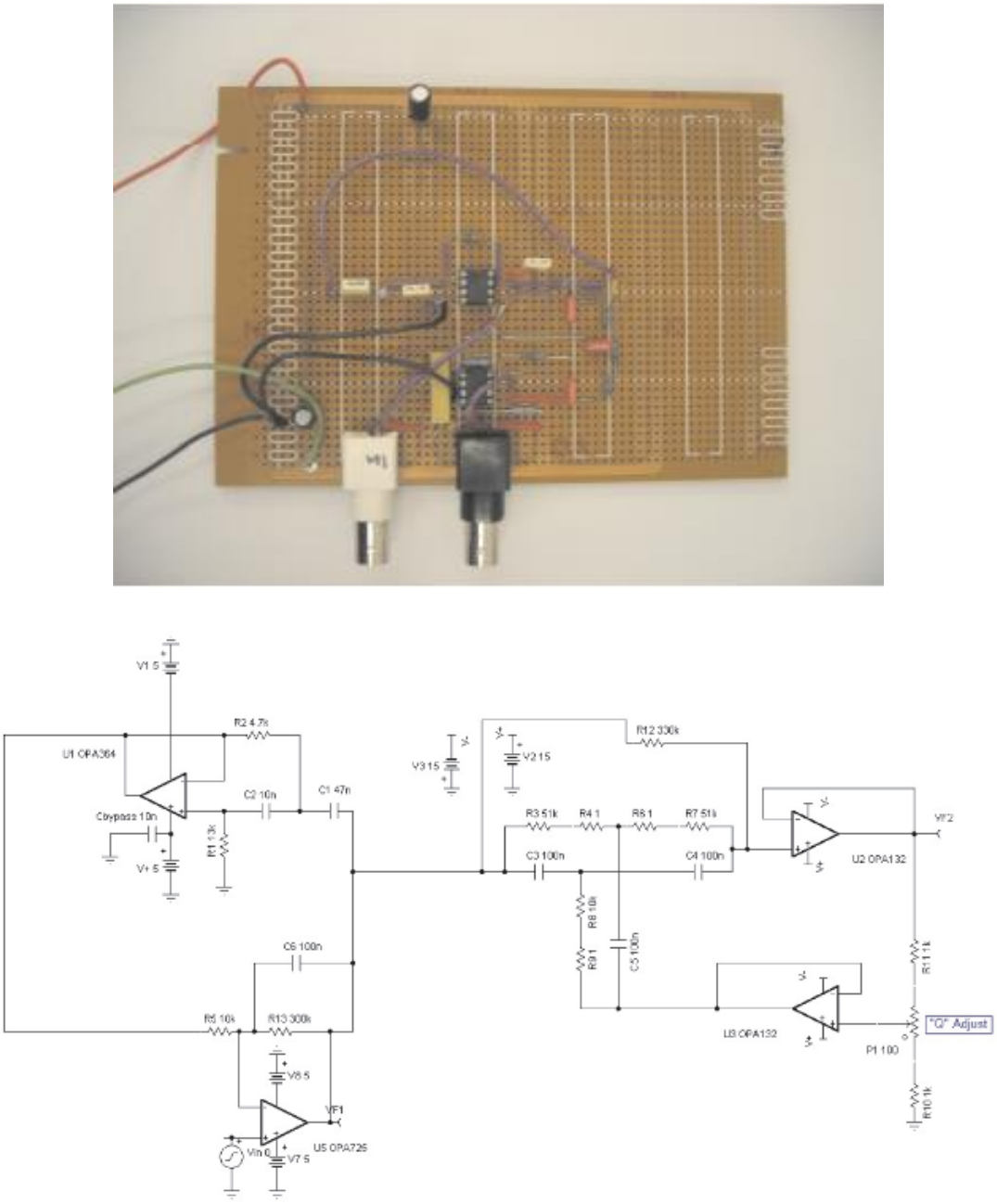

Figure F. 2 – Photograph of the analogue 55-Hz compensator filter circuit board (top) and circuit diagram of the compensator (bottom) [116]

References

[1] D. J. Thompson and J. Dixon, "Vehicle Noise," in *Advanced Applications in Acoustics, Noise and Vibration*, London and New York, E & FN Spon, 2004, pp. 236-291, Chapter 6.

[2] J. Rohlfing, Decentralised Velocity Feedback Control of Thin Homogeneous and Lightweight Sandwich Panels, PhD Thesis, Southampton: University of Southampton, 2009.

[3] Y. H. Lee and A. Nasiri, "Real Time Active Noise Control of Engine Booming in Passenger Vehicles," *SAE International Technical Paper Series, 2007-01-0411,* 2007.

[4] S. K. Jha, "Characteristics and Sources of Noise and Vibraiton and Their Control in Motor Cars," *Journal of Sound and Vibration,* vol. 47, no. 4, pp. 543-558, 1976.

[5] M. Rao, "Recent Applications of Viscoelastic Damping for Noise Control in Automobiles and Commercial Airplanes," *Journal of Sound and Vibration,* vol. 262, no. 3, pp. 457-474, 2003.

[6] F. J. Fahy, "Fundamentals of Noise and Vibration Control," in *Fundamentals of Noise and Vibration*, London, E & FN Spon, 1998, pp. 225-309, Chapter 12.

[7] A. Roure, "Self Adaptive Broadband Active Noise Control System," *Journal of Sound and Vibration,* vol. 101, no. 3, pp. 429-441, 1985.

[8] S. J. Elliott, "A Review of Active Noise and Vibration Control in Road Vehicles, Technical Report, ISVR Technical Memorandum No. 981," University of Southampton, Southampton, 2008.

[9] S. J. Elliott and P. A. Nelson, "Active Noise Control," *IEEE Signal Processing Magazine,* vol. 10, no. 4, pp. 12-35, 1993.

[10] S. J. Elliott, I. M. Stothers, P. A. Nelson, A. M. McDonald, D. C. Quinn and T. Saunders, “The Active Control of Engine Noise Inside Cars,” in *Proceedings of Internoise '88*, Avignon, 1988.

[11] S. Hasegawa, T. Tabata and T. Kinoshita, “The Development of an Active Noise Control System for Automobiles,” *Society of Automotive Engineers Technical Paper, 922 086,* 1992.

[12] S. J. Elliott, P. A. Nelson, I. M. Stothers and C. C. Boucher, “Preliminary Results of In-flight Experiments on the Active Control of Propeller-induced Cabin Noise,” *Journal of Sound and Vibration,* vol. 128, no. 2, pp. 355-357, 1989.

[13] S. J. Elliott, P. A. Nelson, I. M. Stothers and C. C. Boucher, “In-flight Experiments on the Active Control of Propeller-induced Cabin Noise,” *Journal of Sound and Vibration,* vol. 140, no. 2, pp. 219-238, 1990.

[14] A. J. Bullmore, P. A. Nelson and S. J. Elliott, “Theoretical studies of the active control of propeller-induced cabin noise,” *Journal of Sound and Vibration,* vol. 140, no. 2, pp. 191-217, 1990.

[15] M. Zilletti, S. J. Elliott and P. Gardonio, “Self-Tuning Control Systems of Decentralised Velocity Feedback,” *Journal of Sound and Vibration,* vol. 329, pp. 2738-2750, 2010.

[16] C. Bohn, A. Cortabarria, V. Härtel and K. Kowalczyk, “Active Control of Engine-induced Vibrations in Automotive Vehicles using Disturbance Observer Gain Scheduling,” *Control Engineering Practice,* vol. 12, no. 8, pp. 1029-1039, 2004.

[17] F. J. Fahy and P. Gardonio, Sound and Structural Vibration, Radiation, Transmission and Response, Oxford: Academic Press, 2007.

[18] S. Hurlebaus, U. Stöbener and L. Gaul, “Vibration Reduction of Curved Panels by Active Modal Control,” *Computers and Structures,* vol. 86, no. 3-5, pp. 251-257, 2008.

[19] N. Lalor and H. H. Priebsch, "The Prediction of Low- and Mid-frequency Internal Road Vehicle Noise: A Literature Survey," *Proceedings of the Institution of Mechanical Engineers, Part D: Journal of Automobile Engineering,* vol. 269, no. 221, p. 245, 2007.

[20] P. F. Joseph and M. G. Smith, "Aircraft Noise," in *Advanced Applications in Acoustics, Noise and Vibration, Chapter 7,* London and New York, E & F Spon, 2004, pp. 292-346.

[21] M. J. Smith, "Aircraft Noise Sources, Chapter 6," in *Aircraft Noise*, Cambridge, Cambridge University Press, 2004.

[22] S. K. Jha and J. J. Catherines, "Interior Noise Studies for General Aviation Types of Aircraft, Part I: Field Studies," *Journal of Sound and Vibration,* vol. 58, no. 3, pp. 375-390, 1978.

[23] S. J. Kha and J. J. Catherines, "Interior Noise Studies for General Aviation Types of Aircraft, Part II: Laboratory Studies," *Journal of Sound and Vibration*, vol. 58, no. 3, pp. 391-406, 1978.

[24] P. Gardonio, "Review of Active Techniques for Aerospace Vibro-Acoustic Control," *Journal of Aircraft* , vol. 39, no. 2, pp. 206-214, 2002.

[25] S. J. Elliott and P. A. Nelson, "Active Noise Control," in *Advanced Applications in Acoustics, Noise and Vibration, Chapter 8,* London and New York, E & F Spon, 2004, pp. 347-386.

[26] C. R. Fuller, S. J. Elliott and P. A. Nelson, Active Control of Vibration, London: Academic Press, 1996.

[27] S. J. Elliott, P. Gardonio, T. J. Sors and M. J. Brennan, "Active Vibroacoustic Control with Multiple Local Feedback Loops," *Journal of Acoustical Society of America,* vol. 111, no. 2, pp. 908-915, 2002.

[28] S. J. Elliott and T. J. Sutton, "Performance of Feedforward and Feedback Systems for Active Control," *IEEE Transactions on Speech and Audio Processing,* vol. 4,

no. 3, pp. 214-223, 1996.

[29] P. Lueg, “Process of Silencing Sound Oscillations”. USA Patent 2,043,416, 9 June 1936.

[30] H. F. Olsen and E. G. May, “Electronic Sound Absorber,” *Journal of Acoustical Society of Ameria,* vol. 25, no. 6, pp. 1130-1136, 1953.

[31] W. B. Conover, “Fighting Noise with Noise,” *Noise Control,* vol. 2, no. 2, pp. 78-82, 1956.

[32] S. J. Elliott and P. A. Nelson, “Active Noise Control: Low-frequency Techniques for Suppressing Acoustic Noise Leap Forward with Signal Processing,” *IEEE Signal Processing Magazine,* vol. 10, no. 4, pp. 12-35, 1993.

[33] M. J. Balas, “Active Control of Flexible Systems,” *Journal of Optimization Theory and Applications,* vol. 25, no. 3, pp. 415-436, 1978.

[34] M. J. Balas, “Direct Velocity Feedback Control of Large Space Structures,” *Journal of Guidance, Control, and Dynamics,* vol. 2, no. 3, pp. 252-253, 1979.

[35] S. J. Elliott, Signal Processing for Active Control, London: Academic Press, 201.

[36] C. Gonzalez Diaz, Active Structural Acoustic Control Smart Panel with Small Scale Proof Mass Actuators , PhD Thesis, Southampton: University of Southampton, 2007.

[37] J. Q. Sun, “Some Observations on Physical Duality and Colocation of Structural Control Sensors and Actuators,” *Journal of Sound and Vibration,* vol. 194, no. 5, pp. 765-770, 1996.

[38] C. Gonzalez Diaz and P. Gardonio, “Feedback Control Laws for Proof-mass Electrodynamic Actuators,” *Smart Materials and Structures,* vol. 16, no. 5, pp. 1766-1783, 2007.

[39] S. J. Elliott, “Active Noise and Vibration Control in Vehicles, Chapter 11,” in *Vehicle Noise and Vibration Refinement,* Oxford, Cambridge, New Delhi,

Woodhead Publishing Limited, 2010, pp. 235-251.

[40] G. Z. Yao, F. F. Yap, G. Chen, W. H. Li and S. H. Yeo, "MR Damper and its application for Semi-active Control of Vehicle Suspension System," *Mechatronics*, vol. 12, no. 7, pp. 963-973, 2002.

[41] A. Preumont, Vibration Control of Active Structures: An Introduction, Dordrecht, Boston, London: Kluwer Academic Publisher, 2002.

[42] S. H. Kim, J. M. Lee and M. H. Sung, "Structural-acoustic Modal Coupling Analysis and Application to Noise Reduction in a Vehicle Passenger Compartment," *Journal of Sound and Vibration*, vol. 225, no. 5, pp. 989-999, 1999.

[43] "The new 4.0 TFSI engine with "cylinder on demand": high-end technologies for efficiency and refinement," Audi, 2 September 2011. [Online]. Available: http://audiusanews.com/newsrelease.do;jsessionid=41891C77CBD36FADAC67ECDE203FFAF6?&id=2551&allImage=1&teaser=new-4.0-tfsi-engine-cylinder-demand-high-end&mid=19.

[44] "Honda, Performance," 2013. [Online]. Available: http://automobiles.honda.com/accord-sedan/performance.aspx.

[45] "Buick Encore 2013," GM, [Online]. Available: http://media.gm.com/media/us/en/buick/vehicles/encore/2013.html.

[46] L. P. De Oliveira, M. M. Da Silva, P. Sas, H. Van Brussel and W. Desmet, "Concurrent Mechatronic Design Approach for Active Control of Cavity Noise," *Journal of Sound and Vibration*, vol. 314, no. 3-5, pp. 507-525, 2008.

[47] L. P. De Oliveira, P. Sas, W. Desmete, K. Janssens, P. Gajdatsy and H. Van Der Auweraer, "Active Control of Engine Noise Transmitted into Cavities: Simulation, Experimental Validation and Sound Quality Assessment," in *Proceedings of Acoustics '08*, Paris, 2008.

[48] L. P. De Oliveira, K. Janssens, P. Gajdatsy, H. Van Der Auweraer, P. S. Varoto,

P. Sas and W. Desmet, “Active Sound Quality Control of Engine Induced Cavity Noise,” *Mechanical Systems and Signal Processing,* vol. 23, no. 2, pp. 476-488, 2009.

[49] H. Sano, T. Inoue, A. Takahashi, K. Terai and Y. Nakamura, “Active Control System for Low-Frequency Road Noise Combined with an Audio System,” *IEEE Transactions on Speech and Audio Processing,* vol. 9, no. 7, pp. 755-763, 2001.

[50] T. Freudenberg, “Electromagnetic Vibration Damping Mount”. United States Patent 4,624,435, 25 November 1986.

[51] Y. Nakaji, S. Satoh, T. Kimura, T. Hamabe, Y. Akatsu and H. Kawazoe, “Development of an Active Control Engine Mount System,” *Vehicle Systems Dynamics: International Journal of Vehicle Mechanics and Mobility,* vol. 32, no. 2-3, pp. 185-198, 1999.

[52] Y. Yu, S. M. Peelamedu, N. G. Naganathan and R. V. Dukkipati, “Automotive Vehicle Engine Mounting Systems: A Survey,” *Journal of Dynamic Systems, Measurement and Control,* vol. 123, no. 2, pp. 186-194, 2001.

[53] Y. Yu, N. G. Naganathan and R. V. Dukkipati, “A Literature Review of Automotive Vehicle Engine Mounting Systems,” *Mechanism and Machine Theory,* vol. 36, no. 1, pp. 123-142, 2001.

[54] T. Liang and W. Shi, “Study on Electromagnetic Actuator Active Engine Mount with Fuzzy Control,” in *Proceedings of the 2009 IEEE International Conference on Mechatronics and Automation,* Changchun, China, 2009.

[55] B. H. Lee and C. W. Lee, “Model Based Feed-forward Control of Electromagnetic Type Active Control Engine-Mount System,” *Journal of Sound and Vibration,* vol. 323, no. 3-5, pp. 574-593, 2009.

[56] S. Ushijima and S. Jumakawa, “Active Engine Mount with Piezo-actuator for Vibration Control,” *SAE Transaction 930201,* 1993.

[57] Y. W. Lee and C. W. Lee, “Dynamic Analysis and Control of an Active Engine

Mount System," *Proceedings of the Institution of Mechanical Engineers, Volume D: Journal of Automobile Engineering,* vol. 216, no. 11, pp. 921-931, 2002.

[58] "2012 Audi S8 Engine," Audi of America, 10 October 2011. [Online]. Available: http://www.audiworld.com/news/11/2012-s8/content4.shtml.

[59] "Audi S8 Active engine mount with moving coil," Eurocar News, [Online]. Available: http://www.eurocarnews.com/182/0/0/7681/audi-s8-active-engine-mount-with-moving-coil/gallery-detail.html.

[60] D. A. Williams and P. G. Wright, "Vehicle Suspension System". United States Patent 4,625,993, 2 December 1986.

[61] D. Hrovat, "Survey of Advanced Suspension Developments and Related Optimal Control Applications," *Automatica,* vol. 9, no. 5, pp. 1781-1817, 1997.

[62] R. S. Sharp, "Variable Geometry Active Suspension for Cars," *Computing and Control Engineering Journal,* vol. 9, no. 5, pp. 217-222, 1998.

[63] I. Fialho and G. J. Balas, "Road Adaptive Suspension Design Using Linear Parameter-Varying Gain-Scheduling," *IEEE Transactions on Control Systems Technology,* vol. 10, no. 1, pp. 43-54, 2002.

[64] J. Cao and H. Liu, "State of the Art in Vehicle Active Suspension Adaptive Control Systems Based on Intelligent Methodologies," *IEEE Transactions on Intelligent Transportation Systems,* vol. 9, no. 3, pp. 392-405, 2008.

[65] U. Stöbener and U. Gaul, "Active Vibration Control of a Car Body Based on Experimentally Evaluated Modal Parameters," *Journal of Mechanical Systems and Signal Processing,* vol. 15, no. 1, pp. 173-188, 2001.

[66] K. C. Song, J. K. Hwang, J. M. Lee and J. K. Hedrick, "Active Vibration Control for Structural-Acoustic Coupling System of a 3-D Vehicle Cabin Model," *Journal of Sound and Vibration,* vol. 267, pp. 851-865, 2003.

[67] C. R. Fuller and A. H. Von Flotow, "Acitve Control of Sound and Vibration,"

IEEE Control Systems, vol. 15, no. 6, pp. 9-19, 1995.

[68] C. R. Fuller, S. D. Snyder, C. H. Hansen and R. J. Silcox, "Active Control of Interior Noise in Model Aircraft Fuselages using Piezoceramic Actuators," *Journal of the American Institute of Aeronautics and Astronautics,* vol. 30, no. 11, pp. 2613-2617, 1992.

[69] J. P. Carneal and C. R. Fuller, "An Analytical and Experimental Investigation of Active Structural Acoustic Control of Noise Transmission through Double Panel Systems," *Journal of Sound and Vibration,* vol. 272, no. 3-5, pp. 749-771, 2004.

[70] R. Hinchliffe, I. Scott, M. Purver and I. Stothers, "Tonal Active control in Production on a Large Turbo-prop Aircraft," in *Proceedings of the Active2002 Conference*, Southampton, 2002.

[71] B. Petitjean, I. Legain, F. Simon and S. Pauzin, "Active Control Experiments for Acoustic Radiation Reduction of a Sandwich Panel: Feedback and Feedforward Investigations," *Journal of Sound and Vibration,* vol. 252, no. 1, pp. 19-36, 2002.

[72] A. Lepage, F. Mortain and L. Coste, "Active Structural Acoustic Control of a Helicopter Trim Panel," in *Proceedings of Internoise 2005*, Rio de Janeiro, Brazil, 2005.

[73] T. J. Sutton, S. J. Elliott and M. J. Brennan, "Active Isolation of Multiple Structural Waves on a Helicopter Gearbox Support Strut," *Journal of Sound and Vibration,* vol. 205, no. 1, pp. 81-101, 1997.

[74] M. S. Qatu and E. Asadi, "Vibration of Doubly Curved Shallow Shells with Arbitrary Boundaries," *Journal of Applied Acoustics,* vol. 73, no. 1, pp. 21-27, 2012.

[75] G. B. Warburton, "Vibration of Plates and Shells, Chapter 5," in *The Dynamical Behaviour of Structures*, Oxford and New York, Pergamon Press Ltd. , 1976, pp. 220-281.

[76] M. S. Qatu, "Recent Research Advances in the Dynamic Behaviour of Shells:

1989-2000, Part 2: Homogeneous Shells," *Applied Mechanics Reviews,* vol. 55, no. 5, pp. 415-434, 2002.

[77] A. W. Leissa, "Vibration of Shells, Technical Report 19730018197," NASA, 1973.

[78] R. S. Langley, "A Dynamic Stiffness Technique for the Vibration Analysis of Stiffened Shell Structures," *Journald of Sound and Vibration,* vol. 156, no. 3, pp. 521-540, 1992.

[79] R. S. Langley, "Wave Motion and Energy Flow in Cylindrical Shells," *Journal of Sound and Vibration,* vol. 169, no. 1, pp. 29-42, 1994.

[80] R. S. Langley, "The Modal Density and Mode Count of Thin Cylinders and Curved Panels," *Journal of Sound and Vibration,* vol. 169, no. 1, pp. 43-53, 1994.

[81] R. S. Langley, "Application of the Dynamic Stiffness Method to the Free and Forced Vibrations of Aircraft Panels," *Journald of Sound and Vibration,* vol. 135, no. 2, pp. 319-331, 1989.

[82] A. W. Leissa and M. S. Qatu, "Shell Vibrations, Chapter 7," in *Vibrations of Continuous Systems*, New York, Chicago, London, McGraw Hill Professional, 2011, pp. 271-308.

[83] J. E. Greenspon, "Vibrations of a Thick-Walled Cylindrical Shell - Comparison of the Exact Theory with Approximate Theories," *Journal of Acoustical Society of America,* vol. 32, no. 5, pp. 571-578, 1960.

[84] H. Lamb, "On the Flexure and the Vibrations of a Curved Bar," *Proceedings of the Physical Society of London,* vol. 4, no. 2, 1888.

[85] B. Kang, C. H. Riedel and C. A. Tan, "Free Vibration Analysis of Planar Curved Beams by Wave Propagation," *Journal of Sound and Vibration,* vol. 260, no. 1, pp. 19-44, 2003.

[86] P. Chidamparam and A. W. Leissa, "Vibrations of Planar Curved Beams, Rings,

and Arches," *Applied Mechanics Reviews,* vol. 46, pp. 467-483, 1993.

[87] S. M. Han, H. Benaroya and T. Wei, "Dynamics of Transversely Vibrating Beams using Four Engineering Theories," *Journal of Sound and Vibration,* vol. 225, no. 5, pp. 935-988, 1999.

[88] A. W. Leissa and M. S. Qatu, "Beam Vibrations, Chapter 4," in *Vibration of Continuous Systems,* New York, Chicago, London, McGraw Hill Professional, 2011, pp. 103-175.

[89] S. K. Lee, B. R. Mace and M. J. Brennan, "Wave Propagation, Reflection and Transmission in Curved Beams," *Journal of Sound and Vibration,* vol. 306, no. 3-5, pp. 636-656, 2007.

[90] S. K. Lee, Wave Reflection, Transmission and Propagration in Structural Waveguides, PhD Thesis, Southampton: University of Southampton, 2006.

[91] G. B. Warburton, "Vibration of Thin Cylindrical Shells," *Journal of Mechanical Engineering Science,* vol. 7, no. 4, pp. 399-407, 1965.

[92] M. C. Junger and D. Feit, Sound, Structures and their Interaction, Cambridge, London: The MIT Press, 1986.

[93] J. E. Manning and G. Maidanik, "Radiation Properties of Cylindrical Shells," *Journal of Acoustical Society of America,* vol. 36, no. 9, pp. 1691-1698, 1964.

[94] A. W. Leissa and A. S. Kadi, "Curvature Effects on Shallow Shell Vibrations," *Journal of Sound and Vibration,* vol. 16, no. 2, pp. 173-187, 1971.

[95] A. E. Love, Vibration of Shallow Shells: A Review with Bibliography Treatise on the Mathematical Theory of Elasticity, New York: Dover Publications, 1944.

[96] K. M. Liew, C. W. Lim and S. Kitipornchai, "Vibration of Shallow Shells: A Review with Bibliography," *Applied Mechanics Reviews,* vol. 50, no. 8, pp. 431-444, 1997.

[97] P. Gardonio and M. J. Brennan, "Mobility and Impedance Methods in Structural

Dynamics," in *Advanced Applications in Acoustics, Noise and Vibration*, London and New York, E & FN Spon, 2004, pp. 389-447, Chapter 9.

[98] J. Rohlfing and P. Gardonio, "Homogeneous and Sandwich Active Panels under Deterministic and Stochastic Excitation," *Journal of Acoustical Society of America,* vol. 125, no. 6, pp. 3696-3706, 2009.

[99] M. Heckl, "Vibrations of Point-Driven Cylindrical Shells," *Journal of Acoustical Society of America,* vol. 34, no. 10, pp. 1553-1557, 1962.

[100] V. V. Bolotin, "On the Density of the Distribution of Natural Frequencies of Thin Elastic Shells," *Journal of Applied Mathematics and Mechanics,* vol. 27, no. 2, pp. 538-543, 1963.

[101] J. P. Wilkinson, "Modal Densities of Certain Shallow Structural Elements," *Journal of Acoustical Society of America,* vol. 43, no. 2, pp. 245-251, 1968.

[102] D. V. Hutton, Fundamentals of Finite Element Analysis, New York: McGraw Hill, 2004.

[103] L. Tassinari, S. Monleon Cremades and C. Gentilini, "Unified Formulation for Reissner-Mindlin Plates: A Comparison with Numerical Results," in *Proceedings of the International Association for Shell and Spatial Structures (IASS) Symposium*, Valencia, Spain, 2009.

[104] T. Nelson and E. Wang, "Reliable FE-Modeling with ANSYS," in *Proceedings of the International ANSYS Conference*, 2004.

[105] D. J. Ewins, Modal Testing: Theory and Practice and Application, Baldock: Research Studies Press Ltd., 2000.

[106] P. Gardonio and S. Elliott, "Smart Panels for Active Structural Acoustic Control," *Smart Materials and Structures,* vol. 13, pp. 1314-1336, 2004.

[107] C. Gonzalez Diaz, C. Paulitsch and P. Gardonio, "Active Damping Control Unit using a Small Scale Proof Mass Electrodynamic Actuator," *Journal of Acoustical*

Society of America, vol. 124, no. 2, pp. 886-897, 2008.

[108] P. Gardonio and S. J. Elliott, "Modal Response of a Beam with a Sensor-Actuator Pair for the Implementation of Velocity Feedback Control," *Journal of Sound and Vibration,* vol. 284, no. 1-2, pp. 1-22, 2005.

[109] C. Paulitsch, P. Gardonio and S. J. Elliott, "Active Vibration Control using an Inertial Actuator with Internal Damping," *Journal of Acoustical Society of America,* vol. 119, no. 4, pp. 2131-2140, 2006.

[110] C. Gonzalez Diaz, C. Paulitsch and P. Gardonio, "Smart Panel with Active Damping Units. Implementation of Decentralised Control," *Journal of Acoustical Society of America,* vol. 124, no. 2, pp. 898-910, 2008.

[111] D. K. Anthony and S. J. Elliott, "A Comparison of Three Methods of Measuring the Volume Velocity of an Acoustic Source," *Journal of Audio Engineering Society,* vol. 39, no. 5, pp. 355-366, 1991.

[112] S. P. Timoshenko and J. N. Goodier, Theory of Elasticity, New York: McGraw-Hill Higher Education, 1970.

[113] S. J. Elliott, M. Serrand and P. Gardonio, "Feedback Stability Limits for Active Isolation Systems with Reactive and Inertial Actuators," *Journal of Vibration and Acoustics* , vol. 123, no. 2, pp. 250-261, 2001.

[114] S. J. Elliott, J. Rohlfing and P. Gardonio, "Multifunctional Design of Inertially-Actuated Velocity Feedback Controllers," *Journal of Acoustical Society of America,* vol. 131, no. 2, pp. 1150-1157, 2012.

[115] O. N. Baumann and S. J. Elliott, "Destabilization of Velocity Feedback Controllers with Stroke Limited Inertial Actuators," *Journal of Acoustical Society of America,* vol. 121, no. 5, pp. EL211-EL217, 2007.

[116] J. Rohlfing, S. J. Elliott and P. Gardonio, "Compensation Filter for Feedback Control Units with Proof-Mass Electrodynamic Actuators, Simulations and Experimental Studies, ISVR Technical Memorandum No. 991," University of

Southampton, Southampton, 2011.

[117] E. K. Kinsler, A. R. Frey, A. B. Coppens and J. V. Sanders, Fundamentals of Acoustics, New York: John Wiley and Sons, 1999.

[118] M. Zilletti, S. J. Elliott, P. Gardonio and E. Rustighi, "Experimental Implementation of a Self-Tuning Control System for Decentralised Velocity Feedback," *Journal of Sound and Vibration,* vol. 331, pp. 1-14, 2012.

[119] Y. Zhnag, X. Zhang, S. J. Elliott and D. S. Nourzad, "Active Vibration Control of a Double-curved Shell with a Laminated Polyvinylidene Fluoride Actuator," *International Journal of Aerospace and Lightweight Structures* , vol. 2, no. 2, pp. 199-219, 2012.

[120] P. Gardonio, Y. S. Lee, S. J. Elliott and S. Debost, "Analysis and Measurement of a Matched Volume Velocity Sensor and Uniform Force Actuator for Active Structural Acoustic Control," *Journal of Acoustical Society of America,* vol. 110, no. 6, pp. 3025-3031, 2001.

[121] G. B. Warburton, "The Vibration of Rectangular Plates," *Proceedings of the Institute of Mechanical Engineers,,* vol. 168, no. 1, pp. 371-384, 1954.

[122] R. H. Lyon, "Noise Reduction of Rectangular Enclosures with One Flexible Wall," *Journal of Acoustical Society of America,* vol. 35, no. 11, pp. 1791-1797, 1963.

[123] E. H. Dowell, G. F. Gorman, III and D. A. Smith, "Acoustoelasticity: General Theory, Acoustic Natural Modes and Forced Response to Sinusoidal Excitation, Including Comparisons with Experiment," *Journal of Sound and Vibration,* vol. 52, no. 4, pp. 519-542, 1977.

[124] J. Pan, C. H. Hansen and D. A. Bies, "Active Control of Noise Transmission through a Panel into a Cavity: I. Analytical Study," *Journal of Acoustical Society of America,* vol. 87, no. 5, pp. 2098-2108, 1990.

[125] J. Pan, "The Forced Response of an Acoustic-Structural Coupled System,"

Journal of Acoustical Society of America, vol. 91, no. 2, pp. 949-956, 1992.

[126] E. H. Dowell and H. M. Voss, "The Effect of Cavity on a Panel Vibration," *The American Institute of Aeronautics and Acoustics,* vol. 1, no. 2, pp. 476-477, 1963.

[127] P. Gardonio, E. Bianchi and S. J. Elliott, "Smart Panel with Multiple Decentralized Units for the Control of Sound Transmission. Part I: Theoretical Predictions," *Journal of Sound and Vibration,* vol. 274, no. 1-2, pp. 163-232, 2004.

[128] S. M. Kim and M. J. Brennan, "A Compact Matrix Formulation using the Impedance and Mobility Approach for the Analysis of Structural-Acoustic Systems," *Journal of Sound and Vibration,* vol. 223, no. 1, pp. 97-113, 1999.

[129] S. M. Kim and M. J. Brennan, "Active Control of Harmonic Sound Transmission into an Acoustic Enclosure using both Structural and Acoustic Actuators," *Journal of Acoustical Society of America,* vol. 107, no. 5, pp. 2523-2534, 2000.

[130] S. M. Kim, Active Control of Sound in Structural-Acoustic Coupled Systems, PhD Thesis, Southampton: University of Southampton, 1998.

[131] D. J. Nefske, J. A. Wolf and L. J. Howell, "Structural-Acoustic Finite Element Analysis of the Automobile Passenger Compartment: A Review of Current Practice," *Journal of Sound and Vibration,* vol. 80, no. 2, pp. 247-266, 1982.

[132] C. K. Song, J. K. Hwang, J. M. Lee and J. K. Hedrick, "Active Vibration Control of Structural-Acoustic Coupling System of a 3-D Vehicle Cabin Model," *Journal of Sound and Vibration,* vol. 267, no. 4, pp. 851-865, 2003.

[133] F. J. Fahy, "Vibration of Containing Structures by Sound in the Contained Fluid," *Journal of Sound and Vibration,* vol. 10, no. 3, pp. 490-512, 1969.